Plasmonic Substrates and Their Applications in Photocatalytic Water Splitting and Molecular Electronics

Thesis submitted in accordance with the requirements of the University of Liverpool for the degree of Doctor in Philosophy by Joseph Horne.

March 2021

Abstract

This work describes research that investigated the effects of plasmonic substrates on the photocatalytic ability of hematite photoelectrodes and molecular conductance measurements. Initially a platform of plasmonic substrates was developed using nanosphere shadow lithography (NSL). In short, the NSL technique involves the creation of a mask by the self-arrangement of polystyrene beads on a substrate surface, material is then evaporated, or otherwise deposited, through the mask and the mask is then removed to reveal the resultant nanostructures. In optimal conditions the beads arrange in a hexagonally close packed configuration such that the apertures between the beads are triangular in shape and regularly spaced. The NSL fabrication method allows for the production of large-scale hexagonally arranged arrays of triangular nanoparticles. The size and shape of these nanostructures can be altered through selection of bead diameter, angle of deposition, and with complimentary processes, such as radial etching of the bead mask. Arrays of nanotriangles with average side-lengths of (205±1) nm and (88±1) nm were fabricated using masks with 800nm and 300nm diameter beads respectively. Coinage metals, Au, Ag, Al, and Cu were used as deposition targets in NSL to develop equally sized nanostructures with differing plasmonic properties and characterised using UV-Vis and SEM imaging.

These plasmonic substrates were used in order to observe the effects on the water-splitting ability of α-Fe_2O_3 (hematite). Hematite was deposited using electrodeposition and atomic layer deposition on top of plasmonic Au, Ag, and Al substrates fabricated using the NSL method. This represents the first reported case of a direct comparison between identical nanostructure morphologies fabricated using different plasmonic metals and the effects on photocurrent density of a photocatalytic electrode. Photocurrent density measurements were performed using chronoamperometry and the incident photon-to-electron conversion

efficiency (IPCE) was measured in a three electrode photoelectrochemical (PEC) cell. Enhancement in the photocurrent density by a factor of 3.6 was seen for Au nanostructure decorated hematite films made through electrodeposition. TiO_2 layers were used in order to selectively block charge carriers in the films and assist in enhancing the photocatalytic ability of the electrodes. Electrodeposited hematite films with TiO_2 capped Ag nanostructures at the back interface showed great enhancement in the photocurrent density and this was reflected in the IPCE. The champion Ag/TiO_2/hematite electrode gave a photocurrent density enhancement factor of 7 and outperformed the previous champion Au/hematite electrode by almost double.

Atomic layer deposited hematite films were also studied. All saw a reduction in photocurrent density when the metal nanostructure layers were included however, spectral enhancement was seen in the IPCE for some electrode configurations. The inclusion of an alumina intermittent layer, deposited onto the nanostructures by ALD prior to the hematite deposition, gave a real spectral enhancement in the 360nm to 440nm section of the IPCE spectrum for Au/Al_2O_3/hematite composite electrodes. This represents the first reported time of hematite deposited onto metal nanostructures using ALD and the first reported plasmonic enhancement of ALD hematite films.

Au nanotriangle arrays were used as substrates for molecular conductance measurements using conductive scanning probe microscopy techniques (SPM). This work represents the first time that molecular conductance measurements have been performed on nanostructured substrates made using NSL. Spherical Au nanoparticles in aqueous suspensions were also synthesised using a step-wise growth method and deposited on molecular monolayer coated substrates to observe the plasmonic effects on conductance values. These measurements were complimented with FDTD simulations in order to inform the experimental design. Conductance values were measured in both configurations in dark

conditions and under illumination from laser light at various wavelengths and the effects of the plasmonic substrates on the single molecule chemistry.

Acknowledgements

I would like to thank my supervisors, Dr Frank Jäckel, and Prof Richard Nichols, for giving me the opportunity to carry out my PhD, and their continued support and guidance throughout the process. A special thanks to Frank for the hours of proofreading and help throughout the writing up of this thesis.

I would also like to thank other Academic staff at the Stephenson Institute for the use of equipment, technical wisdom, and training that made this research possible.

A big thanks has to go to Vince Vasey, the SIRE's wizard in residence, without whom this project would have failed at the first slight bump in the road.

To all the fantastic postdocs at the University of Liverpool who supported me with experiments, advice and friendship throughout the last four years, namely Dr Mark Forster, Dr David Costa Milan, Dr Oliver Hutter, and Dr Andrea Vezzoli, thank you.

A special mention for the other members of the Jäckel Research Group, Graeme Smith and Nicole Fleck. Thanks for listening to me complaining and for being there throughout the last four years, and to Nicole for being a great housemate for a brief 2-month period. Thanks to all the other people at the SIRE for being great friends and all the hilarious moments that I will keep with me.

Thank you to my parents, Lorraine and Carl, for the unwavering support and love that has made all I have achieved possible.

Finally, I would like to say thank you to Lucy. You have been the most supportive and loving person I could have hoped to share this all with. I will never be able to thank you enough for all that you have done throughout the past 5 years.

Contents

1. Overview

This section provides an overview of the work presented in this thesis. A brief description of what was performed and achieved in the subsequent chapters of this thesis is given. The work began by developing a platform of plasmonic substrates which were then applied in the fields of photocatalytic water-splitting and molecular electronics in order to investigate the potential for enhanced performance of the devices.

1.1. Development of plasmonic substrates

A platform of plasmonic substrates was developed using nanosphere shadow lithography (NSL). This method offers a low-cost and scalable route to large-scale nanofabrication[1] which is a requirement for future possible energy applications due to economies of scale. In order to be realised in future applications, nanofabrication techniques will be required to be comparable in terms of cost and performance as the current technology. Whether that be hydrogen production through steam reforming of methane or, with regards to molecular electronics, current transistor technology.

Nanosphere shadow lithography (NSL) is a bottom-up method of fabricating nanoparticle arrays on a substrate.[1–3] Figure 1-1 shows a basic schematic of the nanosphere shadow lithography. Briefly, an array of hexagonal close-packed nanospheres is formed on the surface as mask layer. Subsequent material layers are then deposited through the mask forming arrays of nanotriangles arranged in a Fisher pattern. The nanosphere mask can then be removed through tape cleaving or sonication revealing the nanostructures on the substrate.

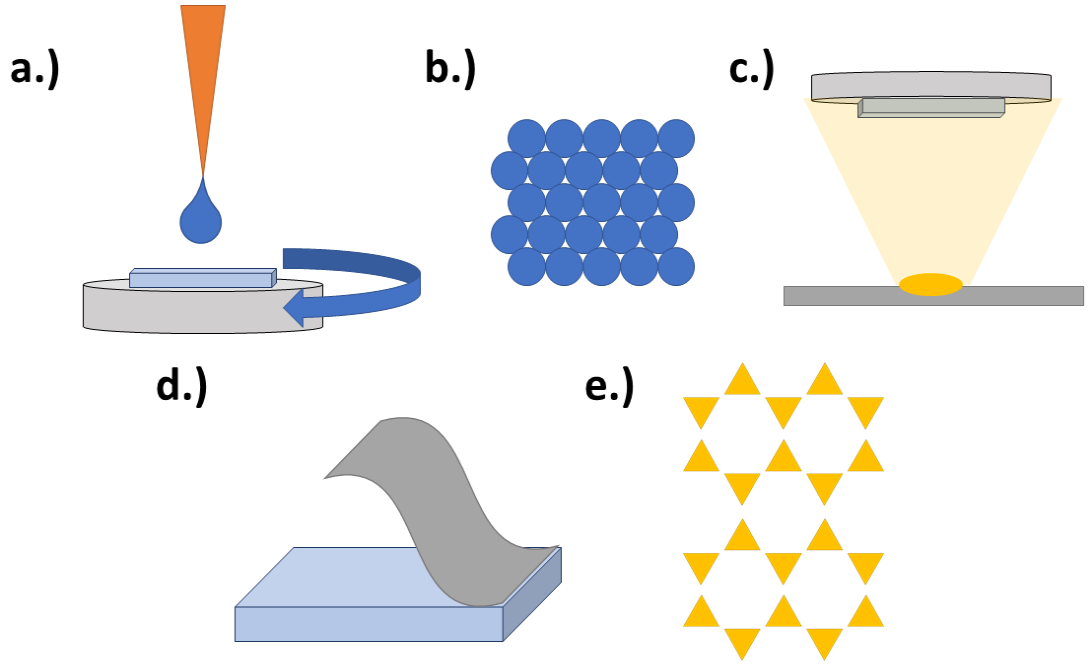

Figure 1-1 – A schematic showing the basic workflow of NSL. A.) Spin-coating of the PS bead solution onto cleaned substrates. B.) The developed mask of PS nanospheres in hexagonal close-packed arrangement. C.) Evaporation or deposition of relevant material. D.) Tape cleaving of the PS mask. E.) The final triangular nanostructures arranged in the characteristic Fisher pattern.

Nanotriangle arrays with varying size parameters were fabricated by utilising different sizes of polymer beads and incorporating plasma etch procedures radially etch the nanospheres in the mask. Utilising polymer beads with different diameters to form the initial bead mask resulted in nanotriangles with different triangle side-lengths and particle spacings. The two bead choices used in this work had diameters of 800nm and 300nm resulting in nanoparticles with side-lengths of 200nm and 90nm respectively. A plasma-etch step was also used to radially etch the polymer bead mask which increased the size of the apertures between adjacent beads. This could be used to increase the sizes of the triangular nanoparticles and, in the extreme, form nanohole arrays.

Nanostructure arrays were also fabricated using an assortment of metals which were chosen due to their known plasmonic properties. These variations allowed for direct comparison between different metals and nanoparticle sizes. The nanostructured substrates that were developed were then applied in two use cases. Firstly, as substrates for Hematite

based photoanodes for water-splitting and secondly as substrates for molecular wire conductance studies.

1.2. Plasmonic Enhancement of Hematite

Hematite (α-Fe_2O_3) is an earth abundant semiconductor material with a reported bandgap of 1.9~2.1eV and a suitable band position to be a photoanode candidate for photocatalytic water-splitting. Hematite can be fabricated using industrially scalable methods such as electrodeposition and a hydrothermal deposition technique. The earth abundance of hematite identifies the material as a low-cost option to produce hydrogen the industrial scales necessary to compete with cheaper non-renewable processes, and the scalability of the fabrication process is necessary to realise large-scale green hydrogen production.

The triangular nanostructure arrays were initially fabricated using gold, silver and aluminium on ITO-coated glass slides through the nanosphere lithography technique. Hematite layers were subsequently grown on top of the metal nanostructures through an electrodeposition technique adapted from Zandi et al[4] and then using an atomic layer deposition technique (ALD). The electrodeposition was performed in a photoelectrochemical cell using chronocoulometry to control deposition thickness. The ALD process was developed by Natalie Bavis in Dr Richard Potter's group at the Electrical and Electronic Engineering department at the University of Liverpool. Figure 1-2 shows illustrations of the sample architectures. The thicknesses of the electrodeposited and ALD deposited films was measured using atomic force microscopy. A small region of the hematite layers was scratched away and the profiles of the films were measured by scanning the AFM tip over the scratch onto the intact film. The films were measured at (415±8) nm and (36±1) nm for the electrodeposited and ALD film respectively.

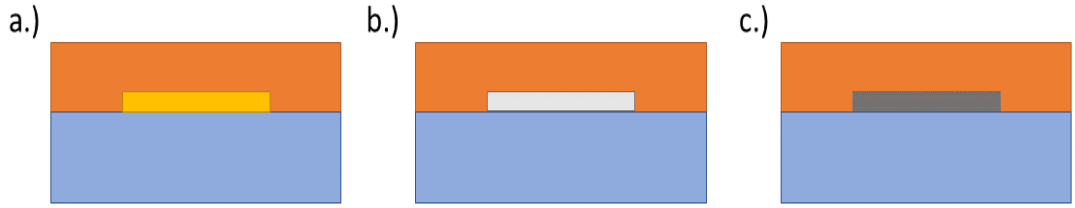

Figure 1-2 Illustration of sample architectures. Metal nanostructures were fabricated on ITO coated glass slides, hematite layers were deposited on top of the nanostructure films. A.) Hematite deposited Au nanostructure films. B.) hematite deposited on top of Ag nanostructures. C.) Hematite deposited on Al nanostructure films. The ITO coated glass substrate is shown in light blue, the hematite layers in orange, and the various metals in relevant colours.

The photocatalytic ability of the films was analysed using photoelectrochemical methods. The electrodes were loaded into a custom three-neck photoelectrochemical cell as the working electrode with apt foil counter electrode and a homemade Ag/AgCl reference electrode. Linear sweep voltammetry was used to test photoresponse, chronoamperometry was used to measure photocurrent densities and IPCE was used to analyse the spectral photoresponse and compare samples.

Intermittent layers of TiO_2 and Al_2O_3 were used as hole-blocking layers to attempt to optimise the photocurrent densities and plasmonic enhancement effects. These layers were deposited onto the metal nanostructures prior to hematite deposition. The sample architectures are shown in figure 1-3. Figure 1-3a to c show the configurations for the samples with the TiO_2 interlayers. The samples were made during the electrodeposition work in chapter 4, with the interlayer chosen as a hole blocking layer in order to boost the plasmonic enhancement by selectively blocking charge carrier transport in and out of the hematite layer. Hematite was deposited using the same electrodeposition method as the samples without the TiO_2 layer. The TiO_2 layers were deposited using plasma sputtering of a TiO_2 target under argon, to a thickness of 3nm. The TiO_2 was sputtered through the PS nanosphere mask after the metal layers were deposited resulting in TiO_2 capped metal nanostructures. This was done in order to ensure that much of the ITO coated substrate

remained uncovered such that electrodeposition could still be performed using the same technique as the prior samples.

Figures 1-3d to f show the configurations for the samples with the Al_2O_3 interlayer. The samples were made during the atomic layer deposition work in chapter 5. Alumina was chosen as a dielectric layer, again to block unwanted charge carrier transport and to assess the effects on the plasmonic enhancement. The Al_2O_3 layers were deposited to a thickness of 1nm using atomic layer deposition and was deposited prior to the hematite layers. The PS nanosphere mask was removed prior to the ALD process such that the alumina layer covered the entirety of the substrate surface and the nanoparticles, this is shown in the figures.

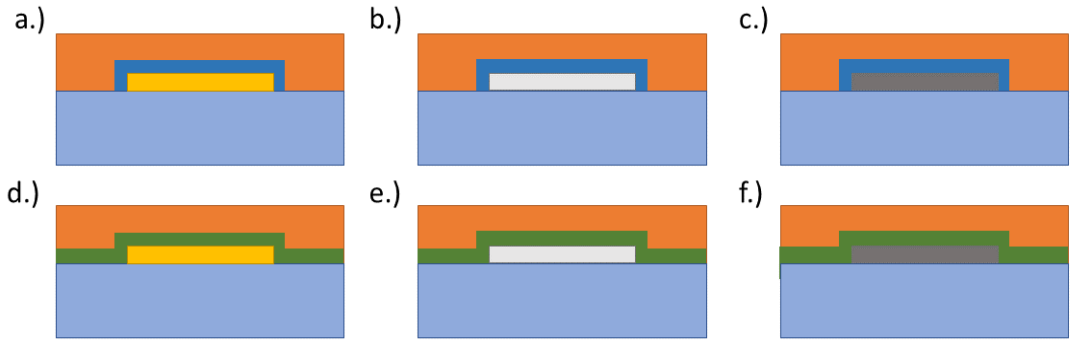

Figure 1-3 Illustrations showing sample architecture with intermittent layers. The TiO_2 layers are shown in deep blue and the Al_2O_3 layers in green. The other elements are shown I the same colours as previously.

1.3. Electronic Characterisation of Molecules on Plasmonic Substrates

Molecular electronics is the study of the electrical properties of organic molecules. In this work the metal nanostructured substrates fabricated previously were used to investigate whether the conductance of certain molecular wires could be plasmonically enhanced using incident light. As well as the gold nanostructured substrates fabricated using NSL, spherical gold nanoparticles on gold substrates were also employed as plasmonic substrates. The

spherical nanoparticles were synthesised using a step-wise growth method taken from Bástus et al.[5]

The samples were made by the formation of self-assembled monolayers (SAMs) of the molecule in question onto the relevant substrate. The SAMs are formed by immersing the substrate in dilute solutions of the molecule, after some time the substrates were removed and rinsed under ethanol. The immersion time for each molecule was optimised during the study. For the Au nanosphere on gold substrate samples the AuNPs were attached onto the SAMs by immersing the substrate in nanoparticle solutions. The immersion times for this process were also optimised during this work. Figure 1-4 shows a schematic of the two sample configurations used in this study.

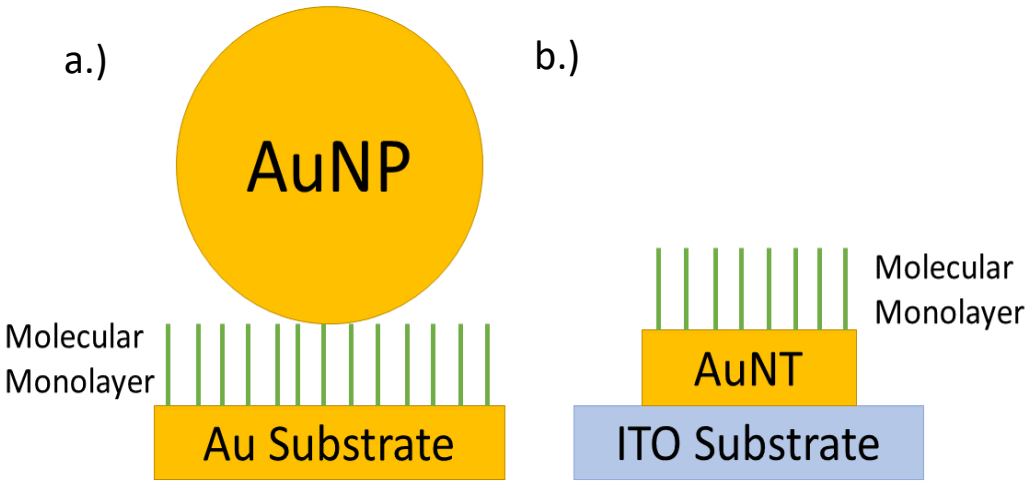

Figure 1-4 – Schematic showing the two different configurations used for in the molecular electronics work. A.) A gold nanoparticle immobilized on top of a self-assembled molecular monolayer on a gold substrate. B.) A molecular monolayer formed on top of a gold nanostructure that was fabricated on an ITO covered glass substrate

In order to measure the conductance of the molecules scanning probe microscopy techniques were employed. These techniques utilise both atomic force microscopy (AFM) and scanning tunnelling microscopy (STM) apparatus. The method of measuring the conductance values is marginally the same for both microscopy techniques. In short, a conductive tip was brought into contact with sample surface. Current-voltage characteristics

were taken by sweeping bias voltage between tip and sample while measuring current flow. The conductance values for the molecules were then calculated using the data gathered. By performing these experiments in dark conditions and under illumination from various lasers, potential plasmonic effects could then be observed.

The first molecule tested was a molecular wire consisting of a 4,4'-bipyridinium moiety with 9 methylene groups attached at either side referred to as 9V9 where V represents the 4,4'-bipyridinium group.[6] The other molecules tested were 1-decanethiol and 1,9-nonanedithiol. Conductance values for 9V9 between an Au substrate and an immobilized AuNP were measured using STM probe contacted to the AuNP. The conductance was measured in dark conditions and under illumination by a 473nm blue laser and a 644nm red laser. Conductance values for 9V9, 1-decanethiol and 1,9-nonanedithiol were measured by attaching SAMs directly onto 200nm side-length Au nanotriangle arrays.

1.4. Bibliography

1. Zhao, J. *et al.* Hole-mask colloidal nanolithography combined with tilted-angle-rotation evaporation: A versatile method for fabrication of low-cost and large-area complex plasmonic nanostructures and metamaterials. *Beilstein J. Nanotechnol.* **5**, 577–586 (2014).

2. Kosiorek, A., Kandulski, W., Chudzinski, P., Kempa, K. & Giersig, M. Shadow Nanosphere Lithography : Simulation and Experiment. *Nano Lett.* **4**, 1359–1363 (2004).

3. Kosiorek, A., Kandulski, W., Glaczynska, H. & Giersig, M. Fabrication of Nanoscale Rings , Dots , and Rods by Combining Shadow Nanosphere Lithography and Annealed Polystyrene Nanosphere Masks. *Small* **1**, 439–444 (2005).

4. Zandi, O., Schon, A. R., Hajibabaei, H. & Hamann, T. W. Enhanced Charge Separation and Collection in High-Performance Electrodeposited Hematite Films. *Chem. Mater.* **28**, 765–771 (2016).

5. Bastús, N. G., Comenge, J. & Puntes, V. Kinetically controlled seeded growth synthesis of citrate-stabilized gold nanoparticles of up to 200 nm: Size focusing versus ostwald ripening. *Langmuir* **27**, 11098–11105 (2011).

6. Haiss, W. *et al.* Wiring nanoparticles with redox molecules. *Faraday Discuss.* **125**, 179–194 (2004).

2. Introduction

2.1. Plasmons

A plasmon is the coherent oscillation of conduction band electrons in a metal, these electron oscillations are driven by the oscillating electric fields from incident electromagnetic radiation.[1,2] At the interface of a metal and a semiconductor, or dielectric, electromagnetic waves can propagate due to the interaction of electromagnetic fields and the oscillations of the free electron gas, these are called surface plasmon polaritons (SPP). In metallic nanoparticles, if the dimensions of the particle are smaller than the wavelengths, λ, of visible light, the SPPs will be confined to the entire surface of the metal and exhibit strong dipolar excitations known as the localised surface plasmon resonance (LSPR). Figure 2-1 shows a basic schematic of the localised surface plasmon generation in a metal nanoparticle under illumination of electromagnetic radiation. The resonant frequency of these excitations, and therefore the plasmon energy, is determined by the dielectric properties of the metal and surrounding medium, and the size and shape of the particle.[1–3]

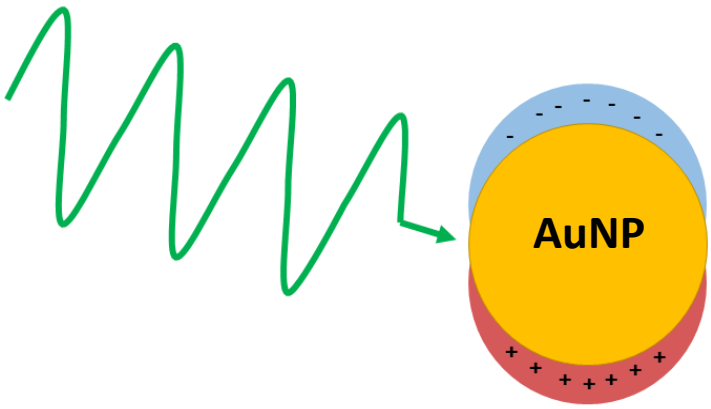

Figure 2-1 – A schematic showing the LSPR. Incident light at a resonant frequency drives an oscillation of the free conduction band electrons. These oscillations are confined to the nanoparticle surface.

Noble or coinage metal nanoparticles such as, gold, silver and copper, which have high electron mobilities can exhibit strong plasmon resonances with energies in the visible region of the electromagnetic spectrum. Localised surface plasmons, owing to the coherent oscillation of electrons around the NP surface, can give rise to strong electromagnetic fields in the near field, scatter light preferentially at the resonance energy and lead to strong localized heating.[3,4] If the metal NP is in contact with a semiconductor, or other absorber, electrons with sufficient energy can be injected from the metal to the absorber before relaxation. These additional hot carriers can then generate a current flow or be used to drive chemical reactions in a process known as hot electron injection.[5,6]

2.2. Plasmonic Enhancement mechanisms

Plasmonic enhancement can work through a variety of mechanisms. Generally, these are near and far-field optical scattering, resonant energy transfer, localised heating, and hot electron injection. The various damping mechanisms of the coherent electron oscillations are what lead to the effects. When driven at resonance the electron oscillations can act as an electromagnetic dipole re-emitting light coherently into the far-field at the resonant frequency, known as light scattering. Light concentration is used to describe the concentration of energy in the high electric fields that occur in the near-field due to the electron oscillation. This oscillation of free electrons can also undergo damping via the Joule effect where energy is dissipated as heat, this localised heating occurs in short timescales unachievable on a macroscopic scale leading to high dynamic control in chemical processes. Hot electron injection occurs when an electron from below the metal Fermi level is promoted to a higher energy level above the Fermi level. This hot-electron can be directly transferred to a nearby acceptor or, as this electron relaxes, electron-electron scattering can cause other high-energy electrons to be transferred to the acceptor located near the NP surface. Plasmon-induced resonant energy transfer is a near-field process by which the oscillating

electron cloud creates a dipole field, which can induce electron-hole generation in a nearby semiconductor. [3,7]

2.3. Importance of photocatalysis for hydrogen production

Hydrogen is used in the chemical process industry to aid with the refinement of oil and steel, and most importantly, in the production of ammonia through the century old Haber-Bosch process. Ammonia is one of the necessary building blocks of life on earth, huge amounts of ammonium nitrate are required each year as fertilizer for the farming industry to supply the planet with food. The vast majority of the hydrogen produced each year (~95%) is made using steam methane reforming. Through this method hydrogen is made by reacting methane from natural gas with steam to produce H_2 and CO. This is often done without any carbon capture resulting in huge amounts of carbon released into the atmosphere. With the threat of climate change and a rapidly increasing human population there is a strong need for a renewable source of hydrogen, that does not contribute to greenhouse gas emission, to produce 'green' ammonia and maintain a reliable food supply for the planets human population and limiting the output of greenhouse gases.[8,9]

Photocatalytic water-splitting offers a route to green hydrogen directly from water using incident solar radiation at the earth's surface. Fujishima and Honda first achieved electrolysis of water using an n-type rutile TiO_2 photoanode and Pt cathode in an electrochemical cell.[10] TiO_2 is a well-studied wide-band gap semiconductor that efficiently converts UV radiation to charge carriers, however in order to develop an efficient water-splitting device smaller band-gap semiconductors are required in order to utilise the maximum amount of solar-radiation on earth.[11–13]

The potential at which overall water splitting occurs is 1.23V at pH 0, with H^+ ions reduced to H_2 at 0V vs RHE (reversible hydrogen electrode) and H_2O oxidised to O_2 at -1.23V vs RHE at pH 0. Therefore, the conduction band of the photocathode material must be higher in energy

than the hydrogen reduction potential in order for the electrons generated through excitation to participate in the half-reaction. This is because the hydrogen reduction pathway presents a lower energy state for the electrons to transfer to. The photoanode valence band must be lower than -1.23V vs RHE in order for the water oxidation half reaction to occur where holes are scavenged from the semiconductor by the water molecules. This therefore requires a semiconductor with a bandgap energy exceeding 1.23 eV and while there a plenty of materials with band-gap energies higher than 1.23eV there are few candidates that meet both of these band position requirements. whereby both bands straddle the water oxidation and reduction potentials, and show good stability in aqueous conditions.[14]

The solar-to-hydrogen efficiency, η_{STH}, of a photocatalytic is used as a comparable metric with water-splitting electrodes and is calculated by taking the hydrogen gas production rate, Φ_{H2}, multiplied by the Gibbs free energy of hydrogen gas (237kJ mol^{-1} at 25°C), $G^0_{f,H2}$, all divided by the total irradiation power, P_{light}, when the sample is illuminated using simulated 1.5AMG solar irradiation.[14]

Equation 1

$$\eta_{STH} = \left[\frac{\Phi_{H2} \times G^0_{f,H2}(kJ\ mol^{-1})}{\mathrm{P}_{light}(mW\ m^{-2})}\right]_{AM\ 1.5G}$$

For each semiconductor material there is a theoretical limit to the η_{STH} based on the material band-gap. The band-gap determines how much of the solar spectrum can be absorbed by the material, therefore the wider the bandgap of the material, the smaller the section of the incident spectrum available to them. This results in a maximum total efficiency as there is a limit to the amount of 'power in' compared to the 'power out'.[9] With a band-gap of around 3.2eV, TiO_2 has a potential STH efficiency of ~2%, meanwhile a well-studied smaller band-gap material, hematite, with a reported band-gap of between 1.9 and 2.2 eV, shows a potential STH efficiency of 16.8%.[14]

In order to reach the efficiencies and costs needed for photocatalytic hydrogen production to compete with steam methane reformed hydrogen low-cost earth abundant materials with high theoretical yields will be needed. To reach these potentials cocatalysts and enhancement systems, such as plasmonics, will be required to complement the semiconductor cells. Co-catalytic systems such as Rh, Pt and Co-Pi (cobalt phosphate)have been shown consistently to enhance efficiency to reach theoretical limits but more study is needed.[14–17] Chapters 4 and 5 of this thesis aim to observe plasmonic enhancement in the photocurrent densities measured for hematite photoanodes, specific examples of studies using hematite as a photoanode will be discussed there in more depth.

2.4. Importance of molecular wires for nanoscale electronic devices

As the electrical junctions in modern semiconductor chips get smaller through advancements in lithography techniques, quantum effects, such as tunnelling, cause detrimental loss of charges. This gives an effective lower limit on the single transistor size, and with that the density of transistor components in modern computer chips. This is set to bring an end to the exponential growth in computing power and speed seen over the last 40 years. As the rapid diminution of solid-state transistor size, famously described by Moore's law and Dennard scaling, comes to an end it is important to plot out a path in which the devices of the future can continue to solve calculations at incrementally compounding rates.[18] One option would simply be to make processors and therefore computers increasing larger in effect to add more transistor junctions and overcome the limited size of the individual transistors. Another path would step away from traditional semiconductor devices altogether and adopt transistors and electrical components devised of organic molecules.

Molecular electronics is the study of the electrical properties of single molecules using techniques such as scanning probe microscopy, and mechanically controlled break-junctions

in order to understand electrical transport through organic molecules design electrical components, such as diodes, capacitors, and transistors at the nanoscale using such molecules. To achieve the production of such devices it is important to be able to reliably and reproducibly observe and design the electrical properties of molecular electrical junctions. [19–23]

2.5. Bibliography

1. Maier, S. A. *Plasmonics: Fundamentals and applications*. *Plasmonics: Fundamentals and Applications* (Springer, 2007).

2. Rivera, V. A. G., Ferri, F. A. & Marega, E. Localized Surface Plasmon Resonances: Noble Metal Nanoparticle Interaction with Rare-Earth Ions. in *Plasmonics - Principles and Applications* (ed. Young Kim, K.) 283–312 (InTech, 2012).

3. Baffou, G. & Quidant, R. Nanoplasmonics for chemistry. *Chem. Soc. Rev.* **43**, 3898–3907 (2014).

4. Atwater, H. A. & Polman, A. Plasmonics for improved photovoltaic devices. *Nat. Mater.* **9**, 205–213 (2010).

5. Ratchford, D. C., Dunkelberger, A. D., Vurgaftman, I., Owrutsky, J. C. & Pehrsson, P. E. Quantification of Efficient Plasmonic Hot-Electron Injection in Gold Nanoparticle–TiO 2 Films. *Nano Lett.* **17**, 6047–6055 (2017).

6. Valenti, M. *et al.* Hot Carrier Generation and Extraction of Plasmonic Alloy Nanoparticles. *ACS Photonics* **4**, 1146–1152 (2017).

7. Cushing, S. K. *et al.* Controlling Plasmon-Induced Resonance Energy Transfer and Hot Electron Injection Processes in Metal@TiO 2 Core–Shell Nanoparticles. *J. Phys. Chem. C* **119**, 16239–16244 (2015).

8. Rapier, R. Life Cycle Emissions of Hydrogen. *The 4th Generation* https://4thgeneration.energy/life-cycles-emissions-of-hydrogen/ (2020).

9. Chu, S. *et al.* Roadmap on solar water splitting: Current status and future prospects. *Nano Futur.* **1**, (2017).

10. Fujishima, A. & Honda, K. Electrochemical photolysis of water at a semiconductor

electrode. *Nature* **238**, 37–38 (1972).

11. Li, J. *et al.* Solar Hydrogen Generation by a CdS-Au-TiO $_2$ Sandwich Nanorod Array Enhanced with Au Nanoparticle as Electron Relay and Plasmonic Photosensitizer. *J. Am. Chem. Soc.* **136**, 8438–8449 (2014).

12. Wang, J., van Ree, T., Wu, Y., Zhang, P. & Gao, L. Metal oxide semiconductors for solar water splitting. in *Metal Oxides in Energy Technologies* 205–249 (Elsevier, 2018).

13. Honda, M., Kumamoto, Y., Taguchi, A., Saito, Y. & Kawata, S. Plasmon-enhanced UV photocatalysis. *Appl. Phys. Lett.* **104**, 061108 (2014).

14. Sivula, K., Le Formal, F. & Grätzel, M. Solar Water Splitting: Progress Using Hematite (α-Fe2O3) Photoelectrodes. *ChemSusChem* **4**, 432–449 (2011).

15. Prévot, M. S. & Sivula, K. Photoelectrochemical tandem cells for solar water splitting. *J. Phys. Chem. C* **117**, 17879–17893 (2013).

16. Cheng, W. H. *et al.* Monolithic Photoelectrochemical Device for Direct Water Splitting with 19% Efficiency. *ACS Energy Lett.* **3**, 1795–1800 (2018).

17. Jeon, T. H., Moon, G. hee, Park, H. & Choi, W. Ultra-efficient and durable photoelectrochemical water oxidation using elaborately designed hematite nanorod arrays. *Nano Energy* **39**, 211–218 (2017).

18. Jones, R. Technological innovation in the linear age – Soft Machines. *Soft Machines* http://www.softmachines.org/wordpress/?p=2188 (2018).

19. Mathew, P. T. & Fang, F. Advances in Molecular Electronics: A Brief Review. *Engineering* vol. 4 760–771 (2018).

20. Akkerman, H. B., Blom, P. W. M., Leeuw, D. M. De & Boer, B. De. Towards molecular

electronics with large-area molecular junctions. **441**, 69–72 (2006).

21. Haiss, W. *et al.* Impact of junction formation method and surface roughness on single molecule conductance. *J. Phys. Chem. C* **113**, 5823–5833 (2009).

22. Morita, T. & Lindsay, S. Determination of single molecule conductances of alkanedithiols by conducting-atomic force microscopy with large gold nanoparticles. *J. Am. Chem. Soc.* **129**, 7262–7263 (2007).

23. Tao, N. J. *Electron transport in molecular junctions*. *nature nanotechnology* | vol. 1 www.nature.com/naturenanotechnology (2006).

3. Background

3.1. Hematite as a water-splitting photocatalyst

Iron is the fourth most abundant element in the earth's crust and as such, Hematite (α-Fe_2O_3) has been extensively studied as a candidate for anodic photocatalytic water-splitting.[1] The low-cost and earth abundance of the material makes it especially interesting for study due to the potential for large-scale low-cost applications. In comparison to other n-type semiconductor water-oxidation photocatalysts such as ZnO or TiO_2, hematite absorbs a considerably larger fraction of the visible spectrum owing to its relatively lower reported band-gap of 1.9-2.2eV.[2–4] The lower band-gap of hematite, compared to TiO_2, WO_3, and $BiVO_4$, means that the maximum theoretical photocurrent density of ~12mA·cm^{-2} is one of the highest possible photocurrents available for currently studied water-splitting candidate materials. This further increases the interest for study as the margin for improvement is vast.[5,6] The band-structure of hematite is ideal for anodic photocatalytic water-oxidation due to the valence band energy being lower than the water oxidation potential.[7] Hematite is an n-type metal-oxide semiconductor. As an n-type semiconductor photocatalyst, hematite operates as a photoanode in the photoelectrochemical cell (PEC) in which minority holes in the valence band oxidise water.[8] The stability of hematite in aqueous solutions and at a broad pH range enhances it suitability for water-splitting.

Hematite has a theoretical potential to achieve photocurrent densities of 12.5 mAcm^{-3} however due to inherent restrictions in the material the current maximum photocurrent densities that have been achieved are around 6 mA.cm^{-3}.[1,9] Despite the high theoretical photocurrent densities available hematite electrodes consistently show low photocurrent densities due to poor electrical conductivity (~10^{-6} Ω^{-1} cm^{-1}), the short (<10 ps) excited state lifetimes, short hole diffusion length (≈2-4 nm), and poor surface oxygen evolution reaction kinetics.[3] Poor electrical conductivity impedes the mobility of charge carriers through the

material increasing the probability of recombination and lowering the amount of useful charge carriers generated through the absorption of incident light. The short hole diffusion length results in a loss of useful charge carriers as only holes generated very close to the interface can be used in the oxygen reduction reaction. Poor surface oxygen evolution kinetics refers to the poor adsorption of OH^- ions at the interface which limits the probability of charges that make it to interface participating in the oxygen reduction reaction. Enhancement systems should be targeted at improving or overcoming the inherent limits such as plasmonic materials to increase charge carrier generation or cocatalysts at the interface to aid the reaction kinetics. This results in a material with large room for improvement and requirement for better understanding and therefore a good candidate to study enhancement effects on.

In order to compete with commercial hydrogen, photocatalytic systems would require STH efficiencies in excess of 25%. Device architectures including cocatalysts and enhancement systems, such as plasmonics, will be required to complement the semiconductor cells. Co-catalytic systems such as Rh, Pt and Co-Pi (cobalt phosphate)have been shown consistently to enhance efficiency to reach theoretical limits but more study is needed.[1,9–11] Tandem devices with hematite, which use complementary semiconductor materials as the photocathode, have shown STH efficiencies of 27% as upper limits in theoretical studies.[5] Chapters 4 and 5 of this thesis aim to observe plasmonic enhancement in the photocurrent densities measured for hematite photoanodes, specific examples of studies using hematite as a photoanode will be discussed there in more depth.

3.2. Plasmonic enhancement of hematite and how it solves the issues

Plasmonic enhancement of the photocatalytic ability has been achieved by introducing nanoparticles made from Au[12] and Ag[13] into the device architecture. The plasmonic device

configuration can be altered in order to overcome specific limiting factors in hematite and there are many ways plasmonic nanoparticles can be incorporated into a hematite-based photocatalytic device. Figure 3-1 shows three ways in which plasmonic NPs can be incorporated into a semiconductor film.

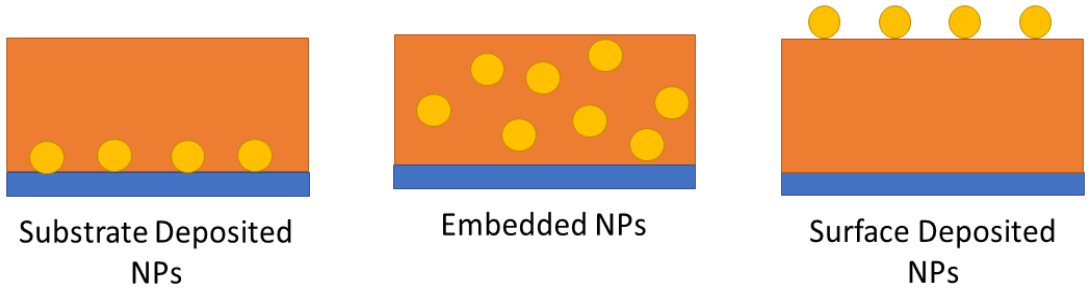

Figure 3-1 - Schematic showing various ways that plasmonic nanoparticles have been incorporated into a hematite film in the literature.

Depositing very thin films of the order of 10's of nanometres can help to overcome short hole diffusion lengths and reduce charge carrier recombination probability. When thin films are excited under bias, the depletion region formed by drifting charges dominates the bulk of the semiconductor this aids the mobility of the excited charges across the electric field in the film.[4] High aspect ratio thin-films maximise the volume to surface area ratio resulting in a higher proportion of total excited charge carriers originating near to the interface that are then able to drift toward the interface and participate in the water-splitting reaction.[4] However, producing thin-films reduces the total absorption of incident light, therefore plasmonic nanoparticles can be introduced in order to boost overall light absorption in the film. These nanoparticles allow for the benefits of thin-film semiconductor devices whilst giving absorption characteristics similar to much thicker films.[14] The plasmonic properties of the nanostructures can be tuned in order to scatter light at wavelengths complementary to the semiconductor absorption. Substrate deposited nanoparticles can also boost the photocatalytic ability of semiconductor films by taking advantages of the other plasmonic enhancement mechanisms such as PIRET[15] and hot electron injection.[16]

Plasmonic metal nanoparticles can be deposited directly onto a substrate in a multitude of ways including drop-casting spin-coating[14] and, as discussed in this thesis, nanosphere shadow lithography.[17] By depositing the nanostructure film directly onto the substrate the morphology and distribution of the nanoparticles can be carefully controlled in turn allowing for accurate tuning of the plasmonic absorption characteristics.[15,16] This fine control of the nanostructure distribution is not possible in embedded systems and difficult in surface deposited configurations due to either rough topology of deposited semiconductor films or issues with adhesion of the metal films. These decorated substrates can then be coated with hematite thin-films using fabrication methods like atomic layer deposition.

Plasmonic nanoparticles can be deposited in conjunction with the semiconductor material resulting in a film that is embedded with nanoparticles.[12,18–20] This increases the surface area of the contact between the semiconductor and metal boosting the efficiency of the nanoparticle surface plasmon enhancement effects.[12,18] With surface mounted nanoparticles any light that is scattered in the direction of the substrate is lost. Whereas in the embedded configuration the nanoparticle is surrounded by the absorber material and reducing these losses. This means that the additional optical absorption gained by including plasmonic nanoparticles is more efficiently utilised and converted into excited charge carriers.[20] The embedded configuration offers the same benefits as the substrate mounted NPs with regards to increasing the overall light absorption from the device. The increased optical absorption characteristics of the film allows for thinner films to be fabricated which can help to overcome short carrier diffusion and poor carrier mobility in hematite.

The increased contact area between the plasmonic metal NPs also means that hot charge-carriers generated by the excited plasmons are more efficiently scavenged by the surrounding absorbing medium compared to both the substrate and surface deposited configurations.[18] This increase in energetic carriers can increase the photocatalytic ability of

the film by providing more charge carriers can reach the interface to contribute to the water-splitting reaction.[18]

Plasmonic nanoparticles can be deposited onto the semiconductor surface in a multitude of ways. These include through immersion of the semiconductor material in a nanoparticle solution[21], electrodeposited or electrophorectically[12], and the calcination of thin metal films deposited directly onto the semiconductor surface.[22] Surface deposited metal nanoparticles can assist with photocatalytic water-splitting directly by acting as co-catalysts and reducing the overpotential of the water oxidation reaction,[21] but can also provide enhancement through plasmonic mechanisms.[12,19,21,22] Light scattered by plasmonic nanoparticles at the semiconductor surface excites charge carriers at the surface which can be immediately used in the reaction occurring at the interface.[22] This also occurs through plasmonic resonant energy transfer, producing more charge-carriers at the interface and boosting the efficiency of the system.[12] Hot-electrons from the excited plasmonic nanoparticles can also participate in the water-splitting reaction either directly, or through injection into the semiconductor at the surface.[19,23,24] Hot electrons injected directly into the semiconductor at the interface can be used more efficiently in the reaction than those that must migrate through the semiconductor. Direct hot-electron injection would occur only when the nanoparticle is in contact with the electrolyte, or reactant, as in the surface mounted configuration. The surface mounted configuration inherently has lower contact surface area to the semiconductor compared to the other configurations which results in less efficient transfer of energy to the semiconductor. The effects of this can be outweighed by the complementary co-catalytic effects and Fermi-level equilibration to produce systems with enhanced performance.[21]

These three configurations all show enhanced efficiency of the possible plasmonic mechanisms that could help to overcome issues that hematite has in meeting the theoretical

maximum current limit. Substrate mounted nanoparticles allow for devices to be made thinner by boosting the overall light absorption and transferring energy through resonance, as scattered light, and as hot-electrons. This will help to overcome the short hole diffusion length in hematite as thinner films require shorter migration of charges to the interface.[17] Embedded nanoparticles may not allow for thinner films however the higher contact area between the nanoparticles and semiconductor results in increased efficiency for the plasmonic enhancement mechanisms. The LSPR energy can be tuned in order to stretch the overall absorption of the device beyond the band-gap absorption of hematite, this added absorbed energy can be transferred into useful charge through PIRET.[12] This would occur most efficiently in embedded architecture due the complete contact area but could also occur in the other configurations. Metal nanoparticles mounted on the surface of the semiconductor can act as cocatalysts and lower the potential required for the oxygen reduction reaction which aids hematite due to its poor surface chemistry.[12,21] Hematite suffers from poor surface chemistry for the oxygen reduction reaction and the co-catalytic effects of metal nanoparticles can act complimentary to the plasmonic enhancement effects.[3,21] The poor electrical conductivity and short excited state lifetimes of hematite[3] are not clearly addressed by the addition of plasmonic nanostructures in the device architecture however, the increased absorption of light and the photon to charge conversion efficiency gains that can be realised with the addition of these structures can go some way to reaching the theoretical limit of hematite solar-to-hydrogen conversion.

3.3. Molecular wires chosen and their issues

In this work three organic compounds were used to measure the effects of plasmonic structures on molecular conductance values. These were 1-nonanethiol, 1,10-decanedithiol and a viologen based dithiol referred to 9V9. The structure of these molecules is shown in figure 3-2.

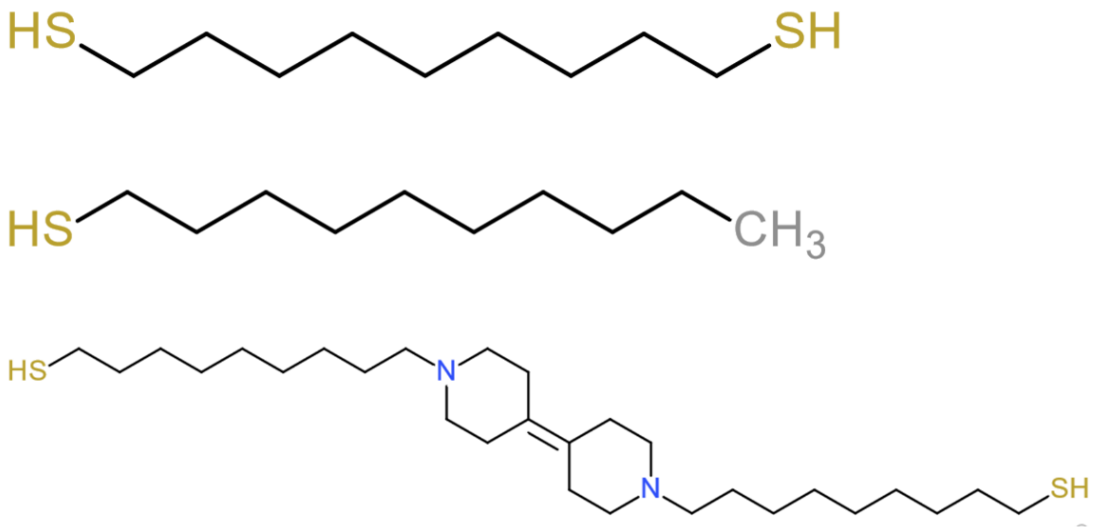

Figure 3-2 Schematics of the molecules that were tested for conductance on plasmonic substrates.A.) 1-nonanethiol, B.) 1,10-decanedithiol, and C.) a molecular wire referred to as 9V9.

Each of the molecules are terminated by -SH groups known as thiols. This group has a high affinity for gold and therefore acts as an anchoring group allowing attaching them to the gold substrate and giving higher probabilities for gold-molecule-gold contact bridge to be made during the experiments.

The understanding and measurement of the electronic properties of single molecules is an essential step in the development of molecular based electronic devices. The study of basic molecules and the effects of plasmonic nanoparticles on the conductance values of those molecules is important to gain understanding into how the field of plasmonics can assist in realising the goal of molecular electronics. Monothiol molecules readily form self-assembled monolayers (SAMs) on gold substrates[25–30] which makes 1-nonanedithiol a good candidate to develop a method of observing the plasmonic effects on conductance values of molecules attached to gold plasmonic substrates. The conductance values of monothiol molecular wires such as 1-octanethiol and 1-decanethiol have been measured in the past using scanning probe microscopy techniques.[29–31] The conductance value for 1-decanethiol given

by Frisbie[30] using a similar technique to the one performed in this work using a gold slide was 0.077nS.

Molecular wires with thiol groups at either end, like 1,9-nonanethiol, make good candidates for electrical studies as they readily make junctions between two gold contacts due to the anchor groups.[26–28,32] When SAMs of dithiols form on gold substrates one of the anchor groups attaches to the substrate and the other is left hanging. These hanging thiol groups make good contact with an electrical probe coated in gold or a gold nanoparticle deposited on top of the SAM this makes for more reliable measurements as the electrical junction formed is more resilient due to the attachment to both contacts.[26,28] A basic dithiol molecule such as 1,9-nonanenedithiol once again provides a good initial subject for further developing a method of measuring conductance of molecules on top of substrate-based metal nanostructures. The conductance values of 1,9-nonanedithiol have not been measured using scanning probe microscopy techniques in the literature.

The viologen moiety at the centre of the molecule referred to as 9V9 (figure 3-2C), is a redox centre. The oxidation state, and therefore the electronic tunnelling properties of this redox centre can be reversibly changed resulting in molecular wires with promising functional behaviours for molecule based electrical devices.[32] Molecular wires with this bipyridyl group at the centre of alkyl chains have been tested before in the literature and shown conductivity characteristics consistent with resonant LUMO (lowest unoccupied molecular orbital) tunnelling.[32] The conductance value for a 10V10 molecule, where the alkyl chains are 10 carbon atoms long, was measured at (0.13±0.03) nS. This was done using a method by which the molecule is trapped between a gold substrate and a spherical gold nanoparticle. The effects of illumination, and therefore plasmonic interactions, was not performed.[32] The conductance value of the 9V9 has not been measured and therefore offers a good candidate to perform novel experimentation whilst introducing potential plasmonic effects.

3.4. How plasmonic enhancement can solve molecular wire issues

Molecular wires often show conductance values measured in nano-siemens, such that any boost in conductance should allow for more careful analysis and understanding of the conductance characteristics and potentially lead to the realisation of molecular devices.[33] Plasmon enhanced charge transfer could boost conductance values to levels such that molecular devices could be realised but also provide pathways to demonstrate characteristics such as photon mediated current switching. These characteristics are necessary for molecular photovoltaics and photodetector devices.[33] Understanding the charge interactions between plasmonic nanostructures and molecules could also lead to discoveries in catalysis and spectroscopy.[33–37]

As discussed previously there are multiple mechanisms by which plasmonic enhancement can occur. Oscillating electric fields at the surface of a plasmonic nanoparticle under excitation lead to huge field enhancement factors in the proximity. The conductance of single-molecule junctions has been shown to be enhanced by localised oscillating fields arising from plasmonic excitation.[34] The highly localised electric fields around the molecule in the junction provide a potential energy for the tunnelling electrons and increases their transmission across the molecule increasing the conductance value measured.[34]

Hot-carrier injection has also been shown as a plasmonic mechanism capable of boosting the conductance of molecules.[33,35,37] In gold-contacted single molecule junctions conductance enhancements of ~30% have been attributed to hot-electron injection from excited plasmons across the junction gap.[35] The hot electrons increase conductance due to the addition of charge-carriers in the junction.[35,37] Hot carriers can also act to reduce molecules forming molecular species that are more conductive than the oxidised state and can be utilised to observe light induced switching effects.[33] Further work to characterise and understand the effects of plasmonic nanostructures in molecular junctions and devices will

aid in the realisation of molecular devices either through increasing the conductance of wires or through light mediated control of the conductance properties.[33–37]

3.5. Bibliography

1. Sivula, K., Le Formal, F. & Grätzel, M. Solar Water Splitting: Progress Using Hematite (α-Fe2O3) Photoelectrodes. *ChemSusChem* **4**, 432–449 (2011).

2. Hamann, T. W. Splitting water with rust: Hematite photoelectrochemistry. *Dalt. Trans.* **41**, 7830–7834 (2012).

3. Ling, Y. & Li, Y. Review of Sn-Doped Hematite Nanostructures for Photoelectrochemical Water Splitting. *Part. Part. Syst. Charact.* **31**, 1113–1121 (2014).

4. Zandi, O., Schon, A. R., Hajibabaei, H. & Hamann, T. W. Enhanced Charge Separation and Collection in High-Performance Electrodeposited Hematite Films. *Chem. Mater.* **28**, 765–771 (2016).

5. Chu, S. *et al.* Roadmap on solar water splitting: Current status and future prospects. *Nano Futures* vol. 1 (2017).

6. Li, J. & Wu, N. Semiconductor-based photocatalysts and photoelectrochemical cells for solar fuel generation: a review. *Catal. Sci. Technol..* **5**, 1360–1384 (2015).

7. Björkstén, U., Moser, J. & Grätzel, M. Photoelectrochemical Studies on Nanocrystalline Hematite Films. *Chem. Mater.* **6**, 858–863 (1994).

8. Lindgren, T., Vayssieres, L. & Wang, H. Photo-oxidation of water at hematite electrodes. in *Chemical Physics of Nanostructured Semiconductors* 83–110 (2003).

9. Jeon, T. H., Moon, G. hee, Park, H. & Choi, W. Ultra-efficient and durable photoelectrochemical water oxidation using elaborately designed hematite nanorod arrays. *Nano Energy* **39**, 211–218 (2017).

10. Prévot, M. S. & Sivula, K. Photoelectrochemical tandem cells for solar water splitting. *J. Phys. Chem. C* **117**, 17879–17893 (2013).

11. Cheng, W. H. *et al.* Monolithic Photoelectrochemical Device for Direct Water Splitting with 19% Efficiency. *ACS Energy Lett.* **3**, 1795–1800 (2018).

12. Thimsen, E., Le Formal, F., Grätzel, M. & Warren, S. C. Influence of Plasmonic Au Nanoparticles on the Photoactivity of Fe 2 O 3 Electrodes for Water Splitting. *Nano Lett.* **11**, 35–43 (2011).

13. Chaudhary, P. & Ingole, P. P. Multifunctional plasmonic Ag-hematite nano-dendrite electro-catalysts for methanol assisted water splitting: Synergism between silver nanoparticles and hematite dendrites. *Int. J. Hydrogen Energy* **43**, 1344–1354 (2018).

14. Shamjid, P., Abhijith, T., Vivek, P., Joel, C. S. & Reddy, V. S. Plasmonic effects of Ag nanoparticles for absorption enhancement in polymer solar cells with MoO3 passivation layer. *Phys. B Condens. Matter* **560**, 174–184 (2019).

15. Li, J. *et al.* Plasmon-induced resonance energy transfer for solar energy conversion. *Nat. Photonics* **9**, 601–607 (2015).

16. Tagliabue, G. *et al.* Quantifying the role of surface plasmon excitation and hot carrier transport in plasmonic devices. *Nat. Commun.* **9**, 3394 (2018).

17. Li, J. *et al.* Plasmon-induced photonic and energy-transfer enhancement of solar water splitting by a hematite nanorod array. *Nat. Commun.* **4**, 2651 (2013).

18. Ratchford, D. C., Dunkelberger, A. D., Vurgaftman, I., Owrutsky, J. C. & Pehrsson, P. E. Quantification of Efficient Plasmonic Hot-Electron Injection in Gold Nanoparticle–TiO 2 Films. *Nano Lett.* **17**, 6047–6055 (2017).

19. Valenti, M., Jonsson, M. P., Biskos, G., Schmidt-Ott, cd A. & Smith, W. A. Plasmonic nanoparticle-semiconductor composites for efficient solar water splitting. *J. Mater. Chem. A* **4**, (2016).

20. Valenti, M., Jonsson, M. P., Biskos, G., Schmidt-Ott, A. & Smith, W. A. Plasmonic nanoparticle-semiconductor composites for efficient solar water splitting. *J. Mater. Chem. A* **4**, 17891–17912 (2016).

21. Li, J. *et al.* Distinguishing surface effects of gold nanoparticles from plasmonic effect on photoelectrochemical water splitting by hematite. *J. Mater. Res.* **31**, 1608–1615 (2016).

22. Yen, Y.-C., Chen, J.-A., Ou, S., Chen, Y.-S. & Lin, K.-J. Plasmon-Enhanced Photocurrent using Gold Nanoparticles on a Three-Dimensional TiO2 Nanowire-Web Electrode. *Sci. Rep.* **7**, 42524 (2017).

23. Baffou, G. & Quidant, R. Nanoplasmonics for chemistry. *Chem. Soc. Rev.* **43**, 3898–3907 (2014).

24. Valenti, M. *et al.* Hot Carrier Generation and Extraction of Plasmonic Alloy Nanoparticles. *ACS Photonics* **4**, 1146–1152 (2017).

25. Love, J. C., Estroff, L. A., Kriebel, J. K., Nuzzo, R. G. & Whitesides, G. M. *Self-assembled monolayers of thiolates on metals as a form of nanotechnology*. *Chemical Reviews* vol. 105 (2005).

26. Haiss, W. *et al.* Impact of junction formation method and surface roughness on single molecule conductance. *J. Phys. Chem. C* **113**, 5823–5833 (2009).

27. Cui, X. D. *et al.* Reproducible measurement of single-molecule conductivity. *Science (80-.).* **294**, 571–574 (2001).

28. Morita, T. & Lindsay, S. Determination of single molecule conductances of alkanedithiols by conducting-atomic force microscopy with large gold nanoparticles. *J. Am. Chem. Soc.* **129**, 7262–7263 (2007).

29. Engelkes, V. B., Beebe, J. M. & Frisbie, C. D. Analysis of the Causes of Variance in Resistance Measurements on Metal-Molecule-Metal Junctions Formed by Conducting-Probe Atomic Force Microscopy. *J. Phys. Chem. B* **109**, 16801–16810 (2005).

30. Wold, D. J. & Frisbie, C. D. Formation of a Metal - Molecule - Metal Junction by Contacting an Alkanethiol Self-Assembled Monolayer with Formation of Metal - Molecule - Metal Tunnel Junctions : Microcontacts to Alkanethiol Monolayers with a Conducting AFM Tip Department of Chemical E. *J. Am. Chem. Soc* **122**, 2970–2971 (2000).

31. Rubio-Bollinger, G. *et al.* Carbon-fiber tips for scanning probe microscopes and molecular electronics experiments. *Nanoscale Res. Lett.* **7**, 2–5 (2012).

32. Haiss, W. *et al.* Wiring nanoparticles with redox molecules. *Faraday Discuss.* **125**, 179–194 (2004).

33. Ai, Y., Nguyen, V. Q., Ghilane, J., Lacaze, P. C. & Lacroix, J. C. Plasmon-Induced Conductance Switching of an Electroactive Conjugated Polymer Nanojunction. *ACS Appl. Mater. Interfaces* **9**, 27817–27824 (2017).

34. Vadai, M. *et al.* Plasmon-induced conductance enhancement in single-molecule junctions. *J. Phys. Chem. Lett.* **4**, 2811–2816 (2013).

35. Fung, E. D., Adak, O., Lovat, G., Scarabelli, D. & Venkataraman, L. Too Hot for Photon-Assisted Transport: Hot-Electrons Dominate Conductance Enhancement in Illuminated Single-Molecule Junctions. *Nano Lett.* **17**, 1255–1261 (2017).

36. Wang, C., Shi, Y., Yang, D. R. & Xia, X. H. Combining plasmonics and electrochemistry at the nanoscale. *Curr. Opin. Electrochem.* **7**, 95–102 (2018).

37. Sprague-Klein, E. A. *et al.* Observation of Single Molecule Plasmon-Driven Electron Transfer in Isotopically Edited 4,4'-Bipyridine Gold Nanosphere Oligomers. *J. Am. Chem. Soc.* **139**, 15212–15221 (2017).

4. Localised Surface Plasmon Resonance Theory

4.1. The quasistatic Approach

For metal nanoparticles with typical dimensions, d, smaller than local variations in the electromagnetic fields (d<<λ) then a quasi-static approach can be used to describe the spatial field distributions. In this case, the phase of the harmonically oscillating electromagnetic field is practically constant over the particle volume, so that the problem can be simplified to that of a particle in an electrostatic field. Spatial field distributions can be found using the Laplace equation $\nabla^2\Phi = 0$, and the electric field equation $E = -\nabla\Phi$. The harmonic time-dependence can be added afterwards once the field distributions are known.[1]

Starting with the simplest of configurations with a homogenous, isotropic sphere of radius, a, located at the origin in a uniform static electric field, where the surrounding media is isotropic and non-absorbing. Jackson[2] showed that the solution to the potentials inside the particle, Φ_{in}, and the potentials outside the particle, Φ_{out}, can be written as;

Equation 2

$$\Phi_{in} = -\frac{3\varepsilon_{NP}}{\varepsilon_{NP} + 2\varepsilon_m} E_0 r \cos(\theta)$$

Equation 3

$$\Phi_{out} = -E_0 r \cos(\theta) + \frac{\varepsilon_{NP} - \varepsilon_m}{\varepsilon_{NP} + 2\varepsilon_m} E_0 a^3 \frac{\cos(\theta)}{r^2}$$

Where E_0 is the amplitude of the electric field, ε_{NP} and ε_m, are the dielectric permittivity functions for the nanoparticle and medium materials respectively, a is the particle radius and r is the modulus of the position vector. Here Φ_{out} represents the superposition of the applied external field, and a dipole field located at the centre of the nanoparticle. Φ_{out} can be rewritten using dipole moment, **p** as;

Equation 4

$$\Phi_{out} = -E_0 r\cos(\theta) + \frac{\boldsymbol{p}.r}{4\pi\varepsilon_0\varepsilon_m r^3}$$

Equation 5

$$\boldsymbol{p} = 4\pi\varepsilon_0\varepsilon_m a^3 \frac{\varepsilon_{NP} - \varepsilon_m}{\varepsilon_{NP} + 2\varepsilon_m} E_0$$

This shows that the applied field induces the dipole moment in the nanoparticle with magnitude proportional to E_0. Polarizability, α, can be introduced by using $\boldsymbol{p} = \varepsilon_0\varepsilon_m\alpha E_0$ to get;

Equation 6

$$\alpha = 4\pi\, a^3 \frac{\varepsilon_{NP} - \varepsilon_m}{\varepsilon_{NP} + 2\varepsilon_m}$$

The polarizability shows a resonant enhancement when $\varepsilon_{NP} + 2\varepsilon_m$ is at a minimum which, for the case of small or slowly varying $Im[\varepsilon]$, is simplified to the Frohlich condition;

Equation 7

$$Re[\varepsilon(\omega)] = -2\varepsilon_m$$

For a spherical nanoparticle of a Drude metal located in air, the Frohlich condition is satisfied for a resonant frequency $\omega_0 = {}^{\omega_p}/_{\sqrt{3}}$. The Frohlich condition shows the strong dependence on resonant frequency with the dielectric environment and little dependence on size.

The potentials from Eq.1 and Eq.3 can then be used to calculate the electric fields using $E = -\nabla\Phi$. This gives;

Equation 8

$$E_{in} = \frac{3\varepsilon_m}{\varepsilon + 2\varepsilon_m} E_0$$

Equation 9

$$E_{out} = E_0 + \frac{3\boldsymbol{n}(\boldsymbol{n}\cdot\boldsymbol{p}) - \boldsymbol{p}}{4\pi\varepsilon_0\varepsilon_m}\frac{1}{r^3}$$

Where $\boldsymbol{p} = \varepsilon_0\varepsilon_m\alpha E_0$ is the dipole moment. This gives the resonant behaviour of α in the internal and dipolar fields. The resonant enhancement of the local dipolar and internal electric field is what gives plasmonic nanoparticles their characteristics on which their applications in optics and sensors rely.

It is also possible to evaluate the electromagnetic fields that are radiated by a small particle excited at its resonant frequency. For a small particle where a<<λ the quasi-static approach is maintained and the particle can be represented as an ideal dipole. Under illumination from a plane wave $\boldsymbol{E}(\boldsymbol{r},t) = E_0 e^{-i\omega t}$, an oscillating dipole moment $\boldsymbol{p}(t) = \varepsilon_0\varepsilon_m\alpha\, E_0 e^{-i\omega t}$ is induced with α given by the electrostatic result in Eq. 5. The scattering of the plane wave from the nanosphere can be represented as radiation by a point dipole.

For an oscillating electric dipole, the total fields $\boldsymbol{H}(t) = He^{-i\omega t}$, and $\boldsymbol{E}(t) = Ee^{-i\omega t}$ can be described in the near, intermediate, and radiation zones can be expressed as;

Equation 10

$$\boldsymbol{H} = \frac{ck^2}{4\pi}(\boldsymbol{n}\times\boldsymbol{p})\frac{e^{ikr}}{r}\left(1 - \frac{1}{ikr}\right)$$

Equation 11

$$\boldsymbol{E} = \frac{1}{4\pi\varepsilon_0\varepsilon_m}\left\{k^2(\boldsymbol{n}\times\boldsymbol{p})\times n\frac{e^{ikr}}{r} + [3\boldsymbol{n}(\boldsymbol{n}\cdot\boldsymbol{p}) - \boldsymbol{p}]\left(\frac{1}{r^3} - \frac{ik}{r^2}\right)e^{ikr}\right\}$$

Where $k = {}^{2\pi}/_{\lambda}$ and **n** is the unit vector of the point of interest. In the near field (kr<<1) the electrostatic result for the dipole field in Eq. 8 is recovered;

Equation 12

$$E = \frac{3\boldsymbol{n}(\boldsymbol{n}\cdot\boldsymbol{p}) - \boldsymbol{p}}{4\pi\varepsilon_0\varepsilon_m}\frac{1}{r^3}$$

And the magnetic field becomes;

Equation 13

$$H = \frac{i\omega}{4\pi}(\boldsymbol{n}\times\boldsymbol{p})\frac{1}{r^2}$$

This shows that in the near-field the fields are predominantly electric in nature as the magnetic field is about a factor of $\sqrt{\varepsilon_0/\mu_0}\,(kr)$ smaller than the electric field component. For static fields as kr tends to 0 the magnetic field completely vanishes.

In the radiation zone, where kr>>1, the dipole fields have the well-known spherical wave form;

Equation 14

$$\boldsymbol{E} = \sqrt{\frac{\mu_0}{\varepsilon_0\varepsilon_m}}\boldsymbol{H}\times n$$

Equation 15

$$\boldsymbol{H} = \frac{ck^2}{4\pi}(\boldsymbol{n}\times\boldsymbol{p})\frac{\boldsymbol{e^{ikr}}}{\boldsymbol{r}}$$

The resonant enhancement shown in polarizability, α, consequently results in an enhancement in the scattering and absorption efficiency of metal nanoparticles. The cross-sections for scattering and absorption (C_{sca} and C_{abs}) can be calculated from the Poynting vector determined from Eq.9 and 10.

Equation 16

$$C_{sca} = \frac{k^4}{6\pi}|\alpha|^2 = \frac{8\pi}{3}k^4a^6\left|\frac{\varepsilon - \varepsilon_m}{\varepsilon + 2\varepsilon_m}\right|^2$$

Equation 17

$$C_{abs} = k\ Im[\alpha] = 4\pi ka^3\ Im\left[\frac{\varepsilon - \varepsilon_m}{\varepsilon + 2\varepsilon_m}\right]$$

For small particles with a<<λ the absorption efficiency dominates over the scattering efficiency, however the scattering efficiency scales rapidly as particle size increases ($C_{sca} \propto a^6$) compared to the absorption ($C_{abs} \propto a^3$) giving rise to real world practical problems with small particles. This makes it difficult to distinguish small particles against a background of larger scatterers and shows that smaller plasmonic particles are less efficient for uses that require light scattering.

Equations 15 and 16 show that the cross-sections for absorbance and scattering, and therefore the extinction, are resonantly enhanced when the Frohlich condition is met. For a sphere of volume V and dielectric function $\varepsilon = \varepsilon_1 + i\varepsilon_2$ in the quasi-static limit, the cross section for extinction from $C_{ext} = C_{abs} + C_{sca}$ becomes;

Equation 18

$$C_{ext} = 9\ \frac{\omega}{c}\ \varepsilon_m^{3/2}\ V\frac{\varepsilon_2}{[\varepsilon_1 + 2\varepsilon_m]^2 + {\varepsilon_2}^2}$$

This again shows the sensitivity of plasmonic resonance to the dielectric environment and highlights the use for plasmonic particles as sensors for local changes in dielectric conditions.[1]

The changes in plasmon resonance peak position and shape with particle size are not captured by the quasi-static approach. These equations only describe the dependence on dielectric environment for resonant enhancement in extinction and therefore the approach

must be broadened. The two regimes in which the quasi-static approach breaks down are in larger particles (>100nm) where the phase changes of the driving field occur over the particle volume and smaller particles (<10nm) where the particle dimensions are smaller than the electron mean-free path.[1]

4.2. Beyond Quasistatics

For particles larger than 100nm the quasistatic approach begins to break down due to phase changes in the driving field over the particle volume. In 1908 Mie described a theory of the scattering and absorption of electromagnetic radiation by spheres in order to explain the colours of colloidal gold solutions. Mie theory expands the modes of the internal and scattered fields into a set of normal modes described by vector harmonics. The electromagnetic fields are expanded in multipole contributions and the expansion coefficients are found by applying the correct boundary conditions at the interface between the surrounding medium and the nanoparticle.[1,3]

The polarizability of a sphere with volume V can be taken from an expansion of the first TM mode of Mie theory.[3]

$$\alpha = \frac{1 - \left(\frac{1}{10}\right)(\varepsilon - \varepsilon_m)x^2 + O(x^4)}{\left(\frac{1}{3} + \frac{\varepsilon_m}{\varepsilon - \varepsilon_m}\right) - \frac{1}{30}(\varepsilon + 10\varepsilon_m)x^2 - i\frac{4\pi^2\varepsilon_m^{3/2}}{3}\frac{V}{\lambda_0^3} + O(x^4)}$$

Here $x = \pi a/\lambda_0$ is the size parameter which relates the radius to the free-space wavelength (λ_0). The x^2 term in the numerator includes the retardation effects of the driving field over the volume of the particle leading to a shift in the plasmon resonance peak position. The x^2 term in the denominator accounts for a plasmon peak position shift due to the retardation of the depolarization field inside the nanoparticle. For Drude and noble metals the spectral peak position of the dipole plasmon resonance red-shifts as the particle size increases. This can be understood as a decrease in the restoring force, and

therefore a lower resonance frequency, for the electron oscillations as the charges at opposite sides are further apart with larger nanoparticles. This term also increases the polarizability magnitude and therefore lessens the influence of the absorption from the imaginary part of the permittivity. The imaginary term in the denominator accounts for the radiation damping which counteracts the increase in polarization strength from the x^2 term in the denominator.[1]

The coherent electron oscillations of the plasmon dipole can decay through photon emission. This is known as radiation damping and is the main cause of the weakening of the dipole plasmon resonance strength as the nanoparticle size increases. The absorption of light through the creation of electron-hole pairs via interband and intraband transition is known as non-radiative decay. Interband transitions occur when lower-lying d-band electrons are excited to the sp-conduction band in noble metals. The intraband transitions occur in the conduction band, with electrons promoted to higher energies within the sp-band. Beyond the quasi-static approach, the plasmon resonance of nanoparticles is damped by the radiative damping and non-radiative decay as two competing processes.[1]

The internal damping processes can be related to the homogeneous linewidth, Γ, of the plasmon resonance through an equation that introduces the dephasing time as T_2.

Equation 19

$$\Gamma = \frac{2\hbar}{T_2}$$

The dephasing time, T_2, can be related to a pure dephasing time, T_2^*, resulting from elastic collisions, and a T_1 term which describes radiative and non-radiative energy losses as a population relaxation or decay time.

Equation 20

$$\frac{1}{T_2} = \frac{1}{2T_1} + \frac{1}{T_2^*}$$

Link et al., used pump probe experiments to examine the details of plasmon-decay through radiative, non-radiative, and photothermal processes.[4] Experimentally it has been shown that in general for plasmon decay, $T_2^* \gg T_1$ such that equation 18 simplifies essentially to $T_2 = 2T_1$. For small gold and silver nanoparticles $5\ fs \leq T_2 \leq 10\ fs$ depending on particle size and the dielectric environment. It has been shown that the observed decay times for gold nanoparticles agree well experimentally with Mie theory and the dielectric data from Johnson and Christy, 1972. However, with silver particles, especially small silver spheres, the experimental data diverges from the theory and shows a decrease in decay time, possibly due to damping processes at the particle surface.[1]

In plasmonic applications where sample heating or molecular fluorescence quenching in the vicinity of metal nanostructures is to be avoided then the contributions to decay time from the radiative decay pathway should dominate over the non-radiative pathways. Sönnischen et al. aimed to maximise the radiative contribution to the decay time to show a reduction in plasmon damping for gold nanorods of varying aspect ratios.[5] This can be described as a maximization of the quantum efficiency, η, for resonant light scattering;

Equation 21

$$\eta = \frac{T_{1,r}^{-1}}{T_1^{-1}} = \frac{T_{1,r}^{-1}}{T_{1,r}^{-1} + T_{1,nr}^{-1}}$$

Here, $T_{1,r}$ is the radiative contribution to the decay time and $T_{1,nr}$ is the non-radiative contribution. The dephasing time for gold nanorods was shown to be higher than that of gold nanospheres with a similar volume. The T_2 time approached a limit of 18fs for nanorods with an aspect ratio of 3:1. This was attributed to less non-radiative damping as

the long-axis mode shifts towards lower energies, limiting the contributions from interband transitions.[1,5]

4.3. Smaller nanoparticles

For smaller nanoparticles, a < 10nm, chemical interface damping begins to contribute to the plasmon decay time. The particle size is less than the electron mean free path and therefore elastic scattering at the particle surface acts to decrease the dephasing time further. The broadening of the plasmon line-width in particles a < 10nm seen experimentally can be modelled as;

Equation 22

$$\Gamma_{obs}(R) = \Gamma_0 + \frac{Av_F}{R}$$

Here, Γ_0 is the plasmon linewidth for larger particles which is generally dominated by interface or radiation damping. $A \approx 1$ and is a factor that includes the details of the scattering processes, v_F is the Fermi velocity of the electrons, and R is the particle radius.[1,6] At particle sizes of a < 10nm a shifting of resonance energy is also seen in addition to the broadening of the peak. The direction of the shift has been experimentally observed to occur in both directions and therefore it would appear to be due to the specific chemical termination of the particle surface.[1]

In particles with radii below 1nm quantum effects begin to influence the plasmon characteristics and the classical description taken so far becomes insufficient. Above this size regime the effects due to the quantized nature of the energy levels have been disregarded due to the large concentration of electrons in metal conduction bands. As the particle volume decreases the quantity of electrons becomes a small absolute number and therefore the amount of energy gained by each electron from incident photon excitations, $\Delta E \approx \frac{\hbar\omega}{N_e}$, becomes significant when compared to $k_B T$. The problem can no longer be

considered a coherent electron oscillation and now has to be treated as a quantum mechanical multiple-particle excitation.

4.4. Multiple Nanoparticles

Applications involving plasmonic nanostructures as sensors or to enhance the performance of complementary materials will often utilise arrays of nanostructures or ensembles of nanoparticles.[7–9] The plasmonic behaviour of particle dimers, trimers, and arrays is expected to be different to that of isolated nanoparticles. The resonance peak position of the entire ensemble is expected to shift due to the interaction between the localized plasmon modes. A first approximation for coupling of localized plasmon modes can be made by treating the system as an ensemble of interacting dipoles.[1]

Assuming a one- or two-dimensional particle array with particle size, a, and separation, d such that $a \ll d$ then a dipolar approximation can be made and the particles can be treated as a set of point dipoles. When the particles are closely spaced, $d \ll \lambda$, the array can be described as an array of point dipoles interacting through the near-field as the near-field interactions scale with d^{-3} and dominate in this regime. Strong localized field enhancement occurs in the nano-sized gaps between particles due to the suppression of the far-field scattering. This suppression occurs due to the excitation of established plasmon modes mediated by the near-field plasmon coupling between particles. These modes occur along the axes of the array or chain. The interparticle hotspots of enhanced electric field can be used to enhance the performance of plasmonic devices.

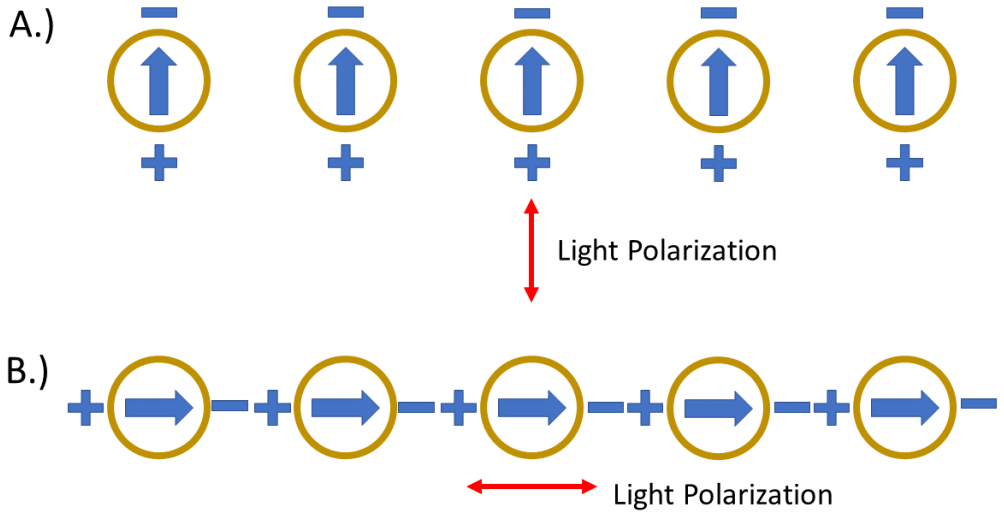

Figure 4-1 - Diagram showing the near-field plasmon coupling between nanoparticles in a chain. A.) Excitation light is polarized perpendicular to the direction axis of the nanoparticle ensemble showing the synchronisation of the dipole direction. Here the restoring force is increased leading to blue-shift in the transverse mode. B.) Excitation light is polarised along the direction of the chain. The restoring force is decreased due to the interaction with the opposite polarity of neighbouring particles. This leads to a red-shift in the plasmon resonance in the longitudinal mode.

The interparticle coupling of plasmon modes leads to spectral shifting of the resonance peak positions compared to the case of isolated nanoparticles. By considering the Coulombic forces associated with the polarization of the particles the direction in which the resonance shifts can be determined. A schematic showing the near-field coupling between nanoparticles is shown in Figure 4-1. The dipole direction of the individual nanoparticles depends on the polarization of the exciting light. Therefore, when the polarization of the light is in line with the directional axis of the ensemble, the restoring force acting on the electron oscillations is decreased. This leads to a red-shift in the plasmon resonance for the longitudinal modes. When the exciting light polarization is perpendicular to the directional axis of the chain, the dipoles share a combined polarity and the restoring force is increased. This gives a blue-shift in the plasmon resonance along the transverse modes.

Maier et al. used far-field extinction spectroscopy on arrays of 50nm gold nanoparticles to measure the shift in resonance energy with interparticle spacing in both transverse and

longitudinal modes. Experimentally it was shown that with a spacing of 150nm the behaviour of isolated nanoparticles was recovered. This demonstrates the scaling of the near-field interaction strength with d^{-3}.[1,10]

With larger interparticle spacings far-field dipolar coupling begins to have a strong influence on the plasmon resonance linewidth and peak position. This far-field coupling terms scales with d^{-1} and has been shown experimentally using 2-dimensional arrays of evenly spaced nanoparticles similar to diffraction gratings. Lamprecht et al. measured the decay time of plasmonic 2-dimensional structures of evenly spaced Au nanoparticles with varying spacing sizes using time-resolved measurements. They showed that the lattice constant of the 2D nanoparticle arrays as the grating order changes from evanescent to radiative in character, had a strong influence over the plasmon damping decay time, T_2. This occurred in the region where $500nm \leq d \leq 600nm$ and led to a redshift in plasmon resonance peak position of 50nm.[1,11] However, for randomly spaced nanoparticle structures with average spaces ranging from 400nm to 1000nm, there was no significant shift or broadening of the plasmon resonance. This shows the importance of regularity in controlling or altering the plasmon line shape or position, and confirms that the changes in resonance are determined by the periodicity of the lattice and not by other factors.[11]

4.5. Coulomb Renormalization

To explain the near-field plasmonic enhancement of electron accepting systems in the vicinity of active plasmon modes Durach et al. presented a theory to define a closed expression surface plasmon dressed Coulomb interaction using renormalization of the Coulomb potential.[12] When a charge carrier in a plasmonic metal nanosystem experiences a transition with frequency, ω, there is an accompanying local electric field oscillation at the same frequency. These fields excite surface plasmon modes with the same frequencies

whose fields then overlap with the original transition derived field. These surface plasmon modes can be delocalized around the entire surface of the nanosystem and can then excite resonant transitions of other electrons. This transition of energy can be described as an electron-electron interaction by way of exchange of a surface plasmon quantum. Therefore, the direct Coulomb interaction between two electrons must be replaced with a transition frequency dependent form. The direct Coulomb interaction is given as;

Equation 23

$$V(r-r') = \frac{1}{(\varepsilon_h|\boldsymbol{r}-\boldsymbol{r}'|)}$$

Where ε_h is the dielectric constant for the embedding medium, and $\boldsymbol{r}$ and $\boldsymbol{r}'$ are the electron coordinates. This expression is replaced with the renormalized expression in the form $W(\boldsymbol{r},\boldsymbol{r}';\boldsymbol{\omega})$ which is the potential created at a point **r** by a charge positioned at point **r'** oscillating with frequency ω.[12]

In the quasistatic approximation and assuming that the size of the system is smaller than any relevant electromagnetic length then W must satisfy the continuity equation;

Equation 24

$$\frac{\partial}{\partial \boldsymbol{r}}\left[\varepsilon(\boldsymbol{r},\omega)\frac{\partial}{\partial \boldsymbol{r}}W(\boldsymbol{r},r';\omega)\right] = -4\pi\delta(\boldsymbol{r}-\boldsymbol{r}'),$$

Where the dielectric function of the system $\varepsilon(\boldsymbol{r},\omega)$ is expressed as $\varepsilon(\boldsymbol{r},\omega) = \varepsilon_m(\omega)\Theta(\mathbf{r}) + \varepsilon_h[1-\Theta(\mathbf{r})]$. In this expression $\Theta(\mathbf{r})$ is the characteristic function equal to 1 when **r** belongs to the metal and 0 otherwise, and $\varepsilon_m(\omega)$ is the dielectric function of the uniform metal.[12]

The expression W can be given in terms of the retarded Green's function of the system G^r;

Equation 25

$$W(\boldsymbol{r},r';\omega) = V(r-r') - \int V(r''-r')\frac{\partial^2}{\partial \boldsymbol{r}''^2}G^r(\boldsymbol{r},\boldsymbol{r}'';\omega)\,d^3\boldsymbol{r}''.$$

The Green's function, G^r, can be presented as a spectral expansion over the surface plasmon eigenmodes $\varphi_n(\boldsymbol{r})$ and the corresponding eigenvalues s_n as;

Equation 26

$$G^r(\boldsymbol{r}, \boldsymbol{r}''; \omega) = \sum_n \frac{s_n}{s(\omega) - s_n} \varphi_n(\boldsymbol{r}) \varphi_n(\boldsymbol{r}'),$$

Where $s(\omega) = {}^{1}/_{[1 - \varepsilon_m(\omega)/\varepsilon_d]}$ is the spectral parameter. This Green's function also separates the dependences on geometry and material properties. The geometric properties of the nanosystem are accounted for in the eigenfunctions and eigenvalues, φ_n and s_n, whereas the material properties are entered through the spectral parameter $s(\omega)$. If the system is in an infinite space then the use of the Green's function in Eq.24 simplifies the equation to;

Equation 27

$$W(\boldsymbol{r}, r'; \omega) = V(r - r') + \frac{4\pi}{\varepsilon_h} G^r(\boldsymbol{r}, \boldsymbol{r}''; \omega)$$

This result in Eq.26 shows the Coulomb interaction renormalized by the full retarded Green's function which also describes the nanoplasmonic enhancement through optical phenomena. The poles of Green's function in Eq.25 correspond to the surface plasmon modes with frequencies given by $s(\omega_n) = s_n$. Close to this this frequency G^r becomes large, as shown by the denominator in Eq. 25, leading to the enhancement of the Coulomb interaction.[12]

The renormalization is shown to be highly resonant, shown by the enhancement in the Green's function as $s(\omega_n) \to s(\omega)$, and long -range with an effective interaction distance length on the order of the nanosystem size. The plasmonic enhancement of the Coulomb interaction is a universal effect and should affect a wide-range of physical phenomena in the vicinity of a metal plasmonic system.[12] This theory accounts for the near-field enhancement effects seen in light-concentration such as Förster resonant energy transfer (FRET) and plasmon-induced resonant energy transfer (PIRET).

4.6. Bibliography

1. Maier, S. A. *Plasmonics: Fundamentals and applications*. *Plasmonics: Fundamentals and Applications* (Springer, 2007).

2. Jackson, J. D. *Classical Electrodynamics*. (Wiley, 1999).

3. Mie, G. Beiträge zur Optik trüber Medien, speziell kolloidaler Metallösungen. *Ann. Phys.* **330**, 377–445 (1908).

4. Link, S. & El-Sayed, M. A. Shape and size dependence of radiative, non-radiative and photothermal properties of gold nanocrystals. *Int. Rev. Phys. Chem.* **19**, 409–453 (2000).

5. Sönnichsen, C. *et al.* Drastic reduction of plasmon damping in gold nanorods. *Phys. Rev. Lett.* **88**, 774021–774024 (2002).

6. Wilcoxon, J. P., Martin, J. E. & Provencio, P. Optical properties of gold and silver nanoclusters investigated by liquid chromatography. *J. Chem. Phys.* **115**, 998–1008 (2001).

7. Li, H. & Wu, N. A large-area nanoscale gold hemisphere pattern as a nanoelectrode array. *Nanotechnology* **19**, 275301 (2008).

8. Chang, Y.-C. *et al.* High-Throughput Nanofabrication of Infra-red and Chiral Metamaterials using Nanospherical-Lens Lithography. *Sci. Rep.* **3**, 3339 (2013).

9. Schade, M. *et al.* Regular arrays of Al nanoparticles for plasmonic applications. *J. Appl. Phys.* **115**, 084309 (2014).

10. Maier, S. A., Brongersma, M. L., Kik, P. G. & Atwater, H. A. Observation of near-field coupling in metal nanoparticle chains using far-field polarization spectroscopy. *Phys.*

Rev. B **65**, 193408 (2002).

11. Lamprecht, B. *et al.* Metal Nanoparticle Gratings : Influence of Dipolar Particle Interaction on the Plasmon Resonance. 4721–4724 (2000).

12. Durach, M., Rusina, A., Klimov, V. I. & Stockman, M. I. Nanoplasmonic renormalization and enhancement of Coulomb interactions. *New J. Phys.* **10**, 105011–105025 (2008).

5. Experimental Methods

5.1. Introduction

This chapter outlines the experimental methods used in this work and gives a brief overview of the underlying principles of the experimental techniques and apparatus. Nanostructured substrates were fabricated through nanosphere shadow lithography (NSL) and the use of multiple deposition techniques, such as resistive thermal and electron beam deposition and radio-frequency plasma sputtering. Citrate-capped spherical gold nanoparticles in suspensions were also fabricated using a wet-chemical Turkevich[1] method adapted by Bastús.[2]. Hematite films were deposited through an electrodeposition technique and with the use of atomic layer deposition. The atomic layer deposition was performed at the Department of Engineering by Natalie Bavis, and all other deposition techniques were performed by the author at the Stephenson Institute of Renewable Energy, both at the University of Liverpool.

Substrates were characterised for their absorption characteristics using UV-Vis-NIR spectroscopy and imaged using atomic force microscopy (AFM) and scanning electron microscopy (SEM). The photocatalytic ability of hematite films was assessed using photoelectrochemical (PEC) methods including linear sweep voltammetry and chronoamperometry. The PEC set-up was also used to create incident photon to charge carrier efficiency (IPCE) spectra.

Self-assembled monolayers of molecules were grown on the nanostructured substrates through substrate immersion in the relevant molecule solution, this was performed by Dr David Costa Milan at the Department of Chemistry at the University of Liverpool. Conductive AFM was also used to perform molecular electronic experiments and run localised current-voltage measurements to assess the conductance of substrates and adsorbed molecules.

Nanostructured substrate geometries were simulated to predict their plasmonic behaviour using the finite-difference time-domain (FDTD) method. This was performed using the Ansys Lumerical FDTD solver software package. Periodic nanotriangle arrays of various size and geometry were simulated to show the predicted absorbance characteristics and localised electric field maps. Gold nanospheres on substrates of glass and gold were simulate to predict and motivate the plasmonic behaviour in the molecular electronics measurements.

5.2. Sample Preparation

5.2.1. Nanosphere Shadow Lithography

Nanosphere shadow lithography (NSL) has been used to produce various morphologies of nanostructured surfaces such as bow-tie antennae, nano-crescents, nano-gaps, and split-ring antennae.[3–6] The NSL process was utilized in this work due to the lack of requirement expensive specialist lithography equipment, reproducibility in nanostructure fabrication, and the scalable nature of the technique. It is low-cost in comparison to electron beam lithography and an industrially scalable technique allowing for the production of nanostructure arrays of controllable size on high aspect ratio substrates.[3,7] NSL substrates have been used to plasmonically enhance photocatalytic water-splitting.[8] However, a direct comparison of the effects of using identical nanostructures made of different plasmonic metals has not been performed.

The NSL process involves the deposition of polystyrene nanospheres on a surface which can then be used as a mask either on their own or in conjunction with other complimentary lithography techniques. Here, large-scale periodic monolayers of PS spheres are deposited straight onto the substrate and used as a single mask layer, which metal is deposited through.

Polystyrene bead solutions with a specified size distribution can be purchased from retailers such as Sigma-Aldrich. This suspension can then be concentrated, diluted, or directly

deposited onto the chosen substrate through numerous methods such as spin-coating or through a Langmuir-Blodgett type deposition. The ideal resultant structure is a monolayer of polystyrene nanospheres arranged in a tight-packed hexagonal pattern on the substrate surface.

Metal can be deposited onto substrates using evaporation techniques. Here, both thermal evaporation and electron beam evaporation were utilised in order to deposit metals through the PS bead mask. Thermal evaporation uses the resistive heating of tungsten or molybdenum boats to heat the source material in a vacuum chamber. The source material is loaded into the evaporation boats with the samples suspended above. A large current is passed through the metal boat causing it to heat up. The source material begins to evaporate and the deposition rate is measured using quartz crystal microbalance (QCM).

E-beam evaporation uses a guided electron beam to heat the source material in a vacuum. The source material is loaded into graphite crucibles and placed in the hearth in the vacuum chamber. An electron gun is used to create the electron beam, which is then guided by an electromagnet onto the source material. Increasing the emission current of the electron gun increases the temperature of the source material until it begins to evaporate. The deposition rate is monitored again using QCM.

The metal is deposited onto the substrate through the apertures between the beads in the mask. For most metals deposited onto glass coated slides an adhesion layer is required. This is generally Ti or Cr, in this work 5nm of Cr was initially deposited before the plasmonic metal layers. The bead-mask is then lifted off through tape-cleaving or a sonication procedure in a solvent such as de-ionized water or isopropanol. The triangular nanostructures remain on the substrate surface due to the adhesion from the chromium interlayer. The resulting nanostructures represent triangular nanoparticles arranged in a Fischer pattern. Figure 5-1 shows a schematic of the NSL process, the beads are shown packed in a hexagonal pattern

with the triangular apertures between them. The triangular nanoparticles arranged in a Fisher pattern are shown on the right of the figure 5-1, this pattern is revealed once the bead mask is removed.

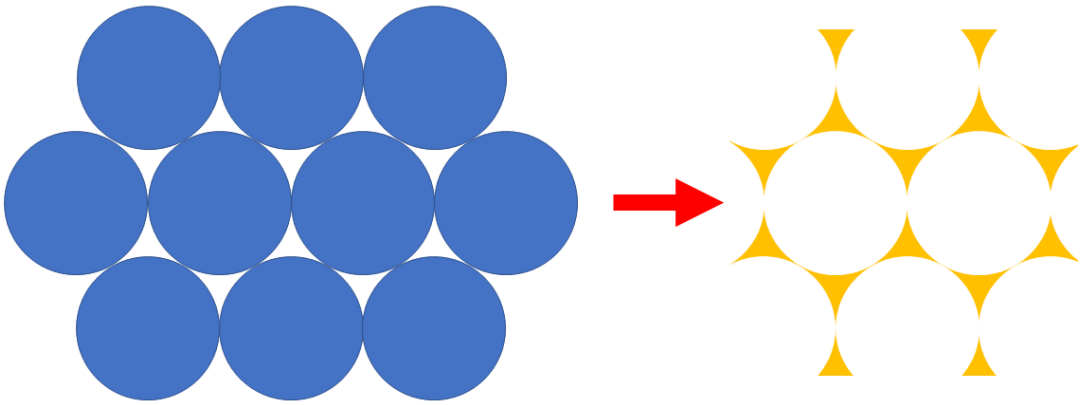

Figure 5-1 – Graphic showing the nanosphere lithography principal. Latex spheres form a monolayer in a hexagonal close packed crystal structure on the substrate surface. Material is evaporated through the roughly triangular apertures between the spheres. When the spheres are removed, triangular nanoparticles, arranged in a Fisher pattern, remain on the surface.

Tin-doped Indium Oxide coated glass slides were purchased from Prazisions & Glas Optik GmbH (PGO). The ITO substrates were cleaned through sonication in 1% Helmanex III solution and Ultrapure water.

Aqueous solutions of Polystyrene Nanospheres 10%wt, with diameters 800nm and 300nm, were purchased from Sigma Aldrich. A solution of Triton X-100, purchased from Sigma Aldrich, and ethanol at a 1:400 ratio was produced. Polystyrene nanosphere (800nm and 300nm diameter) suspensions were redispersed in the Triton X-100 – Ethanol solution at a ratio of 1:2 and 2:7, respectively.

Monolayers of polystyrene nanosphere on the ITO substrates were produced using a spincoating process. 30-50µL of the nanosphere solutions was spincast onto the clean ITO substrates. The spincoating process comprised of steps a) rotation 750rpm, acceleration 1000rpm/s, duration 20 secs; b) rotation 1500 rpm, acceleration 600rpm/s, duration 30 secs; c) rotation 3500 rpm, acceleration 600rpm/s, duration 45 secs; d) rotation 5000 rpm,

acceleration 250rpm/s, duration 60 secs. The solutions were dynamically cast onto the substrates during the last seconds of step a. Monolayer quality can be checked in an optical microscope.

Radial etching of the polystyrene nanosphere masks was done using a 100W Diener Zepto Plasma unit at room temperature under a 0.6-0.8 mBar oxygen atmosphere at different percentage powers for various times.

The substrates are then placed into a resistively heated thermal evaporation chamber (Moorfield MiniLab 080). A 3-5nm Chromium adhesion layer is evaporated onto the substrates. The deposition was typically around 0.4Å/s. Evaporation rates and film thicknesses are monitored using quartz crystal microbalances. Subsequent Ag or Au layers were thermally evaporated on top of the Cr adhesion layer. Au deposition was performed in an Oerlikon UNIVEX 300 bell jar evaporator and Ag films were prepared in a Moorfield M307 bell jar evaporator. Deposition rates were typically kept at around 1Å/s. The Al films were produced using an e-beam evaporator with a lower deposition rate of around 0.1Å/s.

5.3. Metal Deposition Techniques

Diagrams showing the working operations of resistive thermal evaporation and electron beam evaporation are shown in figure 5-2. These methods were used to deposit Ag, Au, Al, Cr, and Cu films in order to produce nanostructures using nanosphere shadow lithography. Films were deposited at a thickness of 35nm throughout, deposition thickness was monitored using calibrated quartz crystal microbalances (QCM).

5.3.1. Resistive Thermal Evaporation

The Ag, Au, Cr, and Cu films were deposited using resistive thermal evaporation. Metal source materials were purchased from Kurt J. Lesker Co. in wire, shot, or powder form. In resistive thermal evaporation the source material is loaded into an evaporation vessel, in

most cases a tungsten dimple boat. For the evaporation of Cr which has a very high melting point, tungsten rods coated in chromium are used. This provides a high surface area for contact with the Cr and the tungsten rod resulting in the chromium being heated to a higher level allowing for a deposition rate to be measured. The source material, in the boat or otherwise, is loaded between two electrodes in the evaporation chamber. The sample is attached to a rotating sample holder suspended above the source material at a requisite distance to assume normal incidence of vaporised material with the sample substrate surface. The chamber is evacuated to a pressure of around $1x10^{-3}$mBar to increase the average path length for energetic vaporised source material and maintain a reliable deposition rate. Once the sample and source material are loaded and the chamber is evacuated to a sufficient pressure, the source material is heated by applying a voltage using the variable power supply between the electrodes and across the source material boat. The inherent resistance of the tungsten boat causes it to heat under the applied voltage, this heating melts the source material and results in evaporation. The vaporised source material deposits on the sample substrate and the walls of the vacuum chamber. Once the required amount of material is deposited the power is reduced and the chamber is vented, the sample can then be retrieved.

Resistive thermal evaporation presents a cheap, fast and scalable option for thin-film fabrication. The vacuum levels required are not as high as other fabrication methods like sputtering or electron beam evaporation meaning that turnaround time is quicker and the equipment is cheaper and more easily maintained. Resistive thermal evaporation can be readily used with a variety of low melting point metals and other compounds like Sb_2Se_3 and ZnS.

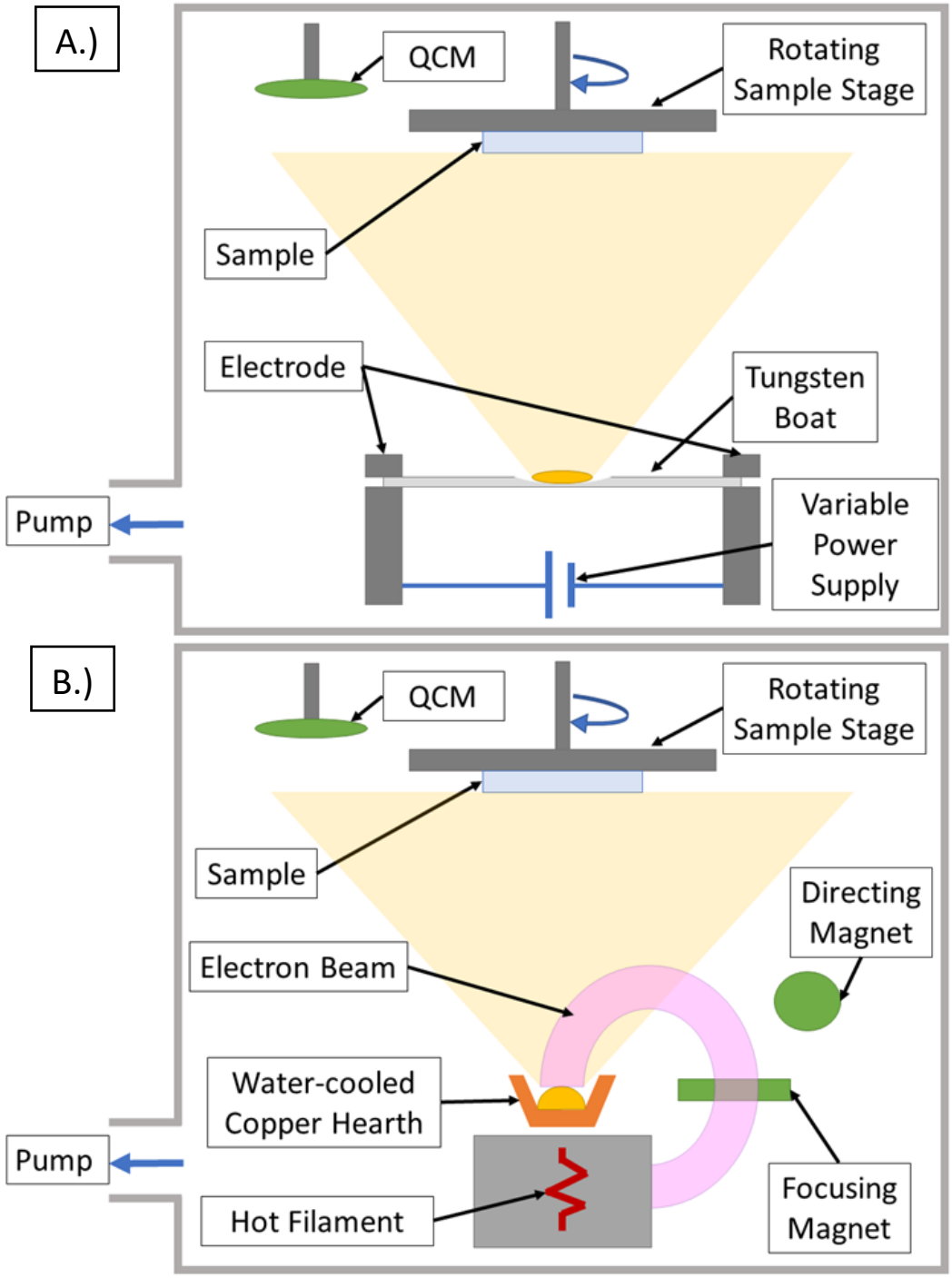

Figure 5-2 – Diagrams showing the working principles of thermal-resistive and electron beam evaporation. Both take placed in pressure regulated vacuum chambers. A.)– Thermal resistive evaoration. The source material placed in a tungsten boat is evaporated by the resistive heating of the boat. The boat is connected to a variable power supply by two electrodes. The sample is placed above the source material on a rotating sample holder. The deposition rate is measured by a calibrated quartz crystal monitor (QCM). B.) – Electron beam evaporation. The source material is placed in crucible on a water-cooled copper hearth. An electron beam is generated through thermission from a filament. The electrons are accelerated through a potential difference in the electron gun and focussed and directed onto the soure material using magnetic fields. The source material is heated by the incident electron beam and evaporates. The sample is placed above the source material on a rotating sample holder and the deposition rate is measured by a calibrated quartz crystal monitor (QCM).

5.3.2. Electron Beam Evaporation

Electron beam evaporation was used to deposit the aluminium films. The bottom of figure 5-2 shows the working principles of an electron beam evaporation apparatus. The source material is loaded into a water-cooled copper hearth either directly into the hearth or in crucibles made of graphite, ceramics, or other materials. The hearth is water-cooled to prevent the source from completely melting which can cause issues like wetting and the hearth itself evaporating. The vacuum chamber is evacuated to much lower pressures than in resistive thermal evaporation, around 10^{-7}mBar, in order to facilitate the electron beam.

In e-beam evaporation the source material is heated through bombardment of electrons, as the high energy electrons collide with the source material their energy is dissipated as heat which in turn causes material vapour to be emitted from the source. A hot filament is used to generate electrons through thermionic emission, these electrons are then accelerated into an electron beam using high voltage. The beam is then focussed and directed onto the source material using magnetic fields from controlled electromagnets. The electron beam can be scanned across the source material surface or directed into the centre of the source material.

As with resistive thermal evaporation the sample is placed in a sample holder suspended above the evaporation source and the deposition rate is measured using a calibrated QCM. The sample holder can be rotated and the sample substrate can be angled from normal with the source material. In this application the sample surface was kept normal to the evaporation source and was not rotated.

5.3.3. RF Sputtering

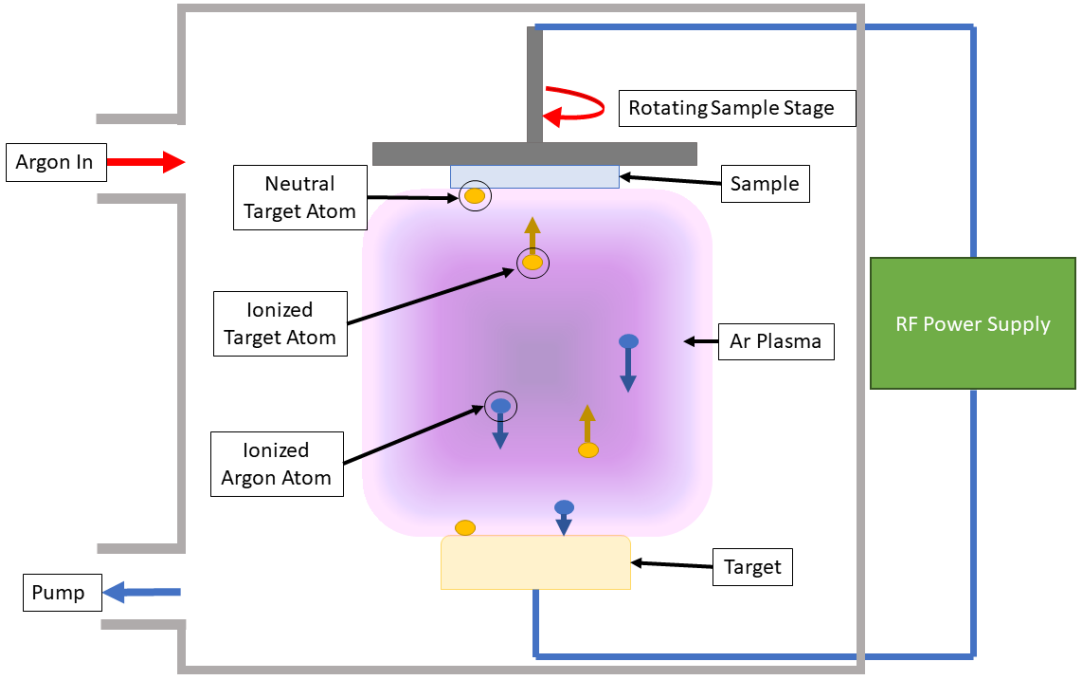

Figure 5-3 - Diagram showing the working principle of radio frequency sputterring. The vacuum chamber is pressure regulated and argon flushed. A large potential difference is established between the sample substrate and the source material target using the power supply.
The radio-frequency AC power supply is connected across the target and sample holder in-line with a blocking capacitor which maintains the DC potential. The alternating current reduces the build-up of charge on the target surface reducing the poisoning of the target surface.
The large bias potential generates an argon plasma in the chamber. Charged argon atoms bombard the target material and ionize soucre material atoms. The ioinized source material atoms are directed towards the sample substrate across the potential difference. The source material atoms are then nuetralized and deposited at the sample substrate.
Deposition rate is monitored using calibration runs where the deposition parameters and time are monitored and the film thickness is measured through AFM or with a profilometer.

Sputtering techniques offer a scalable and controlled deposition technique for thin-film materials.[9,10] Figure 5-3 shows a diagram of the working principles of a radio frequency sputtering chamber. Sputtering deposition techniques use a plasma to bombard a target and remove charged ions from the source material and deposit them onto a substrate. The target and substrate act as opposite electrodes to generate the plasma in the deposition chamber and to allow for charged ions to be drawn to the substrate across the in-built electric field bias. In radio frequency sputtering the bias voltage between the target and substrate is driven by a radio frequency alternating current. The source material target and the substrate act as the cathode and anode with a blocking capacitor placed in series to allow for the DC

charge bias. The radio frequency alternating current blocks the build-up of charge on the surface of the source material which can result in arcing and allows for the deposition of electrically insulating materials.

The sample substrate is loaded onto a rotating sample holder suspended above the targets in the chamber. In order to develop coherent thin-films, the sample is rotated in order to evenly deposit material across the substrate surface. Deposition rate was measured by fabricating calibration samples and measuring the film thickness. Calibration films were deposited onto a plain glass substrate that was masked in order to create a step in the film. Samples can also be scratched to reveal the substrate below the film. The deposition conditions were kept steady and the deposition time was measured. The film thickness was the measured using AFM or a profilometer scanned across the step or scratch in the film. Multiple measurements were taken and the average was divided by the deposition time to calculate the deposition rate. Subsequent fabrication runs then use the calibrated deposition rate and identical deposition conditions.

TiO_2 thin films were produced through RF sputtering of a TiO_2 target in Argon atmosphere. Sputtering was performed at 150W under a 5mTorr Argon atmosphere for the required time. The deposition rate was measured at 0.33nm/min.

5.3.4. Hematite Electrodeposition

Electrodeposition is a method of coating surfaces or substrates with a material from a solution of ionic species, usually salts. Electrodepositions can be carried out in a three-electrode electrochemical cell. Generally, the substrate to be deposited on is set up as a working electrode, with a counter electrode to complete the circuit, a reference electrode is also used in small-scale lab-based experiments to control the potential differences that are applied. Using a potentiostat, a potential difference is established between the working electrode and the counter electrode, this causes the ions in the solution to drift towards

either electrode and be reduced or oxidised. The uncharged elements or compounds will then adhere to the electrodes. Electrodeposition has some advantages over other typical deposition techniques such as scalability, low-cost, and high deposition rates.[11,12] Electrodeposition has been used to synthesise nanocrystalline films of various semiconductor materials including Fe_2O_3, CdTe, ZnO and Cu_2O.[11–14]

Hematite films were produced using a process adapted from Zandi et al[15]. Initially FeOOH films were prepared on undecorated and nanoparticle decorated ITO-coated glass substrates through an electrodeposition procedure. An aqueous solution of 8M NH_3Cl, 0.02M $FeCl_2$, and 0.008M $SnCl_2$ was prepared and degassed for at least 30 minutes under Argon flow. The pH of solution was adjusted to 7.5 through addition of 2M NaOH. The solution was then added to a three-neck electrochemical cell, with the substrate as the working electrode, a platinum foil counter electrode, and a home-made 3M NaCl Ag/AgCl reference electrode. The electrodepositions were performed using a chronocoulometric technique at 0.0V. The FeOOH coated substrates were then calcinated in a furnace in air at 650^{o}C for 30 mins. In this step the FeOOH is converted to Fe_2O_3.

The deposition process used in this study is based on a two-step anodic electrodeposition adapted by Zandi[15] and Spray[16] who also adapted the process first described by Cohen in 1967[17,18]. The addition of the NH_3Cl is crucial in order to maintain the solubility of the Fe^{2+} species at a pH of 7.5[15]. In the first step the Fe^{2+} species from the dissolved $FeCl_2$ are oxidised to Fe^{3+} at the cathode. The second step involves the Fe^{3+} precipitating in aqueous solution as the ferric oxyhydroxide (FeOOH). The Fe^{3+} ions are much less soluble in the neutral solution than the Fe^{2+} and begin to precipitate at the anode as FeOOH, depositing on the substrate surface.[16] The equations are given below.

Equation 28

$$Fe^{2+} \rightarrow Fe^{3+} + e^{-}$$

Equation 29

$$Fe^{3+} + H_2O \rightarrow FeOOH + 3H^{+}$$

The ferric oxyhydroxide films are then be sintered to form Fe_2O_3 films.

Equation 30

$$2FeOOH \rightarrow Fe_2O_3 + H_2O$$

5.3.5. Atomic Layer Deposition

Atomic layer deposition (ALD) is a process which utilises incredibly short reactant, or 'precursor', exposure times, followed by purge cycles, to grow a compound atomic layer by atomic layer. In doing so it works in a highly desirable self-limiting fashion, as once the saturation point of a substrate is reached no further precursor can be added, resulting in highly uniform surfaces of a specified thickness. Plasma enhanced atomic layer deposition (PEALD) utilises a plasma generator to produce radicals which can then react directly with the previously applied reactive precursor species. This method offers enhanced reactivity compared to traditional techniques (eg. water/ oxygen gas), and hence offers advantages such as lower chamber temperatures and improved growth.

Hematite thin films of sub 100nm thickness were produced using atomic layer deposition in collaboration with Natalie Bavis and Dr Richard Potter from the Engineering Department at the University of Liverpool. Blank and nanostructure decorated ITO films were covered with hematite using a procedure developed by Natalie Bavis.

In this instance, overlayers of Fe_2O_3 are produced via a PEALD process that uses a ferrocene ($Fe(Cp)_2$) powder precursor with an oxygen/argon plasma to grow thin hematite films. Short pulses of ferrocene allow for the iron species to coat the ITO substrate before the excess is purged away, followed by short bursts of plasma generated oxygen radicals which react to produce iron oxide. This repeats in a cyclic pulse-purge-pulse-purge sequence to make the nanostructured iron oxide films. This is carried out in a 250°C ALD chamber under vacuum. Overall growth for this process was estimated to be 0.05nm/cycle on Si wafer and 0.08nm/cycle on FTO/ITO glass for the first few hundred cycles. However, a degree of self-limitation is observed with longer sequences and a 1500 cycle Fe_2O_3 run is estimated to produce a film in the region of 50nm thickness.

Samples produced with an Al_2O_3 underlayer to the hematite were preceded by a 10-cycle process using a trimethylaluminium (TMA) precursor and oxygen plasma, created a layer of approximately 1nm thick. These films were annealed at 600^{o}C for 30 mins in ambient conditions in a box furnace.

5.4. Characterisation Techniques

5.4.1. UV-Vis-NIR Optical Spectroscopy

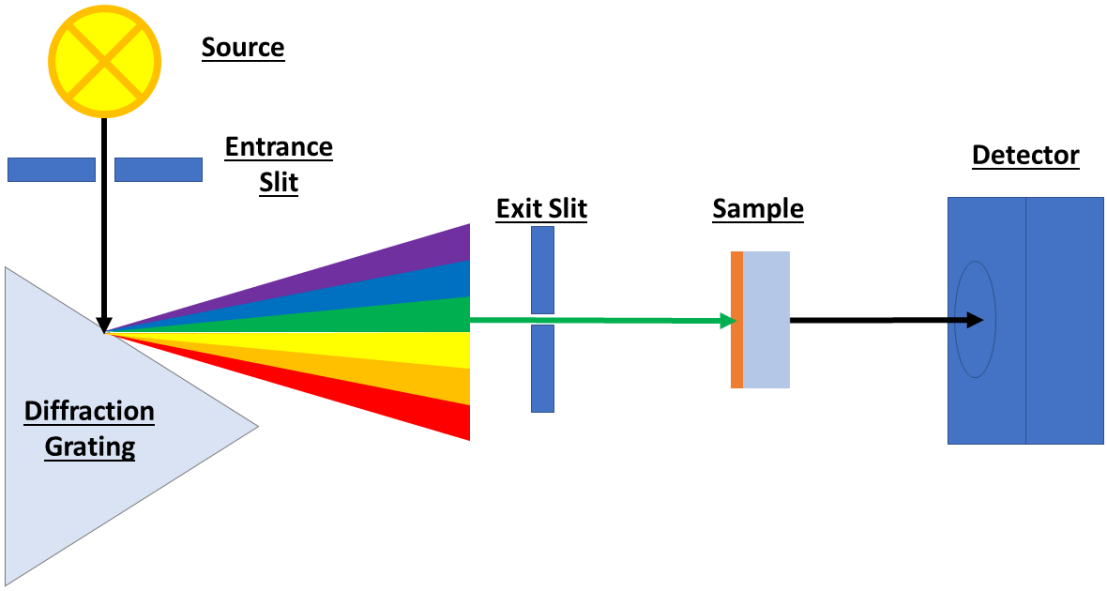

Figure 5-4 – Diagram showing the working principle of a UV-Vis-NIR spectrophotometer. Broadband light is generated at a source, usually a combination of deuterium and tungsten bulbs. The source light passes through an entrance slit onto a diffraction grating. The dispersed light is directed onto a exit slit such that the monochromated light is permitted through. Monochromated light passes through the sample and into the detector. The sample absorbance is measured as a differential between a spectrum measured with no sample or a baseline sample. The wavelength of light is altered by the diffraction grating angle and controlled through the size of the exit slit.

An Optical Spectrometer can be used to measure the transmission and reflectance of substrates and solutions in the UV to visible region of the electromagnetic spectrum. Figure 5-4 shows a basic diagram showing the working principles of a UV-Vis-NIR optical spectrophotometer. Broad spectrum light is generated by a deuterium (190-400nm) or tungsten (300-2500nm) lamp. The light is then passed through an entrance slit onto a diffraction grating and is dispersed. The position of the diffraction grating changes in order to sweep along the light spectrum. An exit slit is used to control the monochromation of the light, with the monochromated light directed onto the sample. The exit slit size can be tuned in order to select the wavelength precision of the light incident onto the sample. The exit slit size also varies the surface area of the sample that is illuminated therefore, a balance must

be struck between wavelength precision and spot size of the incident light onto the sample surface. In the direct geometry the monochromated light passes through the sample and into a detector. The detector measures the intensity of the light that is incident. Spectra are taken as a function of light intensity with respect to a baseline a reference spectrum that is taken without the sample in the pathway. Transmission spectra can be converted to absorption using the Beer-Lambert Law, the equation is given below.

Equation 31

$$A = -log_{10}(T)$$

Where A is absorbance and T is transmittance. Transmittance is given as the percentage of light intensity that passes through the sample, when compared to the baseline spectra.

UV-Vis-NIR spectra were taken using a Shimadzu SolidSpec-3700 UV-VIS-NIR Spectrometer for substrate-based samples. UV-Vis spectra of solution based samples were taken using Shimadzu SolidSpec 3700i. Generally, spectra were taken using the direct geometry and absorbance data was usually taken directly using the apparatus complementary software. Reflection data was attempted but did not return useful data. Substrate based samples were baselined using either no sample or a clean, blank ITO-coated glass slide. Solution based samples were baselined using a cuvette of the pure solvent which was usually ultrapure water.

5.4.2. Scanning Electron Microscopy

A scanning electron microscope (SEM) uses a focussed beam of electrons in order to generate images beyond the diffraction limit of visible light allowing imaging on the nanoscale. The JEOL 7001F microscope that was used in this work has a manufacturer stated resolution of 1.2nm at 30kV acceleration voltage and 3.0nm at 1kV based on the diffraction limit at the de Broglie wavelength for an accelerated electron. The diffraction limit for an

optical microscope is taken as half of the wavelength used, therefore in a best-case scenario the resolution is around 200nm.

In SEM the incident high-energy electrons interact with the sample surface and a variety of signals is generated which can be used to form multiple image types and reveal different information of the sample surface such as topography and composition. Topography information can be taken as an image by collecting secondary electrons from the sample surface. The incident primary electron beam is raster scanned across the sample surface and the secondary electrons are detected. Information about the sample composition can be determined from the characteristic x-rays emitted from sample through EDX.

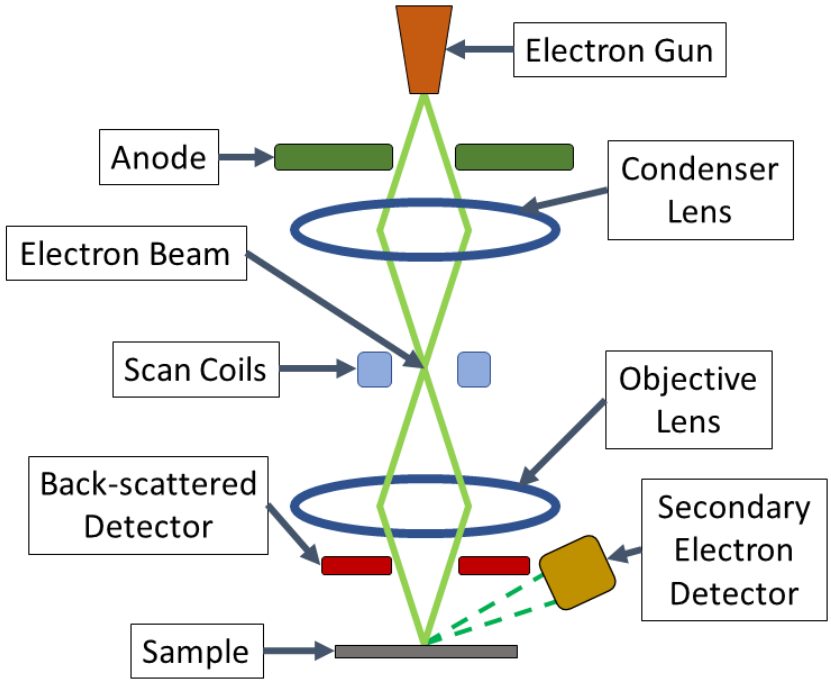

Figure 5-5 – Schematic showing the basic components of a Scanning Electron Microscope.

Figure 5-5 shows the basic working components of an SEM. The primary electron beam is generated in an electron gun either thermally or through field emission. These electrons are then accelerated through a large potential difference in an electron gun and focussed through a series of electromagnetic condenser and objective lenses. The beam is raster

scanned along the sample by manipulation from the scanning coils. Back-scattered and secondary electrons are detected by the relevant apparatus. Other detector types can be used in conjunction with SEM to provide different information about the sample. The primary electron beam can penetrate the substrate surface by up to a few microns, the primary electrons interact with the sample in various ways, and at different depths, the results of these interactions can be detected and used to gain information about the sample. Figure 5-6 shows the interaction volume and types of signal generated.

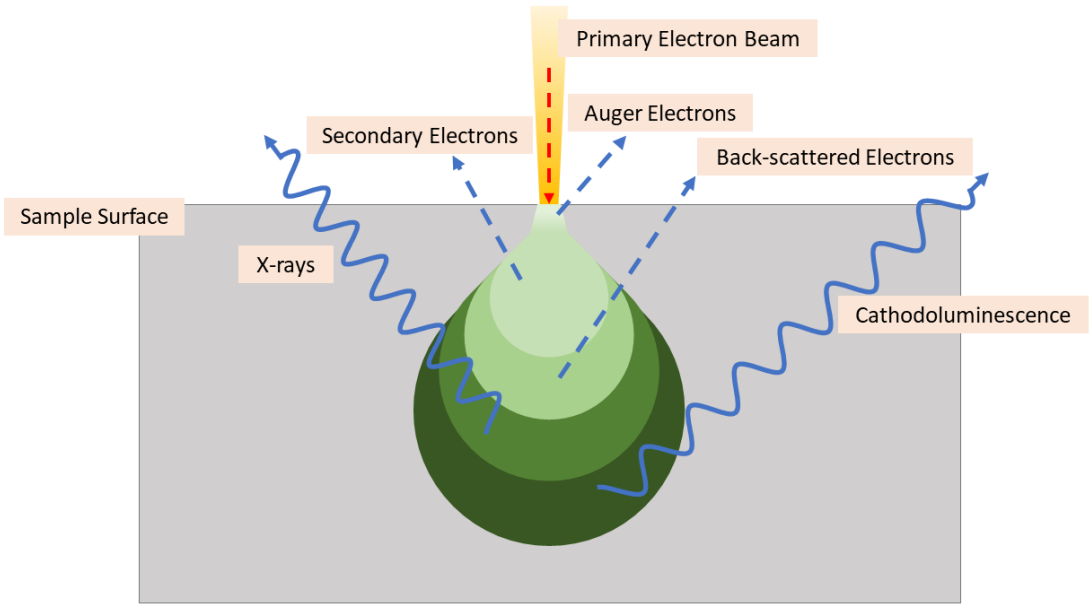

Figure 5-6 – Schematic of the electron beam interaction in SEM. As the electron beam penetrates the sample surface the interactions between the electron beam and the sample releases characteristic EM radiation and energetic electrons. These interactions and the emitted radiation occur and emanate from different depths of the sample surface. Back-scattered and secondary electrons are used for surface imaging in SEM. Auger electrons and x-rays are used to characterise the material composition of the samples using various secondary detectors available to SEM apparatus.

When the primary electron beam interacts with the surface the electrons can either be back scattered or cause secondary electrons and Auger electrons to be ejected from the surface, as the electrons penetrate deeper into the sample the interactions can also cause the emission of x-rays. The SEM apparatus contains a variety of specific detectors which can be used to build images or obtain spectra for the electrons or x-rays that are emitted.[19,20]

The secondary and back-scattered electrons are used mainly to image the sample. Secondary electrons are the main source of surface imaging, their low energy means that they have a low escape depth and the intensity of these electrons collected the detector is sensitive to the path length to the detector and therefore the surface topology. Back-scattered electrons are primary electrons that are reflected from the sample. The energy of the back-scattered electrons is proportional to the atomic weight (Z number) of the sample. Therefore, back scattered images can also give some information about the elemental makeup of the sample. Higher atomic weight materials give a higher intensity of BSEs and therefore the image shows Z-contrast as well as some topographical information.

As the primary electron beam interacts with the surface electrons are promoted to higher energy levels in the atoms, as these electrons relax characteristic x-rays are emitted. These x-rays can be detected in the vacuum chamber and x-ray spectra can be taken. The peaks in these spectra can be assigned to specific elements and composition information can be gained. These EDX spectra can also be mapped as the primary beam is raster scanned along the sample surface giving elemental maps of the surface.[21]

SEM images shown in this work were taken using a high-resolution JEOL 7001F field-emission SEM. Secondary electron imaging was used to obtain topographical information. Settings for acceleration voltage an, contrast and brightness, were altered to optimise image quality.

5.5. Photoelectrochemistry

Photoelectrochemical experiments are achieved by using a three-electrode set-up with a working electrode (usually the sample to be tested), a counter electrode (generally Pt foil or mesh), and a reference electrode such as, Ag/AgCl or SHE. Electrochemical measurements are taken in conjunction with sample illumination in order to study the light absorption characteristics of certain materials.

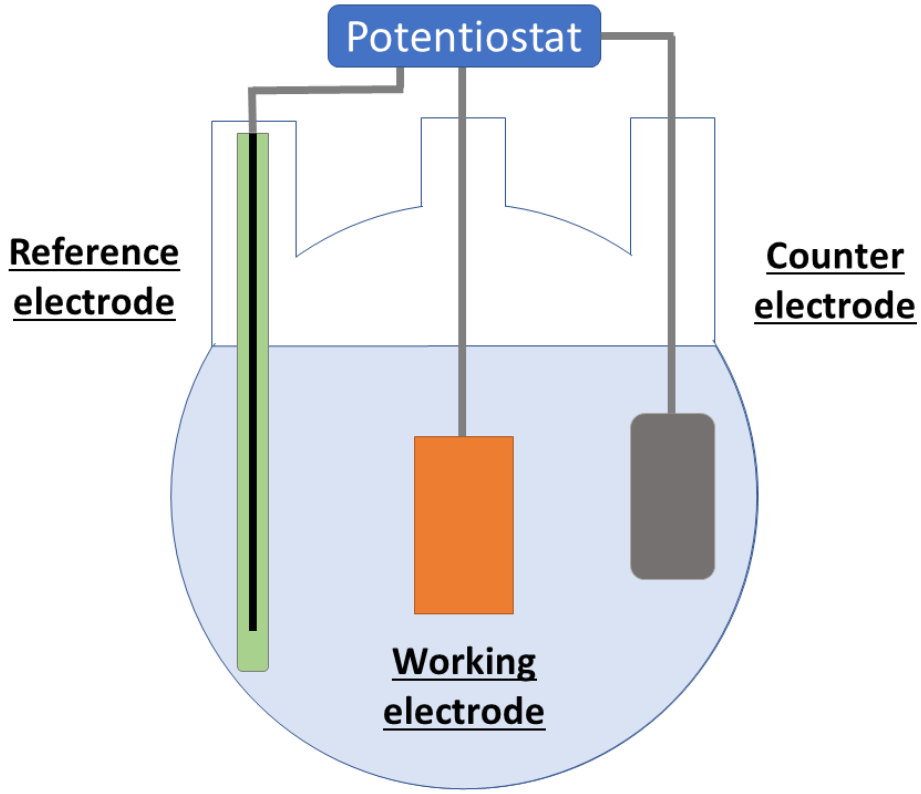

Figure 5-7 – Diagram showing the three-electrode photoelectrochemical (PEC) cell set-up. The cell is filled with a chosen electrolyte, in this study 1M NaOH was used. The three-electrode set-up uses the sample as the working electrode with the potential measured between the counter-electrode, which is usually Pt foil or Pt-wire. There are multiple possible reference electrode formats. In this work a homemade (Ag/AgCl) was used a reference electrode.

A diagram showing the three-electrode set-up is shown in figure 5-7. A potential difference is measured between the counter and reference electrode, and the working electrode is held at the same potential as the reference. The current and voltage between the counter electrode and the working electrode can both be controlled and measured allowing for various measurements to be taken such as current vs voltage scans, or transient measurements like chronoamperometry whereby the current is measured as a function of time as a potential difference is held in place. By measuring how the current or potential difference across the electrodes changes under illumination information about the photoresponse of light sensitive materials can be revealed.

5.5.1. Linear sweep voltammetry and Chronoamperometry

Linear sweep voltammetry is a method of obtaining current-voltage (I/V) curves in an electrochemical cell. The current flow response between the working and counter electrode is measured, as the voltage applied is linearly varied between predetermined values with respect to time in a single scan and in one direction. This differs from cyclic voltammetry, which sweeps in both directions usually multiple times. Positive current flow relates to oxidation reactions at the surface of the working electrode, and negative currents relate to reduction reactions.[22,23] Current-voltage characteristics can be used to determine how a device responds in an electrical circuit and analyse characteristics such as resistance, rectification or power generation.[24] Linear sweep voltammetry can be performed under chopped illumination to show the photosensitivity of the sample across the voltage range. Comparing linear sweep voltammograms taken in dark condition with scans taken under illumination show the photocurrents across the voltage range.

Chronoamperometry is a transient PEC measurement, which applies constant voltage to a sample over time. A fixed bias potential is applied between the counter and working electrode and the current flow is measured as a function of time. By utilising chopped light illumination, it is possible to measure the photocurrent at a specific bias by calculating the difference between the current in the dark conditions and the current under illumination.

General electrochemical measurements were carried out in a custom made four-neck electrochemical cell. The electrolyte used in all experiments was 1M NaOH prepared with Ultrapure water which was degassed under the flow of argon for at least 30 mins. The substrates were attached as the working electrode using a crocodile clip, with a Pt foil counter electrode, and a home-made 3M NaCl Ag/AgCl reference electrode.

Photocurrent measurements were recorded using an Ivium CompactStat potentiostat under illumination of 450 W FL-1039 Xe source (Horiba Scientific) with a homemade water-filter to

minimise sample heating. Chronoamperometry measurements were taken at 0.3V vs the Ag/AgCl reference electrode.

5.5.2. Incident Photon-to-Electron conversion efficiency (IPCE)

Incident photon-to-electron conversion efficiency (IPCE) is the ratio of photogenerated charge carriers collected from the working sample and the number of incident photons. Using the absorbance data for the sample the IPCE can be converted to quantum efficiency which is the ratio of photogenerated charge carriers and the number of photons absorbed by the sample.

IPCE measurements can be used to show the spectral sensitivity of a solar cell device or photocatalytic electrode. Chronoamperometry measurements of the samples are taken under illumination of monochromated light at different wavelengths over a certain spectral window. The photocurrents measured are then normalized to the incident light power at the corresponding wavelength using equation 5, giving the conversion efficiency as a percentage value. The percentage values for IPCE are plotted against the wavelength of the light measured at to give IPCE spectra. The spectral sensitivity of the devices gives information about the utilised absorption of the sample when compared directly to the light absorption. Comparing IPCE spectra between samples information about the differences in photoconversion can be revealed including enhancement and quenching mechanisms.

Equation 32

$$IPCE\% = \frac{I_{SC}(\frac{A}{cm^2})}{P(\frac{Watt}{cm^2})} \times \frac{1240}{\lambda(nm)} \times 100$$

In equation 5 I_{SC} is the measured photocurrent density, P is the incident power from the illumination source, the 1240 value comes from $E = {hc}/{\lambda}$. When correcting for λ in nanometres and energy in eV, the equation becomes;

$$E = {hc}/{\lambda} = {(4.13 \times 10^{-15}) \times (3 \times 10^{8})}/{\lambda(nm) \times 10 - 9} = {1240}/{\lambda(nm)}.$$

Using the electrochemical cell setup described previously, IPCE measurements were taken using a PalmSens3 (Alvatek) potentiostat under illumination from a 100 W tungsten lamp coupled to a monochromator (OBB Corp., typically set to 6 nm resolution). The working electrodes were held at 0.3V vs Ag/AgCl throughout. In order to measure the photocurrents illumination was chopped using a large black slide.

5.6. FDTD Simulation

Finite difference time-domain (FDTD) simulations are performed by solving the Maxwell curl equations for non-magnetic materials around a finite mesh in order to calculate the electromagnetic field and simulate properties such as transmission and reflectance.

Equation 33

$$\frac{\partial \vec{D}}{\partial t} = \nabla \times \vec{H}$$

Equation 34

$$\vec{D}(\omega) = \varepsilon_0 \varepsilon_r(\omega) \vec{E}(\omega)$$

Equation 35

$$\frac{\partial \vec{H}}{\partial t} = -\frac{1}{\mu_0} \nabla \times \vec{E}$$

Equations 6 to 8 show the Maxwell equations for non-magnetic materials utilised in FDTD. Here $\vec{D}$, $\vec{H}$ and $\vec{E}$ are the displacement, magnetic and electric fields and ε_r is the complex relative dielectric constant. The dielectric constant is taken from refractive index (n) for the relevant material from $\varepsilon_r=n^2$. In three dimensions, assuming that the z-axis extends infinitely in both directions, the following statements can be made:

$$\varepsilon_r(\omega, x, y, z) = \varepsilon_r(\omega, x, y)$$

$$\frac{\partial \vec{E}}{\partial z} = \frac{\partial \vec{H}}{\partial z} = 0$$

With these statements the Maxwell equations can be split into the transverse electric (TE) and transverse magnetic (TM). These groups of equations can then be solved using three components for each. The E_x, E_y, and H_z components are used to solve the TE equations and the H_x, H_y, and E_z components ae used to solve TM. For example, the TM case the Maxwell curl equations reduce down to the following:

Equation 36

$$\frac{\partial D_z}{\partial t} = \frac{\partial H_y}{\partial x} - \frac{\partial H_x}{\partial y}$$

Equation 37

$$D_z(\omega) = \varepsilon_0 \varepsilon_r(\omega) E_z(\omega)$$

Equation 38

$$\frac{\partial H_x}{\partial t} = -\frac{1}{\mu_0}\frac{\partial E_z}{\partial y}$$

Equation 39

$$\frac{\partial H_y}{\partial t} = \frac{1}{\mu_0}\frac{\partial E_z}{\partial x}$$

These equations are solved along discrete spatial and temporal grid with each component calculated at different position on the grid cell, known as the Yee cell.[25,26] The Yee cell is shown in figure 5-8. The Yee cell represents the 3D space in the simulation volume and the components are calculated at each time interval. The H components are calculated at the centre of the cell faces and the E components are calculated at the centre-point of the edges as shown in the figure. The software package, or the user, can then extrapolate the components to the cell origin. The size of the Yee cell in x, y, and z in the simulation region is controlled by meshing the simulation region, and changing the size and number of grid cells that populate the simulation volume. [25,26]

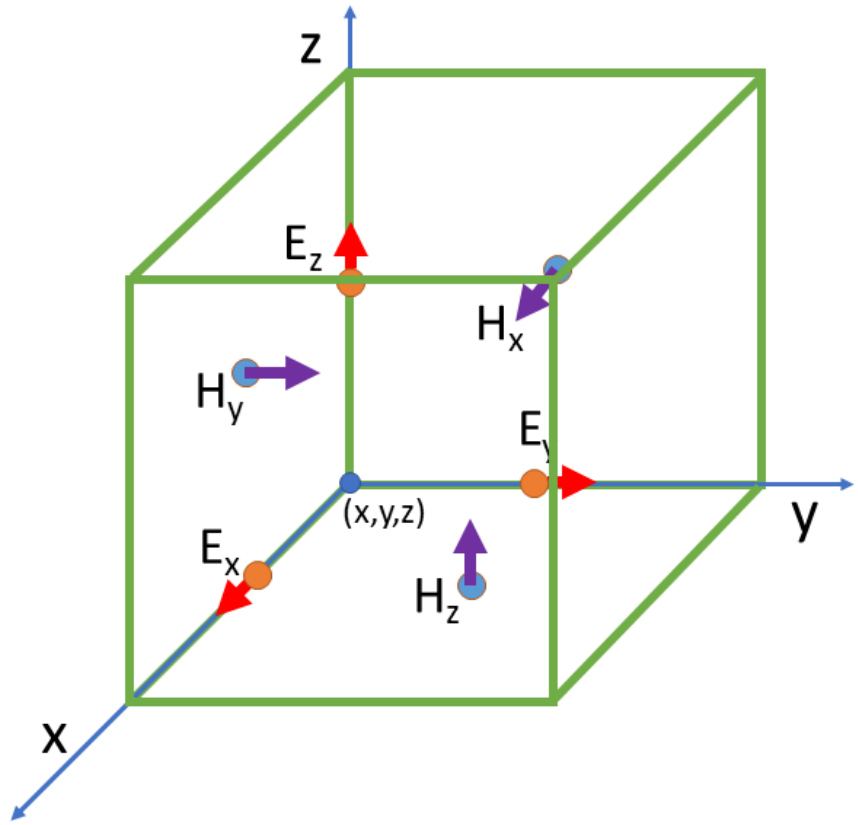

Figure 5-8 – The Yee cell. E components are calculated at the centre point of the cell vertices. H components are calculated in the centre of the cell faces. Arrow direction relates to positive direction.

There are various ways to perform meshing for FDTD. The simplest is a method called staircasing. In this method the material in each Yee cell in the simulation is evaluated and

the entire cell is assigned to a single material. The simulation then calculates E and H components at that grid cell position for the single material. This results in poor resolution in object shapes and a staircasing effect at boundaries of materials with differing permittivity as the permittivity grid coincides with the Cartesian mesh grid. This means that any structure variations that occur on a scale lower than the mesh size, or any layers that are thinner than the mesh cell walls are lost. This can be helped by reducing the mesh size however this also increases the computational load.[27]

Lumerical FDTD software offers methods to improve the mesh resolution to overcome the issues with the simple staircasing method. A non-uniform mesh can be used to include areas of higher mesh resolution around interfaces between permittivity's in the simulation. This increases the mesh resolution around object shapes or thin layers whilst keeping a larger mesh in free-space. This maximises the computational load whilst minimising the implications of the staircasing method such as numerical dispersion and resolution at interfaces.[28]

The Lumerical FDTD also offers a meshing refinement system called 'conformal mesh technology'. This method adapts the Yu-Mittra method at structure boundaries to reduce the effects of the discretization of structure morphology by the mesh grid.[27,29] The software is able to assess the materials found in each cell and apply a rigorous physical description of Maxwell's integral equations near interfaces between two materials. If more than two materials populate the cell the software reverts to the staircasing method for that cell.

The simulation time in FDTD is directly proportional to the total simulation volume due to the spatial and temporal nature of the calculations. However, for free-space radiation or scattering problems the simulation volume should be infinite and therefore requiring an infinite number of grid cells. This is clearly not possible and so artificial boundaries can be used to terminate the simulation domain at set distances from the simulated structures.

These boundary conditions allow for optimization of the computational requirements and can affect the effective simulated structures.

Perfectly-matched layer (PML) boundary conditions can be used for single structures whereas symmetrical and periodic boundary conditions can be used to simulate larger and infinite structures without increasing the simulation volume. PML boundary conditions absorb incident light from the simulation region to reduce reflections that can occur at the boundaries. The PML boundaries act as a material with very specific properties in the simulation at the edges of the simulation volume. At the edge of the PML layer at the interface to the simulation the impedance is matched to whatever material the boundary dissects. The full PML boundary consists of layers of decreasing impedance such that there a minimum impedance at the outer layer. This reduces reflection at the boundary and absorbs the light incident on the boundary.[26,30]

Symmetry and periodic boundary conditions can be used to simulate larger or infinite structures based on a unit cell simulation structure.[31,32] Symmetric and anti-symmetric boundary conditions can be used when the inputted EM fields in the simulation have a direct plane of symmetry with the simulated structures. These boundary conditions can be used to reduce the size of the simulate volume by factor of 2, 4, or 8, which can reduce computing time and allow for optimisation such as higher mesh resolution. The boundaries in the directions in which the structures and fields are not symmetrical are kept as PML boundaries. Symmetrical EM fields have some zero field components at the plane of symmetry. Symmetry boundary conditions then force the relevant field components to zero. This reduces the total number of field components that require simulating. The built-in software then unfolds the simulated data across the symmetry planes to reveal full data. As electric and magnetic field components are perpendicular, as are symmetric and anti-symmetric boundary conditions. Symmetric boundary conditions cancel the field components along the

plane of symmetry of the electric field and anti-symmetric do so for the magnetic field. Therefore, the correct symmetry must be chosen to reveal correct results.

Symmetry boundary conditions can be used to simulate periodic structures. In this case both symmetric and anti-symmetric boundary conditions are used at the same time. The simulation can be setup so that EM source has planes of symmetry with the unit cell of the periodic structure. The x and y minimum and maximum boundaries are set to symmetric and anti-symmetric depending on the orientation of the EM source. Having both boundaries using symmetry boundary conditions maintains periodicity of the structure by effectively repeating the structure and source in both x and y conditions. This only works for when the source and structures are periodic. This helps to reduce computing time by simplifying the simulation region.[32]

Periodic boundary conditions allow for large arrays to be simulated using just one unit cell in the simulation region and can be used when the source is not symmetric with structure. The periodic boundaries work by copying the EM fields absorbed at one side of the boundary and injecting them at the opposite side. For this to work all aspects of the simulation must be periodic. If the illumination source is angled then the fields injected by the boundary conditions would be out of phase with the illumination source, and therefore another boundary condition should be chosen.[31]

Finite Difference Time-Domain simulations were achieved using Lumerical FDTD Solver, a purpose-built software package. Nanostructures and heterostructures are modelled in 3 dimensions using the built-in 3D computer aided design functionality. Infinite arrays were modelled using symmetric and anti-symmetric boundary conditions. Mesh sizes vary depending on material type and simulation time. The choice of source type, such as total-field scattered-field (TFSF), plane-wave, and Gaussian wave, vary depending on the application. Material n,k data were taken from literature tables; Gold – CRC Handbook for

Chemistry and Physics[33]; silver, aluminium, and SiO_2 – Handbook of Optical Constants of Solids by E.Palik[34]; Hematite –Marvin R. Querry[35] and ITO – Tobias König[36].

5.7. Molecular Conductance Measurements on Plasmonic Substrates

5.7.1. Gold Nanoparticle Synthesis

Citrate-capped spherical gold nanoparticles were synthesised through a seed-mediated step-wise growth method based on the Turkevich method as described by Bastús et al.[2,37] This method uses gold nanoparticles with diameters of the order of 8nm as seed particles to then form larger nanoparticles with narrow size distribution in an incremental method. The seed nanoparticles are created in the initial phase of the synthesis where the gold precursor is quickly injected into a boiling sodium citrate solution. The gold precursor is an aqueous solution of $HAuCl_4$. Upon addition, $AuCl_4^-$ ions are reduced by $C_6H_5O_7^{3-}$ ions from the sodium citrate solution. The partial reduction of the Au precursor forms gold monomers that subsequently coalesce to form small clusters of gold. These small clusters act as the seeds for larger particles to grow around and no further particles are formed. The clusters grow as further gold ions are attracted and reduced in the electric double layer surrounding the clusters, until the precursor is consumed.[37] In Bastús' method the nanoparticles formed after one addition step of precursor solution are used as seed particles in the subsequent step. After each step aliquots of nanoparticle solution can be taken or the reaction can be stopped allowing for the selective synthesis of controlled size distribution nanoparticle solutions. Steps can be repeated until Au nanoparticle solutions with an average particle size of ~200nm are formed.[2]

A 2.2mM Sodium Citrate solution is brought to boiling point under reflux in a round bottomed three-necked flask. Once this temperature is reached 0.3ml of 25mM Chloroauric

Acid ($HAuCl_4$) is added rapidly. A colour change is observed as the solution turns to the characteristic ruby red. After 30 minutes the reaction is complete and the solution can be removed for use as small (~10nm) gold nanoparticles or as seeds for further growth steps or to produce other morphologies. In order to grow larger nanoparticles, the entire, as synthesised, seed batch is heated to 90^{o}C, once this is reached 0.3ml of 25mM $HAuCl_4$ is added dropwise into the stirring solution. Once 1ml total of the gold precursor has been added the step is complete. To continue to subsequent steps 18ml of the solution is removed from the reaction vessel and can be stored in the fridge. 17.5ml of MilliQ water is then added along with 0.5ml of 60mM sodium citrate and the temperature is allowed to return to 90^{o}C. Once the temperature is stable the addition of gold precursor can then follow, repeating the steps as before.

5.7.2. Molecular Monolayer Growth

Self-assembled monolayers (SAMs) are formed by the spontaneous adsorption of molecules to a substrate surface. Organic molecules are readily adsorbed to metal and metal oxide surfaces as they help to lower the free energy of the interface of the surface and the ambient environment. SAMs are produced by the adsorption of molecules to the substrate from a solution or gas phase in regular crystalline or semi-crystalline structures. The monolayers form spontaneously and sometimes epitaxially upon substrate exposure to the adsorbate. The molecules are often chosen for their specific functionality such as a head-group that has an affinity for the chosen substrate. Headgroups with very high affinities for certain substrate materials such as thiolated molecules on gold, can displace adventitious organic impurities that have previously adsorbed to the substrate. This ensures that the SAMs are chemically homogenous and increases reliability in further experimentation.[38]

Gold-coated glass slides and nanoparticle decorated substrates were cleaned through sonication in isopropanol for 20 minutes. The cleaned substrates were the immersed

overnight in a solution of the molecule. The self-assembled monolayers spontaneously form during the immersion and are self-limiting. The slides were then rinsed with ethanol to remove excess solution. In the case of gold spherical nanoparticles on gold glass slides the monolayer layer coated gold slides were immersed in a solution of the citrate capped gold nanoparticles. The gold nanoparticles then functionalize and immobilize onto the SAM on the substrate. Immersion time was optimized to form good uniform coverage whilst limiting aggregations.

5.7.3. Conductive AFM

A diagram showing the working principles of atomic force microscopy (AFM) is shown in figure 5-9. Imaging using AFM can be conducted using three methods, these are contact and non-contact, or tapping, modes. AFM uses a nanoscale tip mounted on the end of a cantilever that is scanned across the surface and can be used to image the substrate surface. The tip or the substrate can be manipulated in the x, y, and z axes by piezo electric controllers. The piezoelectrics are used to control the tip sample separation, and the scanning direction when imaging is performed.[39,40]

In contact mode the AFM tip is brought close to the substrate surface such that the cantilever begins to deflect. As the tip approaches the surfaces the cantilever bends downwards due to the attractive van der Waals interactions between the tip and the substrate. As the tip makes contact to the surface the cantilever begins to bend upwards as a force is applied to the surface, the amount of force applied to the sample, and therefore the amount of deflection required, is known as the set point. The AFM control unit acts to keep the set-point stable during the AFM scan. As the tip is scanned at across the surface the tip deflection is measured by a laser and photodiode. The laser light is reflected off the back side of the cantilever into

a segmented photodiode. As the tip deflection angle changes the laser light spot on the photodiode moves. The position of the laser light spot on the photodiode is used to measure the deflection of the AFM tip. As the tip scans across the surface changes in the surface topology causes the tip deflection to change. The control unit alters the tip sample separation using the z-axis control from the piezoelectrics to keep the deflection in line with the set-point. The required z-axis alterations are then used to image the sample topology in the accompanying software.[39]

The non-contact and tapping modes allow for surface imaging in cases where contact from the tip may damage or scratch the surface such as delicate or soft substrates. In non-contact mode, the cantilever is driven to oscillate at the resonant frequency. The tip is scanned across the substrate surface at a distance close enough such that the tip experiences the attractive van der Waals forces but without direct contact established. The magnitude of the forces experienced by the tip are directly proportion to the tip-sample distance. The oscillation of the tip is dampened by the interactions between the tip and the sample surface. The frequency at which the tip is oscillating is monitored by the AFM controller and kept steady by moving the tip in the z-axis as the tip scans across the surface. The required z-axis movements are mapped and translated into an image by software package accompanying the AFM setup.[40]

In tapping mode, the cantilever is driven at resonance similarly to non-contact mode, but the tip-sample separation is reduced until the cantilever lightly contacts, or taps, the surface. The cantilever resonance is kept constant through a feedback loop as the oscillation is dampened by the cantilever touching the surface. As the cantilever is scanned across the surface the amplitude of the oscillations varies due to changes in sample morphology, the tip-sample distance is automatically altered by the external electronics in order to maintain constant amplitude and this data can be interpolated into a topography image. This method

shows greater resolution then non-contact mode as the amplitude of the oscillations is more sensitive to changes in morphology than the frequency due to van der Waals interactions.[41]

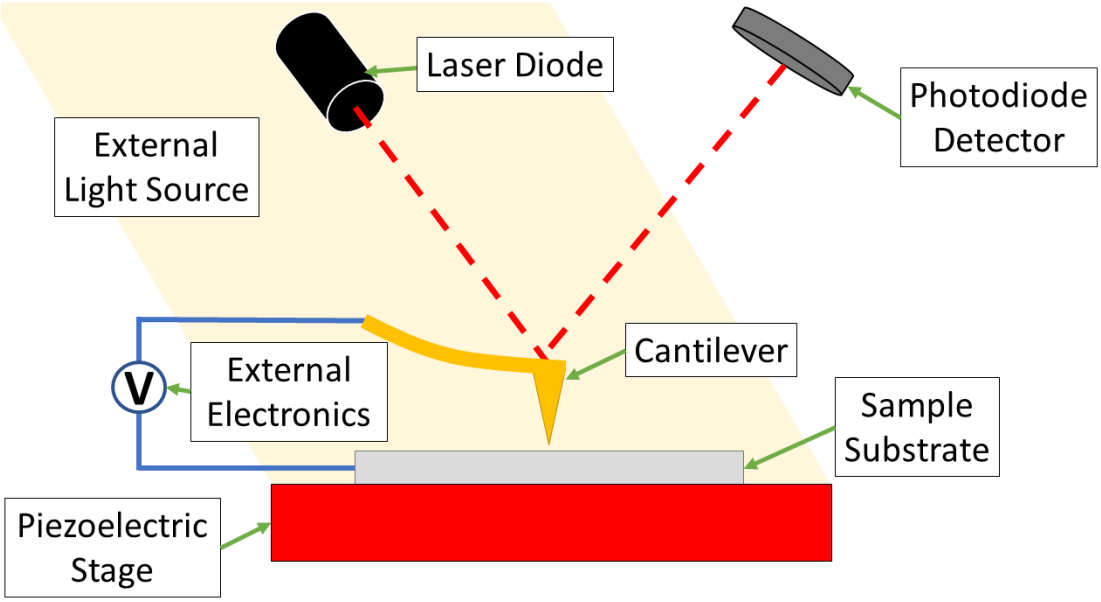

Figure 5-9 – Schematic showing the working principles of conductance AFM. The sample is loaded onto a piezoelectric stage with x,y, and z-axis control. Cantilever is raster scanned across substrate surface using piezoelectric stage x and y axis control. Laser diode is directed toward the back surface of the AFm cantilever and reflected into the photodiode. Laser position on photodiode monitors cantilever deflection Feedback loop electronics maintain constant cantilever deflection or resonance by altering z-axis position. External light sources can be directed onto the substrate surface. In conductance AFM external electronics can be used to measure current flow between tip and sample at variable bias potentials.

The diagram in figure 5-9 shows an AFM set-up capable of performing conductance measurements. Specially fabricated conductive cantilevers that are usually coated in Pt or Gold around the tip are used. Measurements are taken as the tip is scanned across the surface in contact mode method. The tip and sample are electrically connected via the control unit. The current and voltage between the tip and surface can be monitored or controlled allowing for bias to be applied between tip and substrate. This functionality gives the ability to conduct different electrical experiments at microscale and relates local electrical properties to local structure and morphology.[39] Conductance and topology data are recorded independently and then combined in post-processing to reduce potential noise.

These images can then provide higher contrast than just topology data or reveal conductance hot spots or crystal domains. Conductive AFM set ups can be also be used to perform highly localised I-V curve measurements using the tip as a nanoscale probe. The tip is brought into contact with the surface using the z-axis control to set the setpoint and the potential difference is swept between predetermined values while the current flow is measured by the external electronics.[39]

AFM images and conductive AFM measurements were taken using a 5500 Agilent Scanning Probe Microscope with a Keysight 9500 AFM control unit and an Agilent N9410S AFM scanner. The images and spectra were taken using Nano Navigator software. Tapping mode AFM was used to image the samples. C-AFM was done using Au and Pt-coated SiN AFM tips. To perform current voltage characteristic measurements on the monolayers the AFM tips were brought into contact with the substrate surface and I-V curves were generated between a bias of -1 and 1V. The IV curves were manually filtered to remove scans which had been conducted with tip in contact with the ITO substrate or where no contact had been made. Good traces were averaged to produce the final the I-V plots.

5.8. Bibliography

1. Turkevich, J., Stevenson, P. C. & Hillier, J. A study of the nucleation and growth processes in the synthesis of colloidal gold. *Discuss. Faraday Soc.* **11**, 55–75 (1951).

2. Bastús, N. G., Comenge, J. & Puntes, V. Kinetically controlled seeded growth synthesis of citrate-stabilized gold nanoparticles of up to 200 nm: Size focusing versus ostwald ripening. *Langmuir* **27**, 11098–11105 (2011).

3. Chang, Y. C., Wang, S. M., Chung, H. C., Tseng, C. Bin & Chang, S. H. Large-Area Bowtie Nanoantenna Arrays Fabricated with Economic Oxygen Plasma-Assisted Nanosphere Lithography. *Plasmonics* **6**, 599–604 (2011).

4. Swartz, M., Rodriguez, M., Quast, A. D., Cooper, C. T., Blair, S. & Shumaker-Parry, J. S. Aluminum Nanocrescent Plasmonic Antennas Fabricated by Copper Mask Nanosphere Template Lithography. *J. Phys. Chem. C* **120**, 20597–20603 (2016).

5. Gwinner, M. C., Koroknay, E., Liwei, F., Patoka, P., Kandulski, W., Giersig, M. & Giessen, H. Periodic large-area metallic split-ring resonator metamaterial fabrication based on shadow nanosphere lithography. *Small* **5**, 400–406 (2009).

6. Canpean, V. & Astilean, S. Extending nanosphere lithography for the fabrication of periodic arrays of subwavelength metallic nanoholes. *Mater. Lett.* **63**, 2520–2522 (2009).

7. Rybczynski, J., Ebels, U. & Giersig, M. Large-scale , 2D arrays of magnetic nanoparticles. *Colloids Surfaces A* **219**, 3–8 (2003).

8. Li, J., Cushing, S. K., Zheng, P., Meng, F., Chu, D. & Wu, N. Plasmon-induced photonic and energy-transfer enhancement of solar water splitting by a hematite nanorod

array. *Nat. Commun.* **4**, 2651 (2013).

9. CNR-IFN U.O.S. Trento. RF-Sputtering principles. *CNR-IFN U.O.S. Trento* http://www.tn.ifn.cnr.it/facilities/rf-sputtering-facility/rf-sputtering-principles (2021).

10. Hughes, M. What is RF Sputtering? *Semicore Equipment, Inc* http://www.semicore.com/news/92-what-is-rf-sputtering (2016).

11. Gurrappa, I. & Binder, L. Electrodeposition of nanostructured coatings and their characterization - A review. *Sci. Technol. Adv. Mater.* **9**, (2008).

12. Lincot, D. Electrodeposition of semiconductors. *Thin Solid Films* **487**, 40–48 (2005).

13. Cai, J., Li, S., Li, Z., Wang, J., Ren, Y. & Qin, G. Electrodeposition of Sn-doped hollow α-Fe2O3 nanostructures for photoelectrochemical water splitting. *J. Alloys Compd.* **574**, 421–426 (2013).

14. Simon, S., Olumorin, T. I., Guo, B. & Burgess, I. J. Role of Au(I) Intermediates in the Electrochemical Formation of Highly Anisotropic Gold Nanostructures with Near-IR SERS Applications. *J. Phys. Chem. C* **120**, 26150–26158 (2016).

15. Zandi, O., Schon, A. R., Hajibabaei, H. & Hamann, T. W. Enhanced Charge Separation and Collection in High-Performance Electrodeposited Hematite Films. *Chem. Mater.* **28**, 765–771 (2016).

16. Spray, R. L. & Choi, K. S. Photoactivity of transparent nanocrystalline Fe2O3 electrodes prepared via anodic electrodeposition. *Chem. Mater.* **21**, 3701–3709 (2009).

17. Cohen, M. & Markovac, V. The Anodic Deposition of Iron Oxide Films on Platinum. *J. Electrochem. Soc.* **114**, 678–681 (1967).

18. Markovac, V. & Cohen, M. The Anodic Deposition of Iron Oxide Films on Platinum. *J. Electrochem. Soc.* **114**, 678 (1967).

19. William, R. W. Scanning electron microscopy. *Proc. Soc. Anal. Chem.* **10**, 195–196 (1973).

20. NanoScience Instruments. Scanning Electron Microscopy. *nanoScience Instruments* https://www.nanoscience.com/techniques/scanning-electron-microscopy/ (2021).

21. Sharma, S. K., Verma, D. S., Khan, L. U., Kumar, S. & Khan, S. B. *Handbook of Materials Characterization*. *Handbook of Materials Characterization* (2018).

22. Fisher, A. C. Electrochemistry Teaching Notes. *Department of Chemical Engineering and Biotechnology, University of Cambridge* https://www.ceb.cam.ac.uk/research/groups/rg-eme/Edu/linear-sweep-and-cyclic-voltametry-the-principles (2010).

23. Tissue, B. M. Linear-Sweep Voltammetry. *Department of Chemistry, Virginia Tech* https://web.archive.org/web/20130124083041/http://www.files.chem.vt.edu/chem-ed/echem/linsweep.html (2000).

24. Ossila Ltd. I-V curve measurement device. *www.ossila.com* https://www.ossila.com/pages/iv-curves-measurement (2019).

25. Ansys Lumerical. Finite Difference Time Domain (FDTD) solver introduction – Lumerical Support. *Lumerical Support* https://support.lumerical.com/hc/en-us/articles/360034914633-Finite-Difference-Time-Domain-FDTD-solver-introduction (2021).

26. Emagtech. Basic Principles of The Finite Difference Time Domain Method - Emagtech Wiki. *Emagtech Wiki* http://www.emagtech.com/wiki/index.php/Basic_Principles_of_The_Finite_Differe

nce_Time_Domain_Method (2021).

27. Ansys Lumerical. Selecting the best mesh refinement option in the FDTD simulation object – Lumerical Support. *Lumerical Support* https://support.lumerical.com/hc/en-us/articles/360034382614-Selecting-the-best-mesh-refinement-option-in-the-FDTD-simulation-object (2021).

28. Ansys Lumerical. Understanding the non-uniform mesh in FDTD – Lumerical Support. *Lumerical Support* https://support.lumerical.com/hc/en-us/articles/360034382634-Understanding-the-non-uniform-mesh-in-FDTD (2021).

29. Yu, W. & Mittra, R. A conformal finite difference time domain technique for modeling curved dielectric surfaces. *IEEE Microw. Wirel. Components Lett.* **11**, 25–27 (2001).

30. Ansys Lumerical. PML boundary conditions in FDTD and MODE – Lumerical Support. *Lumerical Support* https://support.lumerical.com/hc/en-us/articles/360034382674-PML-boundary-conditions-in-FDTD-and-MODE (2021).

31. Ansys Lumerical. Periodic boundary conditions in FDTD and MODE – Lumerical Support. *Lumerical Support* https://support.lumerical.com/hc/en-us/articles/360034382734-Periodic-boundary-conditions-in-FDTD-and-MODE (2021).

32. Ansys Lumerical. Symmetric and anti-symmetric BCs in FDTD and MODE – Lumerical Support. *Lumerical Support* https://support.lumerical.com/hc/en-us/articles/360034382694-Symmetric-and-anti-symmetric-BCs-in-FDTD-and-MODE (2021).

33. Haynes, W. M., Lide, D. R. & Bruno, T. J. *CRC Handbook of Chemistry and Physics*. (CRC Press, 2016).

34. Palik, E. D. *Handbook of Optical Constants of Solids*. (Academic Press, 1998).

35. Querry, M. R. *Optical constants*. *Contractor Report* https://ui.adsabs.harvard.edu/abs/1985umo..rept.....Q (1985).

36. König, T. A. F., Ledin, P. A., Kerszulis, J., Mahmoud, M. A., El-Sayed, M. A., Reynolds, J. R. & Tsukruk, V. V. Electrically tunable plasmonic behavior of nanocube-polymer nanomaterials induced by a redox-active electrochromic polymer. *ACS Nano* **8**, 6182–6192 (2014).

37. Wuithschick, M., Birnbaum, A., Witte, S., Sztucki, M., Vainio, U., Pinna, N., Rademann, K., Emmerling, F., Kraehnert, R. & Polte, J. Turkevich in New Robes: Key Questions Answered for the Most Common Gold Nanoparticle Synthesis. *ACS Nano* **9**, 7052–7071 (2015).

38. Love, J. C., Estroff, L. A., Kriebel, J. K., Nuzzo, R. G. & Whitesides, G. M. *Self-assembled monolayers of thiolates on metals as a form of nanotechnology*. *Chemical Reviews* vol. 105 (2005).

39. Oxford Instruments. AFM Tools for Nanoscale Electrical Characterization. *Asylum Res.* **12**, 42 (2009).

40. NT-MDT Spectrum Instruments. The Principles of Operation of an Atomic Force Microscope (AFM) dc Contact Techniques. 1–10 (2015).

41. Hong-Qiang Li. AFM Scanning Modes. *chembio.uoguelph.ca* http://www.chembio.uoguelph.ca/educmat/chm729/afm/details.htm (1997).

6. FDTD Simulation and Development of Plasmonic Substrates

6.1. Overview

This chapter outlines the development of the plasmonic substrates used in subsequent chapters and the finite-difference time-domain simulations of the nanostructures. Plasmonic substrates were made using synthesized gold nanospheres which were then deposited onto glass substrates and through nanosphere shadow lithography (NSL). Citrate-capped gold nanospheres were synthesised using a seed-mediated stepwise method outlined by Bastús et al.[1] This method allows for various sizes with narrow size-distribution to be simultaneously synthesised. These nanospheres were then characterised using electron microscopy to measure the size and UV-Visible optical spectroscopy to measure the plasmonic extinction.

Nanosphere shadow lithography was utilised to fabricate nanostructured arrays with different nanoparticle morphologies using gold, silver, aluminium, and copper. It is possible to alter the size, dimensions and shape of the fabricated nanoparticles through altering the size of the polystyrene beads used for the mask layer, plasma etching the bead mask prior to material deposition, or by angling the substrate with respect to the source material during deposition. These nanostructured substrates were characterised using scanning electron microscopy (SEM) and UV-Vis-NIR optical Spectroscopy.

Computer simulations were done using the Lumerical FDTD simulations software package. The simulations were used to motivate and predict the experiments and their outcomes. Finite-difference time-domain simulations were performed for spherical AuNPs in a vacuum, and on SiO_2 and Au substrates to show expected LSPR strengths and positions and to map the electric field intensity enhancements for each experimental configuration. Au nanotriangles in single, dimer, and large-scale array configurations were also simulated to

map the expected E-field intensity enhancement. Au nanotriangle arrays were simulated both in a vacuum and on an SiO_2 substrate to inform the experimental design.

6.2. Introduction

Finite difference time domain simulations have been used to predict the plasmonic behaviour of many nanostructured systems for applications in surface-enhanced Raman spectroscopy(SERS), biosensing, photocatalysis, and many more.[2–7] In the field of photocatalysis FDTD simulations can be used in conjunction with experimentation to give understanding to the plasmonic mechanisms at play and to motivate further work.[6,8,9] Simulations can also be performed to predict new configurations and morphologies of plasmonically enhanced systems for applications.[10] It is for these reasons that simulation can be a powerful tool in the field of plasmonics especially when designing novel devices that incorporate multiple materials or components.

The synthesis of citrate stabilized spherical gold nanoparticles was initially developed in 1953 by Turkevich et al.[11] In this method a solution of chloroauric acid ($HAuCl_4$) is brough to the boil under mechanical stirring. Dilute sodium citrate ($Na_3C_6H_5O_7$) solution is added to the hot, stirring acid and colloidal gold nanoparticles begin to form. Nucleation occurs when the citrate solution is added as it acts as a reducing agent to form elemental gold.[11,12] These initial gold nanoparticles have a size >1.5nm and increase in size until the gold salt in solution is completely exhausted.[12] An electronic double layer exists at the surface of the seed particles and further gold ions are reduced in the layer and attach to the nanoparticle such that it grows in size. The citrate ions act as ligands, bound to the surface by the electronic double layer, stabilising the formed gold nanoparticles in solution.[12]

Bastús et al developed the step-wise seed-mediated growth method used in this work by adapting the original Turkevich method.[1] In this method a 2mM citrate solution is brought to the boil under stirring and a chloroauric acid solution is quickly added to the solution. This

forms a colloid of citrate stabilised gold nanoparticles with a size of around 9nm. This colloid is then used as seed solution for further growth steps. A sample of the seed solution was brought to just under boiling with a further addition of citrate solution. Additional chloroauric acid solution is added to the boiling solution, this time dropwise these gold ions are reduced in the electronic double layer around the seed particles and further growth is observed. The lower temperature at this stage aids to stop further nucleation and focus growth on the already available nanoparticles. This can be repeated with subsequent batches of particles to synthesise particles of controlled size up to 150nm in diameter.[1] The sizes and size distributions of the spherical nanoparticles were measured using electron microscopy techniques. The distribution increased with nanoparticle size however at 180nm the variation was around 5%.

Selectable and controlled size, and morphology are important when considering a synthesis route for plasmonic applications. This is due to the high level of dependency of the plasmonic properties on the size and shape of the nanoparticle. Different morphologies of gold nanoparticles, such as nanorods, nanostars and nanotriangles, have been made using wet synthesis techniques by controlling ligands and reaction conditions.[13–16] These colloid solutions can be deposited onto substrates through drop-casting or spin-coating to create plasmonic substrates.[17–19] Lithography techniques such as nanosphere shadow lithography can also be used to create plasmonic substrates with arrays of gold nanoparticles with various shapes and sizes.[20–27]

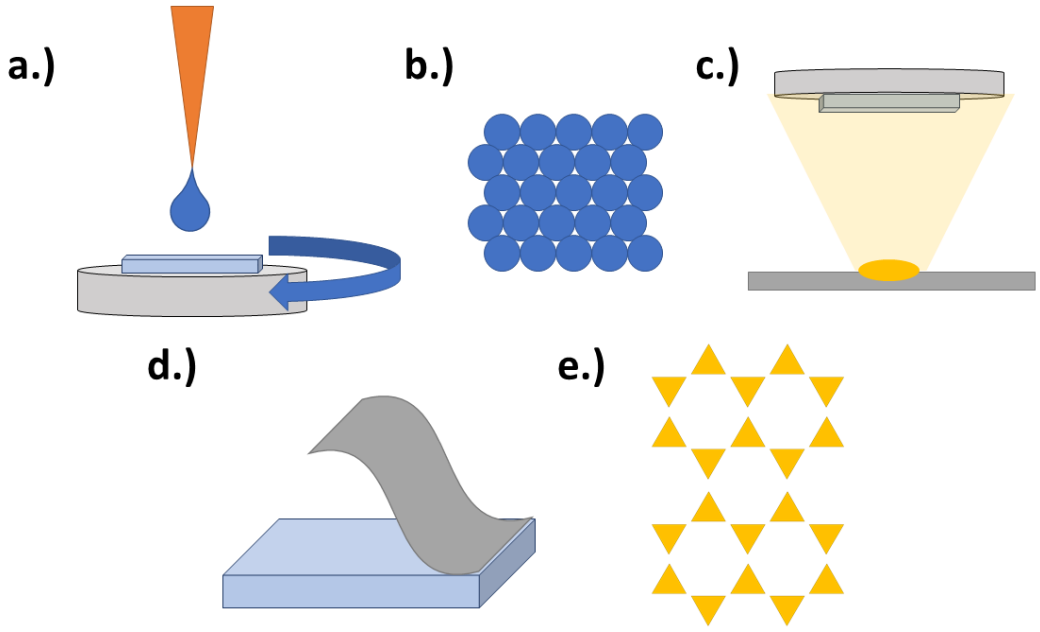

Figure 6-1 – A schematic showing the basic workflow of NSL. A.) Spin-coating of the PS bead solution onto cleaned substrates. B.) The developed mask of PS nanospheres in hexagonal close-packed arrangement. C.) Evaporation or deposition of relevant material. D.) Tape cleaving of the PS mask. E.) The final triangular nanostructures arranged in the characteristic Fisher pattern.

Nanosphere shadow lithography (NSL) is a bottom-up method of fabricating nanoparticle arrays on a substrate. Figure 6-1 shows a basic schematic of the nanosphere shadow lithography. Briefly, an array of hexagonal close-packed nanospheres is formed on the surface as mask layer. Subsequent material layers are then deposited through the mask forming arrays of nanotriangles arranged in a Fisher pattern. The nanosphere mask can then be removed through tape cleaving or sonication revealing the nanostructures on the substrate.

Large area nanosphere shadow lithography was first described as natural lithography by Deckman and Dunsmuir in their 1982 paper.[20] In this paper they improved a process given by Fischer[21] in order to replicate the mask production for larger areas. Through spin-coating of an aqueous latex sphere suspension, large scale monolayer arrays of close-packed spheres were formed which were then used as masks for metal deposition and reactive-ion milling. Metal evaporation over the mask lead to the fabrication of 80nm silver posts positioned in

the interstices of the spheres and reactive in etching produced silicon posts centred at the origin of the latex spheres in the silicon substrate.

After the bead mask has been fabricated heat treatments can be used to reduce the size of the apertures between the beads.[22–24] The size of the apertures can be controlled through the careful consideration of temperature and time. Generally, the masked substrate is placed on a hot-plate or in a low-temperature oven and subjected to a heating cycle, metal is then deposited through the mask using evaporation techniques or sputtering. This method has been used to create arrays of triangular nanostructures with controlled sizes, hemispherical 'dot' arrays and other novel nanostructures such as split-ring resonators.[22–25] Simulations have also been performed that suggest that more complex shapes such as crosses and even shapes with inherent chirality can be fabricated.[25]

The polystyrene bead mask used in NL can also be radially etched by exposing the film to reactive plasma such as O_2 and CF_4.[26,27] The radial etching causes the sphere diameter to reduce whilst maintaining their positions in the lattice, this causes the apertures between the beads to increase in size. This method has been shown to controllably increase the size of the fabricated triangular nanostructures.[26] The extent of the etching is controlled by the time duration of the exposure and can optimized by observation of etched substrates under electron microscopy. As the exposure time increases eventually the spheres are no longer in contact with another in mask. Subsequent deposition of metal results in arrays of holes in an otherwise continuous metal film. [26,27]

Temperature treatment of the fabricated nanostructures has also been shown to controllably alter the morphology of nanostructures fabricated using NSL.[22] As the substrate is heated the metal nanostructures begin to melt, surface tension causes the corners of the triangles to be pulled inwards. The size of the nanotriangles is reduced as the vertices retract leaving smaller, rounded triangles. With increased subjection to temperature the

nanostructures eventually form into hemispherical dots. Due to the repetitive nature of the of the original nanostructures this method forms large scale arrays of hemispherical metal nanoparticles on the substrate.[22]

6.3. Finite-difference time-domain simulations

Computer simulations were done using the Lumerical FDTD simulations software package. The simulations were used to motivate and predict the experiments and their outcomes. Three dimensional models of the experimental nanoparticle configurations were made in Lumerical's built-in 3D CAD feature. Both the nanosphere on a substrate geometry, and the nanotriangle array on a substrate geometry were modelled and the plasmonic responses simulated.

6.3.1. Simulations using Nanospheres

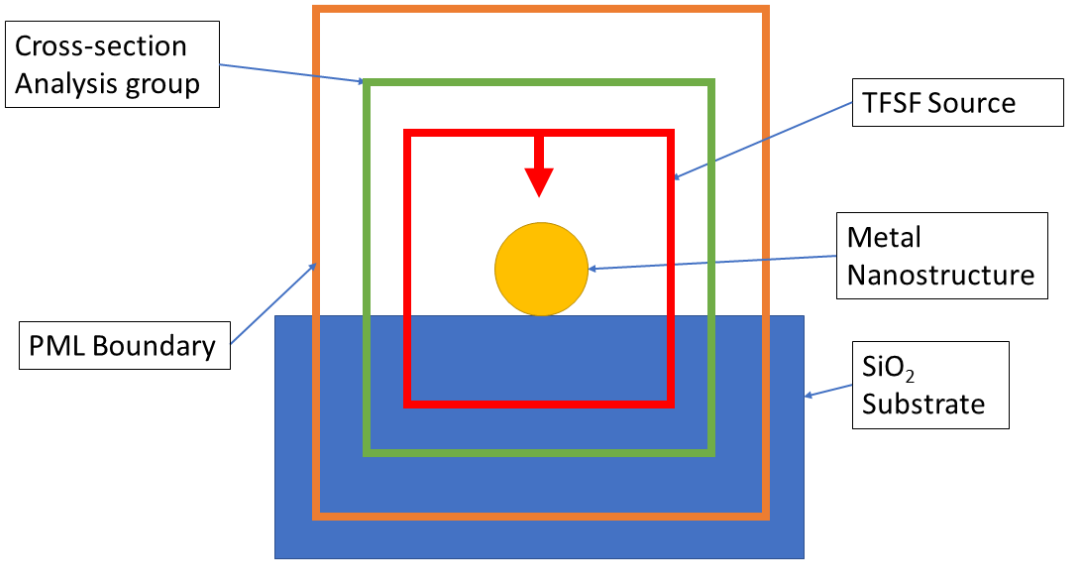

Figure 6-2 - Schematic showing the simulation environment for the nanosphere simulations.

In order to validate the simulations an initial nanosphere size sweep was performed. The scattering cross-section of the nanoparticles was measured using the Lumerical TFSF (total field scattered field) source and the cross-section analysis group. A schematic of the

simulation environment created in Lumerical is shown in figure 6-2. The TFSF source acts to cancel out the input source field at the boundaries and permit the scattered fields from the structures within the boundaries. The cross-section analysis group in Lumerical is a 3D box comprised of power monitors that evaluates the field spectrum that traverses through the boundaries in 3 directions. The scattering cross-section is given by the output of the cross-section analysis group placed outside of the TFSF, as the source attenuates the inputted signal. A single spherical gold nanoparticle is placed at the centre of the TFSF and analysis structure, the dielectric values for the gold structures were taken from CRC textbook[28] and the external media was set as a vacuum with dielectric constant of 1. The diameter of the sphere was swept between 10nm and 80nm at intervals of 10nm, with scattering cross section spectrums calculated at each size.

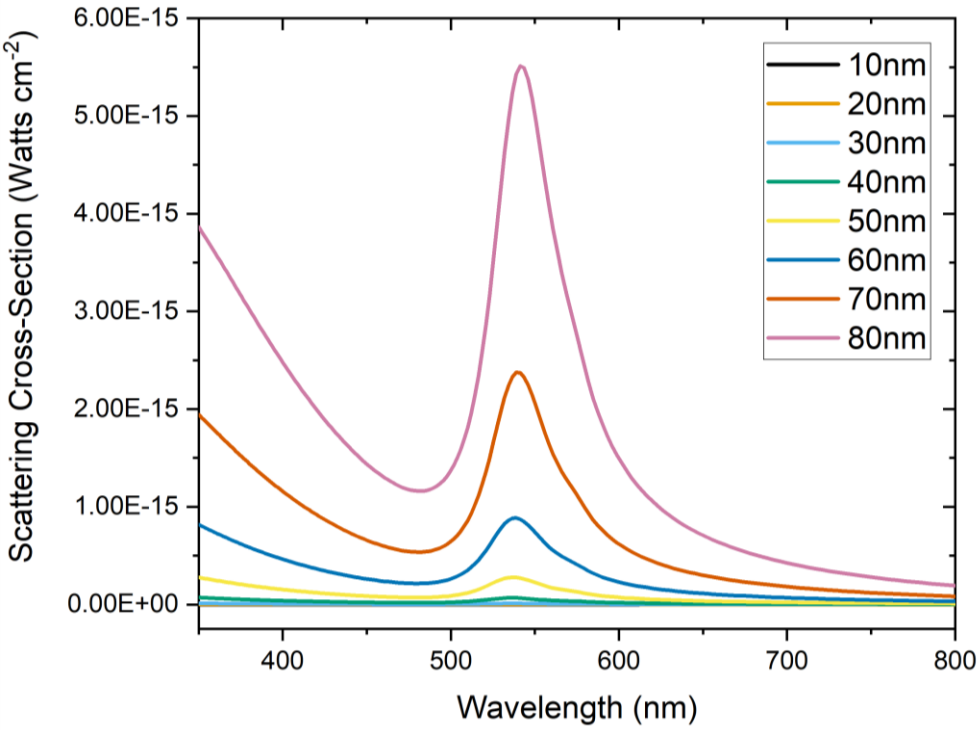

Figure 6-3 - Simulated scattering cross-section spectra for spherical AuNPs with varying diameters using FDTD. This shows the strength of scattering increasing with size in agreement with theory presented in the Introduction of this thesis (Chapter 2).

Figure 6-3 shows the calculated scattering cross-section for the Au nanoparticles with various diameters. From the raw calculated data, it is clear that the amplitude of the scattered power increases with nanoparticle size. In fact, there is a difference of over five orders of magnitude between the peak scattered power at 540nm for the 10nm diameter nanoparticles and the peak scattered power at 541nm for the 80nm diameter nanoparticles. This demonstrates that experimentally, a compromise between larger nanoparticles and stronger electric field enhancement, and the practicality of using smaller nanoparticles to contact fewer molecular wires and more defined areas of the substrate, will have to be struck.

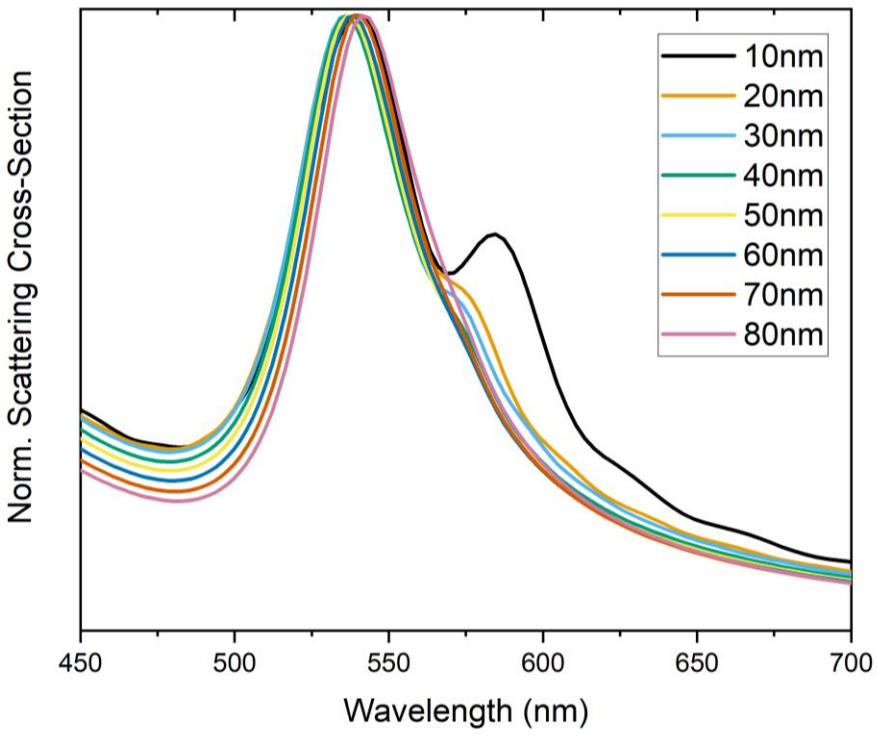

Figure 6-4 - Normalized scattering-cross section spectra for varying diameter AuNPs using FDTD. Data from figure 6-1 was normalized for line-shape comparison.

Figure 6-4 shows the calculated scattering cross-section spectra normalized at the peak position. From this graph there is no certain relationship between nanoparticle size and the position of the peak. Instead, all the peak positions are centred around 540nm, with the

actual peak values sitting at 538.9nm for the 10nm, 60nm, and 70nm, 536.5nm for the 20, 30, 40, and 50nm, and 541.2nm for the 80nm diameter nanospheres. As the size parameters used here are all much lower than the wavelength of the incoming light it is somewhat expected that there would be little shift in resonant energy with size theoretically however, it is shown experimentally later on in this chapter that the peak position would red-shift as one of the size parameters increased.

The shoulder at 585nm in the 10nm diameter AuNP spectrum appears to decrease as the nanoparticle size increases. This shoulder is most likely an artefact of the meshing in the simulation. As the nanoparticle size increases the ration between the dimensions and the minimum mesh size increase also. If the mesh is not tight enough the nanoparticle will appear to show flat facets at the interface with the mesh, leading to a technically non-spherical particle being modelled. The now flat edges and apexes could give rise to extra plasmon modes in the nanoparticles giving this extra peak appearing as a shoulder that decrease as particle size increases. This shows the importance of a properly selected mesh size, however the trade-off for a finer mesh is much longer computational capacity required and is not always achievable.

A single, 30nm diameter Au nanoparticle on a substrate was then modelled in the Lumerical CAD tool. The nanoparticle itself was set to the centre of the simulation region. The substrate was set so that its boundaries sat outside of the total simulation region and therefore was regarded by the simulation as infinite in the y and x axes, and in the negative z-axis. The spacing between the substrate and the nanoparticle was initially set to 1nm. The scattering cross-section analysis group and 2D power monitors set normal to the y-axis were used to calculate the scattering spectrum and E-field maps from the simulations. The incident light is injected normal to the z-axis such that it propagates along the z-axis.

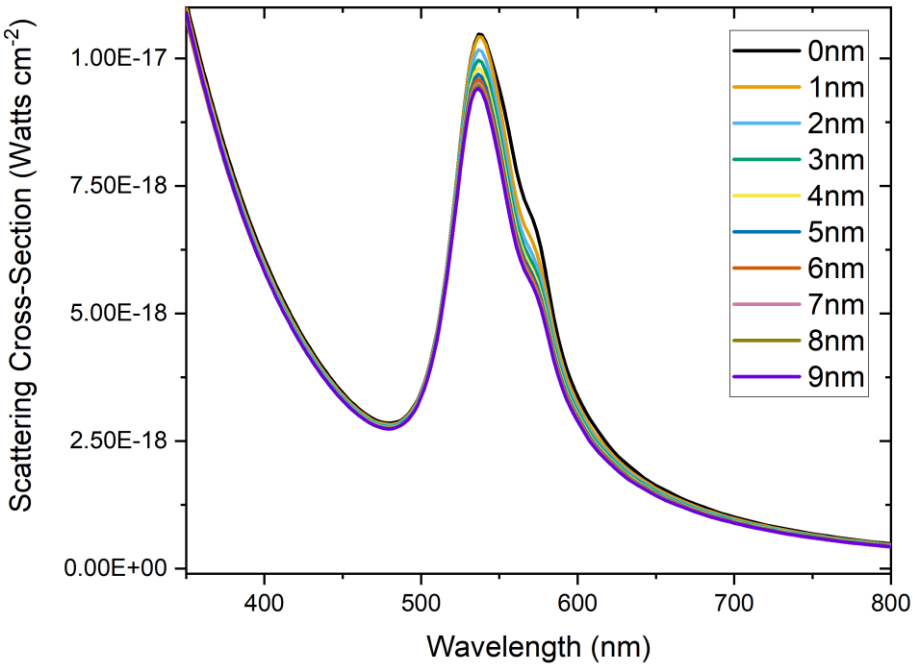

Figure 6-5 – Simulated scattering cross-section for AuNPs on SiO_2 substrate using FDTD. The gap size between NP and substrate was varied between 0 nm (in contact) to 9 nm.

Figures 6-5 and 6-6 show simulated scattering cross-section spectra for the Au nanoparticle on both a SiO_2 and Au substrate at various spacings between the particle and the substrate. The gap spacing between the particle and substrate was manipulated by altering the z-position of both the nanoparticle and substrate 3D models. Both figures show resonance peaks at ~540nm, which suggests that the experiments should be performed using illumination from the 532nm laser as this would excite the plasmon modes at close to resonance resulting in the greatest effect. In figure 6-5 the peak scattering is at its highest when the particle and substrate are in contact and decreases as the gap gets larger. The dielectric substrate is unlikely to dampen or interact with the plasmon modes of the nanoparticle therefore the reduction in the scattered power is likely due to some increased attenuation of scattered light by the glass substrate.

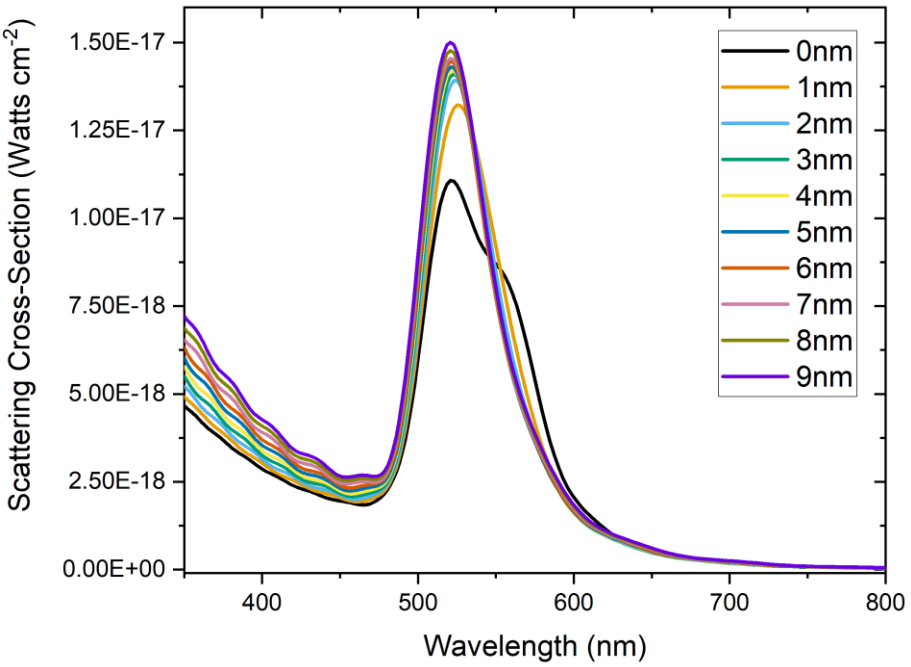

Figure 6-6 - Simulated scattering cross-section for AuNPs on Au substrate using FDTD. The gap size between NP and substrate was varied between 0 nm (in contact) to 9 nm. This shows the damping for AuNPs on Au substrate and the importance of the gap for NP on mirror geometries.

Figure 6-6 shows the scattering cross-section spectra for the AuNP on the Au substrate as the gap spacing is increased. Here, the opposite effect is seen. The peak scattered increases with spacing with the highest peak scattered power seen in the highest spacing configuration. This increase is expected as the AuNP and substrate plasmon modes decouple as the spacing increases. With a conducting substrate the nanoparticle plasmon resonances can be damped by resonant energy transfer to electrons in the substrate conduction band. As energy is transferred and lost though the substrate this damping would manifest as a reduction of the scattered light. These simulation results show the distance dependence on the coupling of the AuNP plasmon modes and the substrate. At 1nm, which is analogous to the height of a molecular monolayer, there is still some quenching of the peak scattered power suggesting that the plasmon modes of the substrate and particle are still coupled. This would manifest as a gap plasmon mode resulting in high E-field enhancement in the gap

which would then have the greatest effect on the conductance of the molecules trapped in the gap.

Figure 6-7 shows electric field maps of a 30nm diameter AuNP on two different substrate configurations. The gap spacing between the AuNP and the substrate is 1nm in both cases. This 1nm gap spacing was chosen to be analogous to the experimental presence of a self-assembled monolayer of molecular wires on the substrate with the AuNP immobilized by the monolayer. The incident source was set to model the 532nm laser which was available experimentally, this wavelength also best aligns with the scattering peaks seen in the previous simulation data. Figure 6-7a shows AuNP on an SiO_2 substrate, while 7b shows an AuNP on a gold substrate. The SiO_2 substrate was chosen as a dielectric substrate similar to glass in order to show the differences between dielectric and conducting substrates. The Au substrate was used as this is the substrate that will be used experimentally.

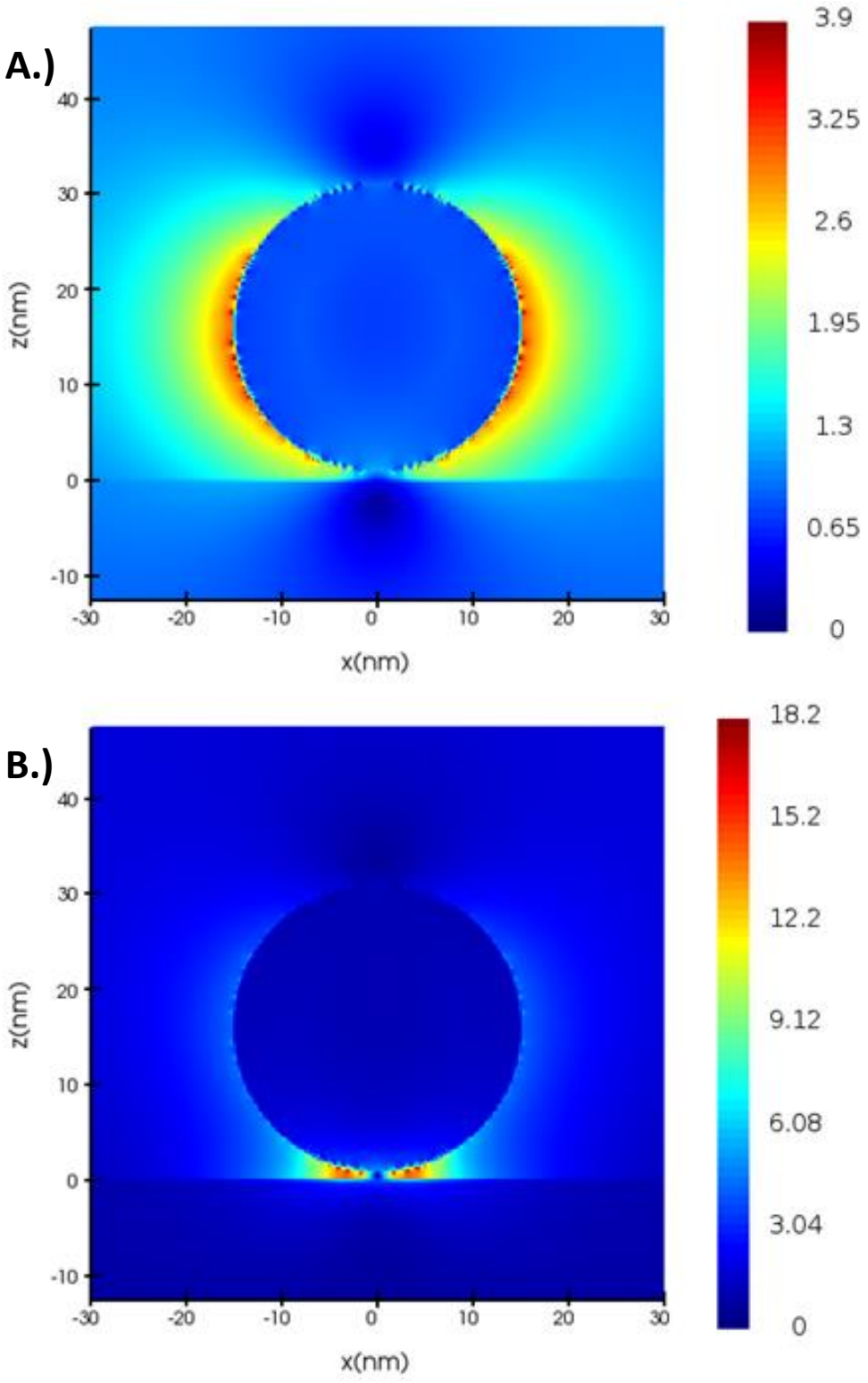

Figure 6-7 – Simulated electric-field maps for AuNPs on substrate with 1 nm gap. The colour bar represents electric field enhancement factor. A.) AuNP on SiO_2 substrate. B.) AuNP on Au substrate. On Au substrate the electric fields are clearly confined in the gap whereas on SiO_2 the field distribution is characteristic of a dipole showing no interaction with the surface.

There are clear differences in where the electric field enhancement occurs between the two substrate configurations. In the top image there is no clear interaction between the AuNP and the substrate which is expected due to the insulating properties. The electric field enhancement map shows field enhancement in the perpendicular to the light propagation direction similar to what is seen on single nanoparticle simulations. In the bottom image there is a clear interaction between particle and substrate. The E-field enhancement is confined to the gap between the substrate and the nanoparticle showing a gap plasmon mode in this configuration. This explains why the scattered power was lower at shorter particle-substrate distances as the plasmon modes couple and energy is lost to the substrate. At the centre of the gap, the E-field enhancement tends to zero, this is due to the direction of the incoming light being top-down leaving this small region in shadow and resulting in little enhancement in the region. A much smaller mesh in this region would fix this however is more computationally demanding. The magnitude of the peak enhancement is very different in both set-ups as seen by the heatmap with a difference also in where the enhancement is confined. With the Au substrate the maximum electric field intensity enhancement seen in the gap is up to a factor of 18 times, which is 4.5 times larger than the maximum enhancement seen in the SiO_2 substrate configuration. This shows that the coupling between the particle and substrate is very strong at these short distances. This result suggests that in order to observe the greatest effect on the molecular conductance, there should be a gold substrate with the AuNP spaced from the substrate at a satisfactory distance.

Experimentally, due to limitations of the apparatus, the illumination source was inputted side on to the substrate. Simulations where therefore run using an AuNP on an Au substrate with a 1nm gap to show the dependence of the E-field enhancement in the gap on the illumination angle. For these simulations a plane wave light source was used as the angle of

the incident light can be altered without interfering with some boundary like with the TFSF source.

Figure 6-8 shows the electric field maps for a 30nm diameter AuNP spaced 1nm from an Au substrate illuminated at various angles. For figures 6-8a – 8e the angles of the incident light are 0^0, 30^0, 45^0, 60^0, and 90^0. The E-field polarization of the incident light was across the image plane such that at 0^0 the polarization was horizontal and at 90^0 the polarization is in the vertical plane of the image. The maximum electric field intensity enhancement in the gap increases as the angle increases. The gap plasmon mode exists in the z-direction and as the z-component of the E-field polarisation direction increases the plasmon resonance strength increases. The largest gap enhancement was seen at 90^0 polarization informing that the samples in the experiment should be lit from the side with polarization monitored and controlled.

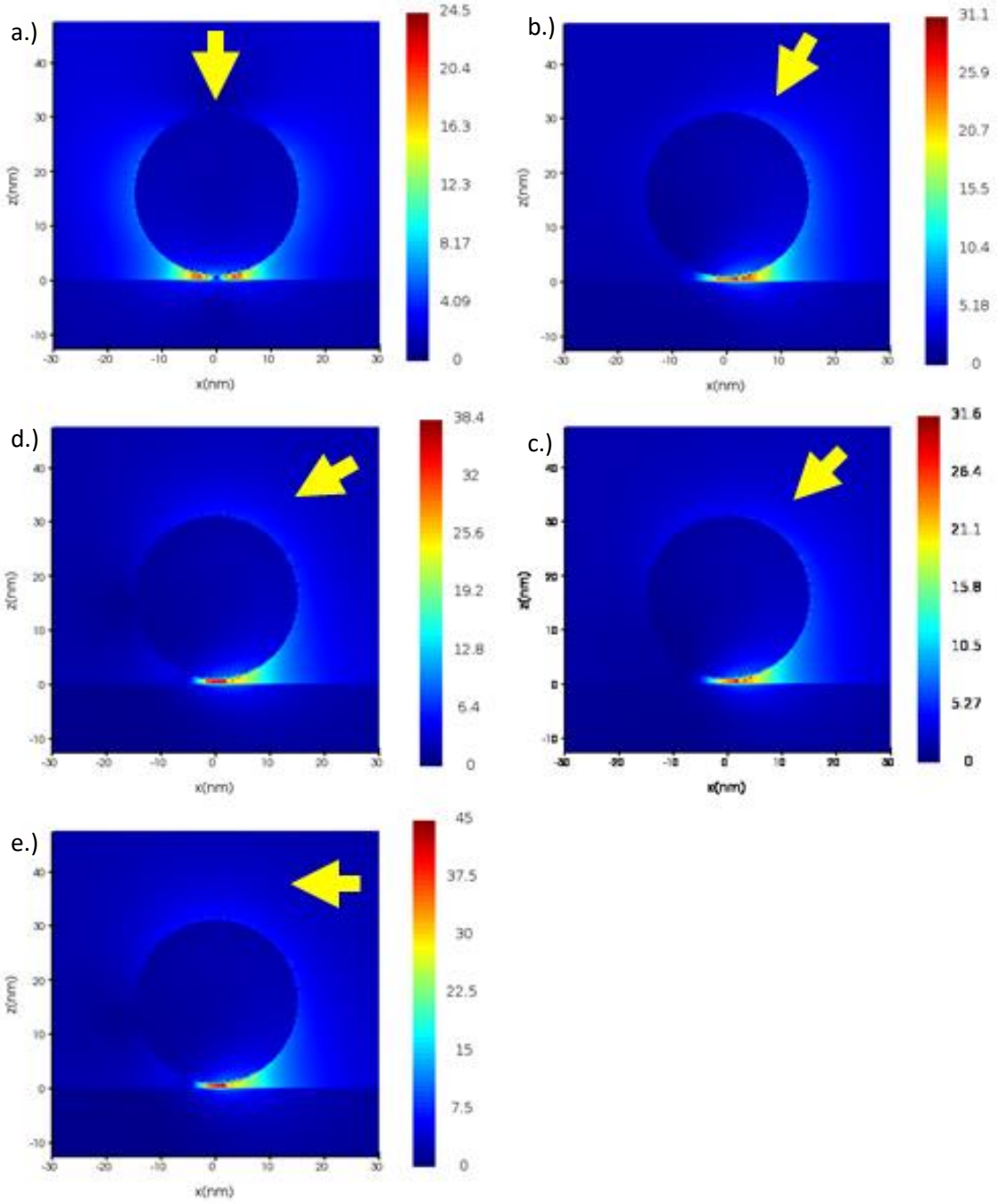

Figure 6-8 – FDTD simulated electric field intensity enhancement maps for an AuNP on Au substrate with a gap of 1nm analogous to the experimental set-up for au sphere on a monolayer. The angles of the incident light are a.) 0^0, b.) 30^0, c.) 45^0, d.) 60^0, and e.) 90^0. E-field intensity enhancement in the gap increases with incident light angle.

6.3.2. Simulations using nanotriangle arrays

Simulations were also performed on the nanotriangle arrays produced by nanosphere lithography. A nanosphere lithography technique was developed to produce nanotriangles with a side-length of 80nm and therefore 80nm side-length nanotriangles were used for the simulation. Beginning with a single gold triangle and building up to full arrays of hexagonally arranged triangles known as Fischer patterns, these nanostructures were simulated in order to motivate and evaluate the experimental results. 3D models of the gold nanotriangles in the various configurations were made in the Lumerical CAD tool. Figure 6-9 shows simple 2D schematic of simulation environment created in Lumerical.

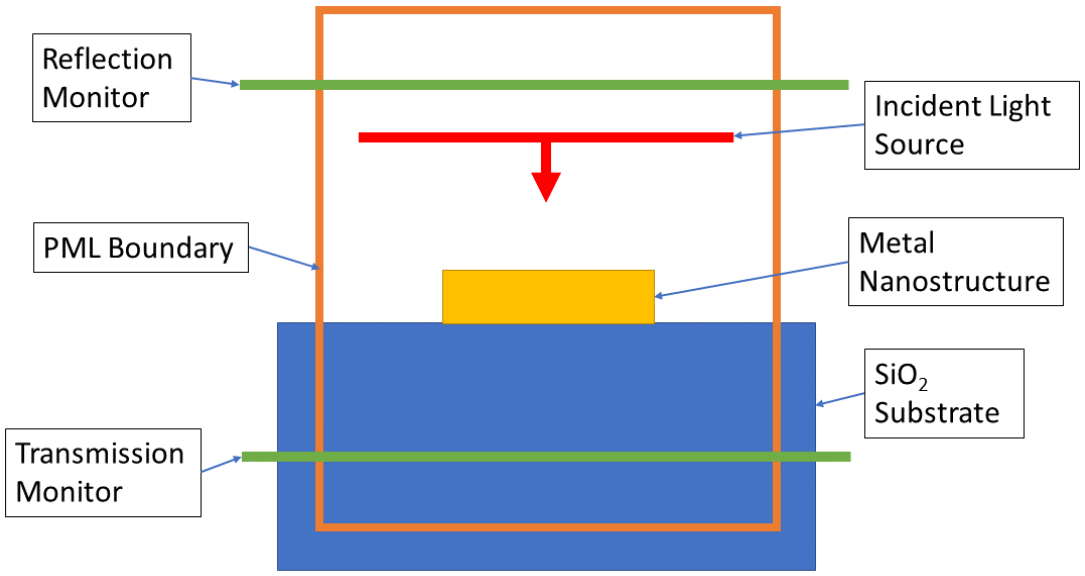

Figure 6-9 - A simple 2D schematic showing the simulation environemtn created in Lumerical for the triangular nanoparticles

6.3.2.1. Single nanotriangle simulations

Initially, a single gold triangle with side-length of 80nm was modelled in a vacuum. Due to the three-fold symmetry of the nanoparticle shape different polarizations of incident light will have differing effects on the active plasmon modes. The polarization of the incident z-normal light in the simulation was altered between perpendicular to the x and y-axes. To

create an analogy to unpolarized light, two sources, that varied only by being polarized at 90 degrees to each other, were used as the input source. A 2D power monitor to image the E-field as a heat map, and the scattering cross-section analysis group to calculate the cross-section spectrum, were used to gather information about the differences in the polarization environments.

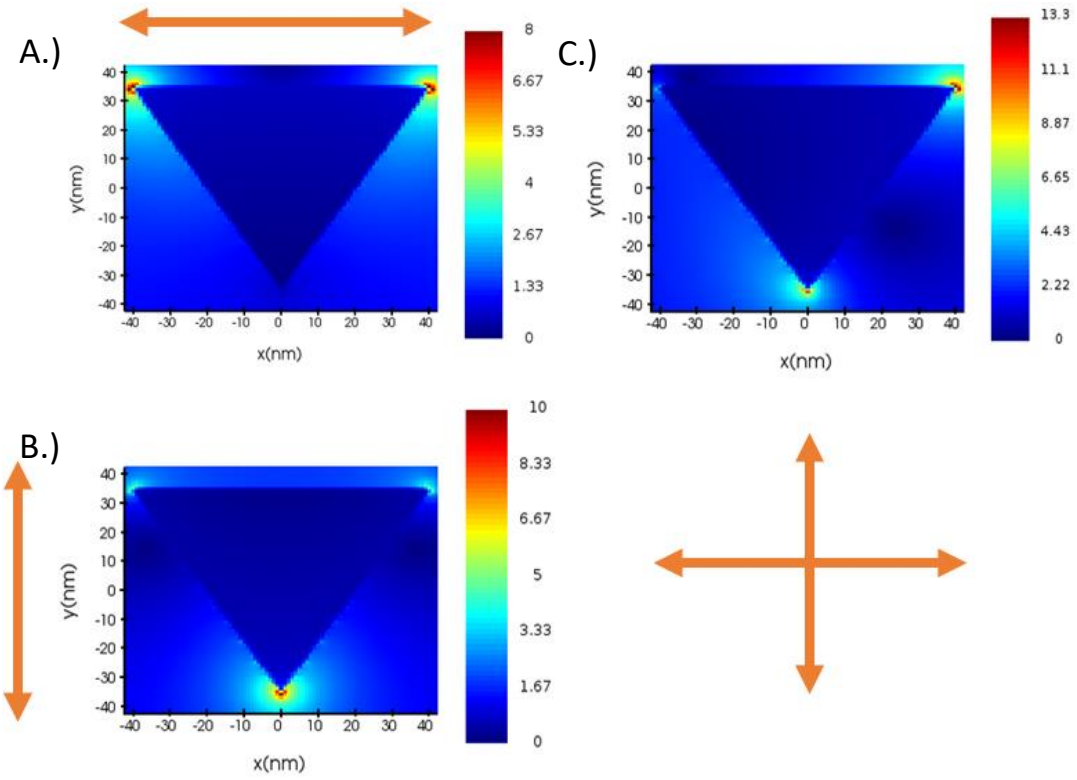

Figure 6-10 – Simulated electric field intensity enhancement maps for Au nanotriangles under different illumination conditions. Arrows signify polarization direction. Colour bar represents E-field intensity enhancement factor. A.) polarized in x-directions. B.) Polarized in y-direction. C.) polarization in x- and y-directions (arrows are beneath) and in-phase. Analogous to unpolarized light.

Figure 6-10 shows the E-field enhancement field maps generated by the simulations with the different light polarizations. The top left image shows the situation in which the input source light is polarized parallel to the y-axis. It can be seen here that the electric field is condensed at the top two vertices along this axis with virtually no electric field enhancement occurring at the bottom vertex. This is expected as the resonant electron oscillations occur parallel to the E-field oscillation direction in the incident light as this is the 'driving force'. The bottom

left image shows the E-field map for the excitation light being polarised along the y-axis. In this situation it can be seen that all three corners of the triangle show electric field enhancement at the tips with the strongest E-field occurring at the bottom vertex. The remaining two vertices give only a fractional field enhancement in comparison. This again is expected as all three vertices terminate along the y-axis with the bottom vertex coming to a point in this axis. The top-right image is the E-field map for the 'unpolarized' analogy where two sources polarized at 90 degrees to one another were used to simulate an incident light source with no overall polarization. Here it is expected that all three vertices will exhibit E-field concentration however in this simulation the top-left corner appears not to show a high E-field enhancement. This is most likely an error in the overlap simulation mesh override region and the monitor positioning.

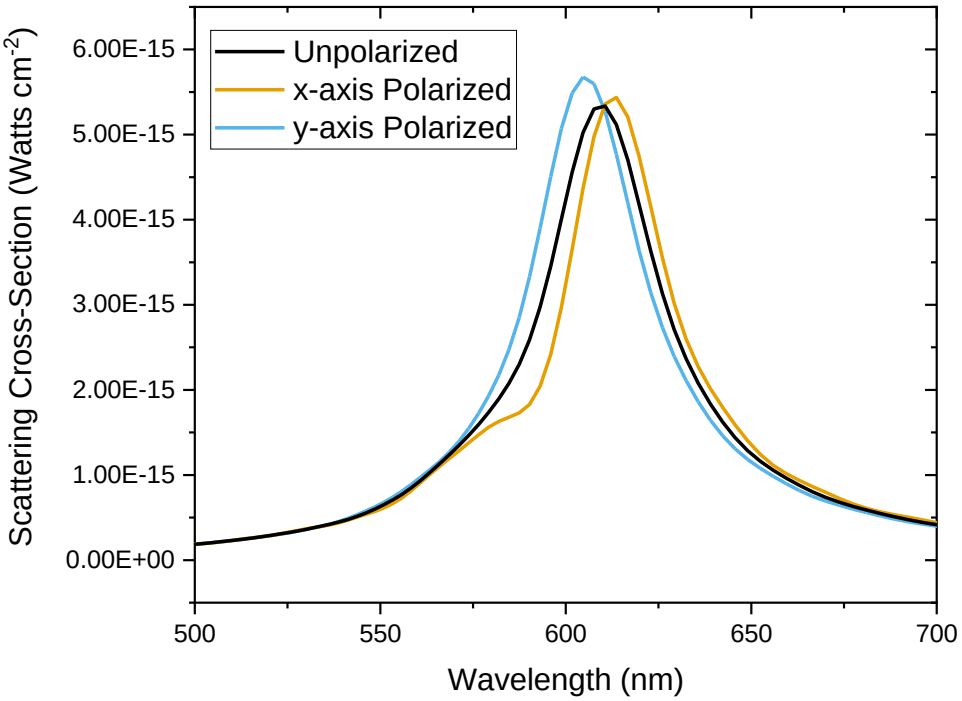

Figure 6-11 – Simulated scattering cross-section spectra for the Au nanotriangle under the different illumination conditions. For 'unpolarized' two incident light sources with polarization in x- and y-directions and in-phase were used to be analogous to unpolarized light in simulation/

Figure 6-11 shows the simulated scattering cross-section from a single triangular Au nanoparticle in vacuum in the three illumination polarization conditions. The simulation with the input light source polarized parallel to the x-axis showed two vertices with evenly distributed electric field concentration in the E-field heat map. The maximum E-field enhancement in this configuration also gave the lowest enhancement of the three setups. From the scattering cross-section the x-axis polarized setup shown in figure 6-11 gives a resonance peak at the lowest energy of the three configurations, this is expected as the longitudinal resonance along the top edge of the triangle is a lower energy resonance as the vertex-to-vertex distance is longer than the triangle height. The larger the size-parameter the lower scattering cross section energy. This mode is also the only one active when the incoming light is polarized along its direction. In the y-axis polarized simulation, the resonance occurs along the bisector of the triangle as the input light is polarized with the E-field component parallel to the bisector direction. This results in a large enhancement concentrated at the bottom vertex with low E-field enhancement at the other vertices. This resonance is expected to have a higher energy than the other linearly polarized situation as the resonant distance is shorter than the triangle edge length seen in the x-axis polarization. The resonance peak shown in the simulated scattering cross-section is centred at the highest energy of the three configurations. For the full polarization simulation, the scattering cross-section shows a resonance peak that sits in the middle of the other two simulation resonance peaks. This is because this configuration is a combination of the two previous simulations and therefore the resonance peak is to be analogous to an average of the two linearly polarized results. Results here agree with similar FDTD simulations on single Au nanotriangles performed by Gao et al.[5]

6.3.2.2. Nanotriangle dimer simulations

Nanotriangle dimers arranged with vertices aligned to one another have been studied as nanotriangle antennae. There is a strong E-field enhancement as the closely spaced vertex concentrated E-fields couple creating highly localised E-field enhancement factors of many orders of magnitude. The nanostructures created using nanosphere lithography are present as arrays of nanotriangle dimers arranged as such antennas. Therefore, nanotriangle dimers were simulated to better understand the dependence on the tip-to-tip gap spacing and aid the design of the final experiments. The incident light source used in these simulations was polarized along the y-axis so that the E-field component of the light was parallel with the direction of the tip-to-tip gap.

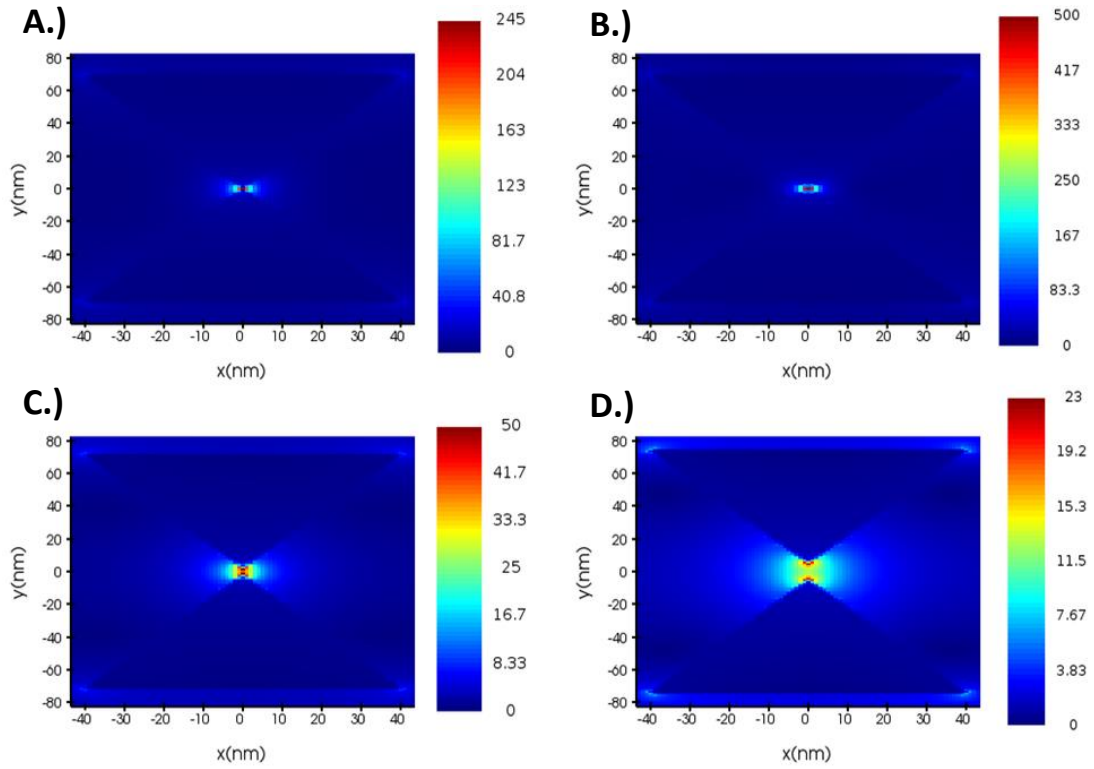

Figure 6-12 – Simulated electric field intensity enhancement maps for AuNT dimers with varying tip-to-tip spacings. Colour bar shows E-field intensity enhancement factor. A.)0 nm gap (touching), B.) 1 nm gap, C.) 5 nm gap, and D.) 10 nm gap.

Figure 6-12 shows the E-field heat maps for four nanotriangle dimer configurations with varying tip-to-tip gap spacings. The incident light was simulated as a 644nm laser, this is

because 644nm is the closest laser available experimentally to the nanostructure resonance energy. The gap spacing was altered in the simulation by controlling the y-position of the individual nanoparticles in the dimer. The gap spacings are; A.) 0nm, B.) 1nm, C.) 5nm, and D.) 10nm. These maps all show that the electric field enhancement when illuminated top-down are concentrated in the gap. The magnitude of the concentrated electric field reaches a peak at short non-zero gap spacings and dies off as the gap increases. At 0nm gap the triangle tips are directly touching at the vertex, here the E-field enhancement is highest around the junction. The top left image shows the E-field map given for the 1nm gap, here the highest enhancement is seen directly in the gap and gives the highest enhancement factor of the four configurations. In the 5nm and 10nm gap configurations it is clear that the highest E-field is concentrated directly on the nanostructure tips but the enhancement spreads into the gap between the vertices. These results agree with previous published simulation studies on bow-tie nanoantenna where electric field enhancement factor in the gap is shown to scale with gap-spacing distance.[29] These simulations show that the highest E-field enhancement occurs where the plasmon electron resonances are concentrated at the triangle vertices and very enhancements are possible with careful consideration of the nanostructure design.

6.3.2.3. Au Nanotriangle Array Simulations

The nanosphere lithography technique used to fabricate the nanostructures experimentally results in periodic arrays of Au nanotriangles arranged in hexagonal Fischer patterns. In order to simulate this effectively a unit cell of a nanotriangle dimer set diagonally at 60^0 of vertical. Using symmetrical boundary conditions, which mirror the simulated structure along their axes, allows the software to simulate the structure as an infinite array. The incident light was polarised with the E-field component parallel to the y-axis in order to excite the horizontal gap plasmon modes in the array. In order to find the absorbed power spectrum two 2D

monitors are used. To collect the reflected power a 2D monitor is placed above the incident light output source near the upper z-axis boundary of the FDTD simulation region, and the transmitted power is collected by a 2D monitor below the nanostructures within close to the bottom of the z-axis FDTD boundary. The outputted spectra from these monitors are normalized to the inputted light spectrum, therefore the total absorbed light can be calculated by addition of the reflection and transmission results and subtracting from 1 across the spectrum. This then results in the absorbed power spectrum from the array.

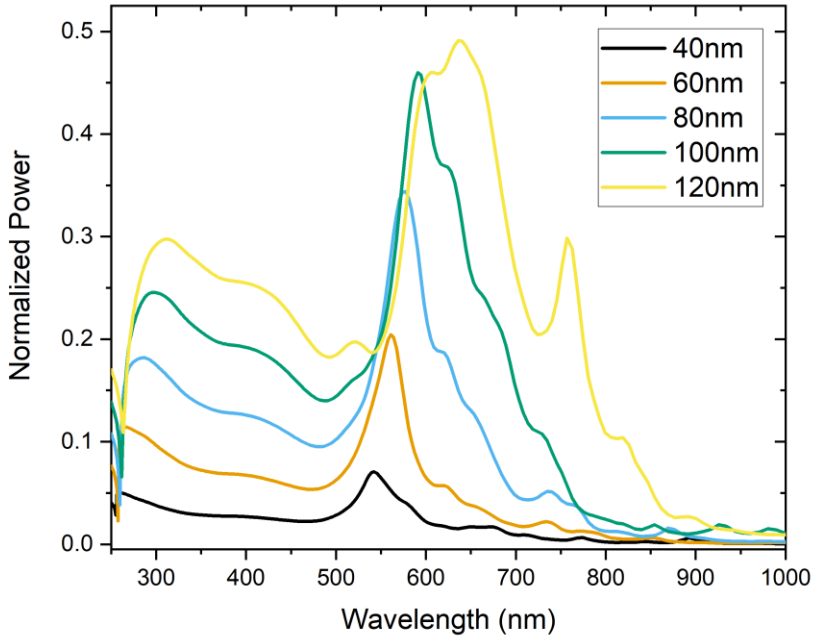

Figure 6-13 – Extinction power spectra for arrays of nanotriangles in a vacuum arranged in a Fischer pattern with varying triangle side-lengths.

The geometry of the modelled structure was calculated to mimic the nanosphere lithography technique so that as the side length of the triangles was changed their position stayed constant and spacing altered in order to simulate the NSL technique using the 300nm diameter sized nanospheres. Simulation sweeps whereby the side-length of the triangles, and therefore the spacing and other associated geometries, was increased. Figure 6-13

shows the absorbed power spectrum of the Au nanotriangle arrays in a vacuum with no substrate. The absorbed spectra show sharp and distinct peaks which is characteristic for an infinite array as the geometries are well-defined. From the plot it is clear that the main peak of the absorption line red shifts with increasing size of the nanostructures. Power that is not reflected or transmitted through the nanostructures must be lost through E-field concentration at the tips or in the gap, therefore the peak absorbed power relates to the E-field concentration. These simulations were set-up to hold the position of the triangles as if the 300nm diameter polystyrene beads were used to fabricate them using NSL. Therefore, as the size of the triangles increases the gap-spacing decreases, this likely contributes to the increase in absorbed power and the prominence of secondary peaks as the side-length increases. The peak absorbed power increases with size of the nanostructures, therefore these simulations highlight the importance of designing the nanostructures to compromise between power absorption and peak position in order to optimise the results.

Figure 6-14 shows the absorbed power spectra for the Au nanostructures on an SiO_2 glass substrate. All the spectra show odd behaviour below ~400nm, this is due to the high simulated glass absorption from the refractive index data for SiO_2 used for the simulation. The peak absorption features in the spectra are less sharp and distinct compared to the results without the substrate and the peak absorption is lower in all cases than the results for the array in a vacuum. The peak positions for the absorption spectra are in broadly the same position as the results without the substrate. This shows that the inclusion of a dielectric substrate quenches the absorption efficiency of the nanostructures without coupling the plasmon modes with the substrate.

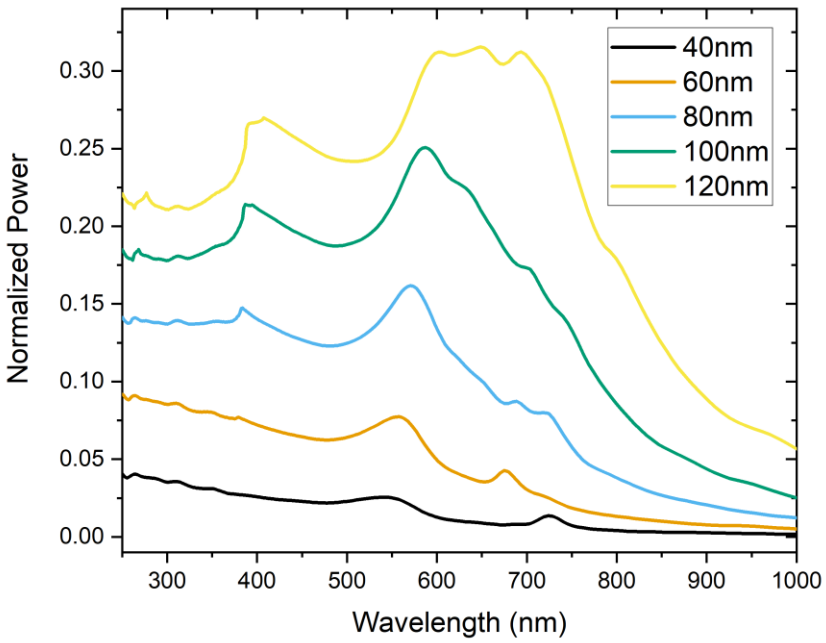

Figure 6-14 - Extinction power spectra for arrays of nanotriangles on an SiO_2 substrate arranged in a Fischer pattern with varying triangle side-lengths.

6.4. Gold nanosphere synthesis and characterisation

Citrate-capped gold nanospheres were synthesised using a seed-mediated stepwise method outlined by Bastus et al.[1] This method allows for various sizes with narrow size-distribution to be simultaneously synthesised. In each growth step a sample of the synthesised particles are removed and the remainder is used as seed particles for the subsequent step. The particles were characterized using SEM imaging on a conductive substrate and UV-Vis spectroscopy in aqueous solution. For the initial seeds from the 1st growth step TEM imaging was required as particles were expected to be sub-10nm in diameter. TEM and SEM imaging, and image analysis were used in order to calculate sphere diameters and size distributions. UV-Vis spectroscopy in aqueous solution was used to determine LSPR position through absorption data.

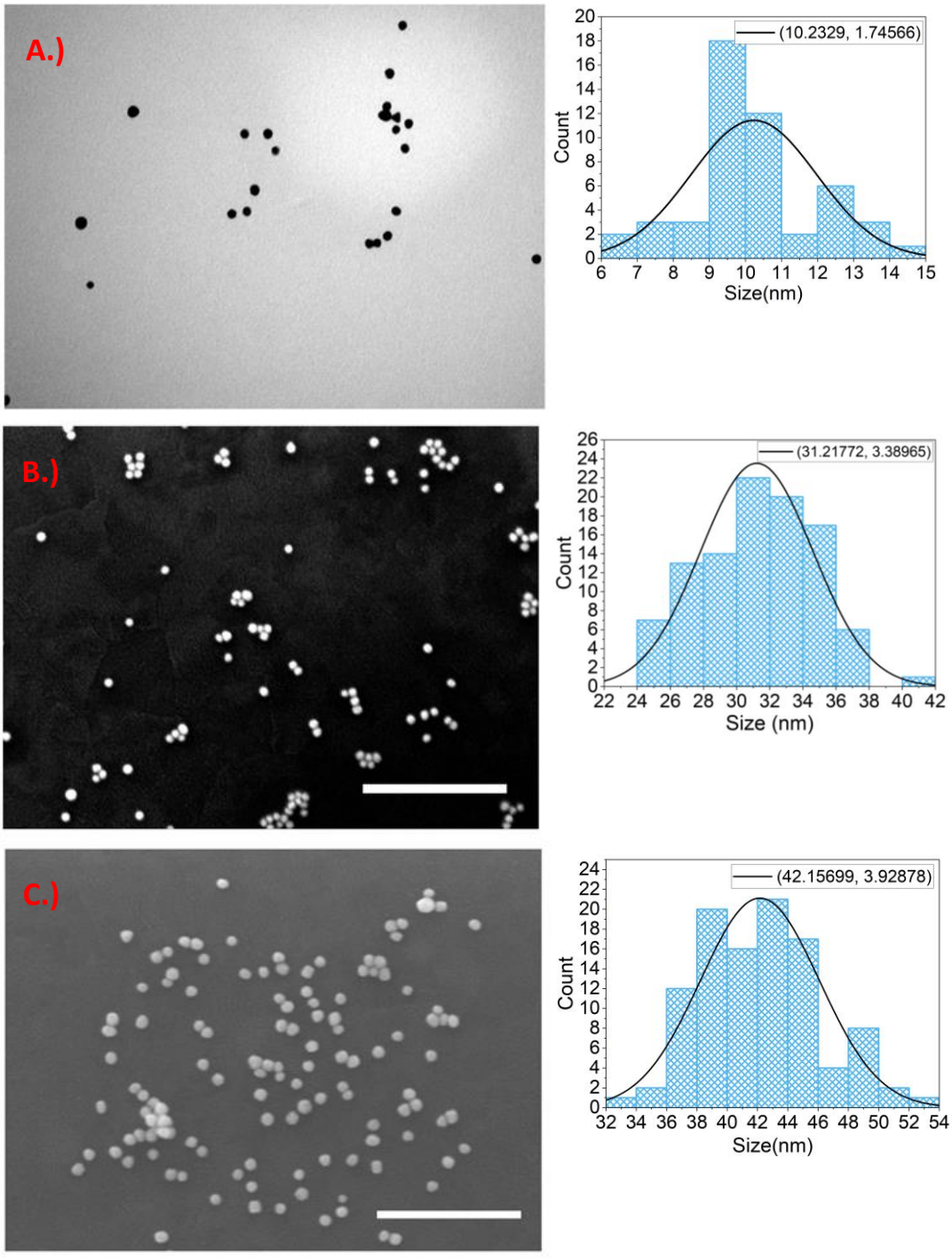

Figure 6-15 – TEM and SEM Images of as-synthesised gold nanoparticles and size distribution plots with normal distribution fittings. A.) – TEM image of Seed growth step. Diameter (10±2)nm. B.) SEM image of 3rd growth step. Diameter (31±3)nm, scale bar = 500nm. C.) SEM image of 5th growth step. Diameter (42±4)nm, scale bar = 500nm. Legends show mean and error on the mean taken from the normal fits.

6.4.1. Imaging and Size measurements

For the initial seed particles, the sizes were determined using image analysis of TEM data. Nanoparticles were drop casted onto lacey carbon coated copper TEM grids from aqueous solution for imaging. For the subsequent growth steps as-synthesised citrate-capped AuNPs from aliquots taken various growth steps were drop casted onto silicon wafer substrates and imaged using SEM. The nanoparticles were then imaged using a JEOL 7001F Field Emission SEM. Images were analysed in ImageJ to obtain average sizes and size distributions.

Figure 6-15 shows selected TEM and SEM images taken from the seed growth step and the 3rd, and 5th growth steps. At least 200 particles were measured for each of the shown growth steps, they were measured using either the imaging apparatus' built-in image analysis software or ImageJ, the sizes listed are the measured diameters for each particle. The measured diameters are then presented as a histogram plot with a Gaussian fit done in OriginPro to give the mean and error on the mean.

Figure 6-15a shows a selected TEM micrograph taken for particles from the seed growth step. TEM was used here for its higher resolution as the sizes were expected to be on the order of 10nm from the paper followed. It was important to image these particles as this step is crucial for the formation of nanoparticles in further steps. The average size was measured to be (10±2) nm which is consistent with the (8.4±1.0) nm given in the paper by Bastus et al. Figure 6-15b shows a selected SEM micrograph of AuNPs from the third growth step on a silicon substrate. The mean diameter for these particles was measured to be (31±3) nm which is very consistent with the (31.1±2.8) nm expected from the paper. Figure 6-15c shows the selected SEM micrograph AuNPs from the 5th growth step and the histogram for the sizes measured. The average diameter was measured to be (42±4) nm which is again very consistent with the (42.2±2.3) nm given in the paper. As the AuNPs get larger the size distribution increases accordingly. Particle sizes much larger than 30nm were not necessary for the molecular electronics measurements and therefore, were not imaged and measured.

6.4.2. LSPR position determination using UV-Vis spectroscopy

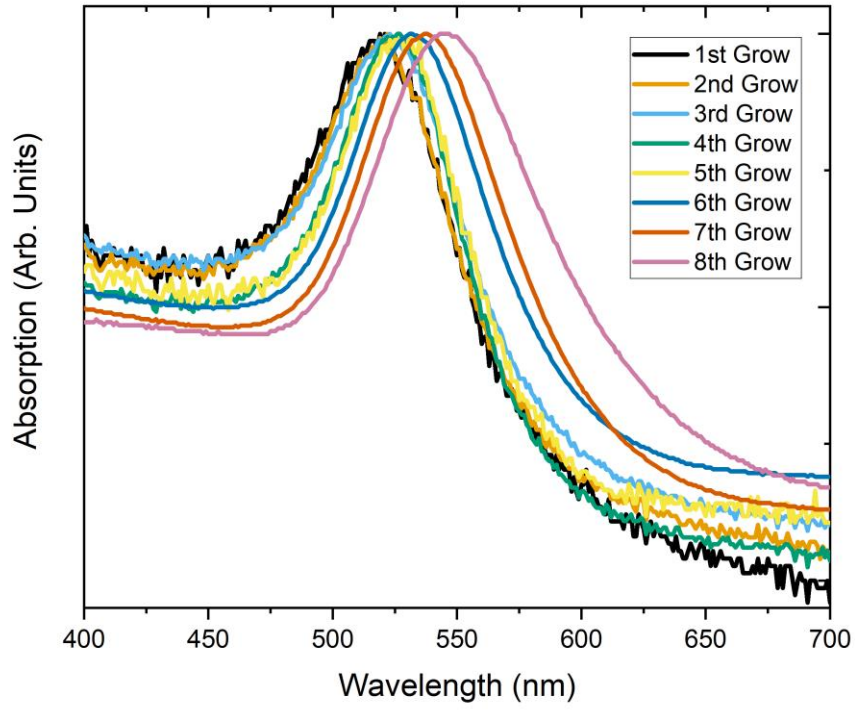

Figure 6-16 - Normalized UV-Vis absorbance spectra for aqueous solutions of AuNPS. Aliquots were taken from each growth step. Nanoparticle diameter increases with each growth step.

Absorbance spectra of the AuNPs in solution can be used to give an estimated LSPR position by showing the absorbance peaks at which light is scattered preferentially by the nanoparticles. Aliquots from each of the growth steps, excluding the seed phase, were placed into a UV-Vis spectrophotometer and absorbance spectra were taken.

The normalized absorbance spectra for aliquots from each growth step from 1 to 8 are shown in figure 6-16. Each spectrum has a clear characteristic peak, these peaks are assigned to the LSPR position for the nanoparticles. When the nanoparticle LSPR matches the incident light the light is scattered preferentially in all directions, this is manifested by an absorbance at this wavelength in the direct method UV-Vis. The peak position of these absorbance features gives the LSPR position. Nanoparticle diameters increase with growth step, however not all

growth step samples were imaged and measured in this work. It was shown in the previous section that the synthesis was consistent with the paper by Bastús et al.[1] with regard to sizes fabricated. Therefore, it is expected that these growth step sizes will be consistent with the literature. The average nanoparticle diameters here then are estimated to range from ~17nm for the first growth step to ~70nm for the 8th growth step.

The absorbance resonance peaks get stronger as the nanoparticle sizes increases and, although the spectra are normalized in figure 6-16, this is evident from the decreasing signal to noise for subsequent growth steps. It is also shown that the LSPR peak redshifts as the size increases, this is in agreement with the theory of plasmonics as discussed in the introduction of this thesis where polarizability of a metal sphere, and therefore the resonance peak position, scales with size. This also demonstrates that the average size increases with growth step. From the plot it is also clear that increasing size leads to an increase in FWHM of the peak. This is due to larger size distribution as the sizes increase which leads to larger spread in the peak.

For the subsequent plasmonic molecular electronics work AuNPs from the 3rd growth step were chosen. These particles have an average diameter of 31nm measured previously and a LSPR peak position of ~525nm. These were chosen due to the compromise between LSPR strength and nanoparticle size. A smaller nanoparticle size is necessary in order to reduce the estimated number of molecules connected to the NP and a strong resonance is required in order to observe the plasmonic effects.

6.5. Nanosphere Shadow Lithography

6.5.1. Variation in bead sizes

Stock solutions of varying bead sizes can be purchased, in this case from Sigma Aldrich, which can then be employed to form varying sized nanostructures. The size of the triangular apertures in the bead mask is directly related to the bead diameter geometrically, and altering the bead size is a straightforward way of changing resultant nanostructure dimensions of side length and tip-to-tip separations. The side-length of the fabricated nanostructures is expected to be roughly half the radius of the beads used in the mask. Therefore, the 800nm diameter beads should result in 200nm side-length nanotriangles and the 300nm bead should produce ~75nm side-length triangle. The size distributions of nanostructures are measured through SEM imaging and image analysis.

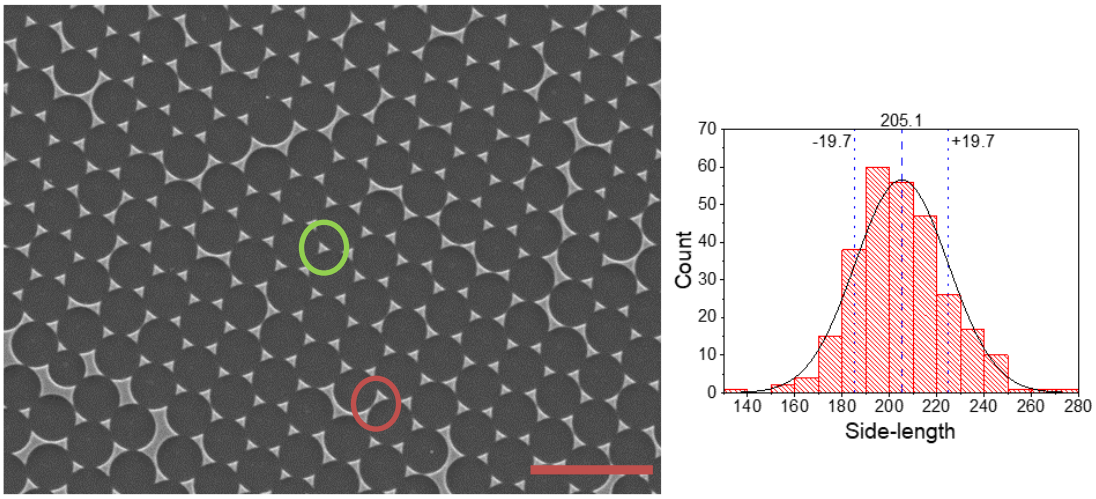

Figure 6-17- SEM image of the resultant nanostructures when NSL is performed with 800nm diameter beads. Scale bar (bottom right, in red) = 2 micron. Green circle highlights a properly formed nanotriangle used for measurements. Red circle highlights an incorrect nanotriangle that would be omitted from measurements. Histogram showing the side-length measurement statistics. Average side-length (205±1) nm.

Figure 6-17 shows an SEM image of the nanotriangle arrays produced using the 800nm diameter beads. The SEM images were analysed using ImageJ image analysis tool and at least 200 different nanoparticles were measured. The image displays a typical array of nanotriangles formed in a Fisher pattern by the nanosphere lithography. As the mask forms

as a close-packed monolayer there are lattice defects such as dislocations, and vacancies that are then transferred to the nanostructure array as can be seen by some of the poorly formed nanotriangles in the image. For the measurements only the properly formed triangles were measured as highlighted in figure 6-17. The measurements were then plotted as a histogram shown to the right of the SEM image in the figure, a Gaussian fit was used to find the mean length and standard error along with the standard deviation. The average side length for this sample was (205±1) nm with a standard deviation of 19.7nm.

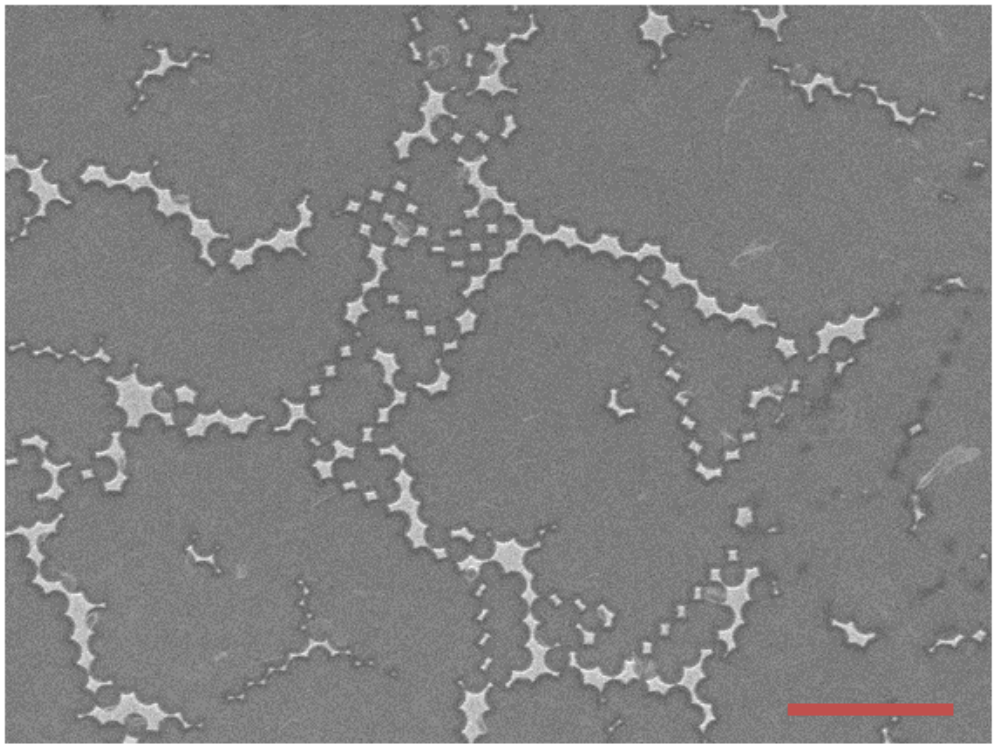

Figure 6-18 – A typical SEM image of the resultant nanostructures when NSL is performed with 300nm diameter beads. Scale bar = 2 micron. It is clear from this image that the apertures between the spheres are closed due to the lack of any nanotriangles.

Figure 6-18 shows a typical SEM micrograph of the substrate surface taken after deposition of gold through the 300nm diameter bead mask. The 300nm bead masks initially resulted in no nanostructures forming after evaporation. It appeared that during the mask development the beads had melted or deformed, closing the apertures between the beads and completely blocking the substrate during the deposition. An oxygen plasma etching step was then

utilised in order to open the apertures and allow the formation of triangular nanostructure arrays.

6.5.2. Effects of plasma etching

Polystyrene beads can be radially etched by exposing the bead masks to oxygen plasma, this step reduces the diameter of the beads in the matrix whilst maintaining the position of the sphere centre. This widens the apertures until the beads are no longer in contact with their neighbours in the mask lattice, and can be used to produce larger triangular nanostructures or, at the extreme, nanoporous metal films. The amount of etching performed can be controlled using exposure time and input power for the plasma chamber. Without an etching step the 300nm bead mask did not result in any nanostructures on the surface, and a radial etching step was required, therefore it was necessary to optimise the etching step in order to consistently develop nanostructures of a necessary size. This section outlines the steps taken to develop a proper a working, reliable etching step.

The 300nm nanosphere bead masks were assembled on ITO glass substrates using the spin-coating process outlined previously, the masked substrates were then placed into a plasma unit with an O_2 line connected to a flow regulator. With the vacuum pump attached to the plasma chamber on, the O_2 flow was controlled such that the pressure in the chamber was held at between 0.6 and 0.8mBar during the treatment process. Initially, the power supplied to the electrodes in the plasma unit was set to 100% of the total 100W power. Substrates were subjected to the oxygen plasma treatment for a variety of time periods and were then used to fabricate nanostructures using resistive thermal evaporation of gold. The resulting nanostructures were then imaged using SEM and the dimensions of the nanostructures were measured using image analysis software ImageJ. The triangular side length was calulated by taking a measurement across one side of only the fully formed triangular nanoparticles in the image. This was done using the software and the values were averaged.

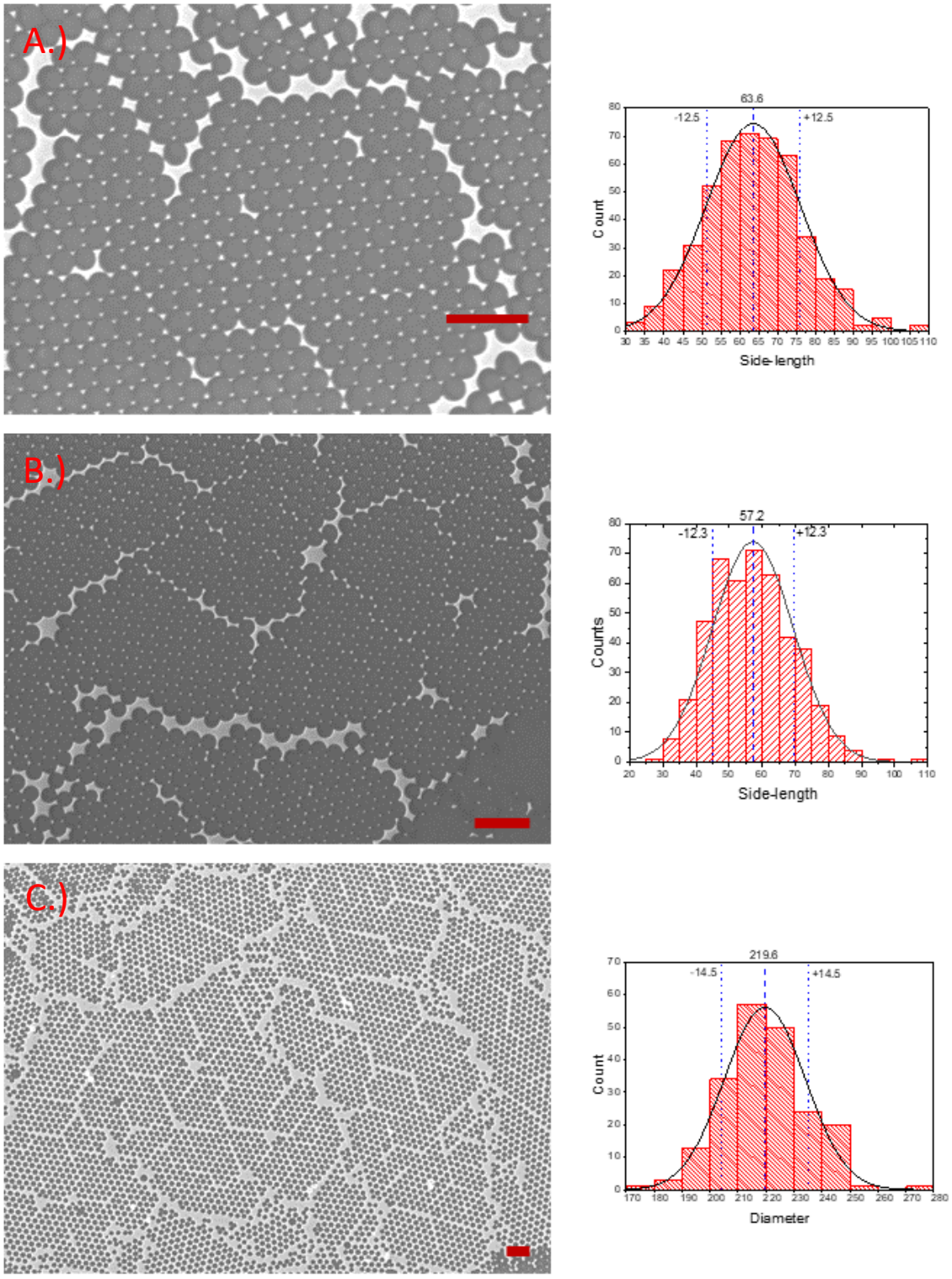

Figure 6-19 – SEM micrographs and histograms of the side-length measurements for each of the etching procedures at 100W. A.) 30s, B.) 60s, C.) 180s. Scale bar = 1 micron. Sizes are measured in nanometres.

Figure 6-19 shows SEM micrographs and the measurement statistics for the nanostructures from three different oxygen plasma etch runs. Figure 6-19a is from a 30 second exposure to

the plasma at 100% power, this image shows an ideal section of the substrate however, much of the other surface area did not show any nanostructure deposition. The histogram shows the counting statistics from the measurements taken. The lines show the mean value and standard deviation from a normal distribution fit to the data. The average side-length measured was (63.6±0.6) nm however the substrate surface didn't show continuous coverage of nanostructures, with large areas showing no successful deposition of gold. This suggested that the etching step had not been successful at etching the entire surface with certain 'hotspots' resulting in higher etching rates in certain areas and other regions of the substrate showing little to no effect. For the subsequent experiments that were to be performed on these plasmonic substrates, complete coverage of the substrate was necessary. Therefore, longer etching procedures were performed. Figure 6-19b shows a 60 second oxygen plasma etch. The average side-length here was (57.1±0.6) nm which is lower than the 30s etch suggesting that the difference made in an extra 30s of etching time was minimal however much more of the substrate showed successful deposition of nanostructures. Figure 6-19c shows an SEM image and the histogram for the measurements from the nanostructures created after a 180s oxygen plasma etch. Here, the longer etching procedure led to a nanoporous gold film on the substrate. With the increased time of the procedure came more consistency in surface coverage. Instead of measuring side-length, pore diameter was measured as there were not triangular structures on the surface. The average diameter for the pores was (220±1) nm which allows for an estimation of etching rate. The initial beads making up the mask started at a diameter of 300nm, after 180s of oxygen etching at 100% power the resultant nanopores had a diameter of 220nm suggesting an etching of 80nm therefore the radial etching rate was 0.22nm/sec.

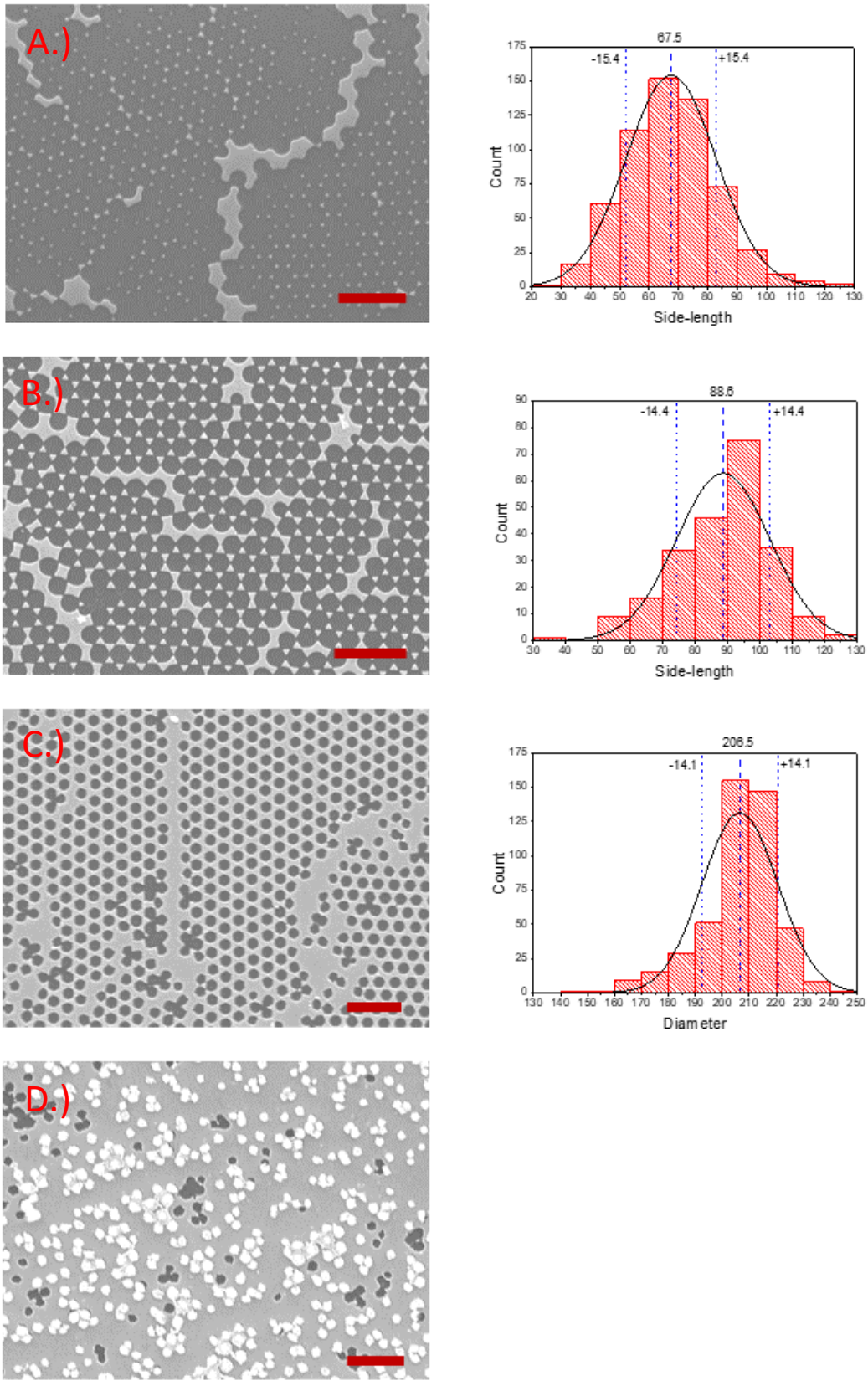

Figure 6-20 - SEM micrographs and histograms of the side-length measurements for each of the etching procedures at 50W. A.) 150s, B.)180s, C.) 300s, and D.) 450s. Scale bar = 1 micron. Sizes measured in nanometres.

At 100% power there was clear uneven etching of the PS beads occurring across the substrate. Therefore, it was decided that by lowering the power input to the plasma change and increasing the exposure time could give more control over the rate of etching and reduce the 'hotspots' of etching occurring. Figure 6-20 shows the SEM images and histograms for the measurements from nanostructures created using an oxygen etch at 50% (50W) power. Figure 6-20a shows the SEM image of the nanostructures produced after a 150s etch, the image shows that the coverage is incomplete with clear vacancies in the expected Fisher pattern. The average side-length of these nanostructures was (67.5±0.6) nm but there are still obvious hotspots and areas with vacancies. Figure 6-20b shows the nanostructures created after a 180s etch procedure, the average side-length was (88±1) nm and, importantly, the majority of the substrate surface showed good coverage of triangular nanostructures. These nanostructures are larger than what should be expected from 300nm beads used in NSL, which is ~75nm, but show large-scale coverage on the surface and therefore strike the balance between expected size and fabrication efficacy.

The nanostructures developed after a 300s exposure to the oxygen plasma are shown in figure 6-20c. Here, as seen previously, the results of the longer exposure time are a nanoporous gold film. The pore diameter was measured and the average size was (206.5±0.7) nm giving a radial etch rate at 50% power of 0.16nm/sec. Figure 6-20d shows the substrate surface after gold deposition through a bead mask that had been exposed to the oxygen plasma for 450s. After such a long exposure the mask was clearly destroyed leading to poor coverage of beads and therefore no coherent array of nanostructures. The excessive heat had also melted some of the beads significantly, making mask removal difficult evidenced by the beads still on the surface.

For subsequent experiments using the 300nm beads, the 180s etch at 50% power was used each time in order to consistently produce nanostructured substrates. This was chosen due

to the good over-all surface coverage of nanostructures and the fact that the nanostructures were still triangular. The O_2 flow rate to the plasma chamber was controlled in order to hold the plasma chamber pressure at 0.6-0.8mBar.

6.5.3. Angled Deposition

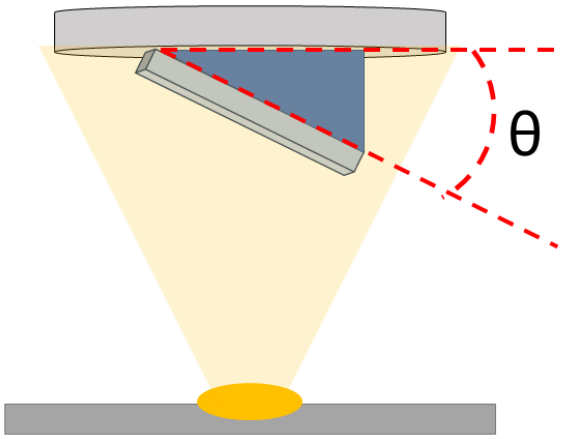

Figure 6-21 - Schematic showing the evaporation set-up for angled deposition.

Figure 6-21 shows a schematic of the angled deposition set-up. The substrate is attached to an angled bracket which can be altered for different angle set-ups. By angling the substrate with respect to the deposition beam the 'shadow' cast on the substrate alters, this changes the relative dimensions of the triangular nanostructures, stretching one or more of the triangle axes. The resultant nanostructures are therefore less like the equilateral triangles formed previously and generally isosceles or scalene. Higher angles reveal smaller areas of the substrate to the deposition beam and smaller nanostructures are developed. In standard deposition the substrate surface sits normal to the evaporated material path in the deposition chamber, angled samples are measured from 0^o being the standard position to 90^o being parallel to the material 'beam'. In this work samples were produced with angles of 10^o, 20^o, 30^o, and 35^o. The 800nm beads were used to form the NSL bead mask as these masks did not require a plasma etch procedure to develop nanostructured substrates. Due to the non-equilateral nature of the resultant nanostructures, the longest edge of each

triangle is measured using ImageJ image processing software and averages and errors were calculated.

Figure 6-22 shows the SEM images and the histograms for the length measurements taken for each angled deposition experiment. Figure 6-22a shows the nanostructures developed by the 10^{o} angle deposition. These do not look much different from the standard sample shown in figure 6-17 and the measurement statistics back that up. The average length for the longest side was (205±1) nm which is consistent with the results from 0^{o} suggesting that there is not much variation between these two angles. Figure 6-22b shows the nanostructures developed by the 20^{o} angle deposition. At 20^{o} the average side length is (161±1) nm showing a significant decrease in nanostructure size compared to the previous results, the triangle shapes were also not equilateral as before and this is shown in the image. The 30^{o} angle deposition results are presented in figure 6-22c. These nanostructures are evidently larger than the 20^{o} run and also show a preferential direction with clearly longer sides making them more obvious isosceles triangles. The average side-length for the longer sides was (190±1) nm. An image taken from the 35^{o} angle run is figure 6-22d. The average side-length for the longer edges was (177±1) nm. The 20^{o} angled deposition returned the smallest nanostructures even compared to higher angle deposition runs and seems to be anomalous. This shows the difficulty in reproducing the nanostructures between runs. If the lattice direction of the mask doesn't align with the direction of the substrate in the deposition chamber, then the nanostructures developed become irregular in shape, and because the nanosphere array in the mask is made up of diversely aligned domains there is inconsistencies in the triangle dimensions across the film. Therefore, for large scale applications, without perfect nanosphere array lattices, the angled deposition is unsuitable for controlling nanostructure morphology.

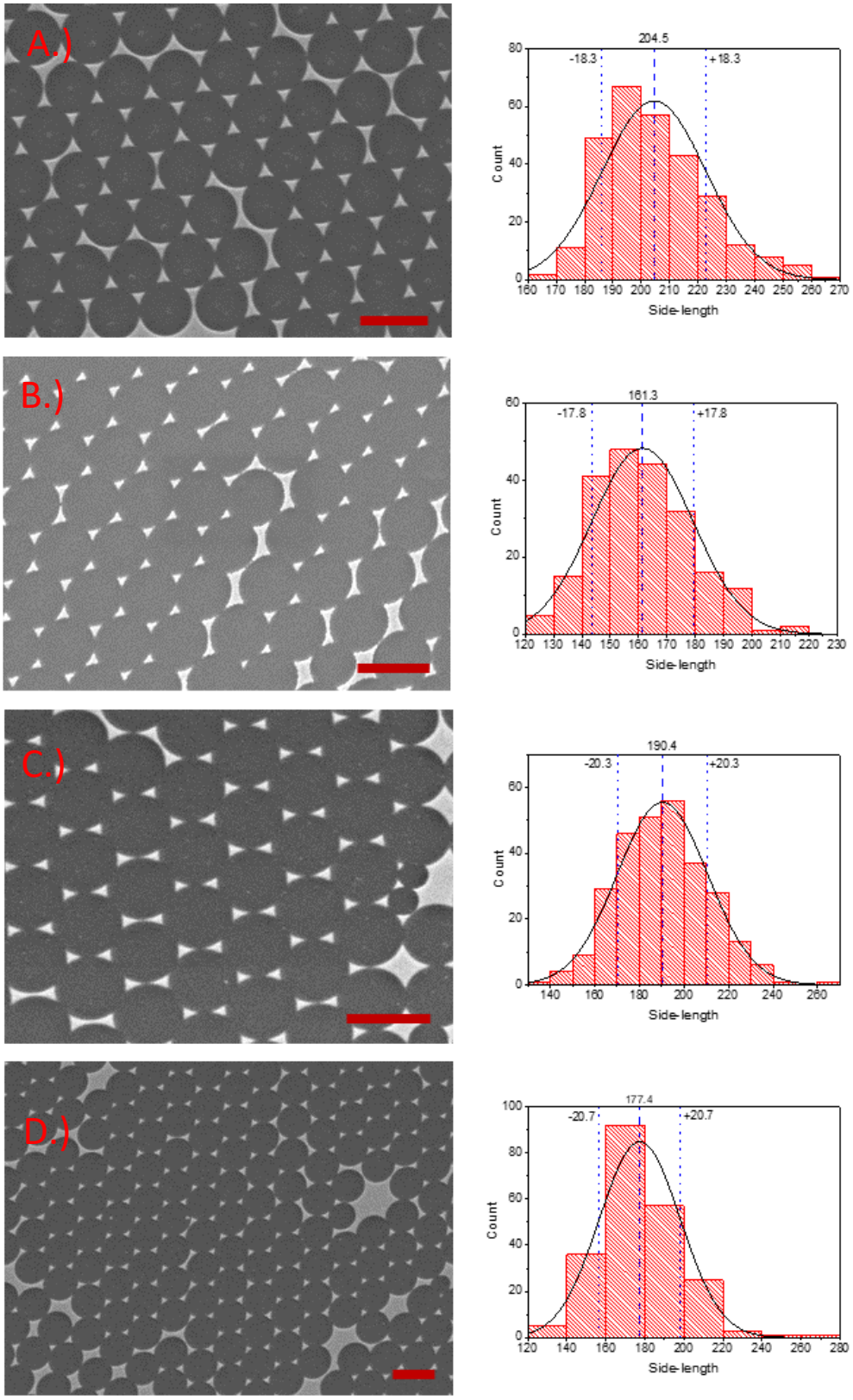

Figure 6-22 – SEM micrographs of the resulting nanostructures from the angled deposition runs and histograms for long side-length measurements. A.) 10°, B.) 20°, C.) 30°, and D.) 35°. Scale bar = 1 micron. Sizes measured in nanometres.

6.5.4. Controlling Plasmon Resonance

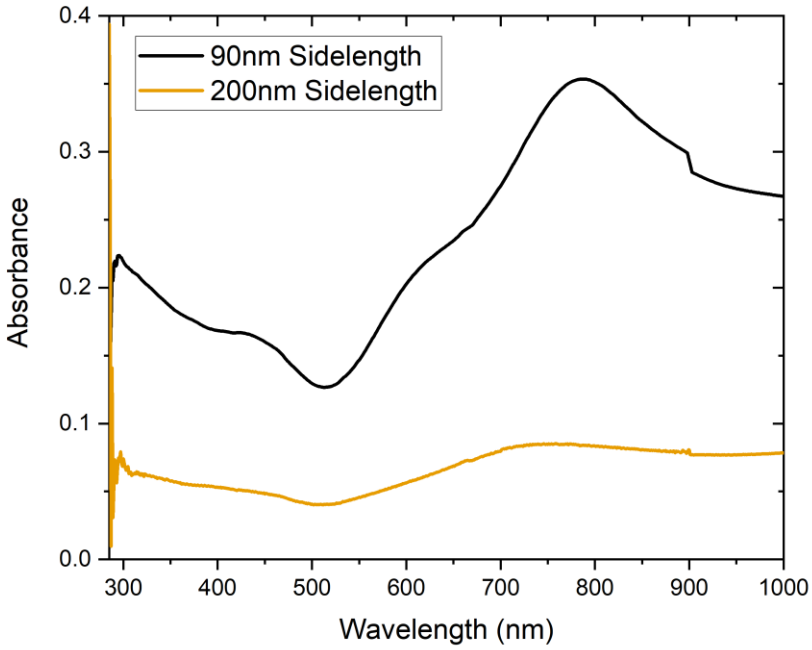

Figure 6-23 – UV-vis absorbance spectra for the 90nm average side-length Au nanotriangle (black line) and the 200nm average side-length Au nanotriangle (yellow line).

Controlling the size and morphology of nanostructures is one way to change the plasmonic properties of the nanostructured substrate, the other way this is possible is by changing the metal of which the plasmonic nanostructures are made of. Figure 6-23 shows optical absorbance spectra for the 90nm and 200nm Au nanostructures made using the 300nm and 800nm diameter bead masks respectively. The optical spectra shown in this work include discontinuities at ~700 nm and 900 nm, these are introduced by the apparatus and are due to a change in illumination source and mirror. Below 250nm the glass slides become opaque and the differential baseline method used results in massive fluctuations in absorbance at wavelengths below 250nm. The 200nm side-length nanotriangles show less total absorbance compared to the 90nm triangles and no discernible resonance peak, this is because of the size not resulting in strong localised plasmonic resonance. The 90nm side-length nanotriangles however, show a strong resonance peak at around 800nm and much higher

overall absorbance. The smaller nanotriangles therefore, are much more suited to plasmonic enhancement experiments. In order to assess the differences between the plasmonic metals the 90nm side-length fabrication process, using the 180s O_2 etch at 50% power, was used with evaporation deposition of either Au, Ag, Al, or Cu.

Figure 6-24 shows the UV-Vis absorbance spectra for 90nm side-length triangle nanostructured substrates composed of the four plasmonic metals. The resonance peak positions clearly shift depending on the metal choice. As expected from theory the order of decreasing peak position energy is Al, Ag, Au and Cu, with the copper nanostructures

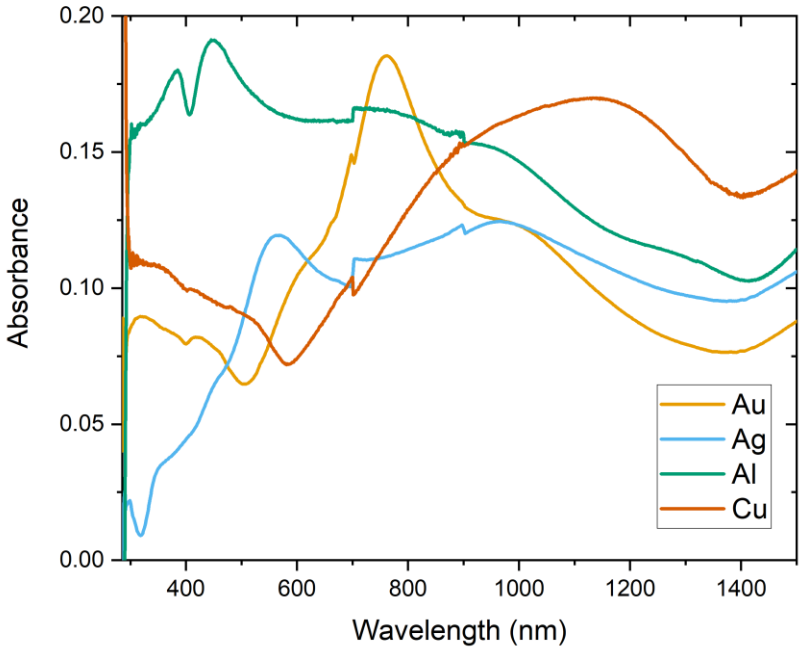

Figure 6-24 - UV-vis absorbance spectra for 90nm average side-length nanotriangles made from Au (yellow line), Ag (blue line), Al (green line), and Cu (red line).

showing a much broader resonance feature than the other samples with a peak at around 1175nm. This figure shows that the choice of metal can be used to tune the LSPR peak position using the same fabrication method and using nanostructures with identical morphology.

6.6. Conclusions

Finite-difference Time-Domain (FDTD) simulations were performed in order to motivate the subsequent experiments in this thesis. The simulations showed that large electric field enhancement could be localised to a small 1nm gap between an AuNP and a gold substrate but not on a SiO_2 dielectric substrate. FDTD also showed large electric field enhancement at the vertices of 80nm side-length nanotriangles.

A step-wise seed mediated growth method for spherical Au nanoparticles was used to synthesise colloidal gold nanoparticle solutions with accurate size control in agreement with the original paper. Characterisation using UV-Vis spectroscopy was performed and showed that the LSPR peak position could be tuned with size control. Gold nanospheres with diameter of (31±3)nm, with an LSPR extinction peak at ~525nm measured by UV-Vis spectroscopy, were synthesised during the 3rd step of the step-wise growth method. These will be utilised in chapter 6 of this thesis to form plasmonic substrates on gold-coated glass slides.

A nanosphere shadow lithography technique was developed using polystyrene spheres with diameters of 800 and 300 nm to produce triangular nanostructures 200nm and 88nm side lengths. Angled deposition was then used to create nanotriangles with different dimensions diverging from the standard equilateral triangle structure made in the standard process. Plasma etching using oxygen was also used to etch the bead mask to create larger equilateral triangles than the standard procedure and nanoporous films of the deposition metal. The differences LSPR peak positions of identical nanostructured films using a range of coinage metals as the deposition material were also shown using UV-Vis spectroscopy.

With the aid of reactive plasma etching arrays of nanotriangles with an average side length of (88±1) nm were fabricated. The optimal radial etching process comprised of a 180s etch time at 50% power (50W) with an O_2 pressure of 0.6mbar in the plasma etching chamber. This fabrication method was used to create plasmonic substrates with gold, silver and aluminium nanostructures. The UV-Vis absorption spectroscopy showed LSPR extinction peaks at 450 nm, 550 nm, and 750 nm for the Al, Ag and Au substrates respectively.

In subsequent chapters in this thesis the nanostructured substrates are applied in the fabrication of plasmonic metal/hematite composite photoanodes for photocatalytic water-splitting and used to as nanostructured substrates for molecular conductance measurements. Nanostructured plasmonic substrates fabricated using the NSL method described in this chapter were used to observe plasmonic enhancement in electrodeposited hematite films and the effects of various plasmonic metals on the photocatalytic ability of atomic layer deposited hematite films. Self-assembled monolayers of molecular wires were attached directly to gold nanotriangles and the conductance values were measured using scanning probe microscopy techniques. The effects on the conductance of the molecular wires under excitation of the surface plasmons of the nanostructures were observed.

6.7. Bibliography

1. Bastús, N. G., Comenge, J. & Puntes, V. Kinetically controlled seeded growth synthesis of citrate-stabilized gold nanoparticles of up to 200 nm: Size focusing versus ostwald ripening. *Langmuir* **27**, 11098–11105 (2011).

2. Yu, W. & Mittra, R. A conformal finite difference time domain technique for modeling curved dielectric surfaces. *IEEE Microw. Wirel. Components Lett.* **11**, 25–27 (2001).

3. Dhawan, A., Norton, S. J., Gerhold, M. D. & Vo-Dinh, T. Comparison of FDTD numerical computations and analytical multipole expansion method for plasmonics-active nanosphere dimers. *Opt. Express* **17**, 9688 (2009).

4. Munechika, K., Smith, J. M., Chen, Y. & Ginger, D. S. Plasmon Line Widths of Single Silver Nanoprisms as a Function of Particle Size and Plasmon Peak Position. *J. Phys. Chem. C* **111**, 18906–18911 (2007).

5. Gao, M., Zheng, X., Khan, I., Cai, H., Lan, J., Liu, J., Wang, J., Wu, J., Huang, S., Li, S. & Kang, J. Resonant light absorption and plasmon tunability of lateral triangular Au nanoprisms array. *Phys. Lett. Sect. A Gen. At. Solid State Phys.* **383**, 125881 (2019).

6. Liu, Z., Hou, W., Pavaskar, P., Aykol, M. & Cronin, S. B. Plasmon resonant enhancement of photocatalytic water splitting under visible illumination. *Nano Lett.* **11**, 1111–1116 (2011).

7. Khoury, C. G. & Vo-Dinh, T. Gold Nanostars For Surface-Enhanced Raman Scattering: Synthesis, Characterization and Optimization. *J. Phys. Chem. C* **112**, 18849–18859 (2008).

8. Linic, S., Christopher, P. & Ingram, D. B. Plasmonic-metal nanostructures for efficient conversion of solar to chemical energy. *Nat. Mater.* **10**, 911–921 (2011).

9. Gao, H., Liu, C., Jeong, H. E. & Yang, P. Plasmon-enhanced photocatalytic activity of iron oxide on gold nanopillars. *ACS Nano* **6**, 234–240 (2012).

10. Ramadurgam, S., Lin, T.-G. & Yang, C. Aluminum Plasmonics for Enhanced Visible Light Absorption and High Efficiency Water Splitting in Core–Multishell Nanowire Photoelectrodes with Ultrathin Hematite Shells. *Nano Lett.* **14**, 4517–4522 (2014).

11. Turkevich, J., Stevenson, P. C. & Hillier, J. A study of the nucleation and growth processes in the synthesis of colloidal gold. *Discuss. Faraday Soc.* **11**, 55–75 (1951).

12. Wuithschick, M., Birnbaum, A., Witte, S., Sztucki, M., Vainio, U., Pinna, N., Rademann, K., Emmerling, F., Kraehnert, R. & Polte, J. Turkevich in New Robes: Key Questions Answered for the Most Common Gold Nanoparticle Synthesis. *ACS Nano* **9**, 7052–7071 (2015).

13. Barbosa, S., Agrawal, A., Rodríguez-Lorenzo, L., Pastoriza-Santos, I., Alvarez-Puebla, R. A., Kornowski, A., Weller, H. & Liz-Marzán, L. M. Tuning size and sensing properties in colloidal gold nanostars. *Langmuir* **26**, 14943–14950 (2010).

14. Trigari, S., Rindi, A., Margheri, G., Sottini, S., Dellepiane, G. & Giorgetti, E. Synthesis and modelling of gold nanostars with tunable morphology and extinction spectrum. *J. Mater. Chem.* **21**, 6531 (2011).

15. Scarabelli, L., Sánchez-Iglesias, A., Pérez-Juste, J. & Liz-Marzán, L. M. A 'Tips and Tricks' Practical Guide to the Synthesis of Gold Nanorods. *J. Phys. Chem. Lett.* **6**, 4270–4279 (2015).

16. Haes, A. J., Zhao, J., Zou, S., Own, C. S., Marks, L. D., Schatz, G. C. & Van Duyne, R. P. Solution-phase, triangular Ag nanotriangles fabricated by nanosphere lithography. *J. Phys. Chem. B* **109**, 11158–11162 (2005).

17. Novikov, S. M., Sánchez-Iglesias, A., Schmidt, M. K., Chuvilin, A., Aizpurua, J., Grzelczak, M. & Liz-Marzán, L. M. Gold Spiky Nanodumbbells: Anisotropy in Gold Nanostars. *Part. Part. Syst. Charact.* **31**, 77–80 (2014).

18. Hu, M., Novo, C., Funston, A., Wang, H., Staleva, H., Zou, S., Mulvaney, P., Xia, Y. & Hartland, G. V. Dark-field microscopy studies of single metal nanoparticles: understanding the factors that influence the linewidth of the localized surface plasmon resonance. *J. Mater. Chem.* **18**, 1949 (2008).

19. Khatua, S., Paulo, P. M. R., Yuan, H., Gupta, A., Zijlstra, P. & Orrit, M. Resonant Plasmonic Enhancement of Single-Molecule Fluorescence by Individual Gold Nanorods. *ACS Nano* **8**, 4440–4449 (2014).

20. Deckman, H. . & Dunsmuir, J. . Natural lithography. *Appl. Phys. Lett.* **377**, (1998).

21. Fischer, U. C. & Zingsheim, H. P. Submicroscopic pattern replication with visible light. *J. Vac. Sci. Technol.* **19**, 881 (1981).

22. B. J. Y. Tan, †, C. H. Sow, *, T. S. Koh, †, K. C. Chin, ‡, A. T. S. Wee, †, A. & Ong†, C. K. Fabrication of Size-Tunable Gold Nanoparticles Array with Nanosphere Lithography, Reactive Ion Etching, and Thermal Annealing. *J. Phys. Chem. B* **109**, 11100 (2005).

23. Kosiorek, A., Kandulski, W., Glaczynska, H. & Giersig, M. Fabrication of Nanoscale Rings , Dots , and Rods by Combining Shadow Nanosphere Lithography and Annealed Polystyrene Nanosphere Masks. *Small* **1**, 439–444 (2005).

24. Gwinner, M. C., Koroknay, E., Liwei, F., Patoka, P., Kandulski, W., Giersig, M. & Giessen, H. Periodic large-area metallic split-ring resonator metamaterial fabrication based on shadow nanosphere lithography. *Small* **5**, 400–406 (2009).

25. Kosiorek, A., Kandulski, W., Chudzinski, P., Kempa, K. & Giersig, M. Shadow

Nanosphere Lithography : Simulation and Experiment. *Nano Lett.* **4**, 1359–1363 (2004).

26. Li, J., Cushing, S. K., Zheng, P., Meng, F., Chu, D. & Wu, N. Plasmon-induced photonic and energy-transfer enhancement of solar water splitting by a hematite nanorod array. *Nat. Commun.* **4**, 2651 (2013).

27. Canpean, V. & Astilean, S. Extending nanosphere lithography for the fabrication of periodic arrays of subwavelength metallic nanoholes. *Mater. Lett.* **63**, 2520–2522 (2009).

28. Haynes, W. M., Lide, D. R. & Bruno, T. J. *CRC Handbook of Chemistry and Physics*. (CRC Press, 2016).

29. Dodson, S., Haggui, M., Bachelot, R., Plain, J., Li, S. & Xiong, Q. Optimizing electromagnetic hotspots in plasmonic bowtie nanoantennae. *J. Phys. Chem. Lett.* **4**, 496–501 (2013).

7. The Effects of Metal Plasmonic Nanostructures on the Photocatalytic Properties of Electrodeposited Hematite Films.

7.1. Overview

An electrodeposition method was developed to deposit tin-doped hematite, α-Fe_2O_3, onto ITO coated glass slides. This method was adapted from Zandi et al[1] to include tin-doping. Electrodes were initially fabricated straight onto ITO without metal nanostructures. These undecorated electrodes were used as control samples in order to observe the effects of the added metal nanostructures. The hematite electrodes were characterised through UV-Vis-NIR and Raman spectroscopy.

In this chapter six different architectures of hematite-based photoanodes were fabricated and tested in order to observe the effects of plasmonic nanostructures on hematite and maximise the photocatalytic ability. Substrates with triangular arrays of plasmonic metal nanostructures were fabricated using the NSL method described in the previous chapter of this thesis. Hematite was electrodeposited onto these substrates using a technique developed in this chapter. Samples were also made in which a TiO_2 interlayer was deposited directly onto the nanostructures using RF-plasma sputtering. This was done to investigate the effects of a selective charge-carrier blocking layer between the plasmonic metal nanoparticle and the semiconducting film. The configurations of these electrodes are shown in figure 7-1.

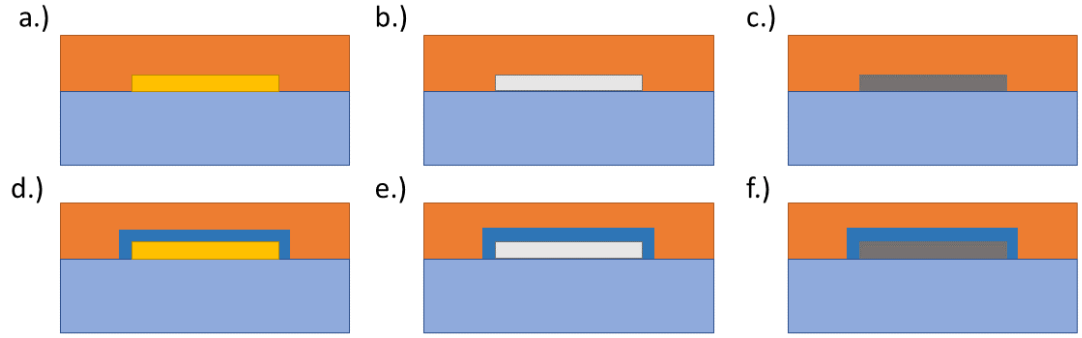

Figure 7-1

The samples were characterised using optical spectroscopy and tested for photocatalytic ability using photoelectrochemical methods. The photoelectrochemical experiments were performed in a three-electrode cell using 1M NaOH as the electrolyte, with the hematite electrodes as the working electrode, a Pt-foil counter electrode, and a homemade Ag/AgCl reference electrode.

7.2. Introduction

7.2.1. Electrodeposition of hematite

There are many established methods of fabricating hematite photoanodes including hydrothermal chemical bath deposition[2–4], electrodeposition[5–9], spray pyrolysis[10], and atomic layer deposition (ALD).[1,11] The widely used hydrothermal synthesis method has been shown to produce nanostructured hematite films through a simple 'one-pot' synthesis route.[2,3,12] This hydrothermal nanorod synthesis method requires low pH of ~pH2.5 and high pressures which renders it unsuitable for substrates that are not acid stable (such as ITO which was used in this thesis).

Electrodeposition is a method of coating substrates with a material from a solution of ionic species. A potential difference is established between the substrate as the cathode and a

counter electrode as the anode. With the electrodes in the solution the metal cations are driven by the electric field toward the anode. The ions are reduced by charges at the surface of the substrate and deposit on the substrate surface. A current flow can be measured across the electrodes to monitor the amount of deposition occurring. Electrodeposition methods can be achieved in many pH ranges as long as the cations are solubilised and therefore are more suitable for ITO substrates.[1] Variables such as pH, deposition potential, and temperature can affect the morphologies of the deposited films.[1,8,9,13]

The electrodeposition method used in this work is a two-step anodic process adapted from work done by Zandi[1] and Spray[8]. Their work builds on initial studies done by Cohen and Markovac in 1967.[9,14] The two steps are an initial deposition onto the substrate surface of FeOOH, and then a calcination step in a furnace where the FeOOH is oxidised to α-Fe_2O_3.

In their paper Zandi et al.[1] report achieving the highest photocurrent density for an electrodeposited hematite film. They presented two methods for electrodepositing hematite layers, one with the electrolyte at a neutral pH and another in slightly acidic conditions. Both electrodeposition methods use an electrolyte containing Fe^{2+} ions in the form of $FeCl_2$. When conducting the electrodeposition in a water bath at 60^{o}C with the electrolyte corrected to pH 4 the films showed a planar flat morphology.[1] The flat, planar morphology formed in acidic conditions was also observed by Spray et al.[8] The planar films produced in the acidic pH electrolyte method achieved photocurrent densities of around 1mA.cm^{-2}, reportedly some of the highest photocurrent densities for planar hematite films.[1] In neutral conditions, with the electrolyte pH corrected to around 7.5, the electrodeposition led to a rough sheet-like nanostructured film. The addition of NH_4Cl in the neutral pH deposition process was necessary in order to hold the Fe ions in solution at the higher pH.

Morphological control can also be achieved in electrodeposition syntheses by the addition of capping agents into the electrolyte. Jiao et al[13] were able to obtain hematite films with

morphologies varying from rhombohedral rods, hexagonal particles, and six-fold symmetric snowflakes by controlling the molar amounts of CH_3OO^-, NH_4F, and pyridine in the electrolyte. [13] These additives cap various crystal facets of the FeOOH as the material grows on the substrate hindering the crystal growth in that direction, allowing other facets to grow preferentially and forming the various shapes. The FeOOH morphologies were transferred to the hematite films after calcination.[13]

It has also been shown possible to control the morphology of hematite electrodes by depositing directly onto a structured substrate template. By electrodepositing onto substrates already covered with polystyrene (PS) microspheres Cai et al. [6] were able to form hollow hematite nanostructures. This template assisted electrodeposition was performed by initially forming a PS microsphere layer on the substrate, depositing FeOOH on top, and then removing the beads through the anneal steps. They demonstrated that these hollow nanostructures exhibit a higher PEC performance than planar films produced with the same deposition conditions without the PS-bead template.[6]

7.2.2. Effects of Interlayers

Literature shows that carrier selective intermittent layers such as hole-blocking layers or dielectric buffer layers can increase the plasmonic enhancement of semiconductor absorption.[15–18] Dielectric layers act to electrically insulate metal nanoparticles from the semiconductor component in a composite heterostructure. Electrical insulation is important to reduce unwanted carrier transport across the junction resulting in recombination or charge loss whilst maintaining the possible enhancement through light-scattering.[17,18]

Semiconductor heterostructures utilising layers which selectively permit the migration of certain charge carriers have been used in photocatalytic systems to enhance spatial charge separation lifetimes and reduce recombination rates.[19–22] The systems are designed by

careful consideration of valence and conduction band positions of the materials of the heterostructures in equilibrium. Photoexcited electrons will migrate and localise in the lowest lying conduction band in the heterostructure as this level is the most energetically favourable. The holes will then localise to the highest energy valence band. Through consideration of the structure charge carriers can be forced to localise in areas of the structure where they can efficiently be extracted either through the relevant water-splitting half-reaction or through electrical contact at the back contact an electrode.[19,22]

Carrier selective blocking layers have been shown to improve the plasmonic enhancement seen in composite photocatalysts by promoting the transport of the useful charge carriers that drive reactions from plasmonic metals to the photocatalysts and blocking the transport of these charge carriers in the reverse direction where they would be lost through recombination.[15] This can promote hot-carrier injection into the semiconductor layer and extraction from the back contact and reduce the probability of these extra carriers recombining resulting in an increase in the photocatalytic ability of the device.[15,16,23]

7.3. Hematite Electrodeposition

Due to the instability of ITO films in acidic conditions the standard chemical bath deposition (CBD) synthesis of hematite could not be employed. Therefore, a pH neutral electrodeposition method adapted from Zandi et al. was utilised.[1] This method was outlined in the experimental methods section 2.3.4 of this thesis. In short, an aqueous solution of 8M NH_4Cl, 0.02M $FeCl_2$, and 0.008M $SnCl_2$ was prepared and degassed, a clean ITO-coated glass substrate was set as the working electrode in a three-electrode set-up. At room temperature FeOOH was electrodeposited onto the substrate at a potential of 0V vs Ag/AgCl reference electrode, with a platinum foil counter electrode. The electrodeposition was controlled through chronocoulometry. The photoactivity of the hematite films was analysed using linear

sweep voltammetry in light, dark, and chopped illumination conditions, and through chopped illumination chronoamperometry. Herein, the electrodepositions were performed using chronocoulometry whereby the ITO substrates were held at 0.0V vs Ag/AgCl until 130mC has transferred across the electrodes. Figure 7-2 shows an SEM micrograph of a completed electrodeposited hematite film, the scale bar represents one micrometre. The film shows a nanostructured stub-like topography with nanosized platelets. This nanostructuring assists the photocatalytic ability of the film by increasing the surface area of the semiconductor-electrolyte interface and reducing the charge travel distance to the junction.

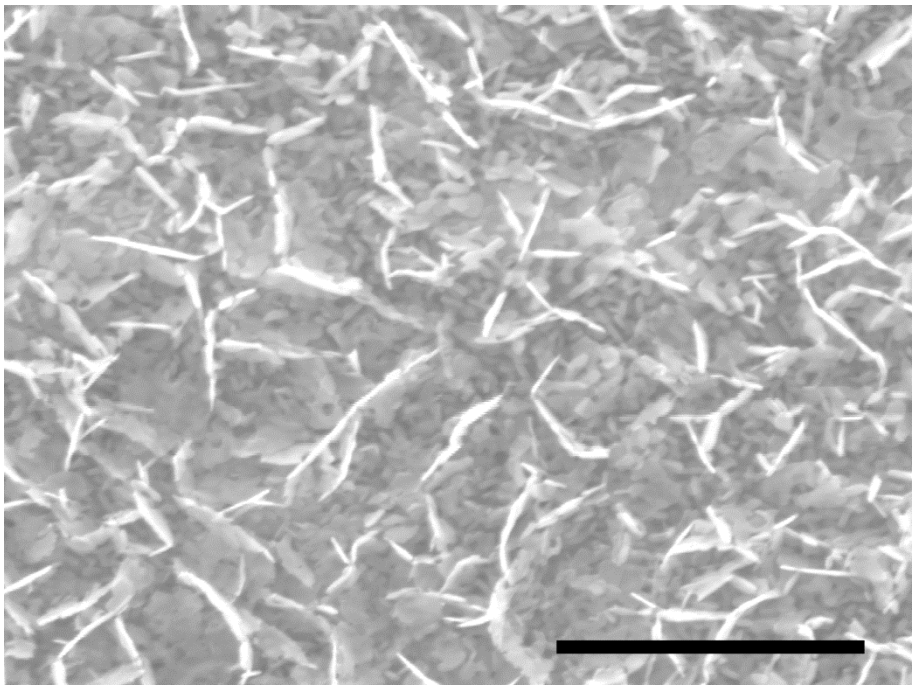

Figure 7-2 – An SEM image of an electrodeposited Sn-doped Hematite film showing nanoplatelet topography. Scale bar = 1 micrometre.

7.3.1. Optimization of Annealing

The electrodeposition procedure provides the formation of an Iron (III) Oxide-Hydroxide (FeOOH) layer. In order to form the photocatalytic Fe_2O_3 layer, the substrates require an anneal step to allow the calcination from FeOOH to hematite. The temperature of the anneal

step affects the crystallinity of the hematite layers and also facilitates doping from the back surface which can improve the photocatalytic ability of the fabricated hematite films.[24]

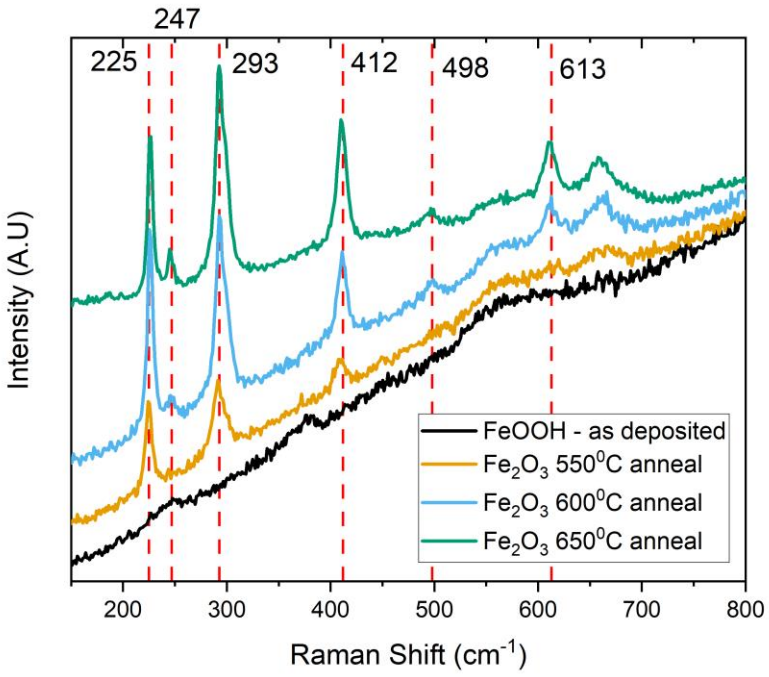

Figure 7-3 - Raman spectra of electrodeposited films with various anneal temperatures. Lines show characteristic Raman peak positions for hematite. All anneal processes took place in a box furnace over 30 minutes in air conditions. As deposited amorphous FeOOH shows little Raman signal peaks. The peak strength and sharpness increase with anneal temperature in hematite films showing increase in crystallinity with anneal temperature.

Figure 7-3 shows the Raman spectroscopy results for the electrodeposited films as deposited and after various anneal temperatures. All anneals were performed in a box furnace over 30 minutes in air. The electrodeposition initially deposits FeOOH films, during the anneal step at temperatures above 550^{o}C, the films are calcinated from FeOOH into Fe_2O_3. This is shown in the figure through the absence of strong Raman peaks in the as-deposited sample. This suggests that the as-deposited film is also amorphous. Hematite gives characteristic Raman peaks with two A_{1g} modes at 225 and 498 cm^{-1} and five E_g modes at 247, 293, 299, 412, and 613 cm^{-1}.[25] These are indicated as lines in the figure. The 299 cm^{-1} line is omitted as it is often seen as a shoulder of the much stronger 293 cm^{-1} peak.[25] Through

higher temperature anneals the Raman peaks become stronger in intensity and more well defined showing an increase in crystallinity at higher anneal temperatures.

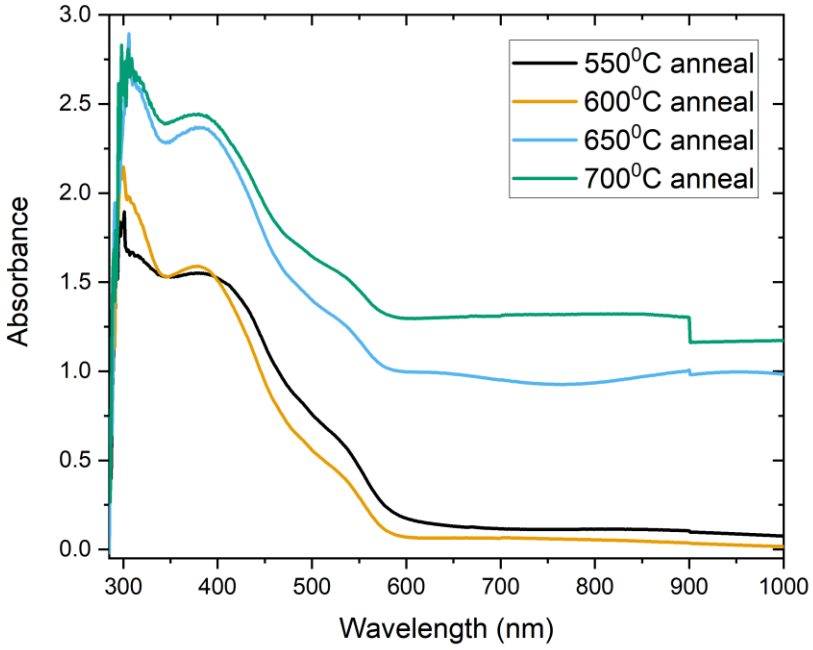

Figure 7-4 - UV-Vis Spectroscopy of electrodeposited hematite samples annealed at various temperatures. Temperatures above 600°C the ITO substrate loses transparency and becomes turbid. This is reflected in the y-axis offset seen in the 650°C and 700°C anneal spectra.

Figure 7-4 shows the UV-Vis absorption spectroscopy results of the samples of various anneal temperature. All the samples show absorption characteristics of hematite with a peak at ~400nm and a shoulder at ~500nm, these absorption features are discussed in more detail later on.[26] At anneal temperatures higher than 600°C it was observed that the ITO coated substrates lost some of their transparency. This can be seen in the UV-Vis spectroscopy, the 650°C and 700°C samples show a large y-axis offset compared to the lower temperatures. This broadband absorption is due to scattering from the now turbid ITO layer on the substrates. It was also observed that the substrates started to melt at 700°C and it was decided to not venture to higher temperatures than this.

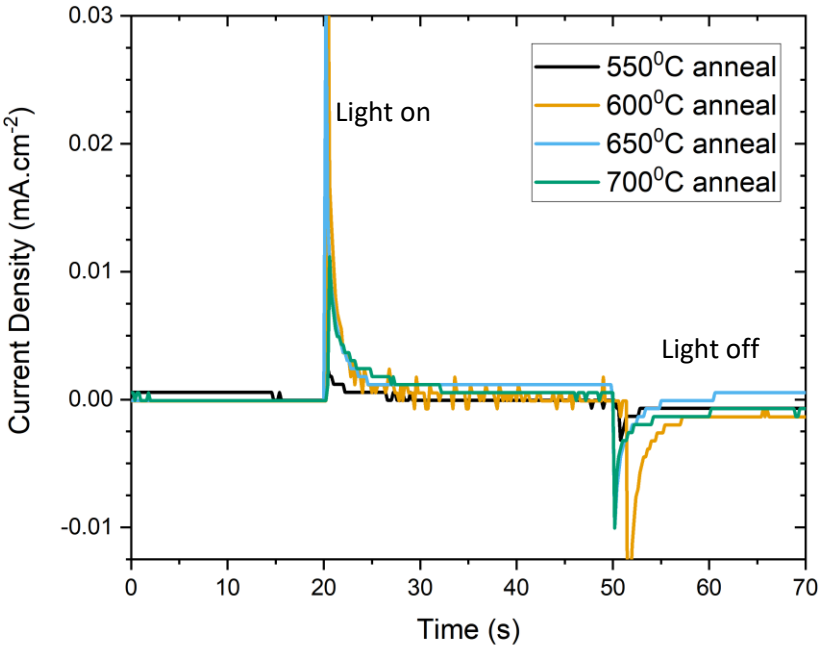

Figure 7-5 – Chopped illumination chronoamperometry of electrodeposited hematite samples annealed at various temperatures. Light is chopped on at ~20s and chopped off at ~50s. All films are photoresponsive but only those annealed at 650°C and 700°C show a tangible photocurrent.

The effect of annealing temperatures on the photocatalytic ability of the hematite films fabricated was assessed through electrochemical methods. Chronoamperometry was used to assess the photoresponse under chopped white-light illumination at 0.3V vs Ag/AgCl. The chronoamperometry results are shown in Figure 7-5. All films showed some photoresponse to the white-light illumination with sharp current peaks and troughs at the onset and offset of the illumination. The 550°C and 600°C anneal samples did not give a measurable, sustained photocurrent, which is measured as the sustained current off-set during the illumination period. The higher anneal temperatures gave some photocurrent but the values seem fairly similar and were still very low. It was decided that an anneal step at 650°C for 30 minutes was optimal in order to achieve photoresponsive hematite films with a measurable photocurrent. High background absorption due to defects in the ITO substrates, shown by the broadband absorption offset in the UV-Vis spectra previously and caused by high anneal

temperatures, would likely inhibit the useful absorption in the hematite and be detrimental to the measured photocurrent densities. Higher anneal temperatures would also affect the underlying metal nanoparticles later in the experiments, causing the nanostructure to melt or migrate through the films. A 650^{o}C anneal was seen as a compromise between these factors.

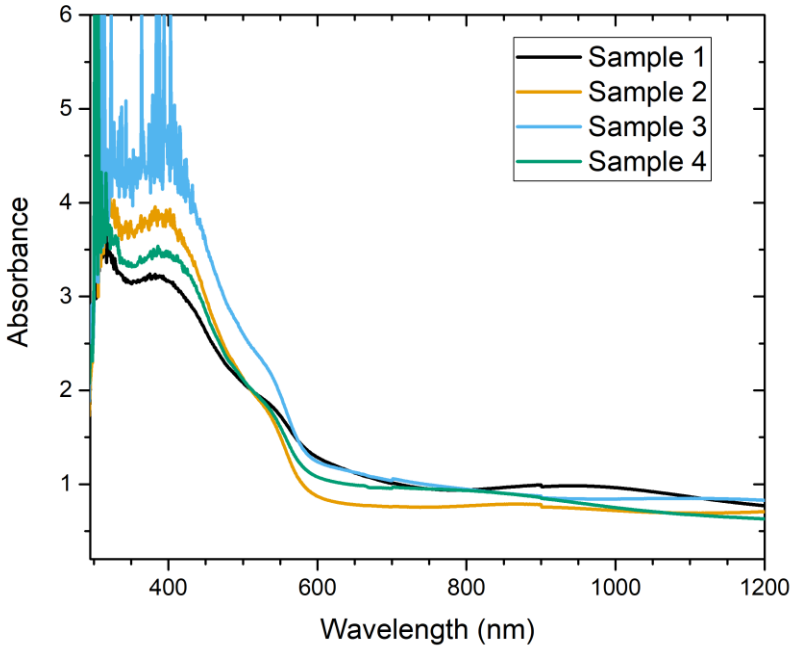

Figure 7-6 – UV-Vis spectroscopy absorbance measurements of four nominally identical electrodeposited hematite samples annealed simultaneously at 650^{o}C for 30 minutes. This figure shows the sample to sample variation in peak absorption which could be indicative of film thickness variation.

Four identical samples were fabricated through chronocoulometric electrodeposition for 130mC at 0V vs Ag/AgCl. These films were annealed simultaneously at 650^{o}C for 30 minutes and then characterised using UV-Vis-NIR spectroscopy and the chronoamperometry method outlined as before. Figure 7-6 shows the UV-Vis spectroscopy absorption results for the four identical hematite films. All films show characteristic absorption properties of hematite with consistent y-axis offsets due to the melting of the substrate, causing the cloudiness in the ITO layer. The peak absorption of the films varies somewhat suggesting some inconsistencies in film thickness across the substrate.

The photoresponses are shown in figure 7-7 and are clearly very low. The average photocurrent for these hematite films was (2.1±0.7)μA.cm^{-2}. Nominally the value for error of 0.7μA.cm^{-2} seems low however, compared to the actual average value, there is a large percentage error of 33%. This is likely due to the slight variation in film thickness seen from the UV-Vis. It was decided that in order to implement plasmonic effects a robust platform of responsive hematite films some elemental doping would be necessary in order to increase the photocatalytic ability of the electrodes and raise the photocurrent densities.

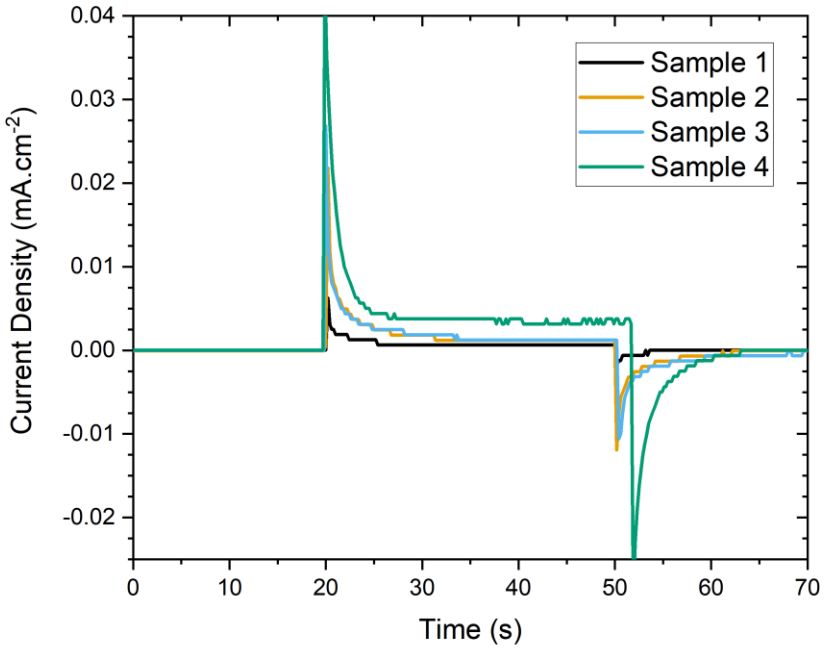

Figure 7-7 – Chopped illumination chronoamperometry results of the four identical electrodeposited hematite samples. The average photocurrent density was (2.1±0.7)μA.cm^{-2}.

7.3.2. Tin-Doping

Elemental doping of hematite has been broadly studied in order to increase the photoactivity of fabricated electrodes. Tin-doping has received a lot of attention in this fields due to the relative earth abundance and availability of tin. It has been reported that Sn^{4+} can be substitutionally doped onto Fe^{3+} sites in the hematite structure, reducing the neighbouring Fe^{3+} to Fe^{2+} to form an electron donor site.[2,24] Tin-doping improves carrier density and therefore increases the photocatalytic ability of hematite films.[2,27]

It is widely reported that hematite films can be tin-doped during an anneal step through migration of tin from the substrate.[2,24] When hematite films are grown on fluorine-doped tin oxide (FTO) coated glass the high concentration of tin in the substrate aids a fast an effective migration of tin through the hematite film.[24] However, in this case the films are grown on tin-doped indium oxide (ITO) coated glass which has a much lower tin concentration and therefore the tin migration and thus the tin-doping is minimal. It was therefore decided that actively doping the hematite with tin by addition of a tin precursor in the electrodeposition electrolyte would enhance the photocatalytic ability and increase photocurrents measured from the electrodes. In order to dope the electrodeposited film $SnCl_2$ was added to the electrodeposition electrolyte. The process is detailed in the experimental methods section. In summary, 0.4ml of a 1M $SnCl_2$ solution was added to the electrolyte that was otherwise unchanged. The films were then annealed at 650^{o}C for 30 minutes.

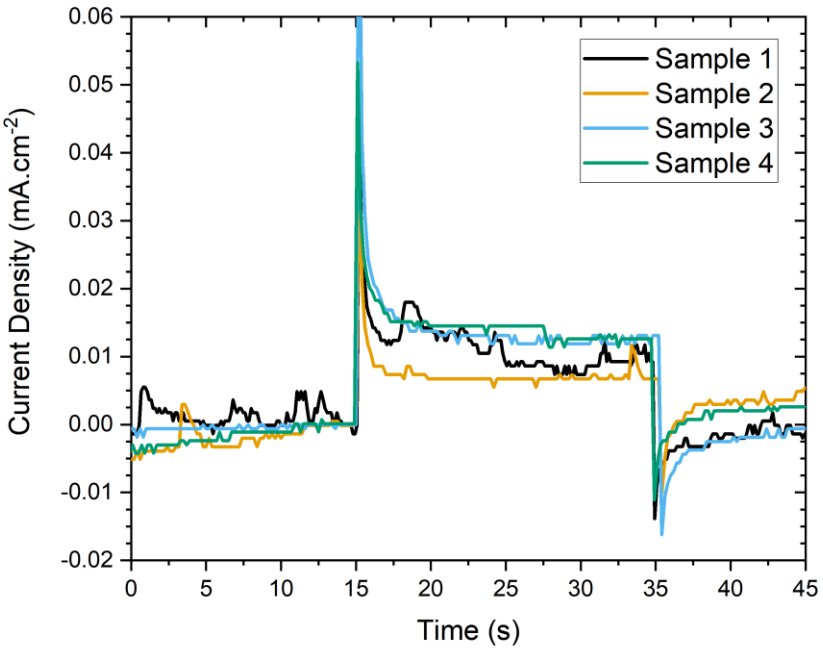

Figure 7-8 - Chopped illumination chronoamperometry results for the four Sn-doped electrodeposited hematite films. The average photocurrent density was (11±2)µA cm^{-2}.

To assess the effect of the tin-doping electrochemical measurements were obtained. The photocurrents of the electrodes using chronoamperometry at 0.3V vs an Ag/AgCl reference electrode under illumination from a 450W Xenon lamp were measured and are shown in figure 7-8. The tin doped films showed higher photocurrent densities compared to the undoped films with an average photocurrent under white light illumination of (11±2) µA.cm^{-2} compared to the undoped hematite films which was (2.1±0.7) µA.cm^{-2}. This shows that the inclusion of the tin salt in the electrodeposition electrolyte has increased the photocurrent by a factor of over 5 and therefore photocatalytic ability which would allude to successful tin-doping. The percentage error of 18% shows that the efficacy of the tin-doping procedure may be quite low compared to other methods with greater control over doping density. It also shows the electrodeposition method has less reproducibility than other established deposition techniques. However, numerically an error of ±2µA.cm^{-2} is quite low and the

percentage error is mainly affected by a low measured photocurrent. The values for photocurrent density here are orders of magnitude lower than state-of-the-art values from literature (~1mA.cm^{-2}). It is likely that tin-doping level is sub-optimal, here it is not expected that unintentional doping due to migration of ions from the ITO substrate would occur as readily as is seen from FTO substrates due to the much lower tin-concentration in ITO. The ITO substrates are also very flat whereas FTO is often rough leading to larger contact surface area at the substrate allowing for more efficient carrier extraction. In this study the tin-doping density has not been quantified but could be done using TOF-SIMS. Due to the tin concentration in ITO and its instability in acidic conditions, ICP-OES was not a viable route.

7.3.3. Film Thickness Measurements

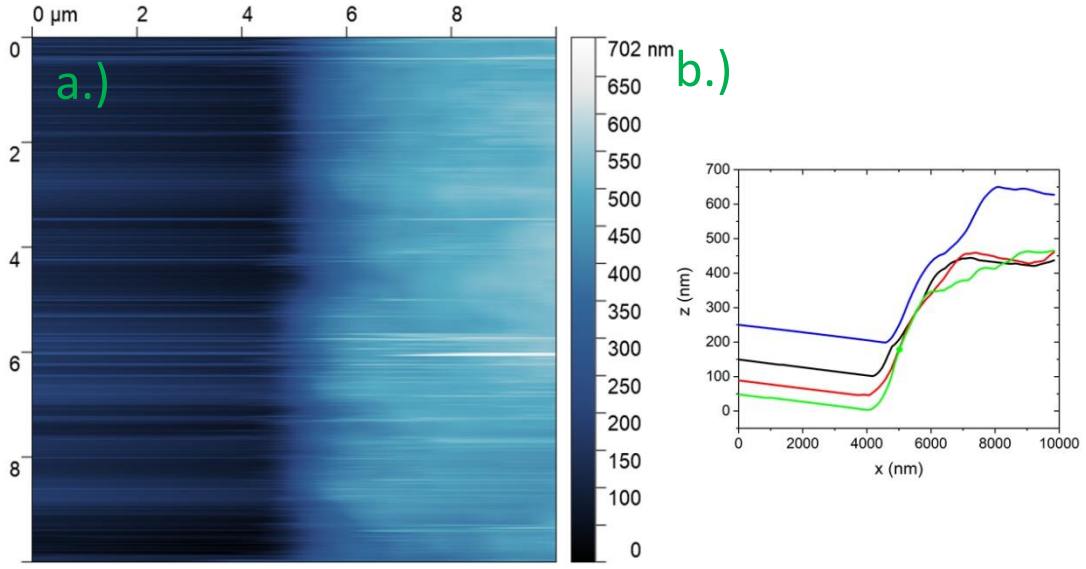

Figure 7-9 – A.) AFM image taken on the electrodeposited hematite sample showing the profile from the scratched area. B.) Plots showing four typical profiles that were used.

The tin-doped hematite films, fabricated using chronocoulometric electrodeposition for 130mC at 0V vs Ag/AgCl and annealed for 30 minutes at 650°C, were imaged using AFM to measure the film thickness. The film was scratched using a scalpel in order to remove an area of material so that a profile could be taken. A 10x10 µm area of the sample was then imaged

in contact mode AFM and profiles were taken and across the sample and the step height measured in Gwyddion software.

Figure 7-9a shows an AFM image of the cliff at the scratched area on the electrodeposited hematite film. 17 profiles in the scan direction (horizontal) were taken along the length of the image and the heights of the step were measured in Gwyddion. Figure 7-9b shows four typical profiles that were measured for this data. The data has been flattened in Gwyddion with a polynomial background submitted however it is clear from the 'flat' portions of the profile plots that not all of the substrate angle has been accounted for. To get accurate measurements of the step height, and therefore the film thickness, the measurements were taken at the minima of the flat substrate side and the maxima of the film side. 17 measurements were taken and averaged to get a value for film thickness and a standard error on the mean was used. The measured average film thickness was (415±8)nm.

7.4. Plasmonic Nanostructure Effects

Once a robust hematite synthesis was developed, the deposition was performed on top of nanostructure decorated ITO substrates. The plasmonic metal nanostructures were fabricated through the nanosphere shadow lithography (NSL) methods outlined in the Experimental Methods section of this thesis. The metals used for the plasmonic substrates were Au, Ag and Al. Gold and silver nanostructures have been broadly used for plasmonic enhancement of semiconductor devices, whereas aluminium nanoparticles have been theorized to work well with hematite due to the overlap with the hematite absorption and Al LSPR but this has not been shown experimentally.[28]

7.4.1. Band Diagrams

Figures 7-10 through 7-13 show the band diagrams constructed for the various types of interface expected from the different device architectures developed herein. Introducing

metal nanoparticle layers at the back surface of the hematite in the electrodes changes the band alignment of the hematite with the back-contact material. Due to the coverage of nanoparticles on the substrate surface, the plasmonic substrates will present a mix of the relevant metal and ITO scenarios as the metal coverage is not 100%. This will change the properties of the back contact and will alter the ability for charges to be extracted and affect the photocatalytic ability of the electrodes. The band diagrams are produced using the Anderson rule following the method given by Kittel.[29] Work functions, Fermi levels and band positions were taken from the literature.[30–34] The images show the Fermi levels and band positions for the substrate material and hematite when isolated and when thermal equilibrium is reached. At thermal equilibrium the Fermi levels are matched and band bending occurs at the interface due to charge transfer. The band bending is equal to the band position shift required to equilibrate the Fermi levels of the two materials in contact.

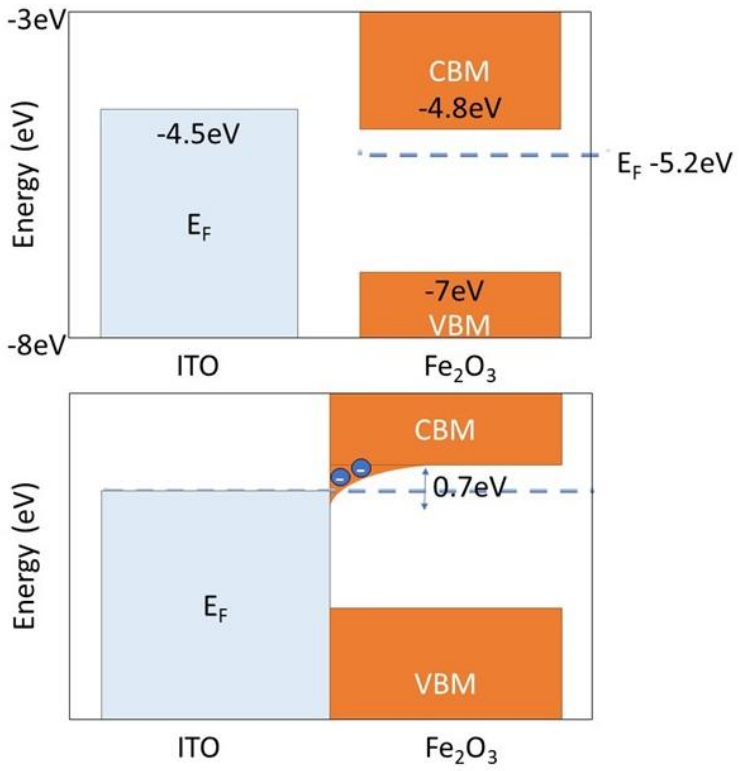

Figure 7-10 - Band alignment diagram for the ITO-Hematite configuration. Top image shows band and Fermi-level positions for each material in Isolation. Bottom image shows band-bending and positions in thermal equilibrium.

Figure 7-10 shows the band alignment for the standard hematite on the ITO conductive substrate electrode. The top diagram shows the relative band and Fermi level positions in isolation. In thermal equilibrium band bending occurs at the interface. To achieve thermal equilibrium, charges transfer from the ITO Fermi Level to the hematite conduction band minima resulting in a region of charge accumulation at the interface. The amount of band bending indicates the size of the accumulation region, here the conduction band bends by 0.7eV. Although there is no Schottky barrier here due to the overlapping of the CBM and ITO Fermi level the accumulation of charges at the interface causes a potential barrier. The potential barrier for electron extraction through the interface is due to charge repulsion from the accumulated electrons. A larger barrier for extracted electrons would result in a higher onset potential for photocatalysis and increased recombination at the interface leading to lower photocurrent densities. For the metal decorated samples, it is clear that the substrate surface is only partially coated by the metal and therefore the effects of the model here are still present. However, the effect of the ITO/hematite band alignment in the metal nanostructure decorated electrode performance should be consistent between the different architectures.

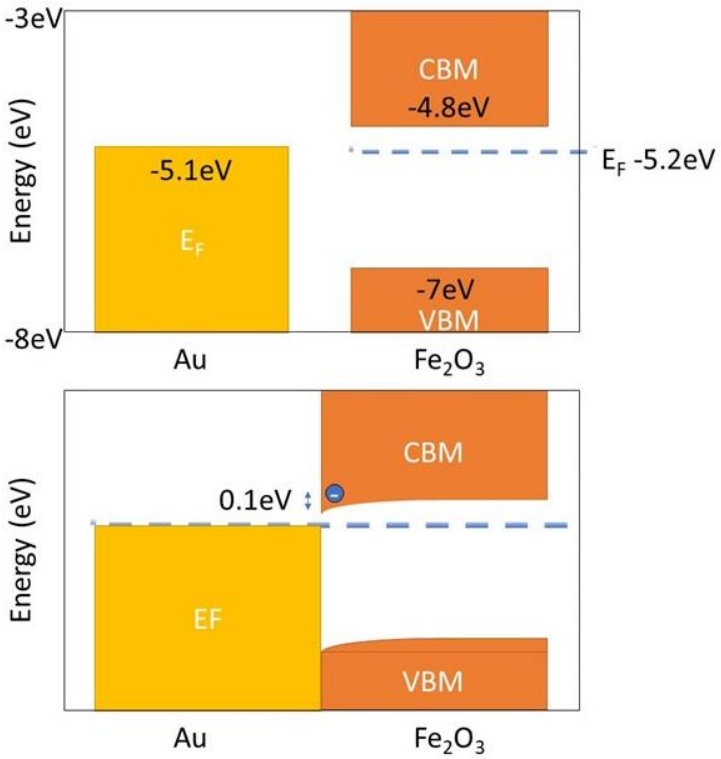

Figure 7-11 -- Band alignment diagram for the Au-Hematite configuration. Top image shows band and Fermi-level positions for each material in Isolation. Bottom image shows band-bending and positions in thermal equilibrium.

The band alignment diagram for the Au decorated substrate is shown in figure 7-11. The Fermi level for Au and hematite are relatively close and therefore the charge transfer and band bending that occurs in thermal equilibrium is lessened compared to the other configurations. This results in a smaller accumulation region at the interface. There is a small Schottky junction of around 0.1eV present in this band alignment diagram which will hinder charge extraction from the semiconductor in operation. The overall effects on charge extraction due to the presence of Au at the back contact are minimal compared to the other configurations. Therefore, the experiment results are expected to be dominated by the effects shown by the ITO band alignment diagrams which will also be present for the Au decorated samples.

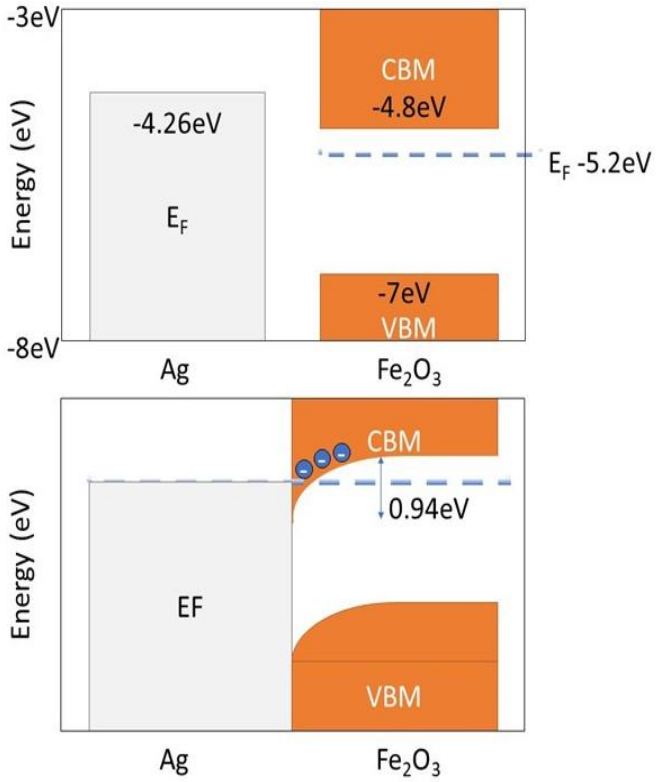

Figure 7-12 - Band alignment diagram for the Ag-Hematite configuration. Top image shows band and Fermi-level positions for each material in Isolation. Bottom image shows band-bending and positions in thermal equilibrium.

Figure 7-12 shows the band alignment diagram for hematite on an Ag substrate. Ag has a lower work function than Au and ITO, therefore in thermal equilibrium the band bending is much larger than both of these situations. The large amount of band bending forms a much larger accumulation region at the interface as charges transfer from the metal Fermi level to the conduction band minima in the hematite.

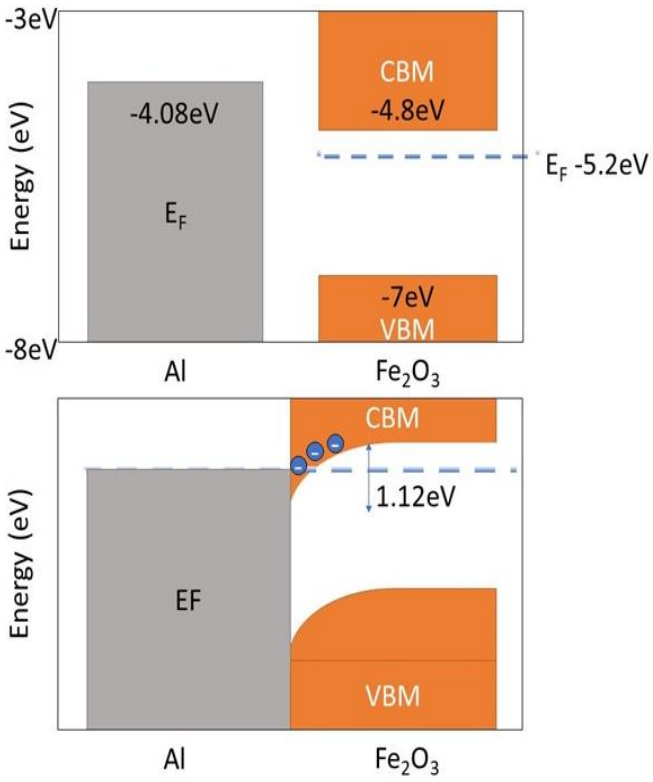

Figure 7-13 - Band alignment diagram for the Al-Hematite configuration. Top image shows band and Fermi-level positions for each material in Isolation. Bottom image shows band-bending and positions in thermal equilibrium.

The aluminium work function is lower at 4.08eV than all the other substrate materials. The band alignments are shown in figure 7-13. In thermal equilibrium the band bending in the hematite is a lot larger than the previous configurations. This leads to the Al-hematite configuration giving the largest accumulation region. This however, is likely not entirely accurate as Al exhibits oxidation at the metal surface. This would cause a thin layer of Al_2O_3 to form at the interface. Al_2O_3 is a very wide band gap dielectric that in practice would affect this band diagram by blocking the charge transfer to the hematite. Therefore, the expected effects of a large accumulation region may not be seen in the experimental work.

7.4.2. UV-Vis-NIR Optical Spectroscopy

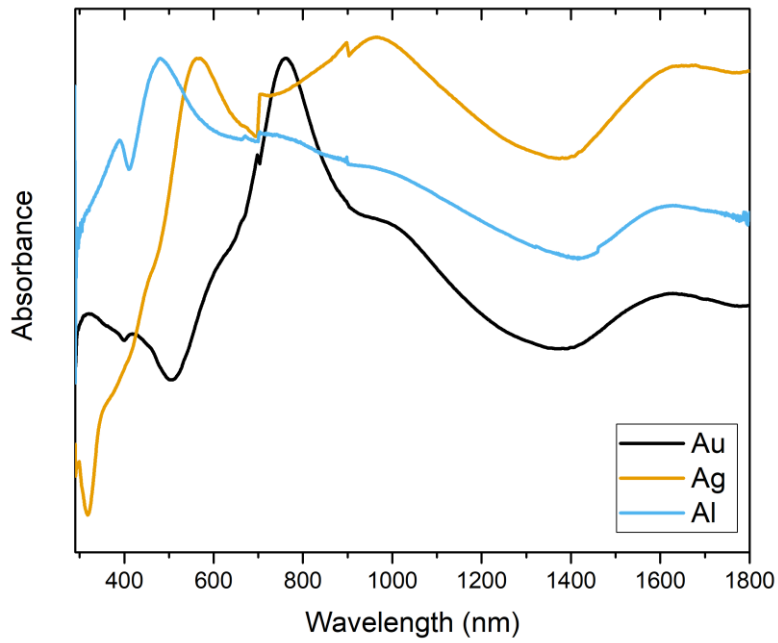

Figure 7-14 Normalized UV-Vis absorbance spectra of the 80nm side length triangle metal nanostructures produced using nanosphere shadow lithography.

Figure 7-14 shows the UV-Vis-NIR optical absorbance spectra recorded between 250-1800 nm for the metal nanostructured substrates with the 90nm side-length nanotriangles. The data here is normalized to the peak value. The spectra show absorption peaks that can be assigned to plasmon modes in the nanostructured films. It can be seen in the figure that the various metals show different LSPR mode positions. As expected, Au nanoparticles show a LSPR peak that is red-shifted in comparison to Ag and Al, with the Al LSPR placed furthest into the blue part of the visible spectrum. The Au, Ag and Al prominent peaks occur here at 762nm, 568nm, and 481nm, respectively. These peak positions present a good range of values in order to assess the effects of plasmonic resonance on the photocatalytic ability of a semiconductor composite. With hematite in particular, this set of plasmonic structures give LSPR values that range from out of resonance with the semiconductor absorption and low overlap with the Au substrates, and resonant, large spectral overlap from the Al substrates.

When used in conjunction with consistent hematite films, these nanostructure films should offer insight into the differences between LSPR peak position and select metals, and the effects on photocurrent densities and photocatalytic ability of the composite electrodes.

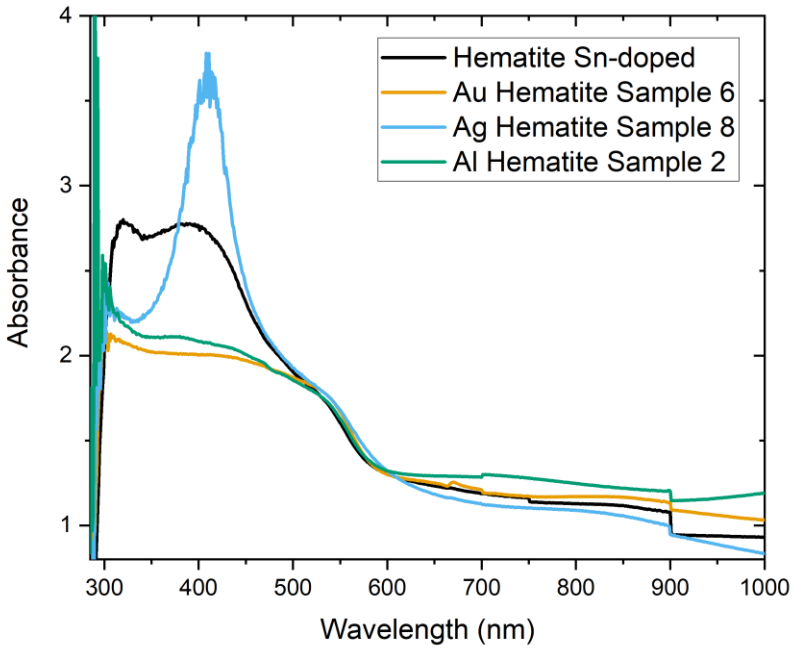

Figure 7-15 UV-Vis absorbance spectra for the undecorated and metal decorated electrodeposited hematite electrodes.

Figure 7-15 shows the UV-Visible optical spectra for specific samples of an undecorated and the metal decorated hematite electrodes. The hematite absorbance spectrum is consistent with hematite absorbance data seen in the literature with a shoulder at 500nm leading to a peak at 400nm.[26] The peak at ~400nm has been assigned to Ligand to Metal Charge Transfer (LMCT) and the shoulder at~500nm has been assigned to d-d transitions from pair excitations.[26,35–37] The data in figure 7-14 has been normalized, however the initial absorbance data for the isolated metal nanostructures peak at 0.25-0.3, the spectra in figure 7-15 show that the absorbance of the films is dominated by the hematite layer. Due to the large difference between the absorption values of the isolated metal NP

array films and the hematite films it would be expected that the LSPR peaks would either be completely dominated by the hematite or only be slightly distinguishable in the spectra.

The metal decorated films all have lower absorption than the hematite standard in the UV region (<350nm). Undecorated hematite spectra with similar characteristics to the Au-hematite, including a flat absorption below 450nm, were observed. This discontinuity was put done to experimental differences in the characterisation that failed to take into account the differences in film thickness across the entire electrode. Therefore, the hematite spectrum here is more of an ideal shape reference.

Absorbance spectra of the Au decorated substrates do not show the gold LSPR peaks through the hematite and ITO absorption. The isolated gold absorption peaks are far lower than the hematite absorption due to the hematite thickness therefore, the Au peaks are not distinguishable in the overall composite material absorbance. The absorbance shows a flat absorbance across the hematite peak absorption region (<450nm). This is often seen in literature for hematite films. Therefore, it is assumed that the Au shows no strong interaction with the hematite.

The Ag decorated substrates show a large peak at ~400nm. This peak at 410nm has a larger absorbance compared to the isolated films suggesting that there is some large interaction effect between Ag and hematite which strengthens the absorption either by the nanostructures or the hematite layer. This large peak could be a strengthening of the 400nm peak in the hematite absorption. The peak in the hematite absorption is due LMCT and has been assigned to a transition from the O_{2p} to Fe_{3d} t_{2g} bands.[26,36,37] It is possible that the charge transfer that occurs between the silver and hematite in thermal equilibrium leads to electrons occupying the lower levels of the conduction band minima. This enhances the absorption of the LMCT occurring at 400nm as the energy levels below these are occupied.

Despite the Al plasmonic structures having a good overlap between the LSPR and the Hematite absorption the LSPR peaks are not revealed in the absorption spectra instead, the entire absorbance spectra is similar to that of Au decorated sample. This could be due to the aluminium particles having melted and the LSPR is no longer as strongly resonant, metal has migrated through the film during the anneal step, or the nanoparticles have completely oxidised in the anneal. As in the Ag configuration a large charge transfer from metal to hematite is expected from the band alignment diagram in figure 7-12. However, the enhancement of the 400nm peak is not seen in the UV-Vis, this could be due to an alumina layer forming on the aluminium nanoparticles. This wide band gap dielectric layer would block the charge transport from the Al to the hematite and the conduction band minimum states would not be occupied. The metal layer could also have integrated into or reacted with the hematite film due to its low melting point and propensity to perform a redox reaction with iron oxides. This would remove the Al layer and therefore the interface.

The reductions and gains in peak absorption between samples could be due to poor efficacy of the hematite electrodeposition leading differences in thickness across the individual sample, and sample to sample. It is also possible that the different metals coating the substrates lead to different efficiencies of the electrodeposition method. The methodology used in the UV-Vi spectroscopy, including differences in slit width can alter the results. This occurs due to smaller regions of the film present in the incident light pathway meaning that the differences in thickness across the film is not accounted for

7.4.3. Electrochemical Measurements to Determine Effects of Metal Nanostructures

In order to test the effects of the nanostructures on the photocatalytic ability of the hematite films, photoelectrochemical experiments were employed. In order to compare and evaluate the effects on the photoresponse chopped illumination chronoamperometry was carried out

at 0.3V vs Ag/AgCl RE. Incident photon conversion efficiency measurements were done in order to evaluate the changes in the spectral response of the various electrodes.

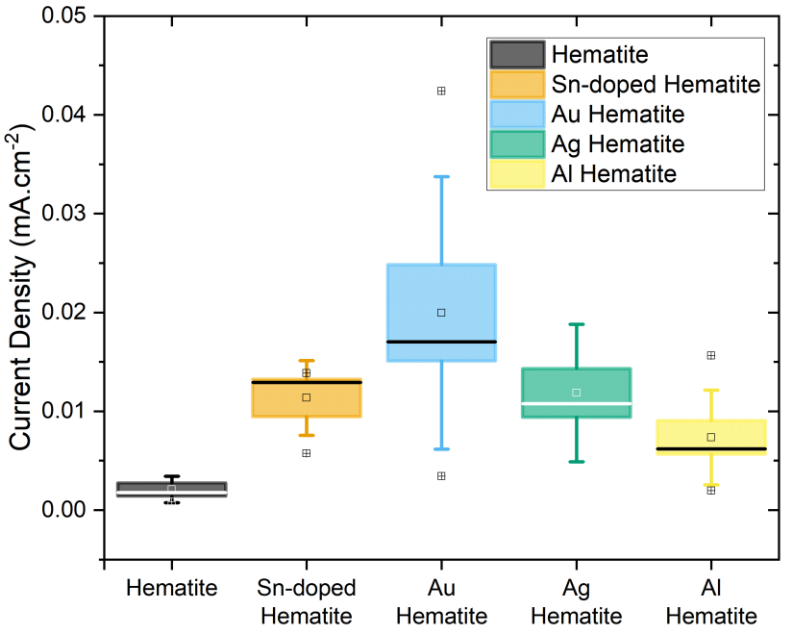

Figure 7-16 – Photocurrent density boxplot for the electrodeposited hematite architectures. 8 samples for each configuration were measured. Hematite data here represents the undoped hematite electrodes fabricated initially. Metal decorated electrodes were fabricated using the same Sn-doped hematite procedure as the undecorated Sn-doped hematite electrodes.

Photocurrents taken from chronoamperometry for each of the films can be used to directly compare the various electrodes. The sustained photocurrent density from each sample of each architecture was measured from the chronoamperometry data and combined. Boxplots in figure 7-16 have been used to effectively display the data and present statistics to show mean photocurrent densities and their error values. The central square marker shows the mean value, the median value is represented by the line dissecting the box, and the box limits represent the standard error on the mean. The whiskers in the boxplot show the standard deviation of the data set, and the square markers outside of this represent outliers and therefore the least effective and champion electrodes in the data set.

Figure 7-16 shows the chronoamperometry photocurrent density results for the electrodeposited hematite, Sn-doped hematite and metal decorated Sn-doped hematite films in a box-plot. The measurements show a broad range of photoresponses alluding to large variation in the electrodeposition method. For the metal decorated electrodes, the champion samples outperformed the average value of the respective data set by more than the standard deviation whereas the Sn-doped hematite showed a much narrower spread with the champion electrode sat within the standard deviation. Each of the sets of electrode architectures show at least one sample that is almost unresponsive in the photoelectrochemistry, these samples are often visibly identifiable as poorly fabricated showing a poor efficacy from the electrodeposition synthesis route.

The Sn-doped hematite electrodes gave an average photocurrent density of (11±2)μAcm^{-2}. For Au decorated electrodes the mean and median photoresponses are larger than undecorated hematite films with a mean photocurrent enhancement of nearly double suggesting successful photocatalytic enhancement from the addition of plasmonic Au nanostructures. Compared to the undecorated Sn-doped hematite electrodes, an enhancement was observed in most Au decorated samples, with a mean photocurrent of (20±5) μA.cm^{-2}. This gives an average enhancement of 1.8 compared to the undecorated tin-doped hematite. The champion electrode with a photocurrent of 42.4 μA.cm^{-2} showed an enhancement of 3.6 when compared to the average photocurrent for undecorated tin-doped hematite electrodes ((11±2)μAcm^{-2}).

The silver decorated electrodes showed a comparable photoresponse to the standard hematite electrodes, showing either no effect of the Ag nanoparticles or multiple competing effects. The average photocurrent for the silver decorated hematite electrodes was (12±2)μA cm^{-2} which is comparable to the mean Sn-doped hematite photocurrent. This is despite the best overlap between LSPR and hematite absorption. This could be due to plasmonic

quenching through some mechanism of lost charge carriers or recombination, or parasitic absorption from the Ag film competing with the hematite absorption. From, the spectral overlap between Ag LSPR and hematite absorption it would be expected that the Ag nanostructures would result in light scattering, and therefore increase in photon pathlength, of photons with energy around the peak hematite absorption. This should result in good plasmonic enhancement. From the band diagrams discussed previously discussed, it is clear that a large charge transfer could occur between metal and semiconductor for the Ag hematite configuration. These electrons should occupy the low conduction band states in the hematite and form a large accumulation region at the interface. This accumulation region would then hinder the extraction of the electrons at the interface due to charge repulsion. This increases the probability of recombination as the electrons are slow to travel through this region. The occupancy of the low-level conduction band states at the interface would also block photoexcited charge creation in a section of the spectrum and lower the photocatalytic ability of the film.

For the Au decorated architectures, the spectral overlap is lower as the LSPR is red-shifted compared to hematite absorption onset, this means that parasitic absorption is less of an issue. Resonant energy transfer between the oscillating localised surface plasmons in the Au produces electron-hole pairs in the hematite boosting the photocurrent density. Unlike Förster resonant energy transfer, plasmon-induced resonant energy transfer (PIRET) can occur when the donor shows absorption at lower energies to the acceptor absorption as is the case here. The high Au Fermi level compared to the hematite conduction band results in sufficient energy from the oscillating plasmons to produce this effect. From the band-diagrams it is also shown that the charge accumulation layer in the Au configuration would be smaller and therefore have less effect on the charge carrier extraction efficiency at the back contact.

The combination of the possibility for PIRET enhanced photocatalytic ability and the lower barrier to charge extraction could be the reason for the observed photocurrent density enhancement in the Au-hematite composite electrodes. Light-scattering is unlikely to have such a great effect here as the spectral overlap between Au LSPR and hematite absorption is poor. Hot carrier injection is also a possibility for the enhancing mechanism due to the fact that the extraction of hot electrons at the back contact would allow hot holes to be injected into the semiconductor film and aid the hole driven water-splitting reaction.

From the box-plot in figure 7-16, the aluminium decorated electrodes have a mean photocurrent of (7±2)μA cm^{-2} which is actually lower than the pristine Sn-doped hematite. The aluminium layers therefore have a negative effect on the electrodes despite the Al nanostructure LSPR having very good overlap with the hematite absorption. This could be due to parasitic absorption from the nanostructure layer. However, in the post anneal absorption data (figure 7-14) it can be seen that the Al absorption is not visible in the spectra, likely because of the Al nanostructures melting and aluminium then migrating through the film detrimentally doping the hematite films leading to reduced photocurrents.

Incident-Photon-Conversion efficiency measurements allow for the analysis of the spectral differences in the electrode's photocatalytic ability. It is possible to see enhancements in various spectral ranges which would allow for the explanation to varying effects of the plasmonic nanostructures. These measurements were performed on the median performing samples in most cases, but were also performed on the champion electrodes and the worst performing electrodes from the data sets.

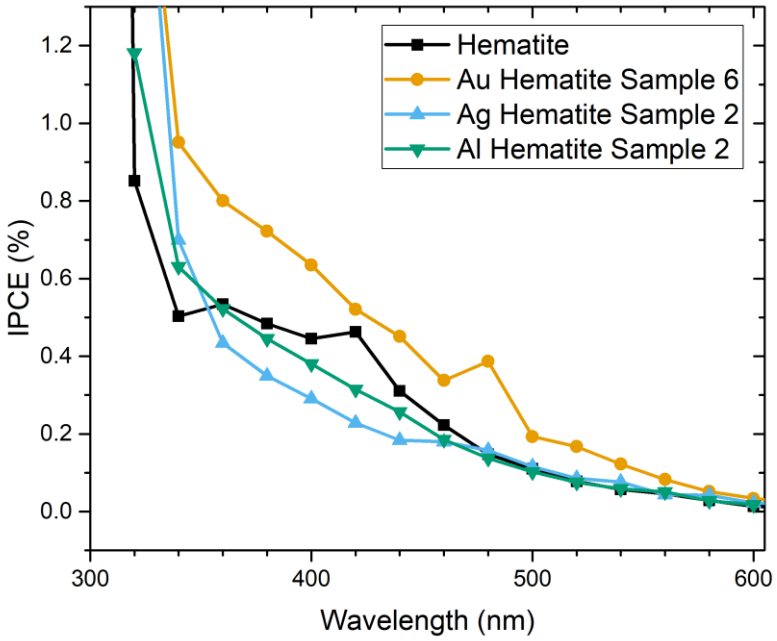

Figure 7-17 - IPCE spectra for undecorated Sn-doped hematite and the 80nm metal triangular nanoparticle decorated Sn-doped hematite samples.

Figure 7-17 shows the IPCE spectra for the undecorated and the metal decorated Sn-doped hematite samples. The samples that were tested and shown here are the median performing samples from the chronoamperometry in figure 7-16. In Figure 7-17 the undecorated tin-doped hematite electrode IPCE spectrum is fairly characteristic and follows the shape of the UV-vis absorbance measurements with a plateau between 340nm-420nm. This feature in the UV-Vis absorbance is usually observed as a peak or plateau and has been assigned to a charge transfer at this energy. This hematite spectrum has been subsequently used as a comparison for all the following IPCE spectra taken. The IPCE spectra from the median samples for each of the have been plotted on the same axes in order to compare the spectral differences in conversion efficiency.

IPCE of Au decorated films show an overall increase in the normal hematite absorption range namely 340-460nm with an observed slight increase around the region where the LSPR peak

exists. The increased IPCE over the whole spectrum justifies the increased photocurrent shown in the chronoamperometry.

The IPCE spectra of Ag decorated films show a decreased photoresponse in the region where the enhanced 400nm peak occurs, but a seemingly increased response around the blue near-UV region. However, this increase cannot be verified here because the absorption of the incident light by both the glass electrochemical cell and the substrate resulting in low incident power hence skewing the IPCE results in this region. The quenching of the IPCE in the region where the absorption is enhanced demonstrates that this effect is detrimental to the electrode performance. When thermal equilibrium is reached and electrons populate the lower conduction band states in the hematite this forbids photoexcited electrons to populate these states and increases the absorption to higher energy levels. This is shown as the enhanced peak in the UV-Vis. This effect only occurs close to the interface meaning that the hematite at the interface is absorbing more of the incident light in the 400nm region. The hole diffusion length is on the order of a few nanometres for hematite and the electrodeposited hematite layers are quite thick. Excitons produced nearer to the back contact have a low probability of participating the water oxidation reaction at the film surface. This increase in absorption deep in the film is therefore a parasitic absorption mechanism and as such reduces the IPCE in this region.

Aluminium decorated hematite electrodes produced IPCE spectra with a similar shape to that of the Ag decorated samples, showing decreased conversion efficiency across the spectrum and through most of the hematite absorption region (>360nm).

7.5. Larger Nanoparticle Films

Using 800nm diameter beads in the NSL substrate fabrication process with Au and Ag it was possible to create nanoparticle decorated substrates with the LSPR peaks shifted away from the hematite absorption region. The triangular nanoparticle fabricated using the 800nm diameter beads have an average side-length of 200nm compared to 80nm side-length triangles for the 200nm diameter beads. The nominal thickness of these metal films is the same as the previous 80nm side-length nanoparticles at 35nm. SEM images of these films can be found in the previous chapter in figure 6-17. By running the same tests with these substrates it could be assessed whether the effects were purely plasmonic or whether there was some metal migration from the back surface during the anneal. As seen in the literature, when annealing hematite films on FTO glass, tin-doping of the hematite occurs from tin migration from the substrate increasing the photoresponse.[2,24] It was therefore important to assess whether the films were being inadvertently doped with Au or Ag and whether this was the reason for the effects seen previously. Using larger nanoparticles could also assess whether the effects were due to LSPR or simply by including metal films at the back contact.

7.5.1. UV-Vis Spectroscopy

The films were characterised using UV-Visible optical spectroscopy before and after electrodeposition of hematite. The optical absorbance spectra are shown in figures 7-18 and 7-19.

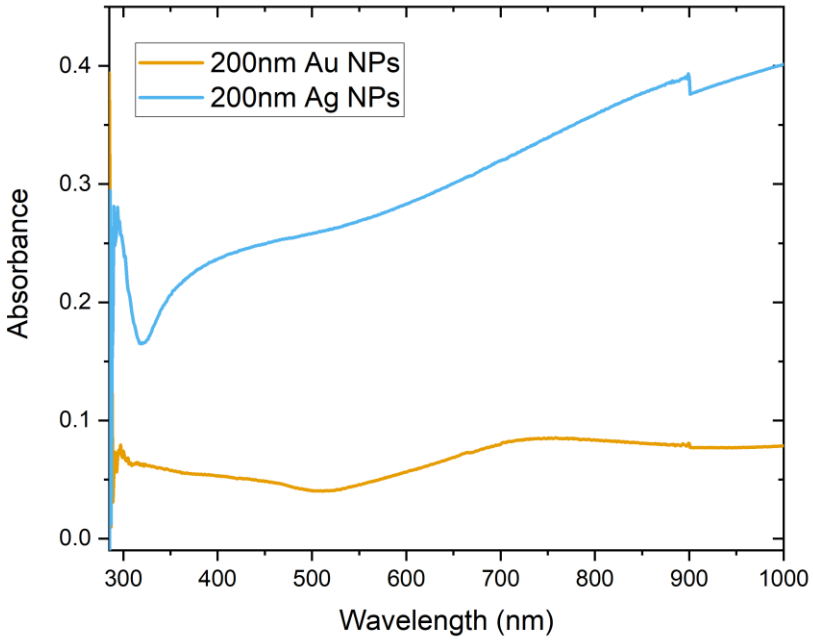

Figure 7-18 – UV-Vis spectra for the Au and Ag 200nm side length triangle array substrates.

Figure 7-18 shows the optical absorbance spectra for the nanoparticle films. The absorbance from the 200nm side-length Au nanoparticle films shows very low absorbance. This low absorbance across the visible spectrum shows no strong resonances as expected due to the LSPR being either eliminated or hugely red-shifted out of the visible spectrum. The Ag spectra does show a comparative absorption to previous plasmonic films however with the absence of a strong resonance peak. Both these results show that these larger nanoparticle films are appropriate for testing the effects due to the presence of the respective metals at the interface of the hematite and the conductive substrate without plasmonic resonance involved.

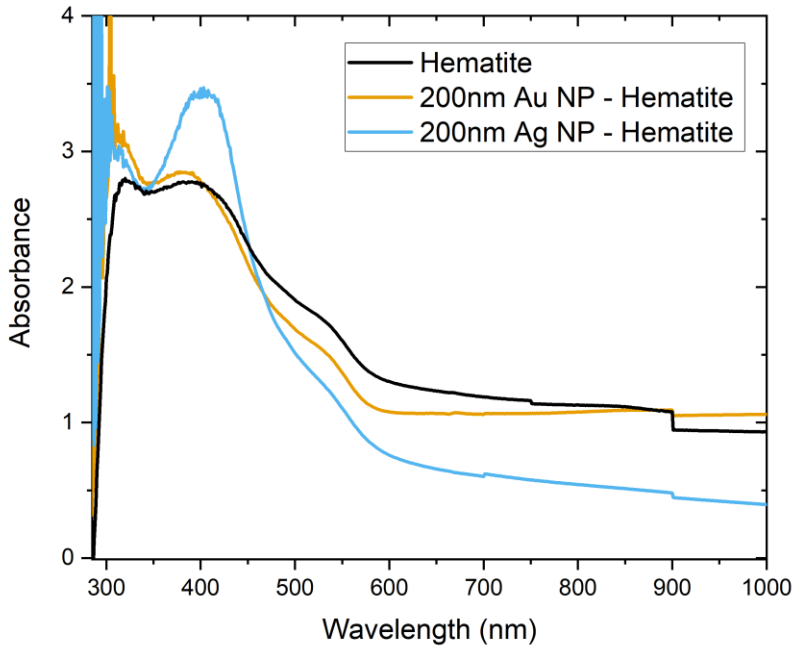

Figure 7-19 – UV-Vis spectra for the Au and Ag 200nm side length triangle array decorated hematite electrodes.

Figure 7-19 shows the absorbance spectra for the undecorated hematite film and completed larger nanoparticle decorated electrodes with the electrodeposited hematite film. The 200nm Au nanoparticle decorated films shows an absorption spectrum very similar to that of the undecorated hematite film. This is not surprising considering the low absorbance shown from the underlying Au nanoparticle film shown by figure 7-18.

The 200nm nanoparticle Ag decorated hematite spectrum shows the same enhanced absorption peak at around 400nm shown in the 80nm Ag nanoparticle decorated films. This result verifies that the effect seen at 400nm is due to the presence of Ag metal at the interface and not down to plasmonic effects. The enhancement of the 400nm peak in the hematite absorption due to the presence of Ag is clearly down to an interface mechanism. The most likely cause is that the charge transfer occurring when the metal and

semiconductor reach thermal equilibrium in contact is boosting the available energy states at this energy. As the electrons pass from the metal Fermi level to the hematite, they occupy the low conduction band states, and increase the available states at the 400nm peak shown by the increase in absorbance at this point. These states are mainly at the metal/semiconductor interface and therefore do not contribute to the water oxidation occurring at the semiconductor/electrolyte interface.

7.5.2. Photoelectrochemistry

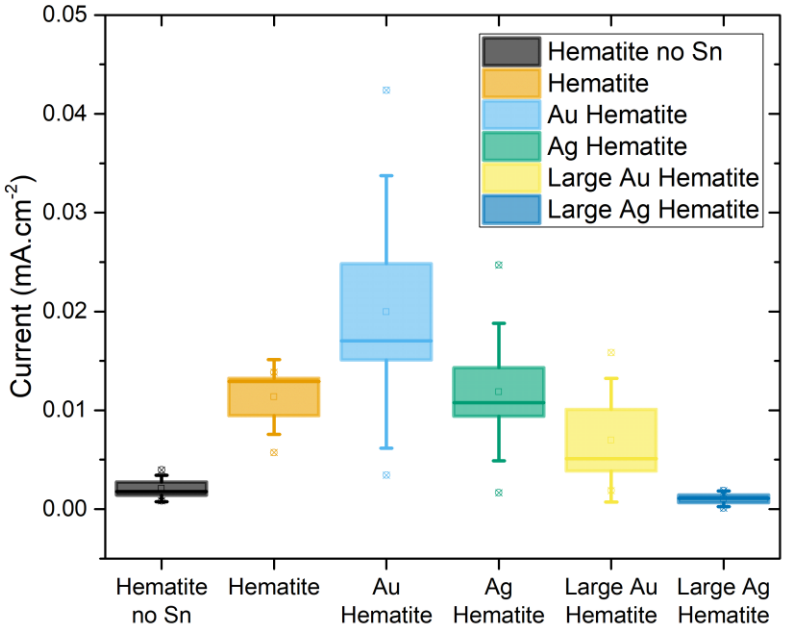

Figure 7-20 Photocurrent density boxplot showing photocurrent denisty values for the large 200nm metal nanoparticle decorated electrodeposited Sn-doped hematite samples.

Hematite electrodes decorated with larger nanoparticles were produced using the same electrodeposition technique and tested in the same manner as before. Figure 7-20 shows the photocurrent density boxplot including the larger nanoparticle films. When compared to the standard hematite electrodes the larger NP decorated electrodes performed worse for both Ag and Au. The average photocurrents were (7±3) $\mu A.cm^{-2}$ and (1±0.4) $\mu A.cm^{-2}$ for the

200nm Au and Ag nanoparticle decorated hematite samples respectively, compared to (11±2) $\mu A.cm^{-2}$ for the undecorated films. In the event that gold doping was responsible for the increased photocurrents observed it would be expected that an increase in gold at the back-surface would lead to an increased doping and therefore a higher photoresponse. However, this was not observed as shown by the low photocurrent densities in figure 7-20, and therefore the positive enhancement effects seen for the Au samples are likely due to some plasmonic mechanism most likely to be resonant energy transfer or hot-carrier injection into the film. Hot electrons can be extracted from the back contact with hot holes being injected into the semiconductor film and participating the oxygen evolution reaction at the interface. The spread of the photocurrents in the Au decorated Hematite electrodes was fairly large, having a percentage error on the mean of 43%, with the champion electrode performing better than the average for the undecorated films at $16\mu A.cm^{-2}$. This variation shows an inconsistency in the film fabrication and therefore operation. The average photocurrent density for the 200nm Au nanostructure decorated electrodes is lower than that of the undecorated electrodes but is statistically consistent with the value. The slight decrease in average photocurrent is then likely due to parasitic absorption from the underlying Au film that does not contributes to the photocatalytic ability of the overall film. From the band alignment diagrams the inclusion of Au at the interface poses little effect on the extraction of electrons compared to the ITO only configuration. Therefore, the inclusion of gold is not expected to impose a potential barrier at the back contact that would detrimentally affect the device.

The decreased average photocurrent densities for these larger nanoparticle samples gives evidence to the hypothesis that the negative effects from the inclusion of the nanoparticle films are due to the presence of metal at the back contact. The reason for the reduced photocurrent could be down to a parasitic absorption, scattering or reflection at the back

surface reducing the light incident on the actual hematite layer, or some semiconductor/metal interface mechanism causing recombination.

The ~200nm Ag nanostructure decorated films were all less photoresponsive than the undecorated films with a small data spread showing that the inclusion of the nanostructure layer was completely detrimental to the photoactivity of the electrodes. The average photocurrent density was (1±0.4)μA.cm^{-2} compared to (12±2)μA.cm^{-2} for the 80nm Ag nanostructure decorated electrodes and (11±2)μA.cm^{-2} for the undecorated electrodes. From the UV-Vis it is clear that the same effect that was seen in the previous Ag containing electrodes is occurring here to boost the absorption at the 400nm peak despite the fact that no strong LSPR peak is seen in the Ag nanoarray substrate absorbance. This result demonstrates that the presence of silver at the back contact reduces the photocatalytic ability of the hematite electrode. A discussed previously this is likely due to the large charge transfer expected from the band alignment diagrams creating a large accumulation region that blocks electron extraction due to charge repulsion and the occupancy of the low-level conduction band states blocking incident photon absorption at the absorption onset. This increases the peak absorption of the hematite but mainly at the interface, where photoexcited holes cannot contribute to the water oxidation. The fact that the average photocurrent density is lower here than in the 80nm plasmonic Ag samples suggests that previously there were plasmonic mechanisms enhancing the photoactivity but were only breaking even.

Aluminium layers were not tested as no possible enhancement was seen in the 80nm triangle incidence. The Aluminium nanostructure arrays were also more difficult to produce due to the necessity of high vacuum electron beam evaporation compared to resistive thermal evaporation and as such this architecture was omitted.

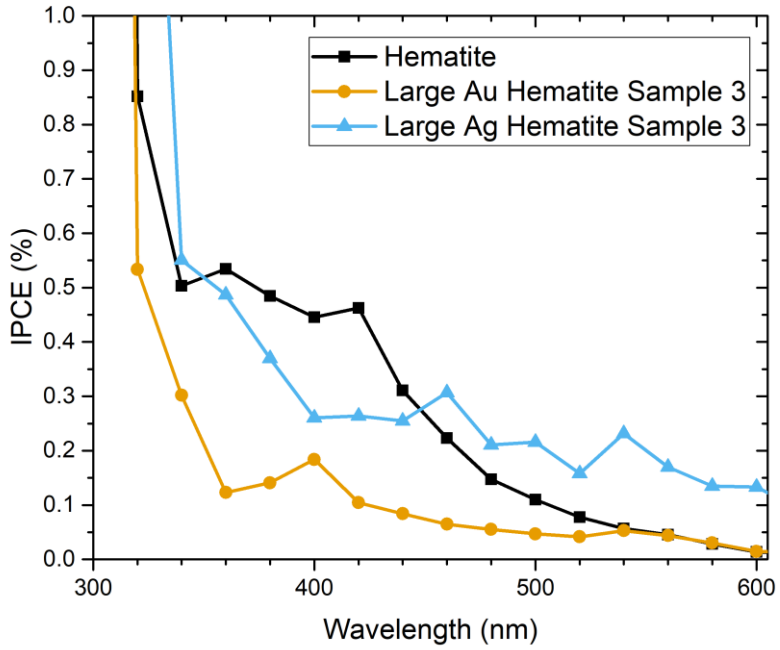

Figure 7-21 IPCE spectra for the undecorated hematite and the large 200nm metal nanoparticle decorated electrodeposited hematite samples.

Incident-photon to electron conversion efficiency measurements were also performed on the larger nanotriangle decorated hematite electrodes. The IPCE spectra are shown in figure 4-21. The large Au nanotriangle decorated hematite electrode (yellow line) shows a reduced IPCE across the 320-540nm range. This agrees with the reduced photocurrent densities shown in figure 7-20. This result shows that the photocurrent quenching is due to an effect on the absorption of the hematite layer in the 320-540nm section of the incident light spectrum. The UV-Vis for the large Au triangle arrays shows very little absorption in this range suggesting that the mechanism is based on the presence of gold at the back contact rather than parasitic absorption. This strengthens the hypothesis that charge accumulation at the gold/hematite interface is reducing the charge extraction efficiency and therefore reducing the IPCE.

The IPCE spectrum for the large Ag nanotriangles (blue line) is also shown in figure 7-21. The spectral shape is flat across the 400nm-600nm range. Compared to the hematite IPCE (black line) the Ag nanotriangle show efficiency quenching in the 360-440nm region and then enhancement in the >440nm range. This is not in agreement with the photocurrent density measurements shown in figure 7-20 from which it would be expected that these samples performed very poorly in IPCE measurements. This result is likely to be some scaling error due to an issue with the technique as the tested electrode was measured again in chronoamperometry and still showed little to no photocurrent, ideally the IPCE data would be retaken for this electrode. Under the assumption that there is a scaling error in the IPCE spectrum the flat line-shape is still indicative of a quenching mechanism occurring as the spectrum does not follow the typical shapes shown in the hematite IPCE.

7.6. Addition of TiO_2 Capping Layer

Despite the increased spectral overlap between the LSPR and Hematite absorption for the Ag decorated substrates compared to the Au decorated substrates, the photocurrent densities show no enhancement with respect to undecorated electrodes. In addition to this the IPCE spectrum shows quenching in the spectral region where the absorption enhancement occurs from the UV-Vis spectroscopy. This reduction in photocatalytic ability has been shown to be instigated by the contact between Ag and hematite. From the band alignments it is assumed that the charge transfer under thermal equilibrium creates an environment that is unconducive for photocatalysis.

Here TiO_2 was chosen as a hole-blocking layer in order to selectively block holes from extraction at the back contact and to promote electron extraction from the hematite semiconductor layer. The valence band position of the TiO_2 can also allow for hot-holes to migrate from the plasmonic metal layer into the semiconductor film. With a sufficient barrier

from the metal Fermi-level to the TiO_2 conduction band the CB position could selectively block hot-electron injection into the hematite. It was also chosen due to the ease of fabrication through RF-sputtering and its ability to adhere to metal nanostructures. 3nm of TiO_2 was sputtered from a TiO_2 target under argon through the bead mask after the metal nanostructures had been fabricated. The bead mask was then removed through sonication. The high-band gap of TiO_2 and the nanoscale thickness of the layer deposited meant that changes in the UV-Vis spectra before hematite deposition, with and without the buffer layer, were not observed.

Sputtering TiO_2 onto the decorated substrates after removal of the bead mask resulted in a complete layer passivating the conductive ITO and making the hematite electrodeposition process impossible. Therefore, the intermittent layer was deposited whilst the polystyrene bead mask was still in place.

7.6.1. Band Alignment Diagrams

In order to understand and explain the effects expected by the inclusion of the TiO_2 layers band alignment diagrams were produced. These diagrams are shown in figures 7-22 and 7-23. As before the top image in each figure shows the Fermi levels and band positions in isolation. The bottom picture gives the configurations in thermal isolation where the Fermi levels are matched and band bending shown. Fermi levels and band positions were taken from the literature.[30,31,33,38]

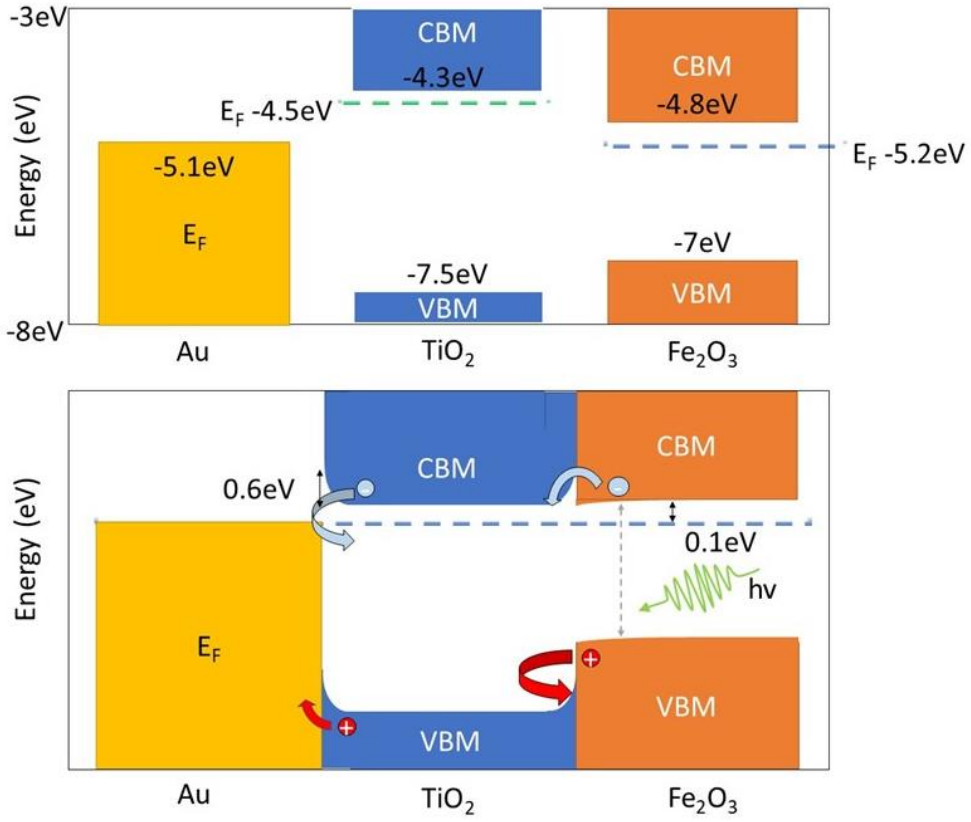

Figure 7-22 – Band alignment diagram for the Au-TiO_2-Hematite configuration. Top image shows band and Fermi-level positions for each material in Isolation. Bottom image shows band-bending and positions in thermal equilibrium.

Figure 7-22 shows the band alignment diagram for the Au-TiO_2-Fe_2O_3 configuration. In thermal equilibrium a Schottky barrier is expected at the Au-TiO_2 interface. Without the TiO_2 layer the barrier was theorised to be around 0.2eV with the band bending down however here the TiO_2 conduction band is expected to bend upwards forming a 0.6 eV Schottky barrier. This will lead to less efficient electron extraction compared to the Au- Fe_2O_3 configuration. Due to the upwards band bending holes will accumulate at the interface, this could lead to hole extraction or loss at the interface as they are quickly scavenged by Au conduction electrons. As the water oxidation half reaction is hole driven the ideal situation would lead to hole reflection at the interface but this is not the case here. In thermal equilibrium the TiO_2 and Fe_2O_3 conduction band minima are well matched and with the low downward band bending in the hematite this should lead to good electron transport across

the interface. Efficient electron extraction helps to reduce recombination in the hematite. The TiO_2 valence band maximum sits well below the hematite VBM which would lead to hole blocking at the interface allowing holes to migrate to the surface and participate in water oxidation. The band bending of the hematite at the interface assists this by forming an area slightly deficient in holes due to electron accumulation meaning holes are more likely to drift towards the surface. The positive effect of good hole blocking by the TiO_2 on the photocatalytic ability of the hematite electrode could be somewhat outweighed by the poor electron extraction at the interface.

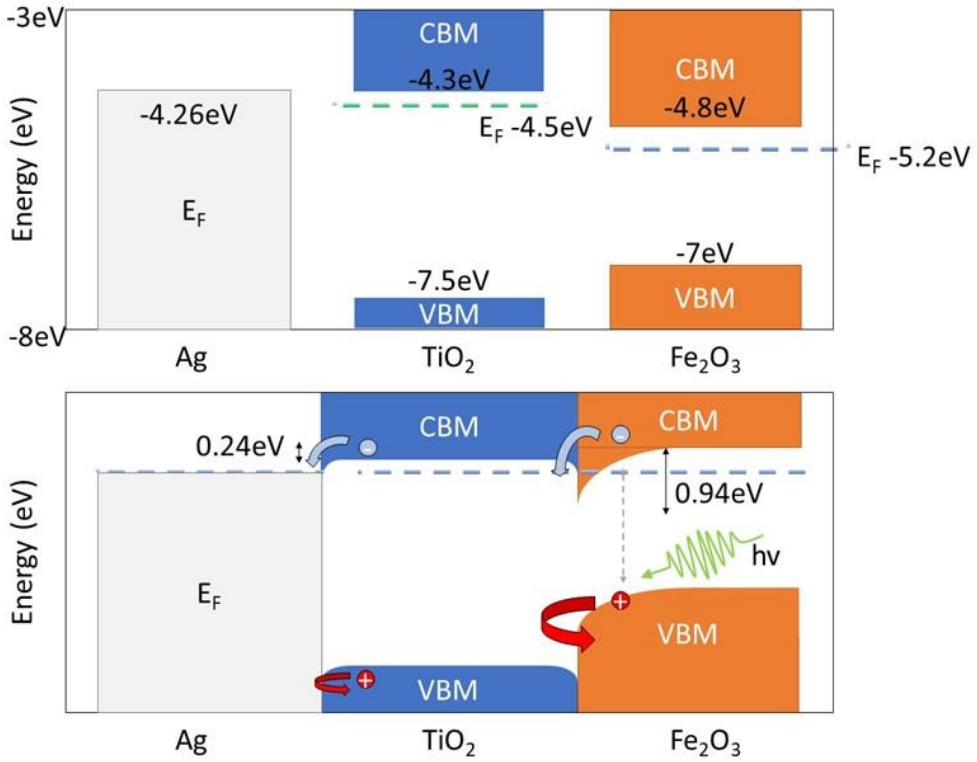

Figure 7-23 - Band alignment diagram for the Au-TiO_2-Hematite configuration. Top image shows band and Fermi-level positions for each material in Isolation. Bottom image shows band-bending and positions in thermal equilibrium.

Figure 7-23 gives the band alignment diagram for the Ag-TiO_2-Fe_2O_3 configuration. In thermal equilibrium the TiO_2 conduction band undergoes slight band bending downwards as charges transfer from metal to semiconductor to match the Fermi levels. Once the Fermi levels are matched there is good contact between the TiO_2 and Ag with only a very small Schottky

junction and only very slight downwards band bending. This small junction allows electrons to be extracted very efficiently at the back contact. The downwards band bending of the valance band results in a hole deficient region which could reduce the probability of holes being scavenged at the interface by Ag conduction band electrons. As before, the TiO_2 and Fe_2O_3 conduction bands are in good alignment for electron transport however, in the Ag substrate case the hematite bands undergo much more severe bending at the interface. Charge transport to the hematite causes a large electron accumulation region at the interface which will generate a depletion region within the TiO_2 resulting in a built-in voltage at the interface. This built-in voltage would somewhat hinder electron transport out of the hematite layer and may result in a higher catalytic onset potential in order to overcome the depletion region, or some increased recombination as the electron mobility is reduced.

Compared to the Ag-Fe_2O_3 tested previously the Ag-TiO_2-Fe_2O_3 is expected to have far superior electron extraction due to the much smaller potential barrier at the interface. This combined with successful hole blocking is expected to increase the photocurrent density measured compared to the Ag-Fe_2O_3. From the band diagrams it is clear that TiO_2 should act as a charge selective blocking layer especially in the case of an Ag substrate.

7.6.2. Optical Spectroscopy

As previously the electrodes were characterised using optical spectroscopy, the absorbance for the nanostructure decorated samples hematite deposited samples are shown in figure 7-24 and 7-25, respectively.

From figure 7-24 it is clear that the addition of TiO_2 has not drastically shifted the position of the LSPR peaks. The peaks, however, appear to have been damped given by the difference in absorbance at the peaks. This could be due to differences in the dielectric environment of the nanoparticles as the oscillations of electrons are damped through resonant energy transfer to the TiO_2 layer that is now present. There is no noticeable absorption onset for the

TiO_2 layer which would occur in the UV section of the spectrum. This was expected due to the thin and selective deposition of the TiO_2 directly onto the nanostructures through the bead mask.

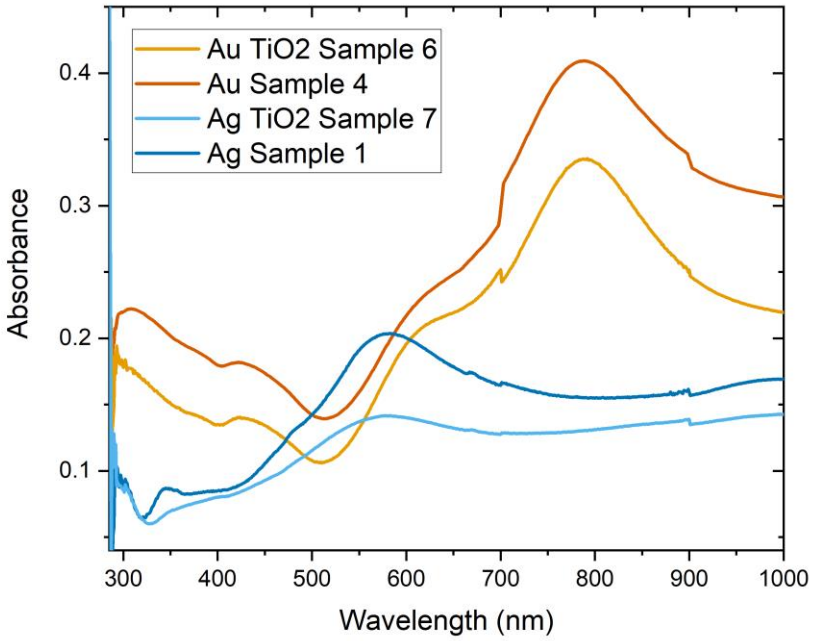

Figure 7-24 - UV-Vis spectra for the Au-, Ag-, Au-TiO_2, and Ag-TiO_2 nanostructures on the ITO substrate.

Figure 7-25 shows the absorbance spectra for the completed electrodes along with a hematite reference. The Au-TiO_2-hematite absorbance spectrum gives a similar absorbance maximum to the Au-hematite spectrum when the y-axis offset is taken into account. This y-axis offset is present due to the underlying absorption through scattering of the ITO substrate. As discussed previously, under annealing the ITO substrate becomes turbid and this cloudiness is manifested as a consistent absorbance across the visible spectrum. Differences in ITO turbidity accounts for the differences in y-axis offsets for each of the tested samples. The hematite absorption features, including the shoulder at ~450nm and the peak at 400nm, are more clearly observed in the Au- TiO_2-hematite sample. This is likely due to a

slightly better hematite film in this sample compared to the sample tested for Au-hematite and is a product of the electrodeposition method. The fact that the peak absorbance is consistent shows a consistent hematite film thickness between the Au-TiO_2-hematite and the Au-hematite. A slight peak at 650nm is visible in the spectrum which would align with the onset for the Au LSPR peak at ~600nm from figure 7-25.

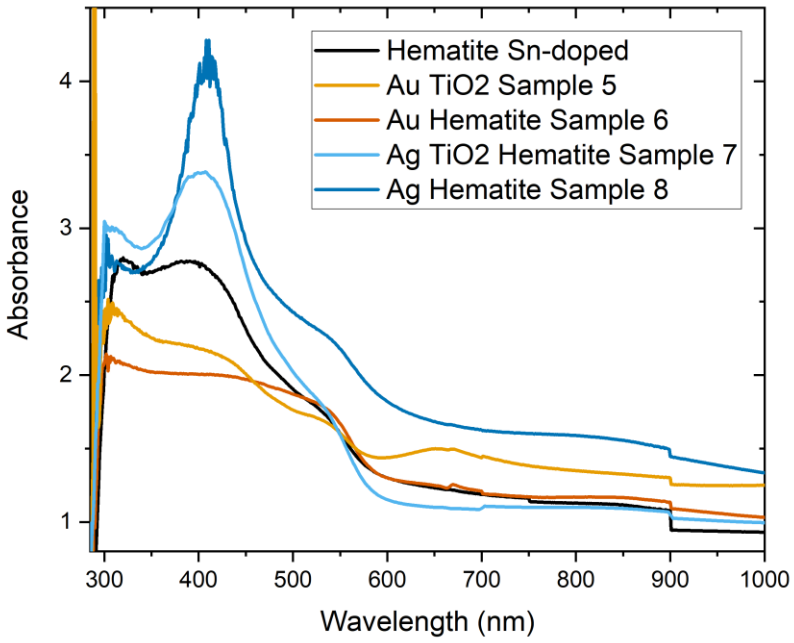

Figure 7-25 - UV-Vis spectra for the the Au-, Ag-, Au-TiO_2-, and Ag-TiO_2-hematite electrode configurations.

The Ag-TiO_2-hematite spectrum shows similar characteristics to the previous Ag containing electrodes with the enhanced peak at 400nm still present. The absorbance gives a similar level to the Ag-hematite spectrum when the y-axis offset is taken into account. From the band diagrams discussed above a charge transfer to the hematite, and therefore the enhancement of the 400nm peak, is expected. However, in this case the charge transfer will result in slight depletion region in the TiO_2 rather than accumulation at the metal/semiconductor interface. This depletion region should aid the production of photoexcited charge carriers and aid photocatalysis.

7.6.3. Photoelectrochemistry

The Metal-TiO_2-Hematite electrodes were then tested using the same photoelectrochemical experiments described for the previous samples.

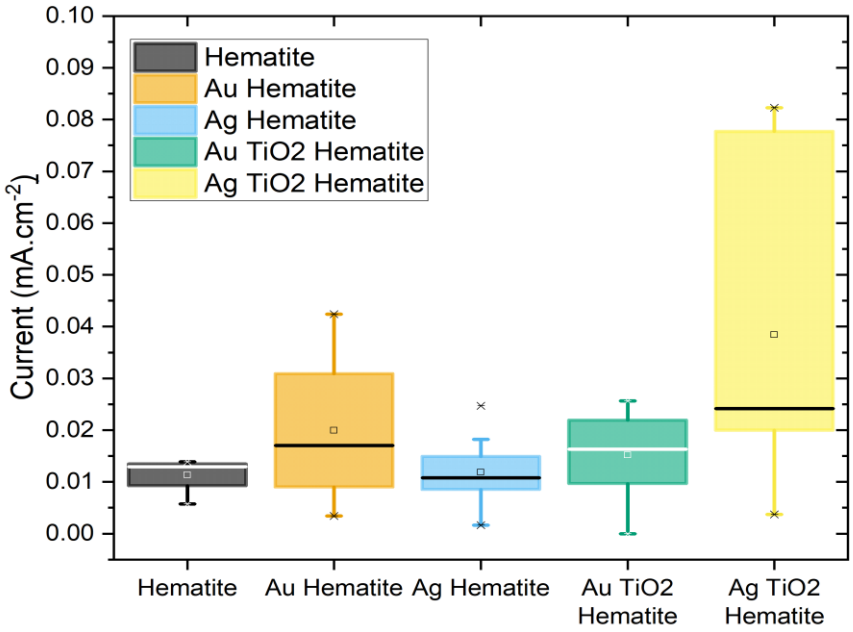

Figure 7-26 - Photocurrent density boxplots including the TiO_2 capped metal nanoparticle samples. 8 samples were used for each configuration. Au/TiO_2/Hematite composites and Au/Hematite show similar average values for photocurrent density. Ag/TiO_2/Hematite composites show enhancement in photocurrent densities compared to the standard hematite films.

The box-plots for these new samples are shown along with the uncapped and standard hematite electrodes in figure 7-26. The Au-TiO_2-Hematite electrodes showed a mean photoresponse of (15±3)µA.cm^{-2}, this value is higher than the undecorated Sn-doped hematite electrodes showing the enhancement still occurs. The mean photocurrent density value is lower than the (20±5)µA.cm^{-2} value given by the Au-hematite electrodes but they are consistent within the uncertainty. The spread of the data was lower than the Au-Hematite electrodes; however, the champion electrodes did not compete with the best uncapped samples. This would suggest that the TiO_2 intermittent layer has little effect on the

mechanism by which the Au nanostructures are affecting the photocatalytic ability of the hematite.

The Ag-TiO_2-Hematite electrodes produced, on average, a higher photoresponse than seen in all other cases, with champion electrodes showing a photocurrent density of 82.3 $\mu A.cm^{-2}$ showing nearly a 7.5x increase on the average for standard hematite electrodes and out-performing the previous champion Au-hematite electrode by almost double. The mean photoresponse for these electrodes was (40±10)$\mu A.cm^{-2}$, compared to (12±2)$\mu A.cm^{-2}$ for the Ag-Hematite electrodes and (11±2)$\mu A.cm^{-2}$ for the undecorated hematite electrodes. This gives an average photocurrent density enhancement of 3.6 times compared to the undecorated films.

The increase in enhancement here shows that the inclusion of the intermittent layer is effective in reducing recombination at the metal/semiconductor interface for Ag and also gives insight into the mechanism by which the Ag-hematite samples are quenched. The intermittent layer is effectively blocking recombination at the interface by reflecting holes back and by reducing unwanted hot electron injection into the hematite films. The buffer layer allows for the light scattering to effectively increase incident light absorption and promote exciton creation. It is now clear that parasitic absorption is not a main contributing factor as this would still be present with the inclusion of TiO_2.The broad spread of these results could be due to the sputter process in which the TiO_2 was deposited, better coverage over the nanoparticles could result in better performing electrodes, and those worse performing electrodes could have spotty or incomplete coverage. This could be down to shadowing from the sample holder in the sputter chamber or poor adhesion.

For both Au-TiO_2 and Ag-TiO_2 there were still outlying electrodes that failed to function properly showing low and almost zero photoresponses again highlighting the potential for

improvement in the reproducibility of this fabrication method. Although the success rate of above 0.75 is still high enough to validate the viability of the study.

As before, IPCE measurements were done in order to evaluate any spectral differences in the photoresponse from the films. The IPCE spectra are shown in figure 7-27. Both Au-TiO_2 and Ag-TiO_2 IPCE curves show an enhancement in IPCE across the spectral range which agrees with the resultant photocurrents discussed previously. However, the shapes are different.

For Au-TiO_2 in the range <420nm the shape of the curve is similar to the undecorated hematite films but with a higher conversion efficiency, however there is a small increase in conversion efficiency at 500nm which coincides with the SPP transmission in the gold absorption spectra and the beginning of the LSPR peak shown in the spectra.

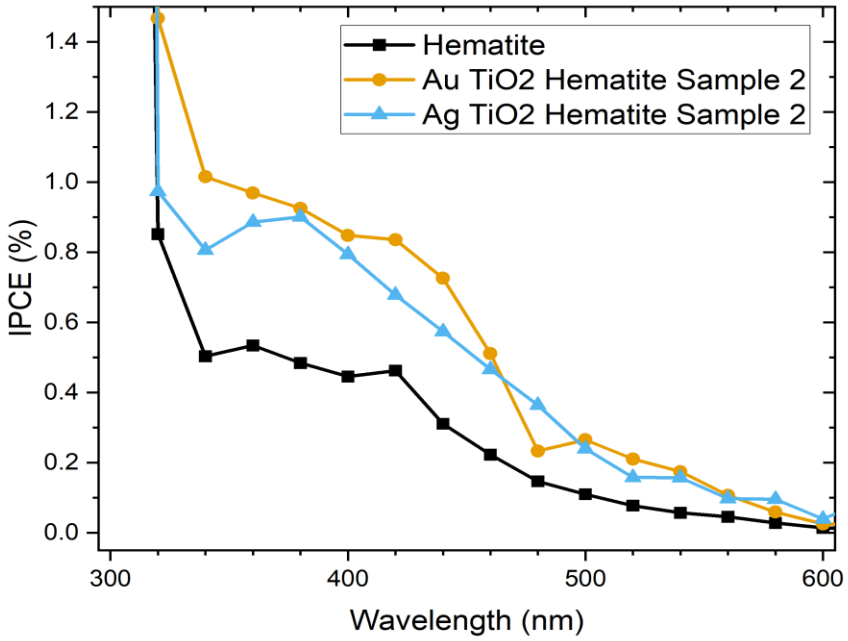

Figure 7-27 – IPCE spectra for the Au-TiO_2-, and Ag-TiO_2-hematite electrodes. The hematite IPCE measured previously is displayed as reference. Efficiency enhancement is seen across the 320nm-600nm range for both Au/TiO_2 and Ag/TiO_2.

The IPCE spectrum for the Ag-TiO_2 when compared to the hematite reference shows some enhancement above 420nm as the curve does not show as steep a drop-off in conversion efficiency as the others show. This region of enhancement aligns with the onset of the LSPR peak Ag absorbance spectrum.

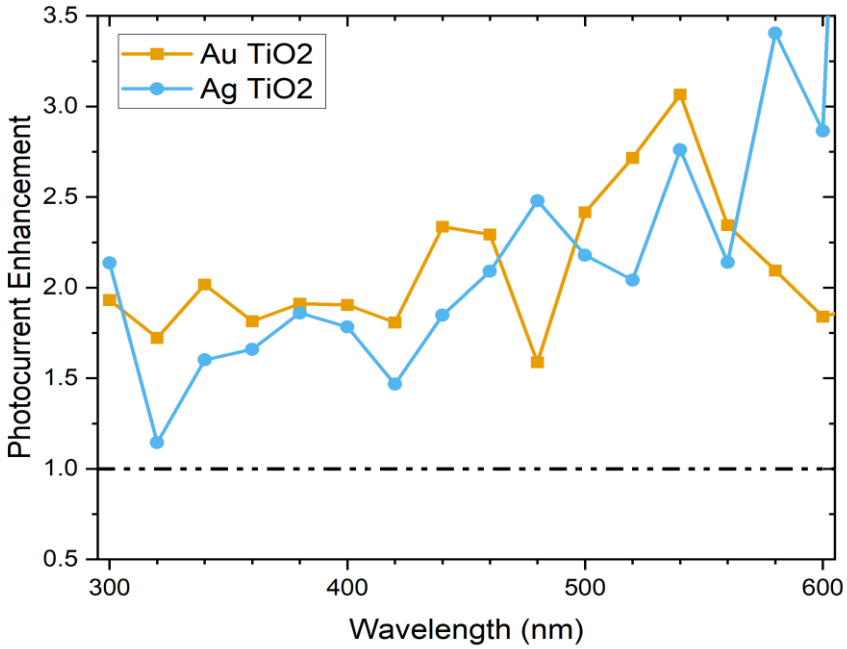

Figure 7-28 - Photocurrent enhancement spectra for the TiO_2 capped nanoparticle samples. This shows the photocurrent enhancement seen across the 300-600 nm range for both the TiO_2 capped nanostructures compared to undecorated hematite electrode.

These effects are more clearly revealed if the plasmonic metal sample spectrum is divided by hematite reference IPCE spectrum, the resultant spectrum is called an enhancement spectrum. In figure 7-28 it is clear that the Au-TiO_2 shows an enhancement across the hematite absorption region but also shows a peak increase at 500nm showing an enhancement in this region that matches the LSPR peak whereas the Ag-TiO_2 line shows that the enhanced IPCE above 420nm is real.

The IPCE spectra show an enhancement in the spectral region expected for each of the plasmonic nanostructures. This enhancement shown indicates that the plasmonic

nanostructures underneath are contributing to the photoresponses of the fabricated electrodes.

The broad spread of the photoresponses achieved for both the Au and Ag decorated electrodes is likely due to inconsistencies in the quality of the TiO2 films fabricated through the sputtering process. Sputtering material through the small apertures in the bead mask is likely to result in inconsistent coverage of the nanostructures on the substrate which would not completely reduce the effects of charge recombination at the metal/semiconductor interface. This is particularly evident from the Ag decorated which saw the largest spread of results in photocurrents. Previously the inclusion of the Ag nanostructered layer was detrimental to the photocatalytic ability of the hematite electrodes, whereas when a TiO_2 passivation layer was employed the Ag decorated samples showed some of the highest photoresponses of all the electrodeposited hematite electrodes. This indicates that a properly passivated Ag decorated electrode has the desired effect on the photoresponse.

7.7. Conclusions

An electrodeposition technique for tin-doped, nanostructured, photoactive hematite was developed through adaptation from Zandi et al[1]. Films were electrodeposited onto ITO coated glass substrates at a potential of 0 V vs an Ag/AgCl reference electrode with a platinum foil counter electrode. The electrolyte constituted of an aqueous solution of 8M NH4Cl, 0.02M FeCl2, and 0.008M SnCl2. The electrodeposition method was achieved using chronocoulommetry set to 130mC. The pristine hematite films were shown to be photoactive through PEC measurements, with a mean photocurrent of (11±2) $\mu A.cm^{-2}$ under broadband illumination from a Xe lamp. The thickness of the films was measured using contact-AFM and a scratching method to remove material. The profile of the edge created

at the scratch was imaged and the height was measured using Gwyddion SPM data analysing software. The average film thickness was measured at (415±8) nm.

This electrodeposition method was then used to fabricate electrodes with plasmonic nanostructure arrays at the substrate. The plasmonic nanostructures using Au, Ag and Al, were first produced on the blank ITO coated substrates using nanosphere shadow lithography. The electrodeposition method was then used to deposit hematite films onto the samples. The samples were characterised using UV-Vis spectroscopy and the effects of the plasmonic nanostructures on the hematite were studied using PEC methods.

Under chopped broadband illumination chronoamperometry the gold nanostructure decorated hematite films showed an average photocurrent of (20±5)μAcm^{-2} with champion electrodes reaching 42.4μAcm^{-2}. Giving an average photocurrent enhancement by a factor of 2, with champion electrodes enhanced by up to 4 times compared to the control hematite samples.

To reduce any recombination of hot-carriers that were inhibiting the electrode performance an interlayer of TiO_2 was added between the metal and the hematite through RF-sputtering. This layer should act as a carrier selective blocking layer for the hematite and also reduce the charge transfer at the metal-semiconductor interface. A 3nm layer of TiO_2 was sputtered through the bead mask after the metal deposition in order to coat the nanostructures but leave the ITO substrate uncovered. It was necessary to make sure that the ITO was left uncovered for the most part as it would not be possible to perform the electrodeposition onto TiO_2. These samples were also characterised using UV-Vis spectroscopy and tested using the same PEC methods used previously.

The Ag-TiO_2 hematite samples gave an average photocurrent of (40±10) $\mu A.cm^{-2}$ with the champion device having a photocurrent of 82μAcm^{-2}, far out-preforming any of the

previous electrodeposited electrodes. This gave an average enhancement factor of 3.6 and champion enhancement factor of 7.5. The introduction of the TiO_2 interlayer to the silver decorated electrodes clearly assisted in blocking the negative effect of the charge transfer and successfully acted as a carrier selective blocking layer assisting the photocatalytic ability enhancement.

The IPCE spectrum for the Ag-TiO_2-hematite electrode shows a vastly different picture to Ag-hematite spectrum given previously. This electrode shows a higher photocurrent across the hematite absorption range when compared to the pristine hematite IPCE, which, when compared to the Ag-hematite which showed quenching of the photocurrent along this spectral range, suggests that the TiO_2 interlayer has assisted in enhancing the photocatalytic ability. The enhancement spectra for the Au-TiO_2-hematite and Ag-TiO_2-hematite electrodes show enhancement across the spectral range for both samples.

7.8. Bibliography

1. Zandi, O., Schon, A. R., Hajibabaei, H. & Hamann, T. W. Enhanced Charge Separation and Collection in High-Performance Electrodeposited Hematite Films. *Chem. Mater.* **28**, 765–771 (2016).

2. Ling, Y., Wang, G., Wheeler, D. A., Zhang, J. Z. & Li, Y. Sn-doped hematite nanostructures for photoelectrochemical water splitting. *Nano Lett.* **11**, 2119–2125 (2011).

3. Yang, Y., Forster, M., Ling, Y., Wang, G., Zhai, T., Tong, Y., Cowan, A. J. & Li, Y. Acid Treatment Enables Suppression of Electron-Hole Recombination in Hematite for Photoelectrochemical Water Splitting. *Angew. Chemie Int. Ed.* **55**, 3403–3407 (2016).

4. Yang, J., Bao, C., Yu, T., Hu, Y., Luo, W., Zhu, W., Fu, G., Li, Z., Gao, H., Li, F. & Zou, Z. Enhanced performance of photoelectrochemical water splitting with ITO@α-Fe2O3 core-shell nanowire array as photoanode. *ACS Appl. Mater. Interfaces* **7**, 26482–26490 (2015).

5. Meng, Q., Wang, Z., Chai, X., Weng, Z., Ding, R. & Dong, L. Fabrication of hematite (α-Fe2O3) nanoparticles using electrochemical deposition. *Appl. Surf. Sci.* **368**, 303–308 (2016).

6. Cai, J., Li, S., Li, Z., Wang, J., Ren, Y. & Qin, G. Electrodeposition of Sn-doped hollow α-Fe2O3 nanostructures for photoelectrochemical water splitting. *J. Alloys Compd.* **574**, 421–426 (2013).

7. Ahn, H.-J., Kwak, M.-J., Lee, J.-S., Yoon, K.-Y. & Jang, J.-H. Nanoporous hematite structures to overcome short diffusion lengths in water splitting. *J. Mater. Chem. A* **2**, 19999–20003 (2014).

8. Spray, R. L. & Choi, K. S. Photoactivity of transparent nanocrystalline Fe2O3 electrodes prepared via anodic electrodeposition. *Chem. Mater.* **21**, 3701–3709 (2009).

9. Cohen, M. & Markovac, V. The Anodic Deposition of Iron Oxide Films on Platinum. *J. Electrochem. Soc.* **114**, 678–681 (1967).

10. Hisatomi, T., Dotan, H., Stefik, M., Sivula, K., Rothschild, A., Grätzel, M. & Mathews, N. Enhancement in the Performance of Ultrathin Hematite Photoanode for Water Splitting by an Oxide Underlayer. *Adv. Mater.* **24**, 2699–2702 (2012).

11. Steier, L., Luo, J., Schreier, M., Mayer, M. T., Sajavaara, T. & Grätzel, M. Low-Temperature Atomic Layer Deposition of Crystalline and Photoactive Ultrathin Hematite Films for Solar Water Splitting. *ACS Nano* **9**, 11775–11783 (2015).

12. Forster, M. Time-resolved spectroscopic studies of hematite photoelectrodes for photoelectrochemical water splitting. *University of Liverpool* (University of Liverpool, 2015).

13. Jiao, S., Xu, L., Hu, K., Li, J., Gao, S. & Xu, D. Morphological Control of α-FeOOH Nanostructures by Electrodeposition. *J. Phys. Chem. C* **114**, 269–273 (2010).

14. Markovac, V. & Cohen, M. The Anodic Deposition of Iron Oxide Films on Iron. *J. Electrochem. Soc.* **114**, 674 (1967).

15. Kawawaki, T., Nakagawa, T., Sakamoto, M. & Teranishi, T. Carrier-Selective Blocking Layer Synergistically Improves the Plasmonic Enhancement Effect. *J. Am. Chem. Soc.* **141**, 8402–8406 (2019).

16. Lei, Q., Chen, R., Tan, J., Long, X., Chen, H., Wang, X., Liu, J., Lei, Z. & Zhang, Z. Construction of a nanocavity structure with a carrier-selective layer for enhancement of photocatalytic hydrogen production performance. *Sustain. Energy Fuels* **4**, 2164–

2173 (2020).

17. García de Arquer, F. P., Mihi, A., Kufer, D. & Konstantatos, G. Photoelectric Energy Conversion of Plasmon-Generated Hot Carriers in Metal–Insulator–Semiconductor Structures. *ACS Nano* **7**, 3581–3588 (2013).

18. Hanske, C., Sanz-ortiz, M. N. & Liz-marzán, L. M. Silica-Coated Plasmonic Metal Nanoparticles in Action. **1707003**, 1–28 (2018).

19. Wu, K., Chen, Z., Lv, H., Zhu, H., Hill, C. L. & Lian, T. Hole removal rate limits photodriven H2 generation efficiency in CdS-Pt and CdSe/CdS-Pt semiconductor nanorod-metal tip heterostructures. *J. Am. Chem. Soc.* **136**, 7708–7716 (2014).

20. Amirav, L. & Alivisatos, A. P. Photocatalytic hydrogen production with tunable nanorod heterostructures. *J. Phys. Chem. Lett.* **1**, 1051–1054 (2010).

21. Sakamoto, M., Inoue, K., Saruyama, M., So, Y. G., Kimoto, K., Okano, M., Kanemitsu, Y. & Teranishi, T. Investigation on photo-induced charge separation in CdS/CdTe nanopencils. *Chem. Sci.* **5**, 3831–3835 (2014).

22. Prévot, M. S. & Sivula, K. Photoelectrochemical tandem cells for solar water splitting. *J. Phys. Chem. C* **117**, 17879–17893 (2013).

23. Valenti, M., Venugopal, A., Tordera, D., Jonsson, M. P., Biskos, G., Schmidt-Ott, A. & Smith, W. A. Hot Carrier Generation and Extraction of Plasmonic Alloy Nanoparticles. *ACS Photonics* **4**, 1146–1152 (2017).

24. Ling, Y. & Li, Y. Review of Sn-Doped Hematite Nanostructures for Photoelectrochemical Water Splitting. *Part. Part. Syst. Charact.* **31**, 1113–1121 (2014).

25. De Faria, D. L. A., Venâncio Silva, S. & De Oliveira, M. T. Raman microspectroscopy of

some iron oxides and oxyhydroxides. *J. Raman Spectrosc.* **28**, 873–878 (1997).

26. Marusak, L. A., Messier, R. & White, W. B. Optical absorption spectrum of hematite, αFe2O3 near IR to UV. *J. Phys. Chem. Solids* **41**, 981–984 (1980).

27. Bohn, C. D., Agrawal, A. K., Walter, E. C., Vaudin, M. D., Herzing, A. A., Haney, P. M., Talin, A. A. & Szalai, V. A. Effect of Tin Doping on α-Fe_2O_3 Photoanodes for Water Splitting. *J. Phys. Chem. C* **116**, 15290–15296 (2012).

28. Ramadurgam, S., Lin, T.-G. & Yang, C. Aluminum Plasmonics for Enhanced Visible Light Absorption and High Efficiency Water Splitting in Core–Multishell Nanowire Photoelectrodes with Ultrathin Hematite Shells. *Nano Lett.* **14**, 4517–4522 (2014).

29. Kittel, C. Introduction to Solid State Physics, 8th edition. *Wiley & Sons, New York, NY* (2004).

30. Tipler, Paul A.; Llewellyn, R. a. Modern Physics - Vol.2. in *Modern Physics Fifth Edition* (ed. Tipler, Paul A.; Llewellyn, R. a.) 196 (W. H. Freeman and Company, 2008).

31. Lohaus, C., Klein, A. & Jaegermann, W. Limitation of Fermi level shifts by polaron defect states in hematite photoelectrodes. *Nat. Commun.* **9**, 1–7 (2018).

32. Zhou, Y., Shim, J. W., Fuentes-Hernandez, C., Sharma, A., Knauer, K. A., Giordano, A. J., Marder, S. R. & Kippelen, B. Direct correlation between work function of indium-tin-oxide electrodes and solar cell performance influenced by ultraviolet irradiation and air exposure. *Phys. Chem. Chem. Phys.* **14**, 12014–12021 (2012).

33. Dweydari, A. W. & Mee, C. H. B. Work function measurements on (100) and (110) surfaces of silver. *Phys. status solidi* **27**, 223–230 (1975).

34. Michaelson, H. B. The work function of the elements and its periodicity. *J. Appl. Phys.* **48**, 4729–4733 (1977).

35. Fan, H. M., You, G. J., Li, Y., Zheng, Z., Tan, H. R., Shen, Z. X., Tang, S. H. & Feng, Y. P. Shape-controlled synthesis of single-crystalline Fe2O 3 hollow nanocrystals and their tunable optical properties. *J. Phys. Chem. C* **113**, 9928–9935 (2009).

36. Hayes, D., Hadt, R. G., Emery, J. D., Cordones, A. A., Martinson, A. B. F., Shelby, M. L., Fransted, K. A., Dahlberg, P. D., Hong, J., Zhang, X., Kong, Q., Schoenlein, R. W. & Chen, L. X. Electronic and nuclear contributions to time-resolved optical and X-ray absorption spectra of hematite and insights into photoelectrochemical performance. *Energy Environ. Sci.* **9**, 3754–3769 (2016).

37. Piccinin, S. The band structure and optical absorption of hematite (α-Fe2O3): A first-principles GW-BSE study. *Phys. Chem. Chem. Phys.* **21**, 2957–2967 (2019).

38. Kashiwaya, S., Morasch, J., Streibel, V., Toupance, T., Jaegermann, W. & Klein, A. The Work Function of TiO2. *Surfaces* **1**, 73–89 (2018).

8. The Effects of Various Metal Plasmonic Nanostructures on the Photocatalytic Properties of Atomic Layer Deposited Hematite.

8.1. Overview

In this chapter atomic layer deposition (ALD) was used to deposit hematite as a continuation to the previous chapter. Plasmonic nanostructured substrates fabricated using NSL were again used as the basis in order to observe any effects due to plasmonic mechanisms and understand possible enhancement of the photocatalytic ability of hematite. Hematite film thickness was measured using a scratching technique to remove an area of material and contact AFM to probe he profile shape and height. The ALD hematite film was shown to be (36±1) nm using this method. ALD deposition of photocatalytic hematite electrodes onto nanostructured substrates made using NSL have not been previously reported. The effects of plasmonic nanostructures on the photocatalytic ability of hematite deposited using ALD has not been previously reported either.

An additional set of electrodes were produced where dielectric alumina interlayers were introduced in order to decouple hot-carrier mechanisms and light-scattering effects from the plasmonic substrates. This was done in an attempt to observe and further understand the plasmonic mechanisms and their enhancement effects. Alumina layers of ~3nm thick were deposited using ALD onto the nanostructures prior to the hematite deposition.

The ALD process was developed by Natalie Bavis in Richard Potter's group from the Department of Engineering at The University of Liverpool. Both these procedures were previously outlined in the experimental methods section. The hematite electrodes were characterised through UV-Vis-NIR and Raman spectroscopy. Electrode performance was analysed through the photoelectrochemical methods of linear sweep voltammetry, chronoamperometry, and incident photon to current efficiency (IPCE).

In this chapter six different architectures of nanostructured hematite-based photoanodes were fabricated along with control samples that did not have the plasmonic metal layers. Schematics of the nanostructure inclusive samples are shown in figure 8-1. These samples were characterised and tested using optical spectroscopy and photoelectrochemical measurements in both as-deposited state and after a 30-minute 600^0C anneal in air conditions using a box furnace. As before the photoelectrochemical experiments were performed in a three-electrode cell using 1M NaOH as the electrolyte, with the hematite electrodes as the working electrode, a Pt-foil counter electrode, and a homemade Ag/AgCl reference electrode.

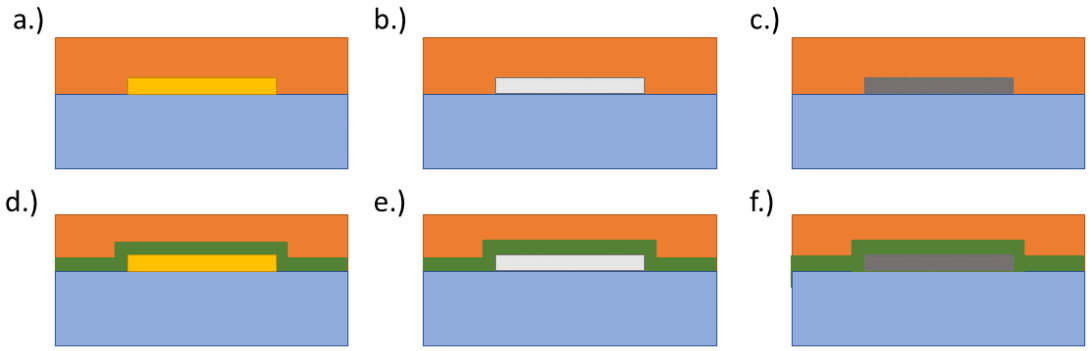

Figure 8-1 – Schematic showing the samples made in this chapter. A.) ALD hematite (ORANGE) deposited onto Au nanostructures (YELLOW) on ITO-coated glass slides (LIGHT BLUE). B.) ALD hematite deposited onto Ag nanostructures (SILVER) on ITO-coated glass slides. C.) ALD hematite deposited onto Al nanostructures (DARK GREY) on ITO-coated glass slides.

D.) Au nanostructured substrates with an alumina (Al_2O_3) interlayer (GREEN) and the ALD hematite deposited on top. Referred to as AHG (Alumina-Hematite-Gold) at times for brevity. E.) Ag nanostructured substrates with an alumina (Al_2O_3) interlayer and the ALD hematite deposited on top. Referred to as AHS (Alumina-Hematite-Silver) at times for brevity. F.) Al nanostructured substrates with an alumina (Al_2O_3) interlayer and the ALD hematite deposited on top. Referred to as AHA(Alumina-Hematite-Aluminium) at times for brevity.

8.2. Introduction

8.2.1. Atomic layer Deposition of Hematite Electrodes

Atomic-Layer Deposition (ALD) is a process by which monolayers of a precursor are deposited and subsequently oxidised in order to build up a uniform, conformal film of controlled thicknesses of a material.[1–7] This is done in a vacuum reaction chamber, usually at

temperatures of around 400-600^{o}C. Generally, the precursors are injected into the chamber, coating the substrates, the chamber is then purged so that the excess precursor is removed and the vacuum is returned before the sample is oxidised. After the oxidation the chamber is purged again before the cycle repeats, growing the films layer by layer. Each of these cycles is self-limiting ensuring that the growth is layer-by-layer and resulting in conformal films over large surface-areas with a high-level control over the thickness.[4,7–10] Film thicknesses can be closely controlled by the number of these cycles that are performed and produced well-defined thin-films on high aspect ratio substrates.[6–8,11] The ALD process is described in terms of cycles, in a general procedure the cycle is made up of a precursor pulse into the chamber, an exposure time, or dwell step, to allow the layers to form, before purging of the chamber,. After that there is an oxidising pulse, such as ozone [4,10] or water[12], to oxidise the surface, and then another dwell step before purging the chamber again. The dwell steps are stages where nothing happens in order to allow the reactions occurring to complete before going on to the next step.

Semiconductor metal oxide films such as TiO_2 and ZnO have been well studied as photocatalytic water-splitting candidates to be deposited using atomic layer deposition. ALD deposited TiO_2 films are often used as coatings in photocatalytic heterostructures in order to prevent the absorbing layers from oxidising or corroding and improving the device chemical stability.[8,13,14] ALD of hematite has been performed using various Fe containing precursors such as ferrocene[9,10], $Fe(O^tBu)_6$[12], and $Fe(thd)_3$[15] and oxidisers such as ozone[4,10], water[12], and O^2 plasma[9].

In this work an O_2 plasma was used to oxidise ferrocene layers to form hematite in a process known as plasma-enhanced atomic layer deposition. This process was previously reported by Ramachandran et al.[9] in 2014. This technique allows for cooler deposition temperatures in the range of 150^{0}C to 350^{0}C which is important when depositing onto metal

nanostructured substrates. At temperatures above 350^0C gold nanostructures will begin to melt and the morphology will begin to change.[16] For the application in this chapter it was necessary to use a low temperature deposition technique to ensure minimal disruption to the nanostructured surface in order to maintain the plasmonic properties of the fabricated decorated substrates.

Ramachandran[9] observed direct deposition of crystalline hematite at deposition temperatures above 250^0C without the need for an additional calcination step.[9] This gives the possibility of the as-deposited films showing photoactivity in photoelectrochemical experiments for water-splitting. The lack of the additional thermal treatment would result in less deformation of the metal nanostructures underneath the hematite layer maintaining the plasmonic properties of the pristine nanostructured films. Ramachandran et al. observed that the growth rate decreased with decreasing reaction temperatures. The growth rate at 250^0C was shown to be 0.8 Å/cycle which is slower than higher temperature runs performed in literature[4,9,10,15] however, this a pay-off for the ability to deposit on temperature sensitive substrates.

8.2.2. Dielectric Interlayers

Dielectric layers have been used to electronically isolate plasmonic nanoparticles from absorbing materials in uses such as shell isolated nanoparticle enhanced Raman spectroscopy (SHINERS), photocatalysis and plasmonically enhanced solar cells.[17–24] The most widespread route to dielectric isolation of plasmonic nanoparticles is the direct synthesis of silica coated gold nanoparticles, known as shell isolated nanoparticles, or SHINs.[17–19,23,25,26] The dielectric shells around nanoparticles aid their chemical stability during the reaction or fabrication of the device in which they are employed. The shell also acts to reduce potential interactions with the surrounding materials to allow undisturbed spectroscopic characterization or reduce recombination in solid state semiconducting devices. [17,18,20–22]

Dielectric buffer layers have been used in photocatalytic devices in which metallic plasmonic nanoparticles have been introduced.[17,20,21,27] Due to the sensitivity of the plasmon resonance to the dielectric environment the plasmon resonance can shift if the nanoparticles are in contact with a semiconducting absorber material. Therefore, an optically transparent layer such as SiO_2 or Al_2O_3 can be used to maintain the plasmonic properties of the nanoparticles.[20] The dielectric buffer layers also help to prevent the strong damping due to the S of the plasmonic oscillations that occur when a plasmonic nanoparticle is in contact with a semiconductor. [24,28] These dielectric layers maintain the plasmonic resonance position of the as synthesised metal nanoparticles and the electric field strength around the nanoparticles.

In order to effectively concentrate light, the dielectric layers should be sufficiently thin, generally in the order of a few nanometres.[19–21] The electric field amplitude around an excited plasmonic nanoparticles decays with distance from the nanoparticle surface. This means that a thin dielectric layer is required so that the field enhancement is not only localised within the shell.[18,21] With optically transparent layers, the light-scattering effects of plasmonic nanoparticles embedded within a device can still result in improved optical absorption. With the plasmon resonance position only slightly modified due to the dielectric medium surrounding the nanoparticle it becomes simpler to design plasmonically enhanced devices.

8.3. Characterisation

Hematite fabricated through the ALD process is initially deposited as an amorphous hematite layer, unlike through the electrodeposition or chemical routes which firstly deposit FeOOH which requires calcination in a furnace to convert to Fe_2O_3. Annealing the ALD deposited films crystallizes the hematite layers which is shown to boost the photoactivity of the

electrodes. The samples were characterized before and after annealing using UV-Vis-NIR and Raman spectroscopy.

8.3.1. Profile Measurements with AFM

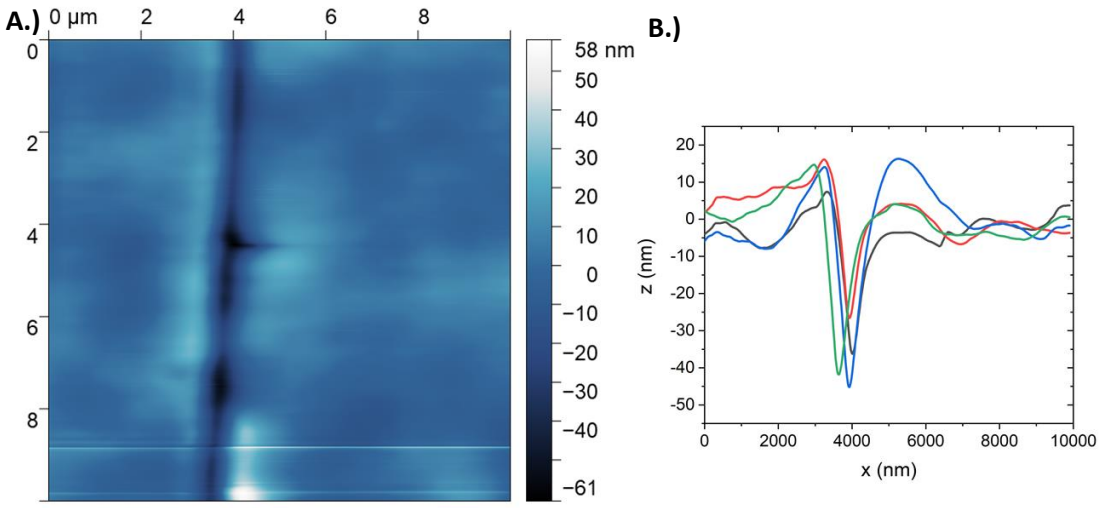

Figure 8-2- A.) AFM image taken around the scratch in the ALD deposited sample. B.) 4 typical profiles used to measure the height.

An ALD deposited hematite film on an ITO coated glass substrate was imaged using contact mode AFM after annealing at 600^0C to measure the film thickness. The film was scratched using a scalpel so that a profile could be taken along the groove. A 10x10 µm area around the groove was imaged and the profiles were taken across the sample image and the step height measured in Gwyddion software.

Figure 8-2a shows the AFM image used to measure the height of the hematite film. Figure 8-2b shows four typical profile scans taken in the horizontal direction and used to measure the film height. The average thickness was measured as (36±1) nm using 34 measurements.

8.3.2. UV-Vis-NIR Spectroscopy

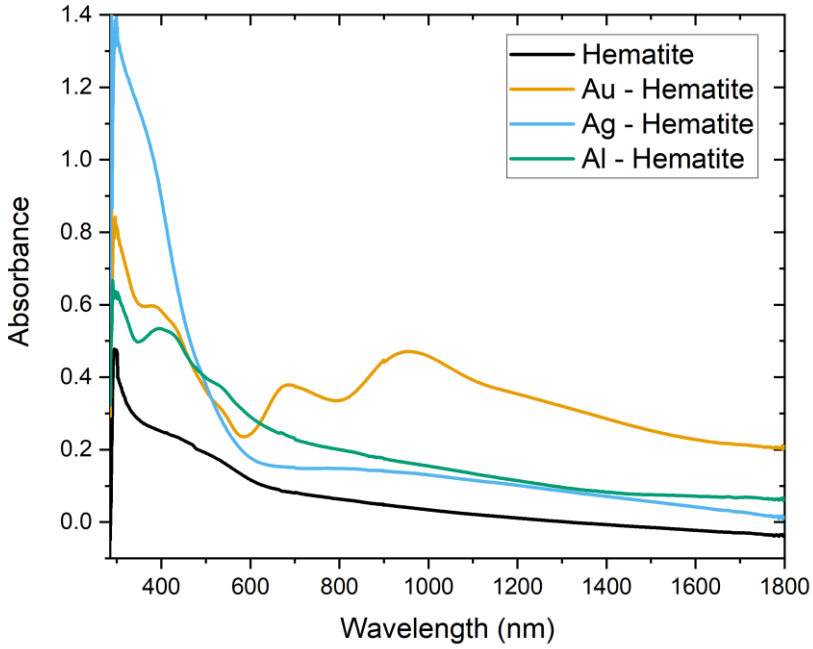

Figure 8-3 - Pre-anneal UV -Vis absorbance spectroscopy data for specific samples of each ALD deposited hematite electrode configuration.

The films were initially characterised through UV-Vis-NIR spectroscopy before and after annealing. The pre-anneal UV-vis spectra for each of the configurations are shown in figure 8-3. Before annealing, the films show absorbance data that are highly consistent with each other suggesting a high reproducibility in thickness and uniformity across the substrate in comparison to the electrodeposition technique. The peak absorbance is lower than in the electrodeposition samples because the hematite layer is of an order of magnitude thinner than the electrodeposited films (36nm compared to 415nm).

In figure 8-3, the samples that include the plasmonic nanostructures also showed highly consistent absorbance line shapes, suggesting good reproducibility and conformity in the ALD process. This could also show good or consistent adhesion of the hematite layers as there are no real outlying samples in any sample set. There is background absorbance in the UV-Vis of the metal decorated samples that does not appear in the undecorated hematite

sample. This suggests that the decorated samples have some background absorption or scattering across the spectrum which is due to the inclusion of the metal layer. This is most likely due to the inclusion of an extra interface causing scattering in all directions across the spectrum that manifests as an absorbance in the UV-Vis spectroscopy.

As can be seen in figure 8-3, with the plasmonic metal decorated samples additional absorbance features are present. When a hematite reference spectrum is subtracted from the absorbance spectra of the metal decorated samples it is possible to develop a representation of the absorption spectrum from the metal nanostructured layer beneath. These are shown in figure 8-4. Here the baseline undecorated hematite absorption spectrum is taken from figure 8-3. This is subtracted from the overall plasmonic metal layer containing sample absorption to give an approximate absorption spectrum of the underlying metal layer. This approximate spectrum has been compared to the UV-Vis data taken of the metal nanostructures prior to the hematite deposition. This allows for analysis of the effect on the hematite overlayer on the LSPR of the metal nanoparticles. When the hematite reference spectrum is subtracted from the Au ALD hematite spectrum a clear gold absorbance spectrum is revealed. It is clear from this spectrum that the hematite overlayer causes the features in the gold absorbance to red-shift.

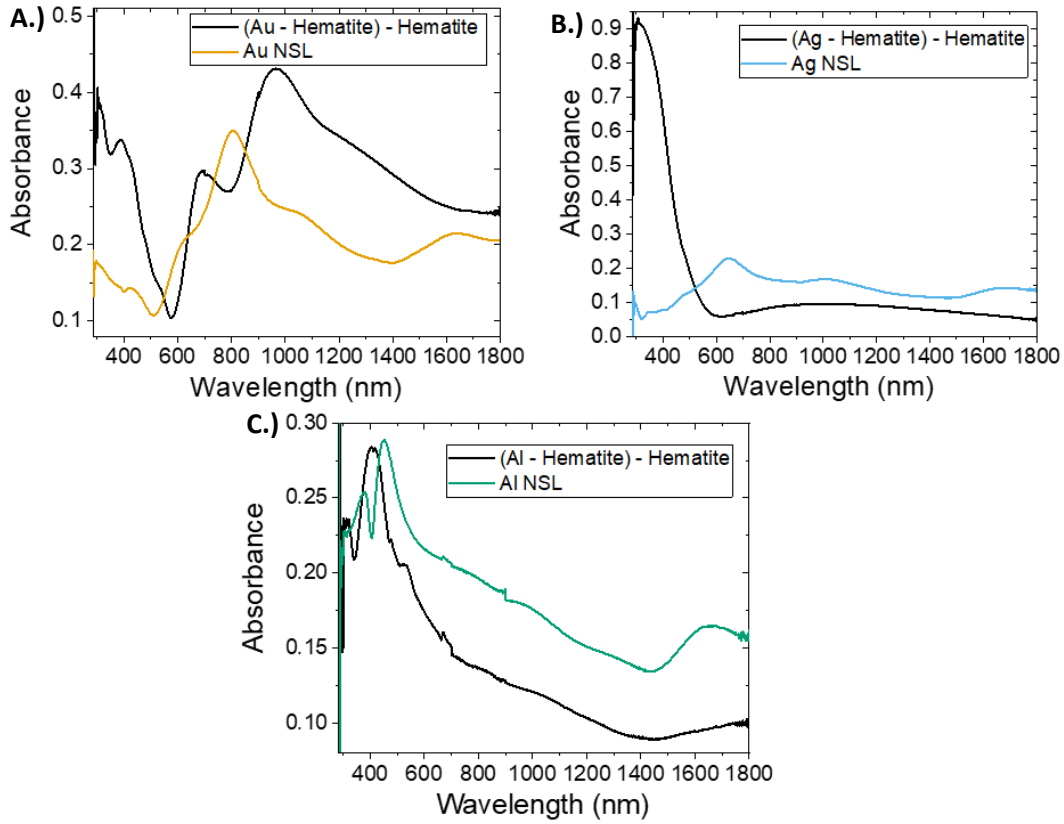

Figure 8-4 - UV-Vis spectroscopy data showing the comparison of the initial nanostructured substrate and the differential metal decorated hematite electrodes. The differential data was formed by subtracting the undecorating hematite UV-Vis spectrum from the metal decorated electrode spectrum. A.) Au nanostructures, B.) Ag, and C.) Al.

For the aluminium decorated sample, the features in the absorbance spectra in figure 8-4c have blue-shifted with the addition of a hematite layer. In the previous electrodeposition chapter band alignment diagrams were shown in figures 7-10 to 7-13. In thermal equilibrium a large charge transfer from metal to semiconductor is expected to result in a large absorbance feature as low-lying conduction band states are occupied by electrons from the Al fermi level. This was seen previously for the Ag hematite heterostructures but not in aluminium. It was suggested that because of the necessary anneal step in the electrodeposition the Al nanostructures had completely oxidised or otherwise been destroyed, and this was why the absorption features were not seen. However, here the hematite layers do not require calcination to be formed, and the strong enhancement of the 400nm absorption feature is not seen. Instead, a blue-shifted aluminium LSPR feature is seen

when the hematite reference is subtracted. This shows that the aluminium structures are intact prior to annealing. The lack of strong interaction suggests that either the native alumina oxide layer on the nanostructures is blocking the charge transfer, or that the higher resistivity and lower electron mobility of aluminium compared to silver restricts the charge transfer.[29]

As can be seen in figure 8-4, the Ag sample showed a strong absorption feature in the 300-500nm portion of the spectrum with none of the other plasmonic absorption features seen prior to hematite deposition observable. A similar strong absorption feature was seen in the electrodeposition work with the Ag containing samples and manifested as strong enhancement in the hematite 400nm absorbance peak. Here the feature is much stronger and stretches further into the UV. The ALD deposition produces much thinner films shown by the peak absorbance, and therefore the accumulation region formed in thermal equilibrium accounts for a much larger percentage of the total film. This will result in a stronger relative absorption enhancement as previously there was a lesser proportion of the hematite film dominated by the accumulation region.

After the samples were annealed at 600^{o}C in air for 30 minutes they were then measured again in the UV-Vis spectrophotometer. Comparisons of the absorbance before and after annealing are shown in figure 8-5. The undecorated hematite UV-Vis absorbance before and after annealing is shown in figure 8-5a. After annealing the hematite absorbance became more characteristic with the absorbance features expected, including the shoulder at ~600nm and the peak at ~400nm, becoming more evident. The absorbance appears to increase but this is mostly from the ITO substrate becoming less transparent after the anneal step and some increase from the hematite as it crystallizes.

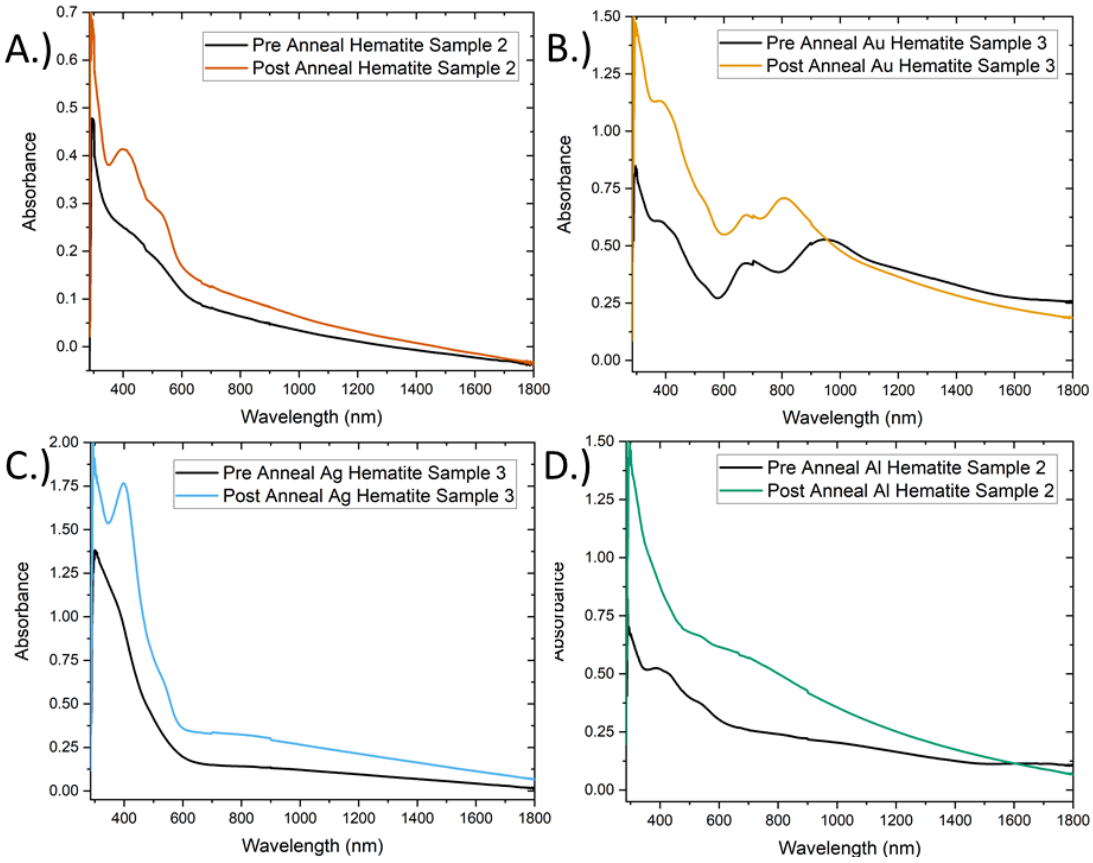

Figure 8-5 – Comparisons of the pre- and post-anneal UV-Vis spectra for each of the electrode configurations. A.) undecorated ALD deposited Hematite samples, B.) Au Decorated, C.) Ag Decorated, and D.) Al Decorated.

The Au hematite UV-Vis absorbance before and after annealing is shown in figure 8-5b. For the Au hematite samples the absorbance peaks from the underlying metal structures can be clearly seen in both spectra in the 600-1100nm range. After annealing it can be seen that the second peak of the gold absorbance has blue shifted. This is most likely due to a decrease in length of some nanoparticle dimension due to melting during the anneal step, leading to a blue shift in LSPR position. This spectrum demonstrates the increase in absorbance due to the ITO as the increase in absorbance for all features including the gold layer would not be attributable to the hematite crystallinity increase at such high wavelengths.

The Ag decorated hematite UV-Vis absorbance before and after annealing is shown in figure 8-5c. The post-anneal absorbance spectrum for the silver containing sample now shows the enhancement of the peak at around 400nm. This is in line with what was seen in the

electrodeposition chapter. The reason for this appearing in the annealed film may be due to the fact that the ligand states that are involved in the transition that the 400nm absorption is assigned to are more available. After annealing in air, the oxygen vacancies present in the film fabricated through ALD are fixed, meaning that more of the ligand states are present resulting in this peak at 400nm being revealed.

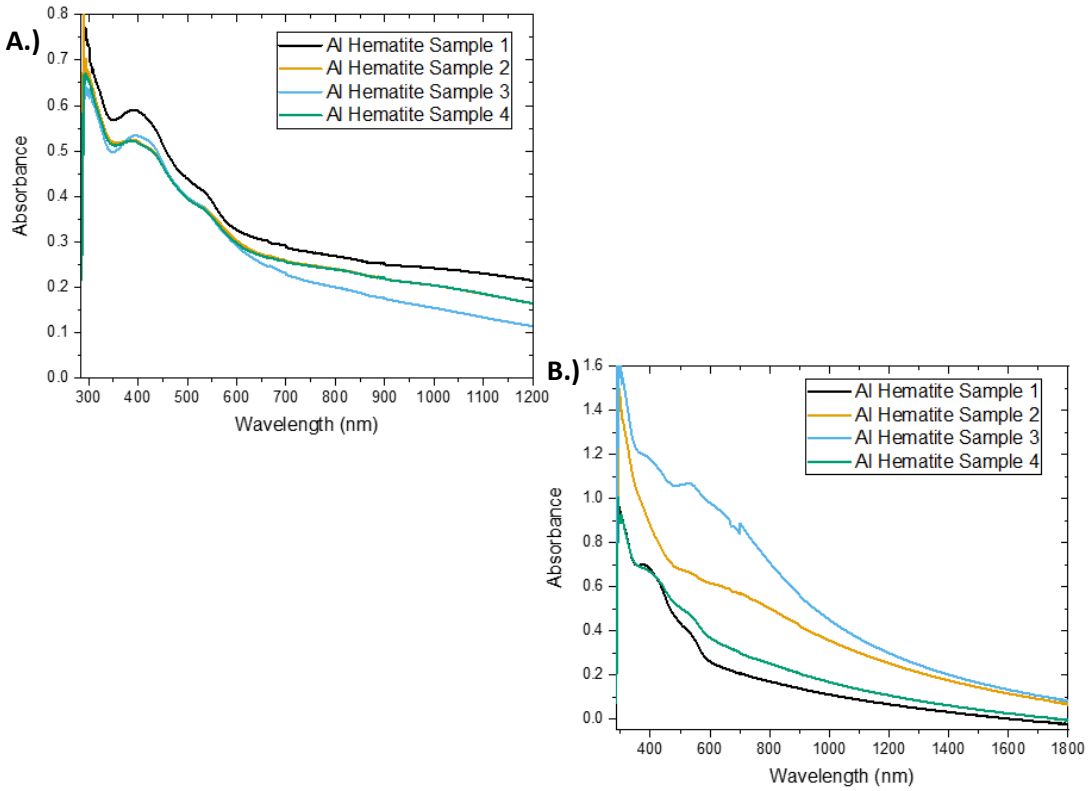

Figure 8-6 - UV-Vis spectra for the entire Al-decorated sample set. A.) is the pre-anneal data. B.) is the post-anneal data. Pre-anneal data is fairly consistent whereas after annealing there is a large variation in shape and absorbance maximum. This suggests that the AL nanostructures have interfered with the hematite in different ways due to the heat of the anneal step.

Aluminium containing samples showed a large change in the absorbance spectra after annealing. Figure 8-5d shows that post anneal the aluminium sample now shows a broad hump in the absorbance below 1000nm, uncharacteristic of hematite or of the Al nanostructures. In figure 8-6a the pre-anneal absorbance spectra for all four Al samples can be seen to be fairly consistent with one another whereas, once annealed all the samples differ in shape and absorbance features. The post-anneal spectra are shown in figure 8-6b.

It is hypothesised that the aluminium has incorporated into the film at various amounts during the anneal step forming various forms of metal oxide within the films or Al doping levels in hematite. This gives varying absorbance shapes as the material is fundamentally changed, this should be reflected in the photocatalytic performance.

8.3.3. Raman Spectroscopy

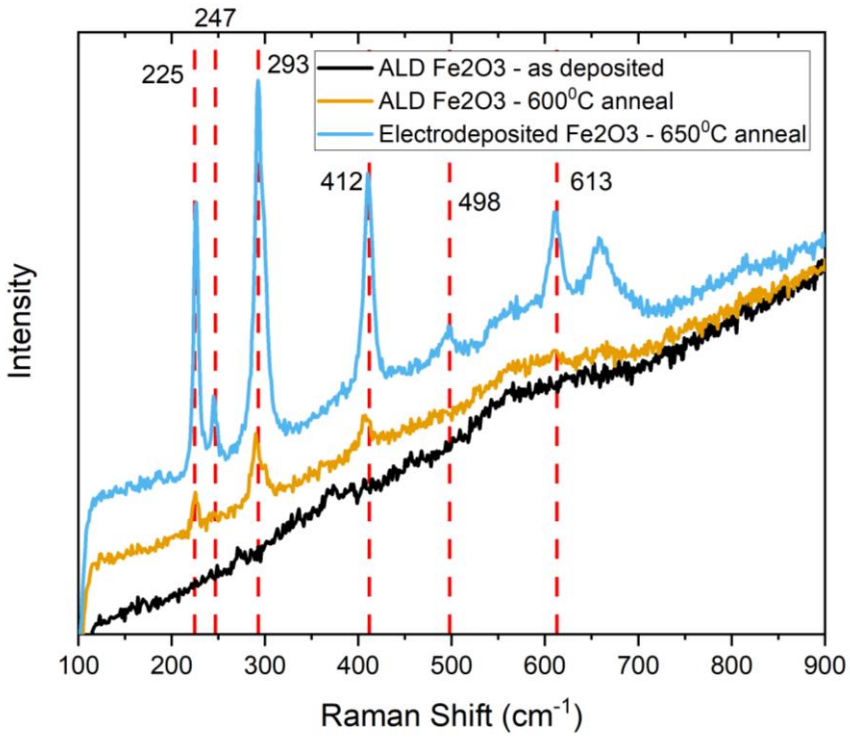

Figure 8-7 – Raman spectra for the as-deposited ALD hematite film, the annealed ALD hematite film, and an electrodeposited sample for reference. Lines indicating the characteristic peaks taken from De Faria et

Raman spectroscopy was employed in order to verify that the deposited layers were in fact hematite and to show the increased crystallinity after the anneal step. Figure 8-7 shows the Raman spectra for as-deposited ALD hematite, ALD hematite after a 600°C anneal step, and electrodeposited hematite annealed at 650°C as a standard for comparison. Hematite gives characteristic Raman peaks with two A_{1g} modes at 225 and 498 cm^{-1} and five E_g modes at 247, 293, 299, 412, and 613 cm^{-1}.[30] These are indicated as lines in the figure. The Raman spectrum of the as deposited ALD hematite film does not show any peaks suggesting an

amorphous film, whereas there are some characteristic peaks with weak signals in the post-anneal spectra which indicates that the anneal step has formed some crystallinity in the film.

8.4. Photoelectrochemistry

As with all previous samples, chronoamperometry and IPCE measurements were taken on each of the ALD fabricated samples in order to reveal and analyse the effects of the nano-decorated substrates. The photoelectrochemical experiments were performed on the samples before and after the anneal step in order to find the effects on the photoresponse.

Unlike in the wet chemical or electrodeposition methods, the ALD fabrication method deposits an amorphous hematite layer initially which does not require a calcination step. Therefore, the unannealed samples can be tested for photocatalytic ability.

8.4.1. Linear Sweep Voltammetry

Linear sweep voltammetry was done in conjunction with chronoamperometry under broadband white light from the Xe lamp in 1M NaOH using a three-electrode set-up with the hematite electrodes as the working electrode, a Pt foil counter electrode, and a homemade Ag/AgCl reference electrode. The working electrodes were swept between -0.4V and 0.8V and the current was measured.

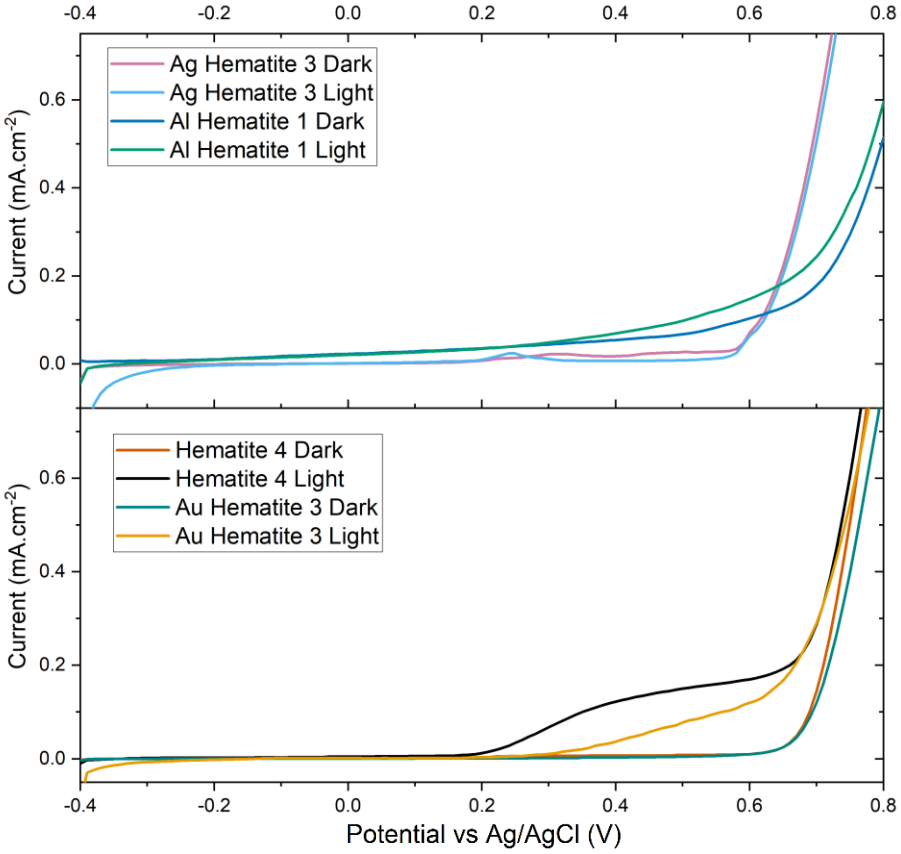

Figure 8-8 Pre-anneal Linear Sweep Voltammetry data for selected samples of each electrode configuration

The pre-anneal linear sweep data is shown in figure 8-8. The onset potential is the potential at which the current in the illuminated scan begins to diverge from the dark scan. This is the potential at which the internal voltages are overcome and charge carriers can cross the semiconductor/liquid junction and begin to oxidise OH^- ions in the electrolyte. For the standard hematite electrodes, the onset potential is shown to be at 0.2V before annealing. The undecorated hematite shows good, steady photoresponse in the voltage range above 0.3V.

The onset potential for the gold decorated samples from the linear sweep data at around 0.3V is higher than that for the undecorated samples suggesting the presence of an additional barrier. This additional potential barrier is due to the Schottky barrier effect at the metal/semiconductor interface which was shown for gold in the band alignment diagrams in

the previous chapter. The Ag decorated sample does not show a steady photoresponse across the voltage range but does have a sharp anodic catalytic onset at around 0.6V. This could be due to uncoated silver catalysing the water oxidation using a mechanism not activated by incident light. The linear sweep voltammetry for the aluminium decorated electrode shows a steady photocurrent at biases above 0.3V. This shows that before annealing, and when the aluminium nanostructures are intact, these samples are able to function as photocatalytic electrodes and perform better than the Ag samples.

Chopped illumination linear sweep (LS) voltammetry was performed with the same parameters as the linear sweep but with manually chopped illumination every 5 seconds. With the chopped illumination it is clearer when the electrodes are reacting in some way to the light even without a measurable photocurrent. Spikes in current are seen when the illumination state changes as charges are generated and rearrange at the surface of the electrode, resulting in a spike of current. However, this does not always result in a sustained measurable photocurrent as the carriers have insufficient energy to cross the junction. The chopped illumination linear sweep of the samples before annealing is shown in figure 8-9. It is possible to see from here that the undecorated samples and the Au and Al decorated samples, have some small response across most of the potential range.

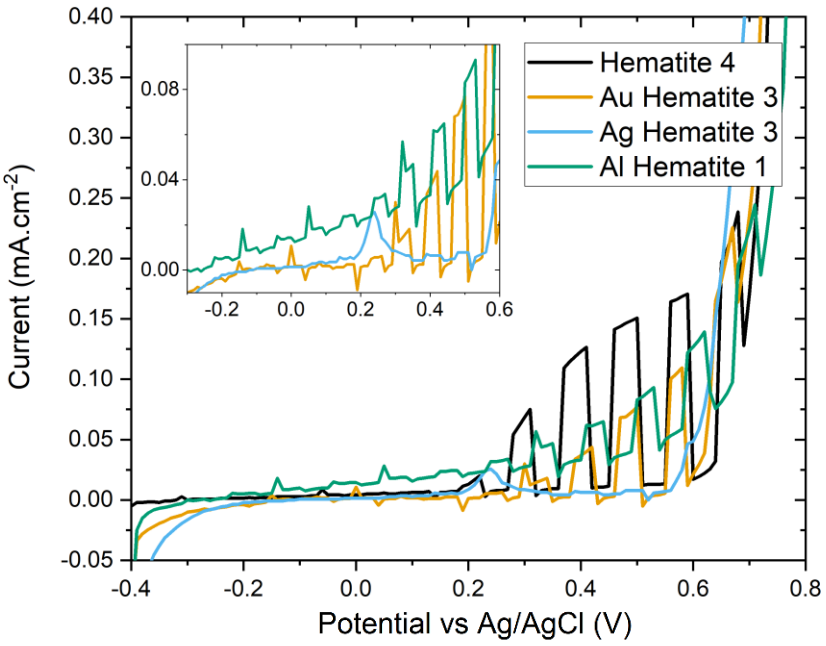

Figure 8-9 - Chopped Linear Sweep Voltammetry data for selected samples of each electrode configuration before annealing. This shows a photoresponse for each of the geometries. Inset is a chosen area of the graph with the Hematite sample 4 trace omitted. The inset graph shows the small photoresponse in the Ag decorated electrode. And the low onset potential for the Au and Al decorated electrodes at around -0.2V.

At low negative bias the Al decorated sample shows a small but measurable photocurrent which appears higher than the Au-decorated sample at the same potential however the photocurrent from the Au sample begins to increase at 0.3V much more quickly than the Al decorated. The higher dark current from the Al decorated sample is also displayed in the chopped illumination LS as the line deviates away from the other samples. The low onset potential for the Al decorated samples seems to disagree with the hypothesis that accumulation causes a potential barrier. However, the low electron mobility in Al compared to Ag could result in less charge transfer than expected from just the band alignment diagrams. The Ag decorated samples show a very small photoresponse across the potential range that was not evident in the continuous illumination LS voltammetry however no real detectable photocurrent is apparent.

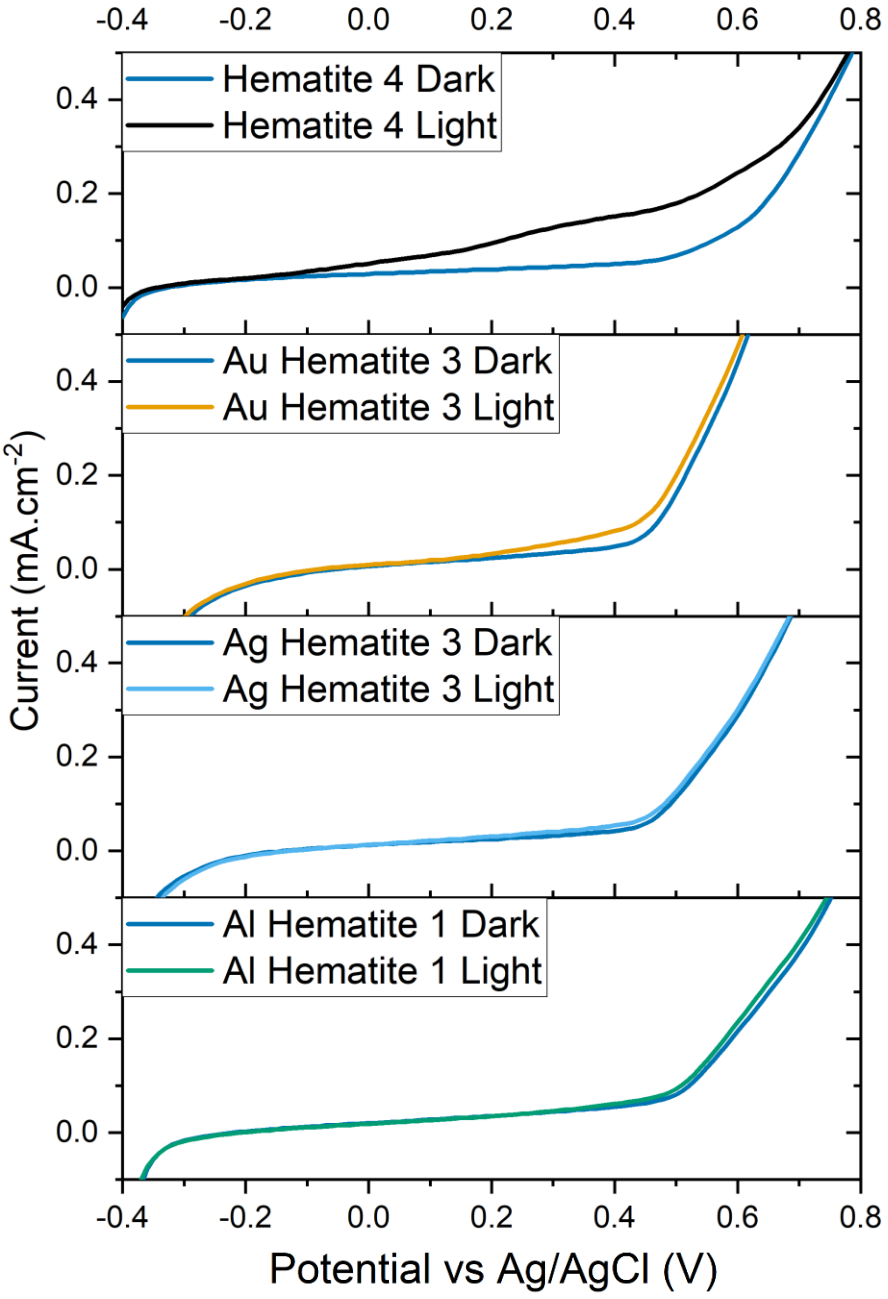

Figure 8-10 Linear sweep voltammetry data for a chosen sample of each electrode configuration after annealing. Sample numbers are shown for continuity.

After the samples were annealed the linear sweep data shows variation in the behaviour of all the samples. This data is given in figure 8-10. The onset potential for the undecorated hematite sample is now a lot lower at around -0.1V, this demonstrates that the anneal step has led to a lower potential barrier due to improved charge transport. The dark scans for the

metal decorated samples all now show a photocatalytic response at around 0.5V, this was previously seen in the Ag decorated sample but for the Au this has shifted down from 0.65V. Before annealing, the LS voltammetry for the Al sample showed a steady increase in the current with respect to voltage, but after annealing there is a sharp response in current at 0.5V. This suggests some change in the catalytic ability of all the samples potentially due to the migration of metal to the surface producing catalytic hotspots for electrolytic reduction of OH- ions in solution. The scans under illumination show that after annealing the Ag samples now have a slightly higher photoresponse at high potentials whereas the Al decorated samples has reduced.

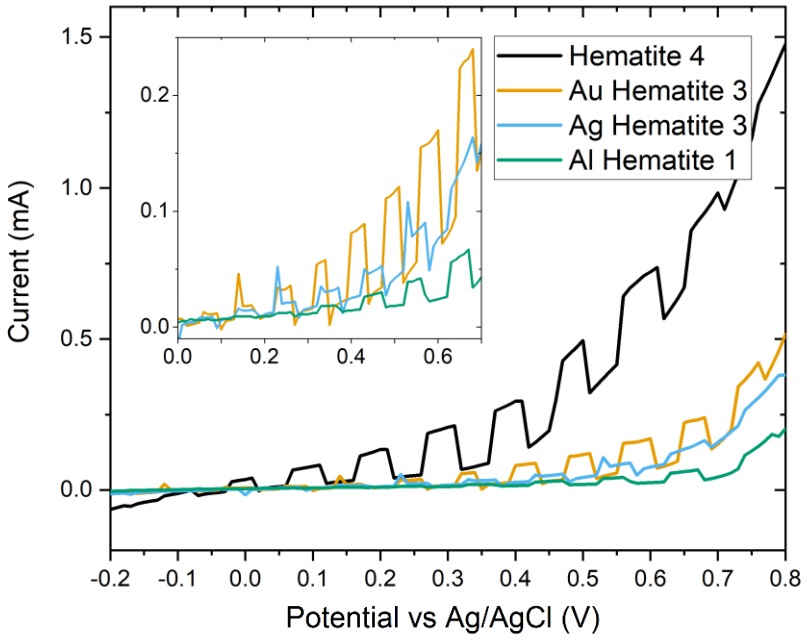

Figure 8-11 - Chopped linear sweep voltammetry data for a chosen sample of each electrode configuration after annealing. Sample numbers are shown for continuity.

The chopped illumination LS data in figure 8-11 shows more clearly at which potentials the metal decorated electrodes are responsive to changes in the illumination conditions. It is clearer from this plot that all three metal decorated samples show some photoresponse. The silver decorated samples show a photoresponse at potentials above 0.1V which was not

evident in the pre-anneal data. The higher onset potential for the Ag decorated materials can be explained using the band alignment diagrams previously discussed. The accumulation region at the interface causes a potential barrier for electrons to be extracted. Like charge repulsion causes electrons to be retarded as they travel through the accumulation region increasing the probability of recombination. The Al decorated samples now only show a small photoresponse at potentials above 0.2V whereas previously they were responsive along much of the potential sweep. The higher photocurrents for each of the metal samples seem to occur at around 0.5-0.6V.

8.4.2. Chronoamperometry

Chronoamperometry with chopped light was performed, as before, at 0.3V vs Ag/AgCl with a Pt foil counter electrode. Photocurrents for each sample before they were annealed were measured and are shown in the boxplot in figure 8-12. In the box-plot the diamond markers signify the single sample results and the central box indicates the mean value for the data set. The whiskers show the standard deviation range above and below the mean value. Each plot has three horizontal lines; the central horizontal line shows the median value for the dataset and the outer horizontal lines represent the standard error on the mean. This is true for all subsequent box-plots.

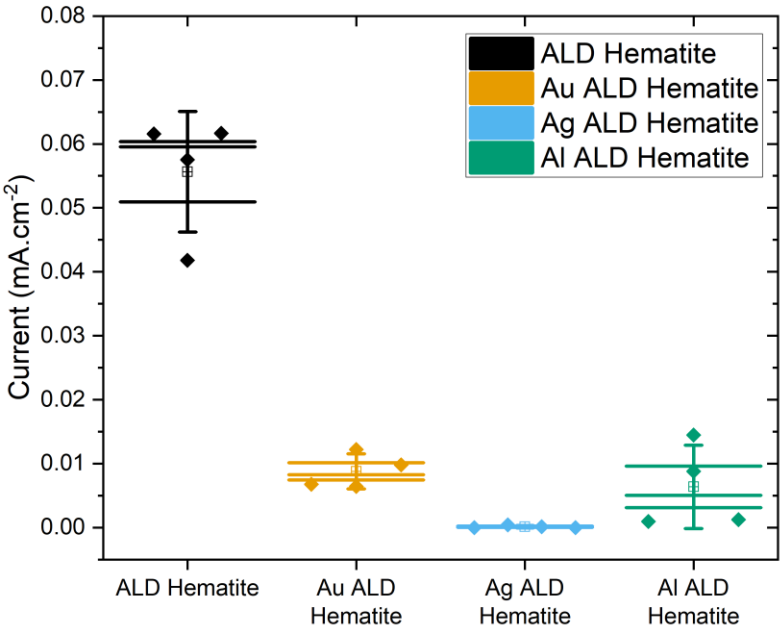

Figure 8-12 Box plots showing photocurrent density at 0.3V vs Ag/AgCl for each of the electrode configurations before annealing. The central square point is the mean, the central line gives the median, the box lines are the standard error, and the whiskers show the standard deviation.

In figure 8-12 the photoresponses are more consistent than the electrodeposited samples and the efficacy of the ALD process is clearly higher than the previous method as all samples operated successfully when compared to the roughly one in four that were unresponsive from the electrodeposition technique. The mean photocurrent for the undecorated ALD hematite samples is (56±5) $\mu A.cm^{-2}$ before annealing. This is higher than the mean photocurrent achieved with the undecorated electrodeposition method and shows that despite no thickness or dopant optimization, the ALD process produces hematite films with a higher photocatalytic ability. This could be due to better orientation or crystal structure in the ALD process or simply by virtue of being much thinner.

All of the metal decorated electrodes showed overall decreased or quenched photocurrents in comparison to the standard hematite. For the Au decorated samples, the mean photocurrent was (9±1) $\mu A.cm^{-2}$. The Au samples showed the least amount of photocurrent

quenching with a low spread compared to the other metal decorated samples. This could suggest the presence of two competing mechanisms within the film such as a plasmonic enhancement effect and a recombination or carrier loss effect at the metal semiconductor interface. From the band alignment diagrams a small Schottky junction is expected for the Au hematite interface. It is likely that this junction is having a larger effect on the ALD hematite films compared to the electrodeposited films. This is because the ALD films are much thinner than the electrodeposited films and therefore the pathlength of plasmonically scattered is lower. This means that the plasmonic enhancement of the Au nanostructures cannot compete with the recombination caused by the Schottky barrier.

The most severe quenching was seen in the Ag samples, these samples gave a mean photocurrent of (0.1±0.1) $\mu A.cm^{-2}$. There was no discernible photoresponse in two of the Ag electrodes that were fabricated. This suggests that there was a dominating negative effect from including the silver nanostructures in the hematite electrodes. The large charge accumulation region provides a significant potential barrier increasing the onset potential for these samples above 0.3V, therefore no photocurrent is seen at this bias.

With an average photocurrent of (6±3) $\mu A.cm^{-2}$, the Al nanostructured electrodes showed a similar level of reduced photocurrent as the Au samples but with a larger spread. this would suggest irreproducibility in the fabrication or quality of the Al nanostructures as the strength of the negative mechanisms is varied between samples.

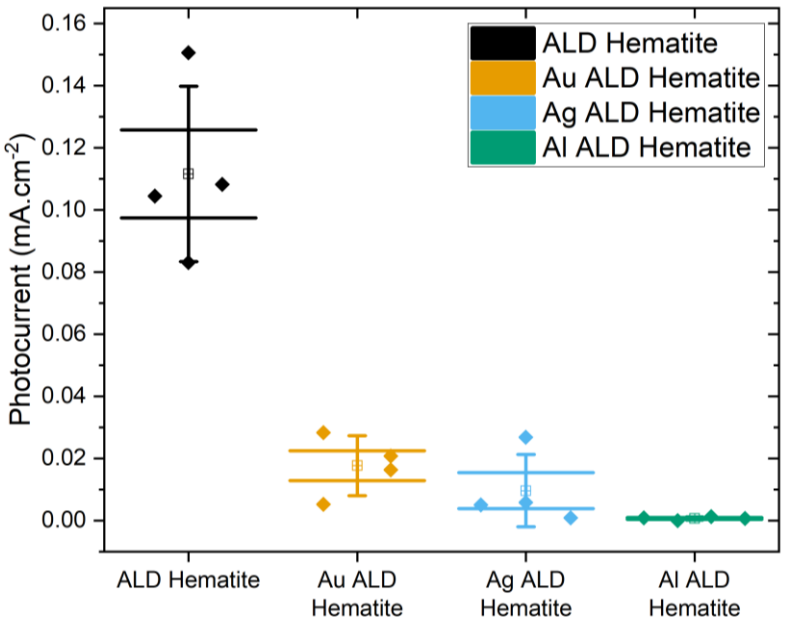

Figure 8-13 - Box plots showing photocurrent density at 0.3V vs Ag/AgCl for each of the electrode configurations after annealing.

The samples were then annealed in air at 600°C for 30 minutes in a box furnace and tested again using the same chronoamperometry technique as previously. The photocurrents were measured as before and are shown in the boxplot in figure 8-13. From the electrochemistry results from the undecorated samples, it is possible to see that the anneal step increases the photocurrents of the electrodes. The mean photocurrent for the undecorated hematite films after annealing was (110±10) $\mu A.cm^{-2}$, giving a photocurrent increase by a factor of roughly 2 through annealing. This is due to the increased crystallinity in the films, which has been shown through the Raman spectroscopy, which gives greater charge transport and increases the photocatalytic ability.

The mean photocurrent for the Au decorated samples after they were annealed was (18±5) $\mu A.cm^{-2}$. The photocurrent enhancement from annealing was therefore also a factor of 2. This is consistent with the undecorated samples. This suggests that the anneal step has increased the photocatalytic ability of the hematite layer as it did in the undecorated samples

but the charge transfer is still hindered by some mechanism involving the gold at the back surface.

The Ag decorated electrodes gave a measurable photocurrent density after the anneal step, however the mean photocurrent was still lower than that for Au decorated films at (10±6) $\mu A.cm^{-2}$. This suggests that the onset potential has shifted to lower voltages through annealing. The increase in measured photocurrent density here shows again the effectiveness of the anneal step. The fact that the hematite has become more crystalline could mean that gains are made through the possibility of more efficient charge transfer in crystalline materials. The photocurrent is still being quenched due to the inclusion of the Ag nanoparticles due to the potential barrier at the interface. The outlying overachieving sample here may be due to that sample having a poorly fabricated Ag nanostructured layer or that the nanostructure layer was damaged in the anneal step result in a higher photocurrent density.

After the anneal the Al decorated samples average photocurrent was (0.6±0.3) $\mu A.cm^{-2}$ as seen in figure 8-14. This is a reduction in average photocurrent by an order of magnitude. It is obvious from the UV-VIS-NIR spectroscopy that, unlike the other samples, the underlying Al layer has been affected by the anneal. It is possible that Al has migrated into the hematite layer and adversely doped the hematite layer. This would account for the reduction in photocurrent and the inconsistent UV-Vis spectra for these samples.

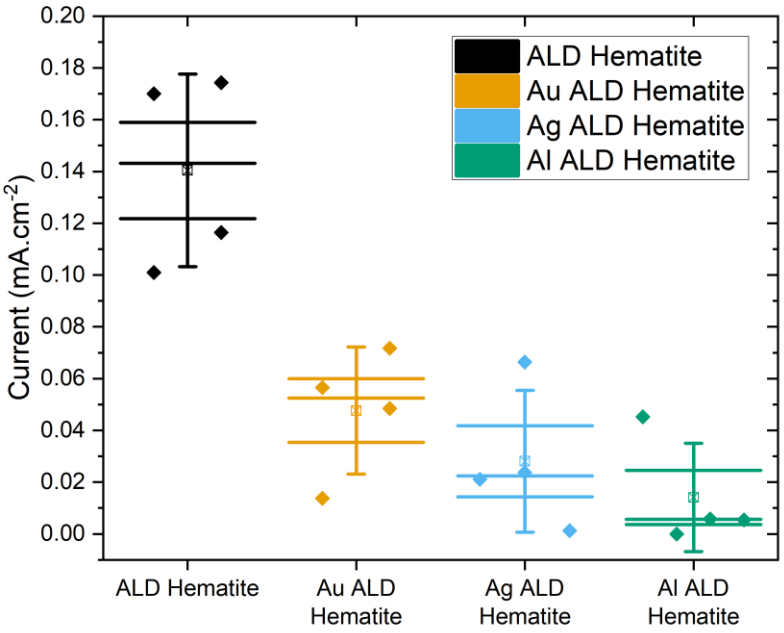

Figure 8-14 - Box plots showing photocurrent density at 0.55V vs Ag/AgCl for each of the electrode configurations after annealing.

The linear sweep voltammetry in figure 8-11 shows that the photocatalytic onset potential for all the metal decorated samples is shifted to higher voltages than the undecorated samples. Due to this the post anneal samples were also tested using chronoamperometry at a higher potential of 0.55V. Chronoamperometry was performed on all samples as before but with the potential bias set to 0.55V rather than the previous 0.3V. This data is shown in figure 8-14. At this potential the mean photocurrent for the undecorated samples is (140±20) $\mu A.cm^{-2}$. This represents a 27% increase in photocurrent by increasing the potential bias.

From figure 8-14 the average photocurrent for the Au decorated samples is (50±10) $\mu A.cm^{-2}$. Compared to the (18±5) $\mu A.cm^{-2}$ achieved at 0.3V, this represents an increase of 280%. This result agrees with what was seen in the linear sweep voltammetry where the onset potential for the Au decorated samples was higher than the undecorated samples. With a higher onset potential, the Au decorated samples reach an optimal photocurrent at a higher bias and the increase in photocurrent with respect to bias happens rapidly in this potential range.

The average photocurrent for the Ag decorated samples at 0.55V is (30±10) $\mu A.cm^{-2}$ giving an increase of 300% from the (10±6) $\mu A.cm^{-2}$ achieved at 0.3V previously. As a percentage increase this is high and correlates with what was seen in the linear sweep and with the Au samples, but both these values are still low compared to the undecorated sample. The average value here is being shifted by one outlying data point that shows a high photocurrent which is reflected in the standard error.

At 0.3V bias the Al decorated samples were nearly completely unresponsive to light however at the higher bias there is now a photoresponse from most of the films, with one major outlier. The average photocurrent for the Al decorated samples is (10±10) $\mu A.cm^{-2}$ at 0.55V shown in figure 8-14. The large error is reflective of the fact that one of the electrodes had a high photocurrent compared to the others. Most of these electrodes still show a very low photoresponse.

At the higher bias of 0.55V the metal decorated electrodes still perform worse than the undecorated electrodes although the percentage differences between the photocurrent densities from the decorated and undecorated samples have reduced. The metal nanoparticle decorated samples have higher onset potentials than the undecorated hematite samples. Therefore, the percentage increase in performance between 0.3 V vs Ag/AgCl and 0.55 V vs Ag/AgCl is higher, as expected, for the decorated samples. The reduction in photocurrent density due to increased recombination at the interface is more pronounced for the ALD fabricated substrates due to the decreased thickness of these films. For the Au decorated substrates the recombination due to the Schottky barrier outcompetes the gains made by plasmonic light scattering due to the decreased pathlength of scattered light. In Ag the accumulation region inhabits a larger proportion of the film reducing the electron extraction efficiency and reducing the photocurrent at 0.3V to near zero. For

aluminium the annealing step has destroyed the nanostructures shown in UV-Vis and reduced the photoresponse.

8.4.3. IPCE

As previously, IPCE was employed in order to spectrally resolve any effects on photoresponse that were occurring. The IPCE spectra are shown in the graph in figure 8-15, the inset plot is a rescaling of the original graph. As expected from the chronoamperometry the spectra for the nano-decorated samples are largely quenched across the spectrum in comparison to the undecorated ALD hematite sample.

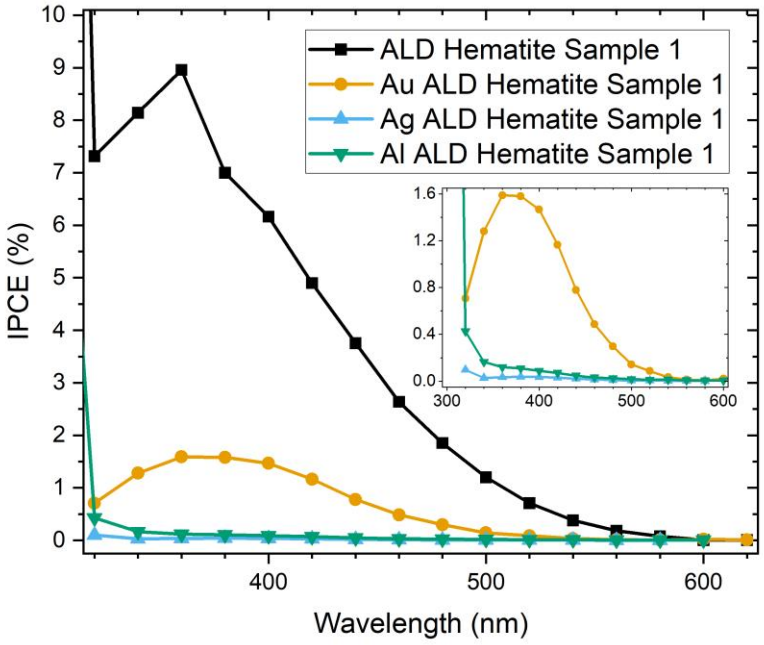

Figure 8-15 - IPCE spectra for each of the electrode configurations after annealing. Bias potential is 0.3V vs Ag/AgCl. Shows photocurrent density reduction in cases with a metallic nanostructure layer included. Sample numbers are shown for continuity.

The IPCE line shape of the undecorated ALD hematite electrode shown in figure 8-15 is a characteristic IPCE spectrum which shows the spectral features expected from the UV-VIS. Despite the reduced photoresponse across the spectrum, the shape of the Au decorated electrode IPCE is not similar to a simply poorly performing hematite electrode. The inset plot

shows that the line-shape for the Au decorated samples shows a peak in comparison to the Ag and Al samples which are broadly flat across the spectrum.

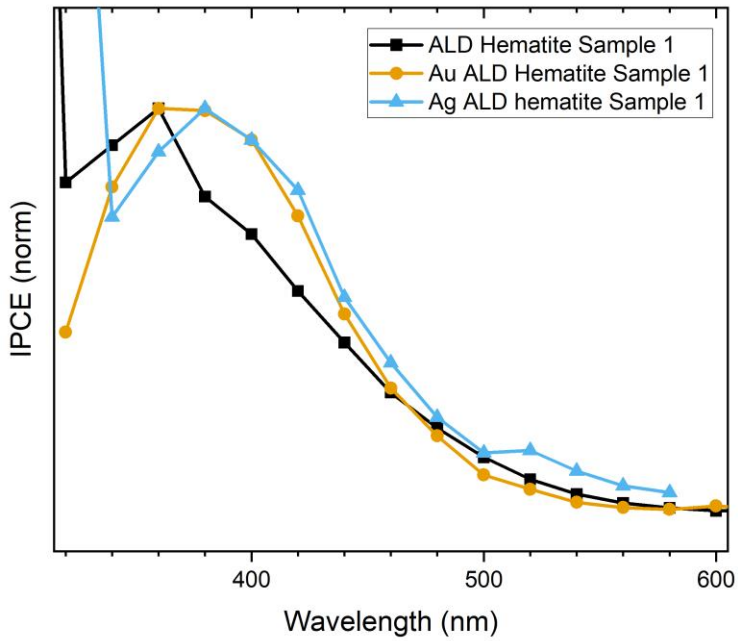

Figure 8-16 Normalized IPCE spectra from figure 5-14. 0.3V Vs Ag/AgCl bias potential. Shows spectral relative enhancement for Au and Ag decorated samples. Al samples are omitted due to the low IPCE values

The IPCE for undecorated, Au, and Ag decorated samples was normalized to their local maxima in the range 360-380nm. This data is shown in figure 8-16. When the spectra are normalized to the peak at 360nm it is clear that the Au electrode has an increased relative IPCE in the range 360-460nm than would be expected for a hematite electrode, suggesting a relative spectral enhancement. The conversion efficiency is clearly reduced across the spectrum for the Au samples but the shape of the curve suggests there is some boost in the conversion efficiency outside the normal hematite absorption spectrum shown by the IPCE line-shape boosted in the region above 360nm. This further suggests that there are competing mechanisms at play.

The Ag and Al IPCE spectra were largely quenched and flat across the spectrum. These spectra seem to show a somewhat similar shape with the Al samples, somewhat unexpectedly, showing a higher IPCE across the spectrum. This could just be done to the margin of error as the Ag Sample 1 showed a much higher photoresponse in comparison to the Al Sample 1 in the chronoamperometry. The shape of these plots is what may be more important. The Al lines show no peak in the spectrum so this, with the fact that the spectrum is largely reduced, suggests that the electrodes are just unresponsive due to the incorporation of Al into the hematite film. In the normalized IPCE data in figure 8-16 we see that the shapes are quite different. The Ag lines show a peak at 380nm suggesting that there may be some mechanism that is working advantageously for the electrodes photocatalytic ability but is overshadowed by a detrimental effect that is reducing the photoresponse massively over the spectrum. This would suggest that the negative mechanism quenching the photocurrent is stronger in the Ag containing films than the Au films as both show a relative spectral enhancement but the Ag photocurrent is reduced by a larger factor than the Au containing electrodes.

8.5. Addition of an Alumina Spacer Layer.

As discussed previously, the inclusion of an interlayer between the metal/Hematite interface should block any unwanted charge transfer that could be shortening carrier lifetimes. Through the ALD process it is possible to deposit Al_2O_3 films prior to Fe_2O_3 in the same deposition run. A dielectric layer should stop or reduce any charge recombination occurring at the interface but should also block or reduce any metal migration into the hematite film. Removing or reducing the possibility for recombination at the metal/hematite interface should allow the plasmonic effects of light concentration and field enhancement to dominate the mechanisms at the interface and improve the plasmonic enhancement. The dielectric

spacer layer at the back contact of the electrode could also assist with hematite's overall photocatalytic ability by blocking holes at the contact but allowing the more mobile electrons to tunnel through the barrier assisting the hole-driven water splitting occurring at the semiconductor/electrolyte interface.

In order to achieve this the plasmonic substrates were prepared as before, then using ALD a 1nm layer of Al_2O_3 was deposited on top of the substrates before the hematite layer was deposited. The hematite layer was deposited using the same method and number of cycles as previous. By keeping the hematite layer consistent with the previous experiments, it is possible to make direct comparisons to the electrodes that do not contain the alumina spacer layer. The samples were tested using the same photoelectrochemical experiments as before, pre and post a 600^{o}C anneal step. The samples were annealed using the same step as previous, a 600^{o}C in air using a box furnace for 30 minutes.

8.5.1. Band Diagrams

Band diagrams for the alumina including electrode configurations were produced to guide the explanations of possible junction effects. Information for the Fermi levels, band positions and work functions were taken from the literature.[31–35] Band diagrams were drawn using the method described by Kittel.[36] The alumina layers deposited by ALD are expected to be un-doped as no intentional doping was performed, therefore the Fermi-level is expected to sit quite centrally as in the pure material. Alumina is a wide band-gap dielectric, for sufficiently thin layers electrons will be able to tunnel through the junction and block holes from extraction at the back contact. Thin dielectric layers have been used in solar cells and transistors to increase the charge extraction at the junction by removing the Schottky junction effects.[37] The thin alumina layer should also act to block migration of unwanted dopants into the hematite layer. Alumina was chosen due to the ease of fabrication through ALD and its good adhesion to metal layers.

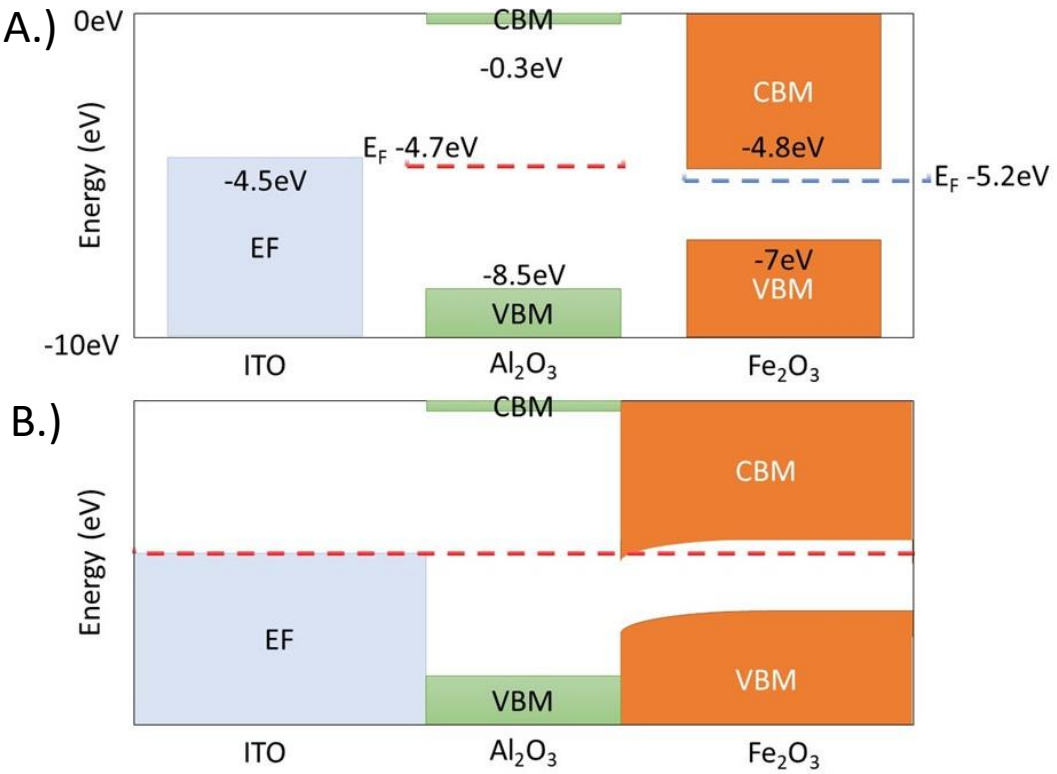

Figure 8-17 Band alignment diagrams for the ITO-alumina-hematite configuration. A.) is band positions in isolation. B.) demonstrates band-bending in thermal equilibrium.

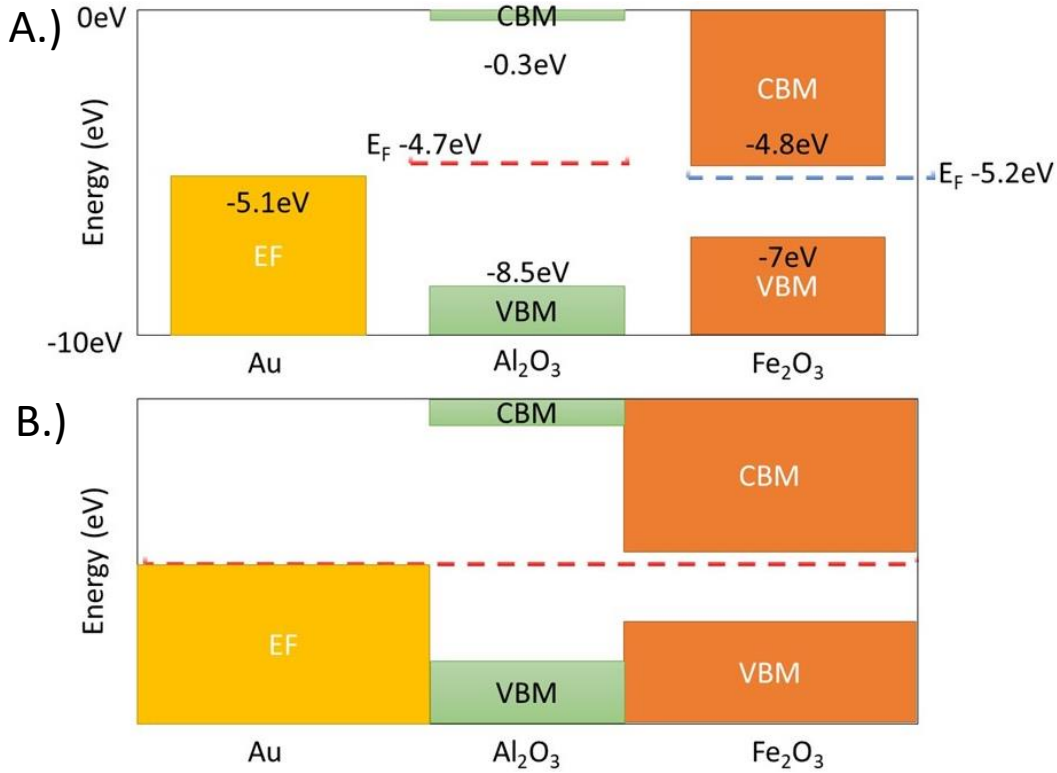

Figure 8-18 Band alignment diagrams for the Au-alumina-hematite configuration. A.) is band positions in isolation. B.) demonstrates band-bending in thermal equilibrium.

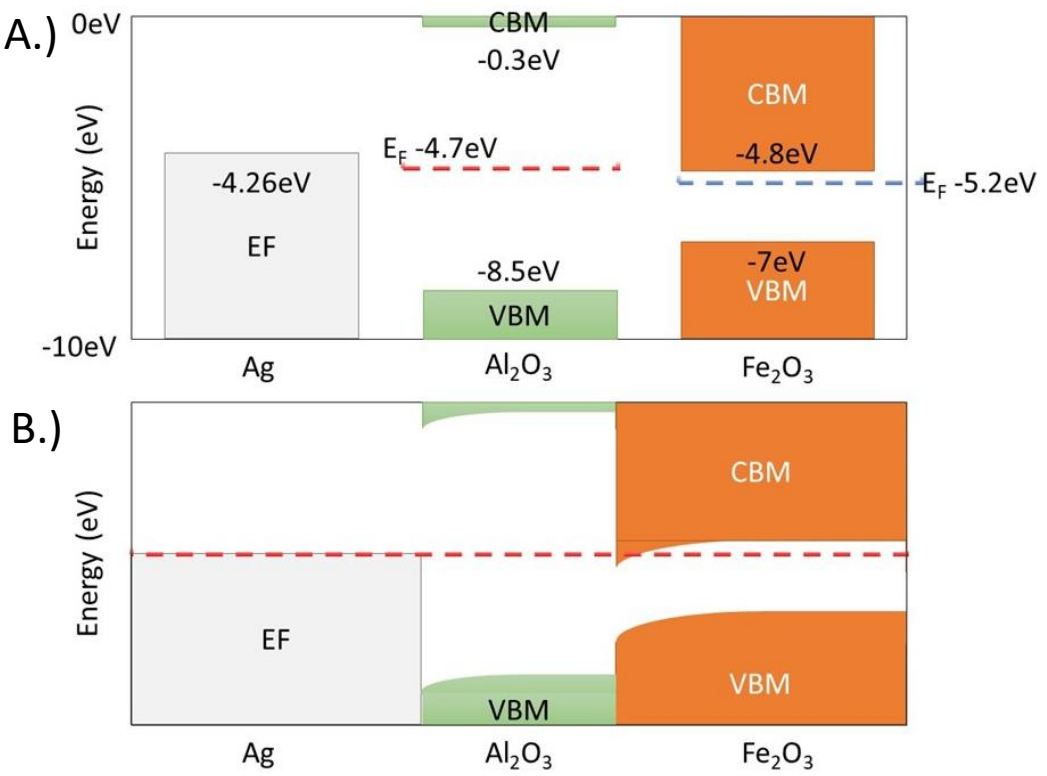

Figure 8-19 Band alignment diagrams for the Ag-alumina-hematite configuration. A.) is band positions in isolation. B.) demonstrates band-bending in thermal equilibrium.

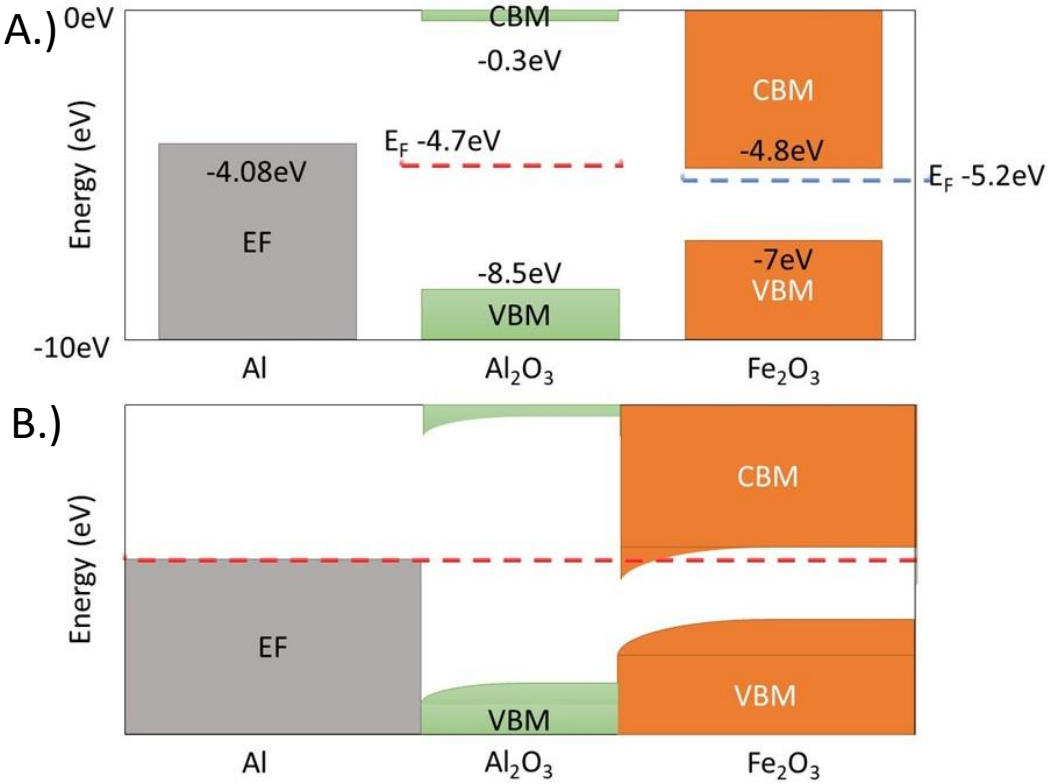

Figure 8-20 Band alignment diagrams for the Al-alumina-hematite configuration. A.) is band positions in isolation. B.) demonstrates band-bending in thermal equilibrium.

The band diagrams for the various configurations are shown in figures 8-17 to 8-20. Figure 8-17 shows the band alignment diagrams for the ITO-Al_2O_3-Hematite configuration. In equilibrium, the central band-gap of alumina is expected to lead to little band bending as the Fermi levels equilibrate. Band bending is expected to occur in the hematite layer leading to accumulation of electrons at the interface, this should aid the transport of holes to the hematite surface to contribute to the water oxidation. There is clearly a large gap between the conduction bands of the alumina and the hematite which would hamper the extraction of electrons. However, at 1 nm thick, the alumina layer should be sufficiently thin to allow the tunnelling of charges through the junction.

For the metal nanostructure architectures, the interface at the back contact consists of the ITO-alumina-hematite junction and the relevant metal-alumina-hematite junction. This is because the ITO substrate is coated with metal nanostructures and not a continuous metal film. Figure 8-18 shows the band alignment diagrams for the Au configuration. There is little band bending expected for the alumina or the hematite due to good match of the Fermi-levels in isolation. The alumina layer should act to block holes and remove the small Schottky junction seen previously in the Au-hematite case. This is dependent on the alumina layer allowing tunnelling through the junction.

Figures 8-19 and 8-20 show the band alignment diagrams for the Ag and Al metal containing configurations respectively. The Ag and Al containing configurations both show much larger band bending for both semiconducting materials due to the low work-functions of the metals compared to Au and ITO. Both cases result in accumulation of electrons in the hematite at the interface which could result in increased recombination at the interface as electron extraction is impinged. From the band alignments it is clear that holes should be more easily swept towards the hematite surface due to the hole depletion region at the interface. the valence band mismatch of the alumina and hematite should reflect holes from being

extracted or recombining at the interface. In these cases, the alumina layer should also act to block the metals from oxidising or migrating into the film during the anneal step, which would stop negative unintentional doping.

8.5.2. UV-Vis Spectroscopy

The alumina containing electrodes were characterized using UV-Vis-NIR spectroscopy. Alumina is a wide band-gap semiconductor that is not absorbing in the range that was tested therefore it is not expected to be seen in the UV-Vis spectroscopy. The UV-Vis absorbance spectra for selected samples before annealing is given in figure 8-21. The pre-anneal spectrum for the alumina-hematite electrode shows a characteristic hematite absorption with an absorbance at 400nm of 0.25. This value is consistent with the value for the previous non-buffer layered samples showing that the film thickness is consistent with the previous samples.

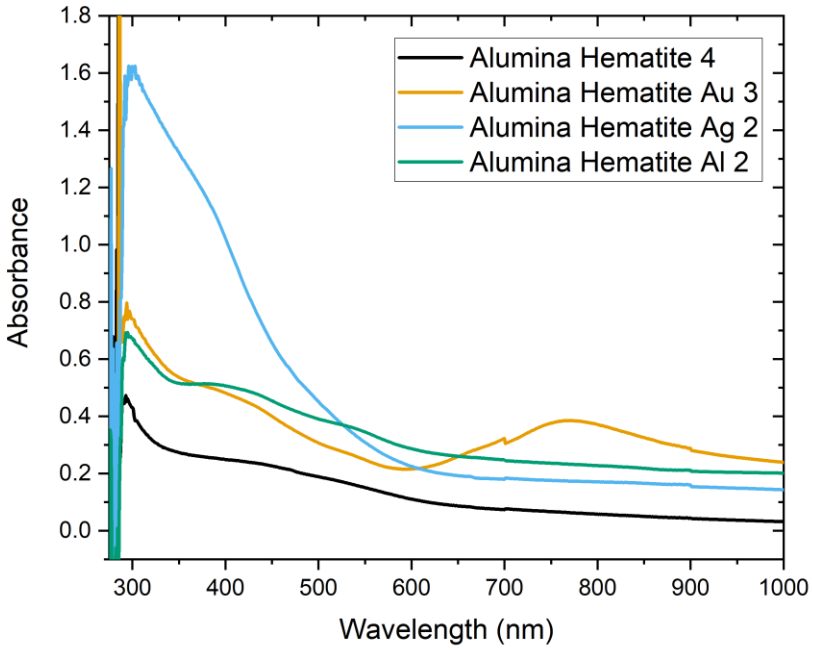

Figure 8-21 - UV-Vis spectra for chosen samples of each configuration including the alumina layer before annealing.

The metal decorated samples all show a background absorption manifested as a y-axis offset compared to the undecorated sample as before. The absorbance spectrum for the Au-alumina hematite sample shows an absorbance at 400nm of 0.48 however there seems to be a consistent y-axis offset of around 0.2 along the spectrum. The Au LSPR peak is visible in this spectrum as a hump centred at around 800nm. Th Al-alumina-hematite absorbance spectrum, given in green, shows an absorbance fairly similar to the undecorated sample with an absorbance at 400nm of 0.5 with a y-axis offset of about 0.15. There is no obvious LSPR peak in the spectrum, however the peak absorbance at 400nm, with the y-axis offset taken into account, would be higher than the undecorated sample.

The Ag-alumina hematite sample absorbance shows a large enhancement of the absorption in the blue-region of the spectrum. The absorbance at 400nm is 1 and increases into the UV. This phenomenon has been seen in all previous Ag containing samples and has been attributed to an enhancement of the 400nm absorption feature in hematite. Previously it was discussed that this feature was due to electrons occupying low-level conduction band states when the charge transfer from metal to semiconductor under thermal equilibrium occurs. The inclusion of the alumina layer has clearly not stopped this from occurring. From the band diagrams this should also be the case for the aluminium decorated samples, however that is not the case. Previously it was discussed that the absence of this effect in the aluminium samples could be due to the native oxide layer blocking the charge transfer. Here there is an aluminium oxide layer coating the Ag nanoparticles yet this phenomenon is still observed. It is likely due therefore, to the much higher mobility of electrons in the Ag metal than the oxide layer. The higher mobility of electrons means that the tunnel probability is higher for this junction. This could be tested by systematically increasing the alumina layer and observing the absorption characteristics.

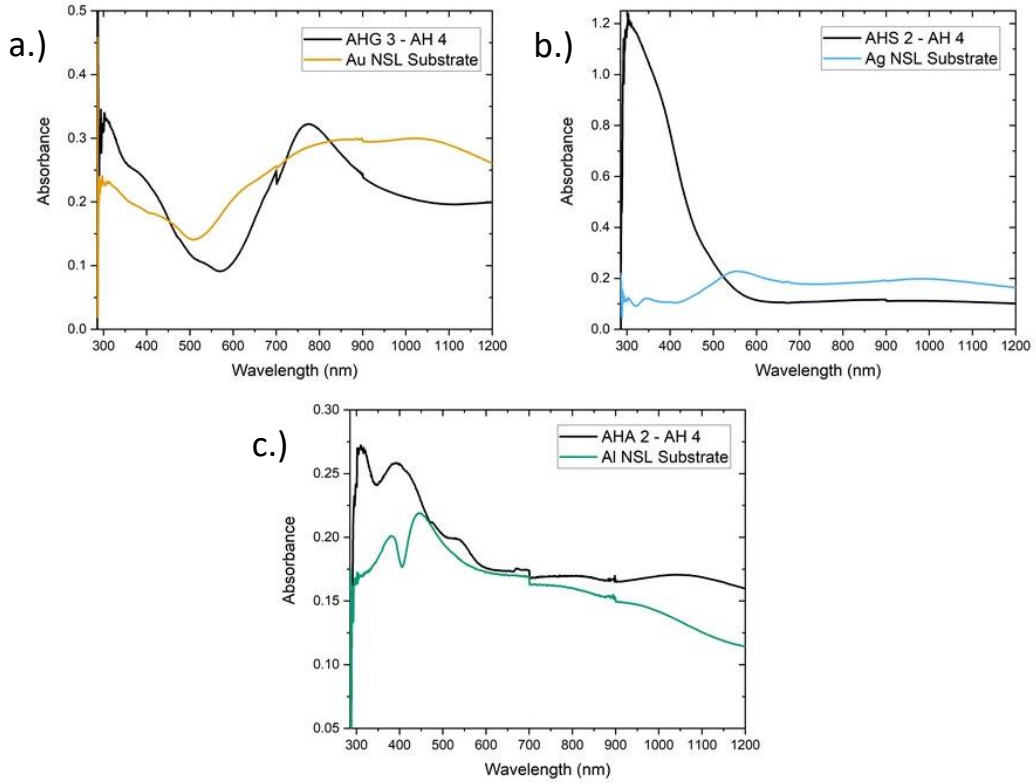

Figure 8-22 - UV-Vis spectroscopy data showing the comparison of the initial nanostructured substrate and the corrected metal decorated alumina-hematite electrodes. AH4 refers to the undecorated alumina-hematite sample.

A.) BLACK – the result of the optical absorbance data from the subtraction of the Alumina-Hematite optical absorbance spectrum from the Au-Alumina Hematite optical absorbance spectrum. YELLOW – The optical absorbance data taken from the initial Au nanostructures on the ITO-coated glass slide. B.) BLACK – the result of the optical absorbance data from the subtraction of the Alumina-Hematite optical absorbance spectrum from the Ag-Alumina Hematite optical absorbance spectrum. BLUE – The optical absorbance data taken from the initial Ag nanostructures on the ITO-coated glass slide. C.) BLACK – the result of the optical absorbance data from the subtraction of the Alumina-Hematite optical absorbance spectrum from the Al-Alumina Hematite optical absorbance spectrum. GREEN – The optical absorbance data taken from the initial Al nanostructures on the ITO-coated glass slide

Figure 8-22 shows the comparison between the corrected aborption spectra for the metal/Al_2O_3/hematite electrodes and the initial nanostruture film absorption spectra. The corrected data is taken by substracting the Al_2O_3/hematite absorption spectrum from the relevant metal inclusive spectrum. Figure 8-22a shows the Au case. Here the peak at ~780nm is clearly strengthened after the alumina and hematite layers are added and the other features (such as the dip at ~600nm) have red-shifted. Figure 8-22b shows the same for the Ag decorated samples. Here the same absorption increases at ~300nm as observed in previous Ag inclusive samples is seen suggesting the inclusion of the alumina layer has not

affected the mechanisms discussed occurring. Figure 8-22c shows the same data for Al layers included. Here the absorbance features of the aluminium nanostructure layer, such as the peak ~470nm in the nanostructure data, are still seen and have been blue shifted.

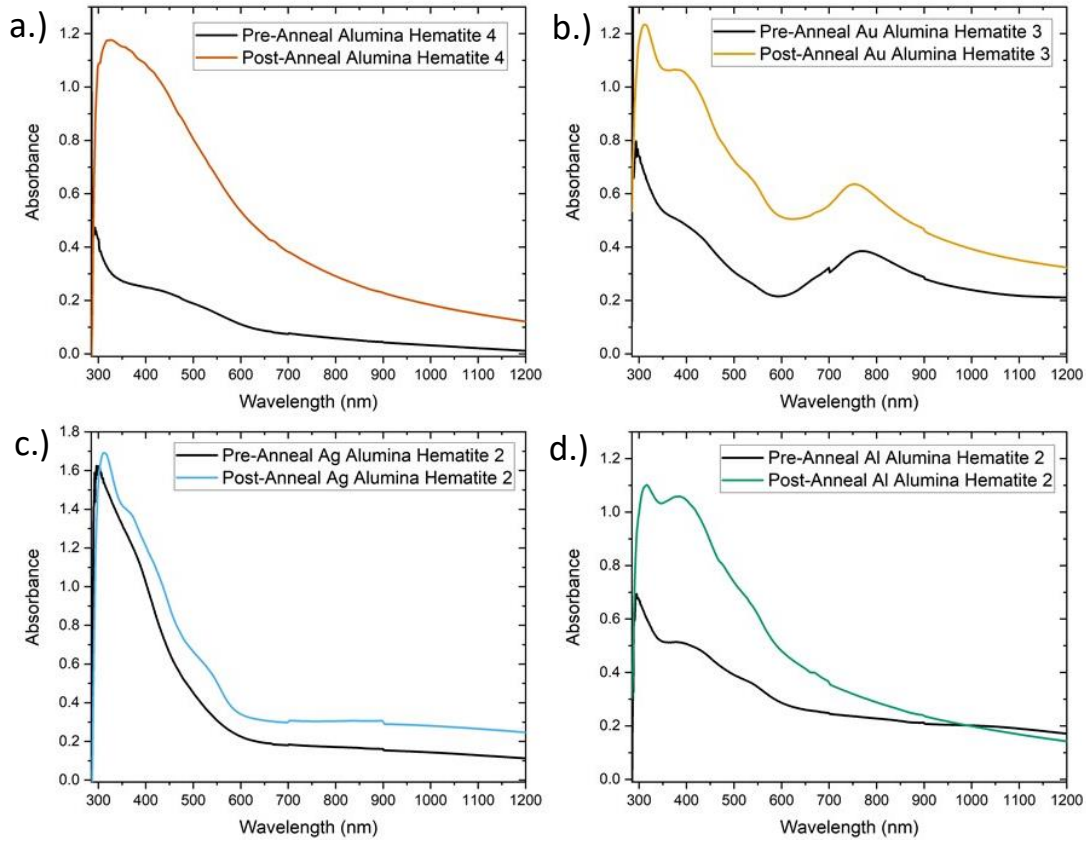

Figure 8-23 – comparisons of the UV-Vis spectrum for each configuration before and after annealing.

Figure 8-23 shows the comparison of the UV-Vis absorbance before and after annealing. The control hematite layer in figure 8-23a shows a strong increase in absorbance after annealing suggesting that the film has become more crystalline during the step. This is reflected in the metal nanostructure inclusive data as all show higher absorption across the tested spectrum.

8.5.3. Linear Sweep Voltammetry

The photoelectrochemistry performed on these samples utilised the same methodology as applied to the previous samples. Linear sweep voltammetry was performed using a potential

sweep between -0.4V and 0.8V in the same three-electrode cell set-up. The samples were tested before and after the 600^{o}C anneal step.

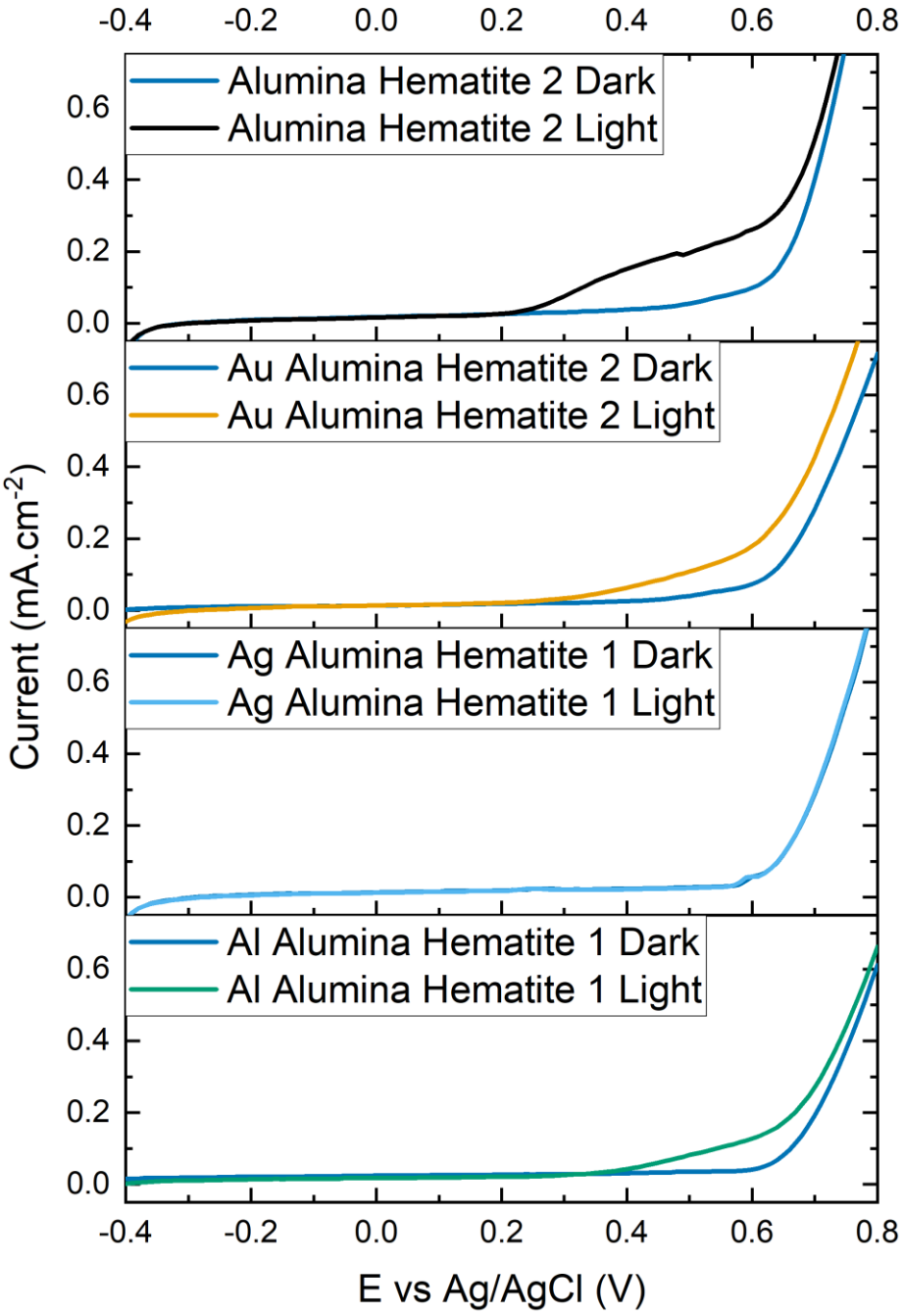

Figure 8-24 - Linear sweep voltammetry data for the various metal decorated, alumina layered electrodes prior to annealing. Sample numbers shown for continuity between figures.

The pre-anneal linear sweep data is shown in figure 8-24. From the light and dark linear sweep, the onset potential for the undecorated sample appears to be at around 0.25V. This is shifted to a slightly higher potential than the sample without the spacer layer. Without the alumina spacer layer, the onset potential for the undecorated samples was around 0.2V, this shift of 50mV would account for the presence of a dielectric layer now present at the back surface creating a potential barrier in the form of a tunnel junction for the electrons to cross in order to be successfully extracted from the hematite. Otherwise, there is still a consistent photocurrent above this potential.

For the metal decorated samples, a photocurrent is only clearly visible in the Au and Al samples from this linear sweep voltammetry. The onset potential for the gold samples appears at around 0.25-0.3V, this does not appear to be shifted by much in comparison to the 0.3V onset seen in the sample without the alumina spacer. From the Au-alumina-hematite band alignments it is expected that the addition of the spacer layer should fix the Schottky junction barrier effects and the sample should achieve a lower onset than without the alumina layer. This sample is therefore limited by the ITO-alumina-hematite characteristics and an onset potential similar to the undecorated sample is expected. The aluminium decorated sample the onset potential now occurs at 0.4V instead of 0.3V from before the spacer layer was included. This would agree with the addition of an extra barrier layer as the tunnel junction still produces an accumulation layer and an additional tunnel junction. The Al decorated sample now shows a larger and more sustained photocurrent above the onset potential than seen in the samples without the dielectric layer. From the linear sweep data shown in figure 8-24, the Ag decorated sample doesn't show any discernible photocurrent across the potential sweep.

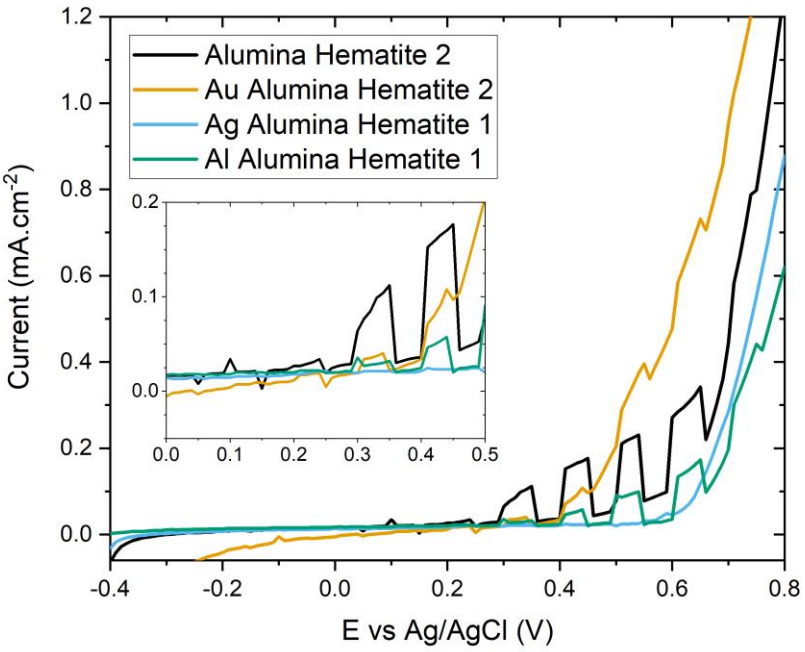

Figure 8-25 - Chopped linear sweep voltammetry data for the various metal decorated, alumina layered electrodes prior to annealing. Sample numbers shown for continuity between figures.

The chopped illumination linear sweep data for the samples taken before annealing is shown in figure 8-25. This data shows more clearly where the onset potentials lie, and also how the samples show some photoresponse at lower potentials without a coherent photocurrent. The silver containing samples still show no photocurrent coinciding with the linear sweep data in figure 8-24.

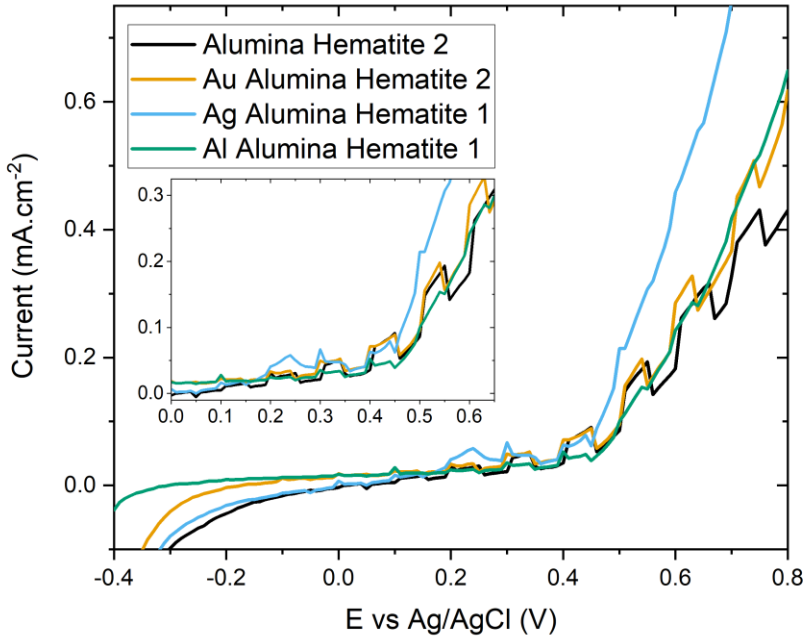

Figure 8-26 - Chopped linear sweep voltammetry data for the various metal decorated, alumina layered electrodes after annealing. Sample numbers shown for continuity between figures.

After annealing the samples were tested again. The linear sweep data for after the anneal step is given in figure 8-26. The onset potentials for the hematite electrode have not shifted after annealing and still occurs at around 0.25V. Previously in the samples without the added dielectric buffer layer, the onset potential for the pristine hematite electrodes shifted from 0.2V to -0.1V after annealing. This would suggest that even with higher crystallinity in the hematite, and better charge transport properties, the potential barrier from the alumina still dominates the electron extraction mechanism. This is also seen in the Au decorated samples where the onset potential has not shifted after annealing, whereas previously the onset shifted by -0.1V. The chopped illumination linear sweep data in figure 8-26 shows reduced photocurrents for all samples compared to figure 8-25. This shows that the photocurrents expected will be lower after annealing.

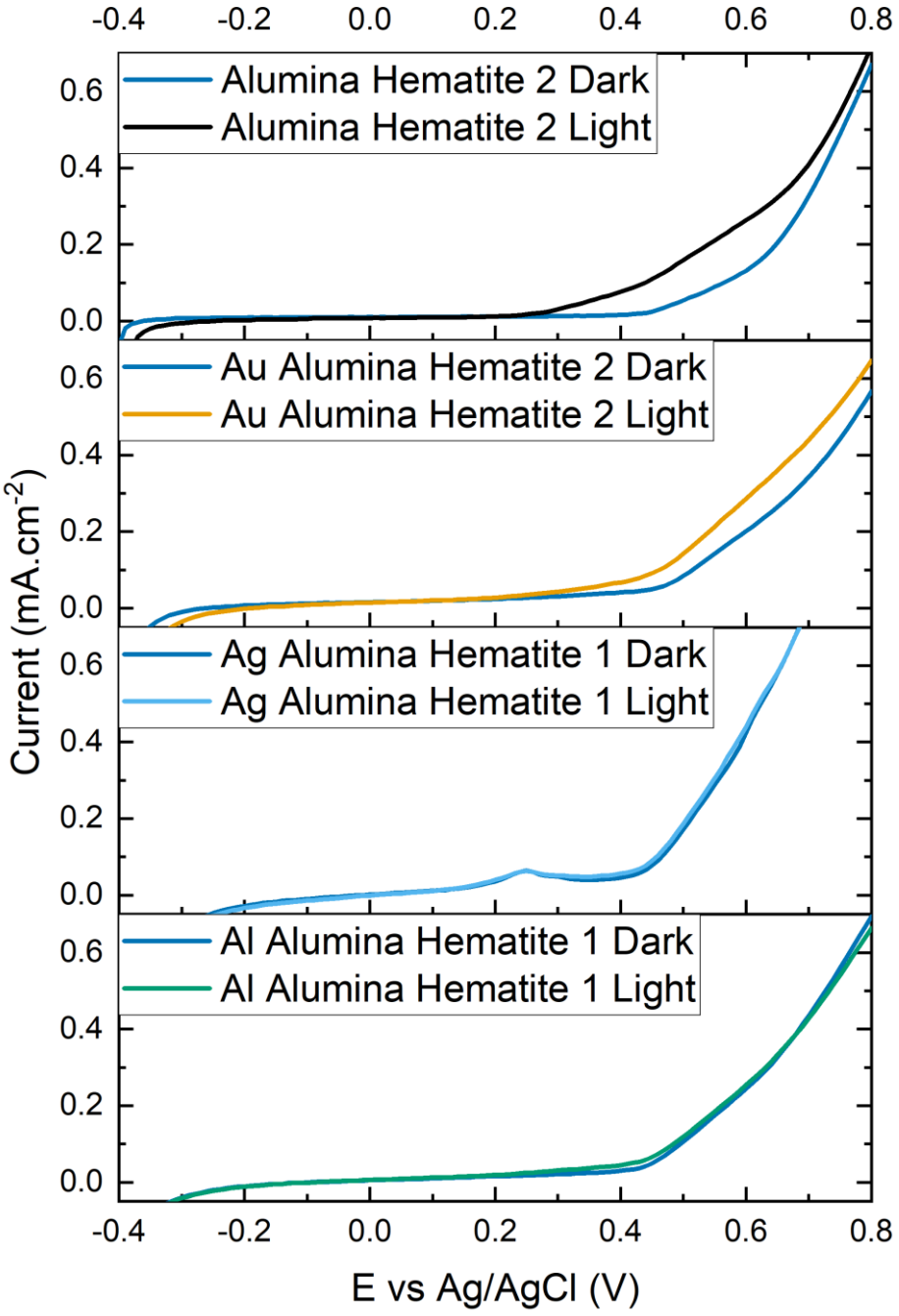

Figure 8-27 - Linear sweep voltammetry data for the various metal/alumina/hematite composite electrodes after annealing. Scans performed under illumination and in the dark to show photocurrents across the bias potential range. Sample numbers shown for continuity between figures.

The post-anneal linear sweep in figure 8-27 shows that the aluminium decorated samples now show reduced photocurrents after annealing. This is shown consistently by the chopped

illumination linear sweep data in figure 8-26 where the post anneal test shows very little photoresponse when compared to the pre-anneal data in figure 8-25. This further demonstrates that annealing of the film has negatively impacted the photocatalytic ability of the film. It is expected that the alumina layer will block unintentional doping of the aluminium into the hematite film so this reduction in photocurrent must be down to increased losses. As the alumina spacer layer is most likely more crystalline in structure after annealing it is expected that the potential barrier is higher, reducing the tunnelling efficiency. A reduction in the ability to extract electrons increases the amount of recombination at the interface and as such, hampers the photocatalytic performance of the electrode. The silver decorated films still show no photocurrent in the linear sweep but do show some response to illumination in the chopped linear sweep in figure 8-26.

8.5.4. Photocurrents

Chronoamperometry was performed both before and after annealing in order to evaluate the average photocurrents for the electrodes. the data is presented as boxplots with the means and standard errors calculated.

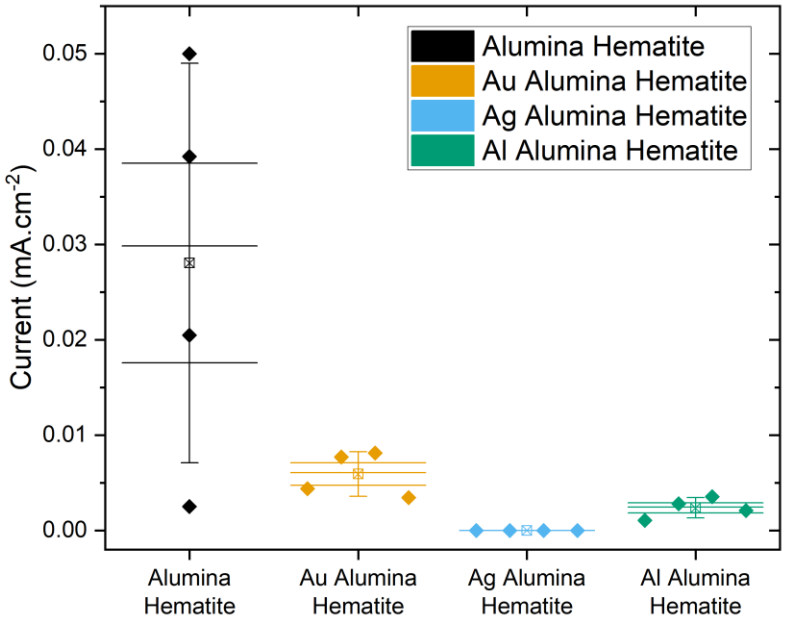

Figure 8-28 - Boxplots showing the photocurrent densities for each of the architectures prior annealing. Bias potential 0.3V. Diamonds show individual sample photocurrent density values. Other markers are as previous.

The boxplot in figure 8-28 shows the photocurrents from the electrodes before annealing at a bias of 0.3V vs the homemade Ag/AgCl reference electrode. At a bias of 0.3V the average photocurrent from the undecorated hematite samples is (30±10)µAcm^{-2}. This shows a decrease of 46% compared to the previous electrodes that did not contain the buffer layer in the same experiment. This decrease in photocatalytic ability with the addition of the 1nm Al_2O_3 buffer layer is, as discussed previously, most likely down to the inclusion of a potential barrier which hinders the extraction of electrons from the hematite layer and increasing recombination in the film. One of the samples in this sample set is shown to be mostly unresponsive to light. This sample is an outlier compared to the others and is most likely due to an error in the fabrication process. The error on the mean photocurrent is largely affected by the inclusion of this unresponsive film in the statistics.

The mean photocurrent from the Au decorated electrodes from figure 8-28 is (6±1) μAcm^{-2}, this represents a 33% decrease in photocurrent when compared to the samples without the buffer layer. The decrease in average photocurrent seen here is of a similar level to the one seen in the undecorated samples when including the buffer layer. This photocurrent drop is most likely due to the same mechanisms discussed before. The photocurrent here, when compared to the undecorated samples, is largely quenched. From the linear sweep it is shown that the onset potential for the metal decorated samples is around 0.3V and therefore testing the photocurrents at this bias will show lower photocurrents in the metal decorated samples.

The silver decorated samples show no photocurrent density across the board. This shows that the inclusion of the buffer layer has not mitigated the negative mechanism that has affected the mean photocurrents in all previous Ag containing electrodes. The addition of the buffer layer has also affected the photocatalytic ability of the hematite in these electrodes which has led to unresponsive films.

From the linear sweep data, it was shown that the onset potential for the Al decorated films was around 0.4V, therefore it was not expected for the Al films to produce much photocurrent at a bias of 0.3V. The mean photocurrent for the Al films was (2.4±0.5)μAcm^{-2} which represents a decrease of 60% in photocurrent when including the dielectric layer. The reasons for this are the same as discussed for the gold decorated samples.

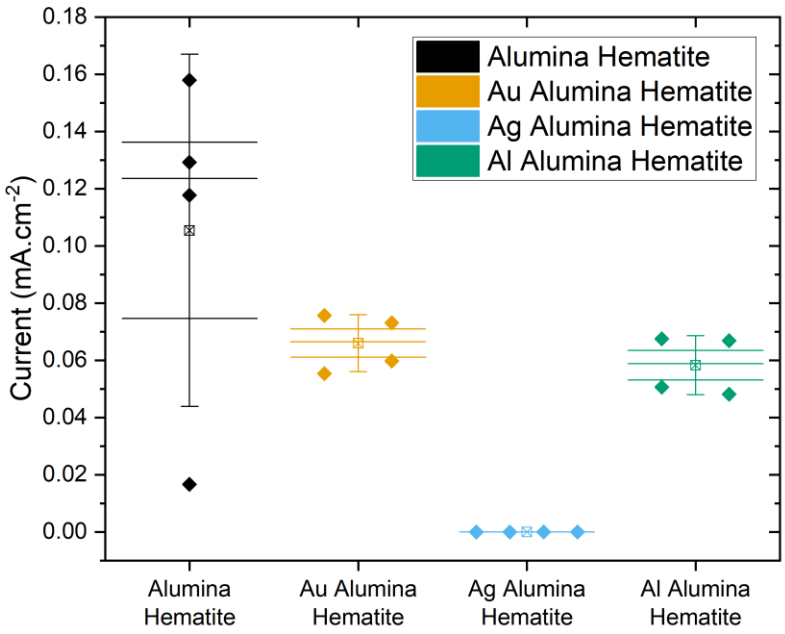

Figure 8-29 - Boxplots showing the photocurrent densities for each of the architectures prior annealing. Bias potential 0.55V. Diamonds show individual sample photocurrent density values. Other markers are as previous.

Due to the high onset potential for all electrode configurations the electrodes were also tested at a bias of 0.55V vs Ag/AgCl. This data is shown in the boxplot in figure 8-29. This bias is higher than the onset potential shown for the electrodes from the linear sweep voltammetry and therefore can be used to give higher photocurrents from all electrodes and better assess the effects of the metal layers. At 0.55V the pre-annealed hematite electrodes had an average photocurrent of (100±30) μAcm^{-2}. This is an increase by a factor of almost 4 compared to what was given at 0.30V. This concurs with the linear sweep voltammetry which showed that the photocurrent increases with respect to potential in this bias range.

From the boxplots it is clear that the photocurrents for the Au and Al samples have increased by a larger factor with respect to bias potential than the undecorated electrodes. This is evident by the shrinking of the gap between the Au and Al boxes, and the undecorated mean. The average photocurrents for the Au and Al decorated samples was (66±5) μAcm^{-2} and

(58±5) μAcm^{-2}, respectively. For the Au decorated samples this gives an increase in photocurrent by a factor of 11 compared to what was given at 0.3V bias, and for the Al decorated samples this is an increase by a factor of just over 24. This is compares to the factors of 2.8 and 3 for the Au and Al decorated samples without the alumina layer respectively. These huge increases between potential biases are due to the fact that at around the onset potential the photocurrents are low due to the potential not being sufficient to overcome internal voltages or potential barriers. The photocurrents rapidly increase as the bias is increased and this is what is seen here at the higher bias potential. The reason for the Al decorated samples showing a larger increase is due to the higher onset potential seen in the linear sweep. The Ag decorated samples are still unresponsive at the higher bias potential which was to be expected from the linear sweep. It is clear that the alumina layer has not combatted the large charge transfer between Ag and Hematite and silver samples are still quenched more than the other metal samples.

The boxplot in figure 8-29 shows a different pattern than previous ALD samples. Despite still being lower than the undecorated samples, the differences between the Au and Al decorated samples and the undecorated hematite are less stark than previous. At 0.55V the average photocurrent for the pre-anneal Au decorated samples including the buffer layer is reduced by 33% compared to the relative undecorated films whereas, at 0.3V this difference was 79%. For Al, the increase in bias voltage has resulted in a 42% deficit in photocurrent compared to the 91% at 0.3V. These represent the lowest reductions in photocurrents after the inclusion of a metal layer seen so far. This suggests that the inclusion of the buffer layer has achieved somewhat at reducing the detrimental recombination or charge-loss effects that were experienced prior, however the alumina layer has not succeeded in revealing any plasmonic enhancement of the photocatalytic ability of the films and has actually reduced the photoresponse for the undecorated films.

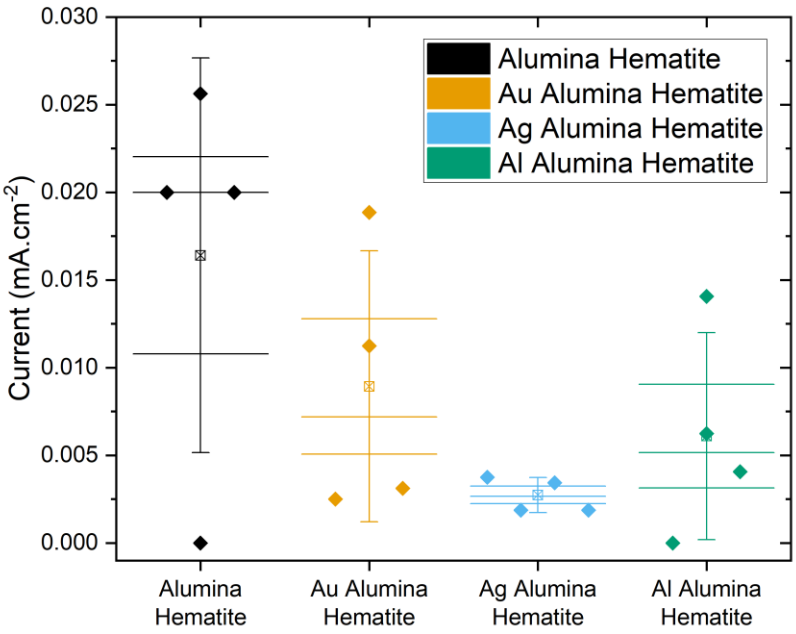

Figure 8-30 - Boxplots showing the photocurrent densities for each of the architectures after annealing. Bias potential 0.3V. Diamonds show individual sample photocurrent density values. Other markers are as previous.

The samples were annealed, as before, at 600^{o}C in air, for 30 minutes. After annealing the samples were tested again using chronoamperometry. The photocurrents under white illumination at 0.3V and 0.55V bias versus the homemade Ag/AgCl reference electrode are shown in figures 8-30 and 8-31, respectively.

After annealing the mean photocurrent at 0.3V vs Ag/AgCl (figure 8-30) for undecorated hematite electrodes with the alumina layer was (16±6) µAcm^{-2}. As before there was one sample that remained unresponsive at this bias even after annealing. This outstanding sample seems anomalous when compared to the others and is clearly affecting the mean value and the standard error from the statistics. Before annealing this value was (28±10) µAcm^{-2}, therefore the average photocurrent decreased by 43% through annealing. Previously, in the samples without the alumina layer, an increase in photocurrent was observed by annealing the samples instead here the opposite is true. Whereas before, the

anneal step led to crystallization of the hematite film which increased the photocurrent here it would seem that the alumina layer has been affected by annealing. This has resulted in the buffer layer acting as a larger potential barrier and hindering the charge carrier extraction. The alumina layer should block any dopants from migrating from the substrate into the hematite layer during the anneal step. In previous work the photocurrent densities increased after annealing and in part this is due to unintentional doping. It is possible that the alumina layer here has blocked dopants from the ITO substrate that were acting to increase the photocurrent. Usually, unintentional doping from substrate migration is assigned to tin atoms, that was not expected here due to the low concentration of tin in the ITO substrate. However, it is possible that other elements present in the ITO substrates, act to dope the hematite film. With the included alumina layer these dopants are blocked and the result is a decrease in photocurrent density after annealing. This could be tested using sensitive characterization techniques such as low energy ion scattering (LEIS) in conjunction with surface plasma etching.

Comparing this average photocurrent to that achieved by the relative samples without the alumina layer at the same bias reveals that the addition of the alumina layer has diminished the photocatalytic ability of the hematite films drastically. At the same bias the comparative films without the alumina layer gave an average photocurrent of (110±10) μAcm^{-2} giving a decrease in average photocurrent density due to the inclusion of the extra layer of 85%. Further demonstrating that the added alumina layer has not assisted in increasing the photoresponse of the hematite electrode.

For the Au decorated samples the average photocurrent from figure 8-30 is (9±4) μAcm^{-2}. The average value is unchanged compared to the pre-anneal data in figure 8-29 however, the spread of the data is increased and this is reflected in the standard error. This increase in spread of the data is shown clearly by the data points in the figure. One sample is a clear

outlier with a high photocurrent density and there are two samples now achieving photocurrents lower than the mean and outside the error. This shows that the anneal step has affected certain films in different ways. Either the anneal step and improved crystallinity in the buffer layer has led to isolate the metal nanoparticles and reduce recombination at the metal/SC interface or has reduced electron extraction and decreased the electrodes photocatalytic ability. Both of these could occur simultaneously and the photocurrent reflects which mechanism is having a stronger effect.

Without the alumina layer the gold decorated electrodes achieved an average photocurrent density of (18±5)μAcm^{-2}. The inclusion of the alumina layer therefore results in a decrease of 50% in the average photocurrent density. This decrease in photocurrent density is not as severe as was seen in the undecorated sample. This demonstrates that the inclusion of the alumina layer has acted to heal the Schottky barrier at the back-contact but the electrode is still hindered by the tunnel junction.

After annealing it is now clear that each of the silver decorated films displays some small photocurrent. The mean photocurrent for the Ag-decorated films in figure 8-30 is (2.7±0.5) μAcm^{-2}. The fact that these films now show a photoresponse shows that the crystallization of the hematite film can still have a net positive effect on the photocatalytic ability of the electrodes. Compared to the previous samples without the additional alumina layer, which gave an average photocurrent density of (10±6) μAcm^{-2}, this represents a decrease of 73% through the inclusion of the buffer layer. This is a similar level to the undecorated films suggesting that the alumina film has had little effect on mitigating the negative mechanisms that arise when incorporating Ag nanostructures into the electrode architecture. As seen in the UV-Vis the alumina layer did not mitigate the effects seen of silver metal in the electrode architecture (the enhancement of the 400nm absorption peak) and this corroborates with what is shown here.

For the Al films after annealing the mean photocurrent at 0.3V bias is (6±3) μAcm^{-2}. This shows an increase on average photocurrent by 150%. Looking at the boxplot in figure 8-30 shows that this result is dominated mainly by one highly performing electrode at nearly $15\mu Acm^{-2}$. Without this outlier the average would more likely be around the pre-annealed level. This again shows that the annealing step affects films differently and could be evidence for nonuniformity in the anneal process due or in the fabrication process that is amplified by the anneal step. This result represents an increase in photocurrent density due to the inclusion of the alumina film. Previously, without the buffer layer, the average photocurrent density was (0.6±0.3) μAcm^{-2}, giving a photocurrent increase of 90% due to the inclusion of the alumina layer. This is the only configuration that has shown an overall increase in photocurrent compared to the non-buffer layered samples. This would suggest that the added dielectric layer has blocked the migration of atoms into the hematite, and halted the unintentional negative doping that was occurring before. From the UV-Vis it was clear that the nanostructures underneath was altered during the anneal, shown by inconsistent absorption spectra. Therefore, it is unlikely that the added layer has stopped the melting of the nanostructures but has blocked the material from entering the hematite resulting in a higher photocurrent density.

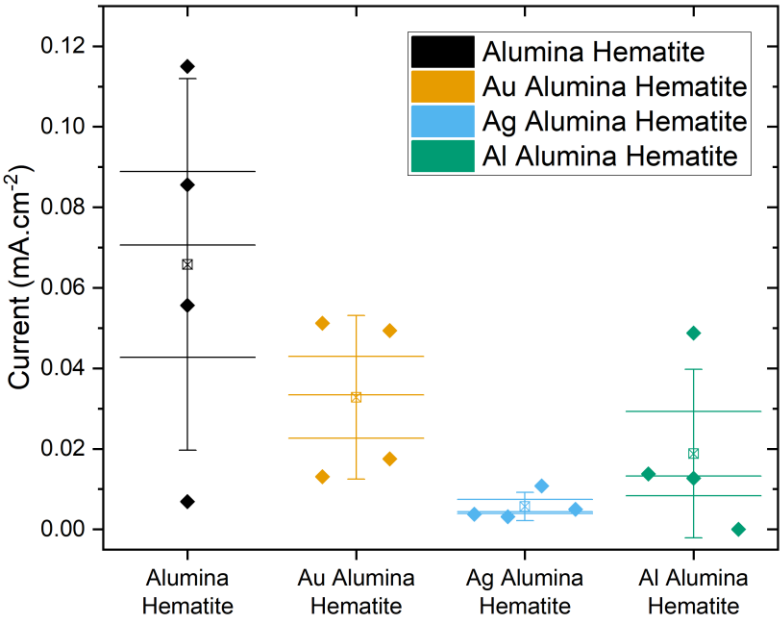

Figure 8-31 - Boxplots showing the photocurrent densities for each of the architectures after annealing. Bias potential 0.55V. Diamonds show individual sample photocurrent density values. Other markers are as previous.

The samples were also tested, as before, at 0.55V bias potential vs Ag/AgCl. The data for these photocurrents is given in the boxplot in figure 8-31. At this bias potential the mean photocurrent for the undecorated hematite electrodes with the 1nm alumina buffer layer is (70±20) μAcm^{-2}. The large error on this average photocurrent is due to the anomalous electrode that was vastly underperforming compared to the others. At this higher potential the post-annealed films still performed worse than in their pre-annealed state. This is an increase from the photocurrent at 0.3V by a factor of 4. From the linear sweep it shows that with a high onset potential and a fast increase in photocurrent with respect to potential this is somewhat expected. A large increase in photocurrent was seen across all samples at this voltage when compared to that at 0.3V and is explained through the same observations. This value for the undecorated hematite samples represents a 50% decline in photocurrent compared to the relative value for the samples without the buffer layer. This again shows

that the inclusion of the buffer layer has failed in increasing the photocatalytic ability of the electrodes and has actually had the reverse effect.

A lower average photocurrent was seen here for the Au and Ag decorated samples when compared to equivalent values for the non-buffer layered samples. The Au decorated samples gave an average photocurrent of (30±10)μAcm^{-2} representing a decrease of 40% compared to the electrodes without the buffer layer. The decrease in photocurrent due to the inclusion of a buffer layer is again less than that experienced by the undecorated hematite. This suggests that the decrease in photocurrent is mainly due to the inclusion of a tunnel junction at the back-contact between the hematite and the ITO, and that some gains are made by isolating the nanoparticles from direct contact with the semiconductor. This result also gives a decrease in photocurrent of 54% compared to the same samples prior to annealing. This suggests that the annealing has affected the buffer layer and formed a larger potential barrier for the electrons to tunnel across and be extracted.

The average photocurrent for the Ag decorated films was (6±2)μAcm^{-2} which is a decrease of 80% compared to the (30±10)μAcm^{-2} achieved without the buffer layer. This again demonstrates that the added alumina layer is adversely affecting the photocurrent and is not acting to properly isolate the Ag nanoparticles from the semiconductor layer. This is now however a measurable photocurrent density when compared to the pre-anneal values for the same samples.

The Al samples tested at 0.55V gave an increased average photocurrent when compared to the samples without the buffer layer. The mean photocurrent for the Al samples from figure 8-31 was (30±10) μAcm^{-2} giving a 50% increase in photocurrent from the samples without the alumina layer. The result here also represents a decrease of 66% decrease compared to the pre-anneal value from the same sample set again demonstrating that the anneal process has affected the underlying nanostructure layer and impacted the overall photocatalytic

activity. This value however is clearly dominated by an anomalous high achieving sample at around 45µAcm^{-2} which is stretching the mean to higher values. The median of the photocurrent value sits at 13µAcm^{-2} however this is still higher than the average value for the films without the buffer layer. Here the buffer layer has potentially benefited the films and allowed the photocurrent to increase. These films still do not compete with the standard pristine ALD hematite films however, and the added layers have not furthered the photocatalytic ability of hematite films.

8.5.5. IPCE

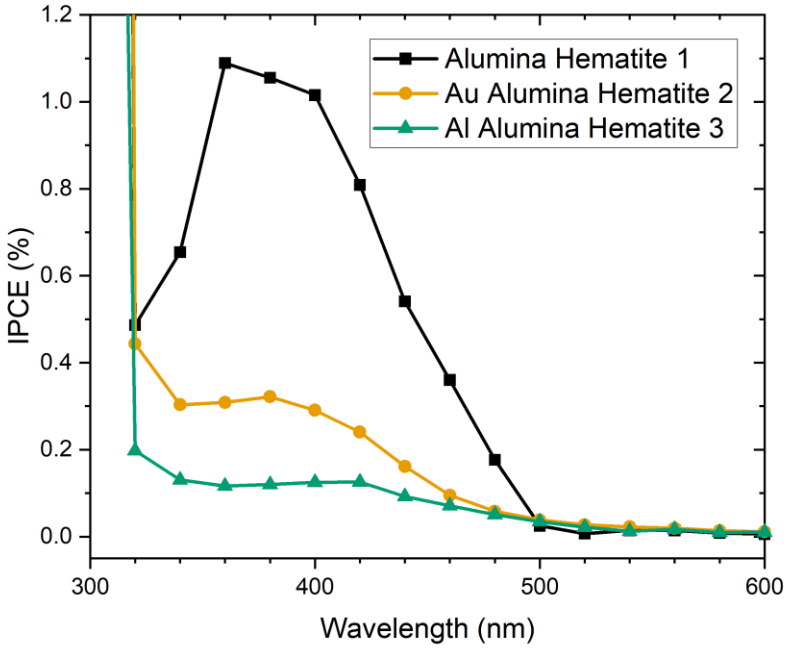

Figure 8-32 - IPCE spectra for selected samples from each architecture prior to annealing. Bias potential 0.3V Ag inclusive samples not shown due to their inactivity under illumination. Sample numbers given for continuity between figures

As before IPCE measurements were conducted. Here the IPCE was done at biases of 0.3V and 0.55V vs Ag/AgCl both before and after the 600^{o}C anneal step. The pre-anneal data at a bias of 0.3V is shown in figure 8-32. The undecorated hematite sample performed better than any of the metal decorated samples in the chronoamperometry and therefore achieved a higher IPCE percentage over the spectrum. The Ag samples did not show any photocurrent

across the potential range in the linear sweep voltammetry and therefore were not tested in the pre-anneal IPCE. The scales of all three curves are what is expected from the chronoamperometry at the same bias, with the undecorated hematite performing far better than the gold and aluminium decorated films. The Au and Al-decorated electrodes are clearly quenched along the spectrum.

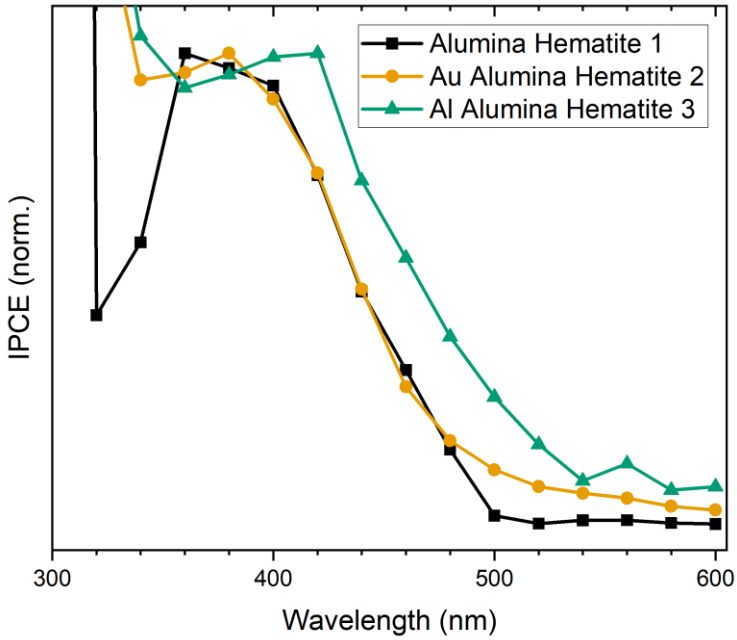

Figure 8-33 Normalized IPCE spectra for selected samples from each architecture prior to annealing. Data taken from figure 5-31. Shows relative spectral enhancement for Al decorated electrode. Bias potential 0.3V. Sample numbers given for continuity between figures.

Figure 8-33 shows the IPCE curves once they are normalized to their relative local maxima in the range 340-440nm. In the normalized Au decorated IPCE most of the spectrum follows the same shape as the hematite curve. The higher normalized IPCE in the region of 480nm to 600 nm on the Au-decorated sample curve potentially shows some stretching of the useful absorbed light into longer wavelengths than the undecorated sample. This could suggest some spectral enhancement at higher wavelengths despite the overall photocurrent being quenched by some adverse mechanism. Regardless, the standard IPCE results are low and

any enhancement is only relative. For the Al-decorated samples there appears to be some relative spectral enhancement in the region above 380nm. The peak IPCE in the visible region occurs at a higher wavelength of 420nm compared to the 360nm and 380nm for the undecorated and Au-decorated hematite electrodes respectively. This shows that the conversion efficiency of light to useful charge carriers is occurring at higher wavelength in the Al-decorated electrodes at this bias, suggesting that the inclusion of the metal nanoparticles is stretching the absorption region for the films further into the visible spectrum.

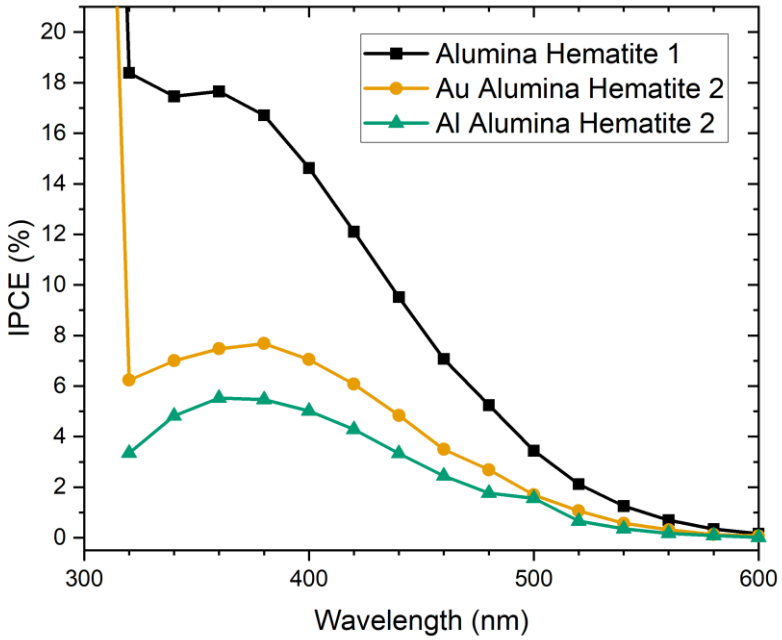

Figure 8-34 - IPCE spectra for selected samples from each architecture prior to annealing. Bias potential 0.55V. Ag not included due to poor performance. This figure shows reduced efficiency when metal layers are included. Sample numbers included for continuity.

IPCE was also performed on the samples prior to annealing at a bias of 0.55V. This data is shown in figure 8-34. At this bias the photocurrents achieved in the chronoamperometry were higher for all samples and this is also reflected in the IPCE data. The peak IPCE values here are higher than previously seen. The undecorated hematite sample IPCE shows a smoother curve overall than prior IPCE at lower biases. This suggests that this bias potential

gives an optimal performance from the electrode and the curve is more characteristic and similar to the UV-Vis absorption spectra. This similarity with the UV-Vis suggests that the absorbed light is converting to useful charge at a similar efficiency across the spectrum. This is due to the higher bias more efficiently extracting the majority carriers from the film, allowing for more efficient charge transfer at the semiconductor/electrolyte interface. Both the Au-decorated and Al-decorated films show a smooth curve to the IPCE but both are clearly quenched in comparison to the undecorated hematite. This agrees with what was seen in chronoamperometry with the Au-decorated films achieving a higher average photocurrent to the Al-decorated films.

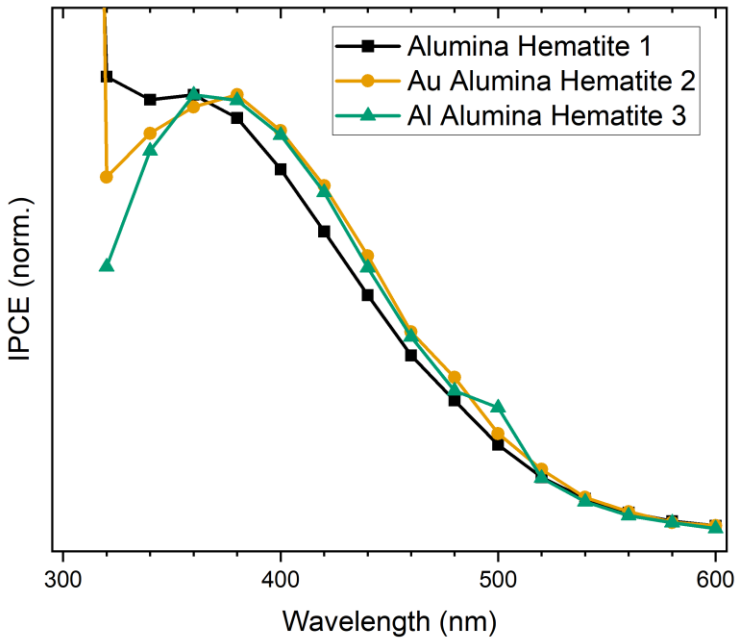

Figure 8-35 - Normalized IPCE spectra for selected samples from each architecture prior to annealing. Bias potential 0.55V. Data taken from figure 8-34. Shows reative spectal enhancement for Au and Al inclusive films

The IPCE curves were again normalized to the local maxima in the 340-440nm range. This data is shown in figure 8-35. In this figure the relative spectral enhancements are less obvious. The Au-decorated electrode IPCE peaks at 380nm compared to the 360nm for the

undecorated hematite electrode and shows some spectral enhancement in the region from the peak at 380nm to the tail at 500nm. The Al-decorated electrode showed a spectral enhancement across the same region however shows a plateaued peak at 360-380nm. This suggests that both metal nanostructures stretch the absorption to higher wavelengths. In the UV and blue region below 360nm, the undecorated hematite film IPCE plateaus and then increase quickly. This is similar to the UV-Vis spectroscopy where the hematite films became completely absorbing as the wavelength decreased. The UV- light is being absorbed by the film and in the IPCE it is shown that some of this light is converted to useful charge. In the metal decorated samples, the IPCE curves drop off at wavelengths below their respective peaks. This suggests that ultraviolet light that is absorbed in the film is not as efficiently converted to useful charge carriers compared to the undecorated film. This drop-off at lower wavelengths could be due to the fact that UV light only penetrates the first few nanometres of the films. These initial few nanometres of the film are inhabited mainly by the metal layers and therefore the UV-light is being absorbed and the energy dissipated by the metal nanoparticles through mechanisms that do not benefit the film's photocatalytic ability, such as back-scattering or localised heating. The reason why the IPCE values at 300nm are high is because the calculated incident power on the electrode at these wavelengths is very low due to absorption for glass in the light path and the low power output by the lamp at this wavelength. Therefore, if a photocurrent is measured at 300nm the calculated IPCE is very high as the incident power is very low. For the aluminium decorated films, a photocurrent could not be measured at this wavelength therefore that data point isn't included.

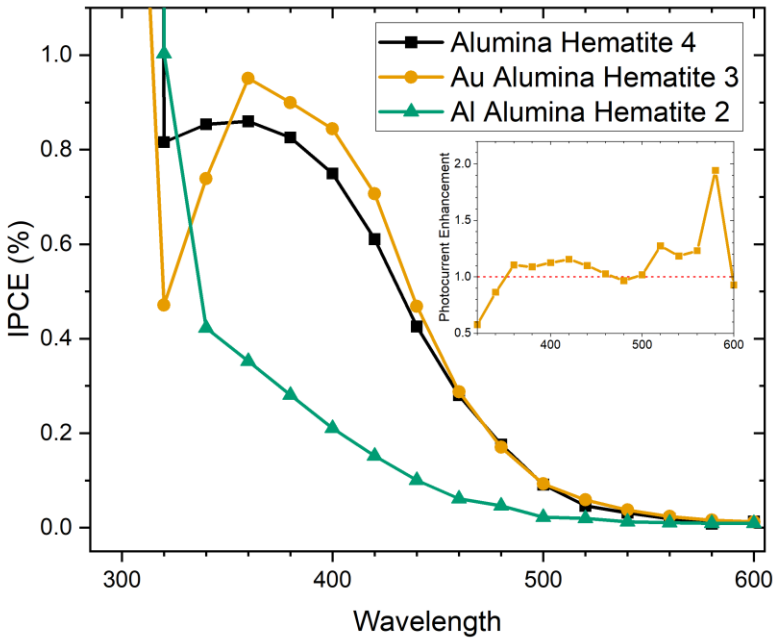

Figure 8-36 - IPCE spectra for selected samples from each architecture after annealing. Bias potential 0.3V. Sample numbers included for continuity. Real spectral enhancement shown for Au inclusive nanostructures. Al now shows reduction across the spectrum. Inset is the real enhancement factor plot.

The electrode films were then annealed at 600^{o}C for 30 minutes and the photoelectrochemical experiments were performed again. The IPCE was done at 0.3V and 0.55V as before. The 0.3V bias IPCE data is shown in figure 8-36. At 0.3V bias vs Ag/AgCl in the chronoamperometry, the silver decorated samples were practically unresponsive to light, therefore it was not possible to measure reliable photocurrents under the less powerful monochromated light. Therefore, the silver IPCE was not performed at 0.3V bias and is not included in figure 8-36. The chronoamperometry showed that the anneal step reduced the photocatalaytic ability of the films and this is supported by the IPCE. For the undecorated hematite films the peak IPCE at 360nm is 0.86% whereas prior to annealing the IPCE at the same wavelength was 1.09%. This decrease may be small but massively contrasts the effects of annealing on the IPCE shown in samples without the alumina layer. The IPCE values achieved by these samples is also much lower than the comparable result for the films that did not contain the alumina buffer layer. In Figure 8-15 the undecorated hematite sample

had an IPCE of 8.96% at its peak at 360nm. This is over an order of magnitude higher than what was achieved for the alumina layer inclusive sample again showing that the included buffer layer only hinders the photocatalytic ability of the films.

The undecorated hematite IPCE curve is somewhat characteristic despite showing more rounded features compared to the unannealed sample and also does not show the drop off in IPCE at wavelengths below 360nm. The Au decorated IPCE line now shows real spectral enhancement in the region between 360nm and 480nm. The inset plot shows the photocurrent enhancement factor given by dividing the Au-decorated IPCE values by those from the undecorated hematite film. This shows a real enhancement over most of the spectrum above the peak at 360nm. At wavelengths below 360nm the gold decorated IPCE shows a quenching of the photon conversion efficiency suggesting that the incident UV light absorbed by the film is not converted to useful charge. This would suggest that the inclusion of the gold nanostructures is enhancing the conversion of incident photons to useful charge carriers at wavelengths above 380nm but is hindering the utilisation of higher energy photons to create charge carriers and therefore the photocatalytic ability. The UV quenching of the photocurrent is hindering the overall photoresponse and this is shown by the low values of average photocurrent under white light illumination given by the chronoamperometry.

The Al-decorated film IPCE gives a line shape with no local maxima suggesting that the film's photoresponse is being quenched across the spectral range especially in the region that is most absorbing for the hematite. Therefore, the inclusion of the Al nanostructures is disadvantageous to the film's photoresponse. This quench in IPCE across the hematite absorption suggests that the light that is absorbed by the metal nanostructure has its energy dissipated through mechanisms that do not promote charge carriers in the hematite film. Essentially the aluminium layer acts to parasitically absorb a large portion of incident

photons before they can be absorbed by the hematite layer. This explains the poor performance of the Al-decorated films in the chronoamperometry.

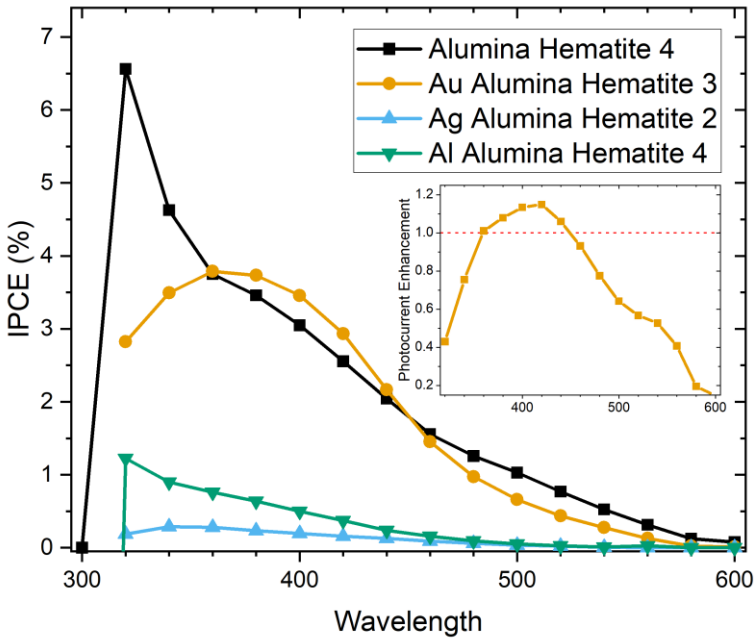

Figure 8-37 IPCE spectra for selected samples from each architecture after annealing. Bias potential 0.55V. Ag and Al nanostructure inclusive electrodes show reduction in efficiency acros the 320-600nm spectrum. Au nanostructure films show real spectral enhancement in the 360-440nm range. Inset – the real enhancement factor plot.

The IPCE measurements were additionally performed on the same samples at the higher bias of 0.55V. This data is given in figure 8-37. The overall IPCE percentage values are much lower here than was shown for the samples prior to annealing at the same potential (Figure 8-34). At this potential the line shape of the undecorated hematite IPCE differs from the same sample results at 0.3V. The local peak at 360nm is not apparent in this IPCE spectrum and instead there is a slight shoulder to the curve at 380nm. This suggests that the intraband transition in hematite that was responsible for this peak in the UV-Vis spectra and the IPCE is no longer as dynamic as previously. This peak had been less apparent in the previous higher bias IPCE spectrum but in this figure, it is almost completely gone. This could be due to the

higher bias extracting charge carriers more efficiently across the absorption spectra, or due to the added alumina layer quenching these intraband transitions.

The IPCE spectrum for the Au decorated electrode at 0.55V shows some real spectral enhancement. At 0.3V the real spectral enhancement occurred at all wavelengths above 360nm except 480nm, whereas at 0.55V the real enhancement only occurs between 360-440nm. The enhancement factor is shown in the inset plot in figure 8-37. This enhancement factor shows the photocurrent quenching at its maximum at UV and in the red regions of the visible spectrum. This damping compared to the undecorated sample either side of the peak shows that overall, the Au-decorated sample is quenched either through an added potential barrier or parasitic absorption layer apart from where the peak enhancement at 420nm is boosting the photocatalytic ability. This is also shown by the fact that the Au-decorated samples still perform worse in the chronoamperometry.

In the linear sweep and chronoamperometry, the Ag-decorated showed a photoresponse at this higher potential of 0.55V. Therefore, the IPCE was performed on the Ag-decorated electrode at 0.55V. The IPCE spectrum for the Ag-decorated samples correlates with what was shown in the chronoamperometry as the IPCE values were lower than all other samples across the spectrum. The Al-decorated IPCE shows the same shape as the 0.3V scan in figure 8-15. The spectrum doesn't show any local maxima or minima and instead shows a steady decrease in conversion efficiency as the incident photon energy decreases. This means that the conversion efficiency is mainly related to the energy of the incoming photons and not as affected by the possible electron transitions in the hematite film suggesting that the inclusion of the aluminium layer has hindered the photoresponse of the hematite across the spectrum. For the undecorated and Au-decorated samples the increase in bias voltage from 0.3V to 0.55V has resulted in increase in IPCE value by a factor of around 3.5 at 360nm, whereas for the Al-decorated sample the IPCE at 360nm has only doubled at 360nm due to the voltage

increase. This shows that the voltage increase has not affected the photocatalytic ability of this sample to the same extent.

8.6. Conclusions

In this chapter an ALD process was used to fabricate consistent hematite films on a variety of plasmonic and non-plasmonic substrates. This work represents the first reported time that hematite has been deposited onto metal nanostructures using atomic layer deposition, and the first reported time that ALD films fabricated using PEALD have been tested for their photocatalytic ability for water-splitting. A consistent comparison between the effects of identical Au, Ag, and Al plasmonic nanostructures on ALD deposited photocatalytic electrodes is also presented for the first time. The average thickness of the ALD deposited hematite films was measured as (36±1) nm using 34 AFM measurements across a scratched profile in one of the as-deposited films.

Before annealing, the hematite electrodes showed a good photoresponse verifying that the as-deposited films were photoactive hematite. The linear sweep voltammetry in figure 8-8 showed a photoresponse at biases above 0.2V. Chopped illumination chronoamperometry was used to measure a photocurrent at a bias of 0.3V. The average photocurrent for the undecorated pre-anneal hematite electrodes was (56±5) $\mu A.cm^{-2}$. The annealed hematite samples gave an average photocurrent at a bias potential of 0.3V, under white-light illumination of (110±10) $\mu A.cm^{-2}$. Here the anneal step resulted in a doubling of the average photocurrent, this was attributed to the increased crystallinity in the hematite film, shown by the Raman spectroscopy. This increased crystallinity reduces the charge recombination in the film and allows for more efficient carrier extraction at the front and back contacts. The post-annealed samples were also tested at 0.55V bias. This was done because the onset

potentials for these samples was higher than seen in the electrodeposition chapter and therefore this higher bias would be probing the photocurrent in a potential region where all films were more photoactive. The average photocurrent for the annealed undecorated hematite samples was (140±20) $\mu A.cm^{-2}$.

The metal decorated electrodes all showed lower photocurrents than the undecorated films. The chronoamperometry and the IPCE showed that despite low overall average photocurrents there were some relative spectral enhancements in conversion efficiency from the nanostructure decorated electrodes. Therefore, if it were possible to isolate the negative impacts of including another junction and recombination site in the film and promote the positive plasmonic mechanisms then plasmonic enhancement could occur. This correlates to what was seen in the electrodeposition chapter where the inclusion of a TiO_2 buffer layer on top of the gold and silver nanostructures resulted in enhancement of the photocatalytic ability of the films. A dielectric layer could be used to properly mitigate against the damping effects of the metal-semiconductor interface and maintain the plasmonic properties of the deposited film.[24,28] In order to achieve this here a 1nm Alumina buffer layer was ALD deposited on top of the metal nanostructures and blank ITO substrates prior to the ALD deposition of the hematite. Al_1O_3 was chosen as a novel aspect as SiO_2 has been broadly reported in literature.[17–19,23,25,26]

IPCE experiments were also performed on the buffer layered samples at potential biases of 0.3V and 0.55V. The IPCE measurements were taken before and after annealing and are given in figures 8-32 to 5-35. The IPCE spectra were normalized to local maxima in the 360-420nm range, this is shown in figure 8-33. Here it can be seen that there appears to be some relative spectral enhancement in the Al-decorated films in range of 380nm and above suggesting that if the quenching mechanisms had been fully removed then some plasmonic enhancement effect could have stretched the useful absorption to higher wavelengths. For the Au-

decorated films there appears to be some relative enhancement above 480nm, allowing lower energy light to be usefully absorbed. This would be expected from plasmonically enhanced films as the Au LSPR absorption peak occurs in the red region of the visible spectrum compared to the Al LSPR which occurs in the blue region.

After annealing the IPCE measurements were performed again. Here, realspectral enhancement was observed for the first time in the ALD fabricated films. Except for the measurement at 480nm, the Au decorated films showed enhancement in conversion efficiency at wavelengths above 380nm. At 0.55V the IPCE measurements for the Au decorated again showed spectral enhancement, this time in a narrower wavelength window of 360-440nm. Despite both films now operating more optimally at this higher bias potential the Au-decorated film still shows some spectral enhancement over the undecorated sample. This suggests that despite the alumina film overall quenching the photoresponse of the film, it has enabled some positive effects of the gold nanostructures presence to materialize.

In the electrodeposition chapter, the addition of a TiO_2 buffer layer led to real enhancement from the Au and Ag nanostructure decorated films. In these electrodes the buffer layer was deposited through the NSL bead mask directly onto the nanoparticles via RF-sputtering. The difference here is that the alumina layer coats the entire substrate blocking the hematite from contacting the ITO conductive substrate layer. This layer forms a physical and potential barrier to the conductive substrate and causes recombination. Future work should be done to directly coat only the metal nanostructures with a dielectric or hole-blocking material prior to the ALD fabrication of the hematite film. Selective coating of the nanostructures was shown to produce enhancement in chapter 4. Here it is shown that the Au/Al_2O_3/hematite electrodes showed relative spectral enhancement in the IPCE suggesting that overall plasmonic enhancement is possible. Selective coverage of the metal nanostructures could help to realise this.

8.7. Bibliography

1. Zandi, O., Schon, A. R., Hajibabaei, H. & Hamann, T. W. Enhanced Charge Separation and Collection in High-Performance Electrodeposited Hematite Films. *Chem. Mater.* **28**, 765–771 (2016).

2. Hou, B., Shen, L., Shi, H., Kapadia, R. & Cronin, S. B. Hot electron-driven photocatalytic water splitting. *Phys. Chem. Chem. Phys.* **19**, 2877 (2017).

3. Krishna Kumar, M., Krishnamoorthy, S., Kheng Tan, L., Yang Chiam, S., Tripathy, S. & Gao, H. Field Effects in Plasmonic Photocatalyst by Precise SiO 2 Thickness Control Using Atomic Layer Deposition. **1**, 300–308 (2011).

4. Steier, L., Luo, J., Schreier, M., Mayer, M. T., Sajavaara, T. & Grätzel, M. Low-Temperature Atomic Layer Deposition of Crystalline and Photoactive Ultrathin Hematite Films for Solar Water Splitting. *ACS Nano* **9**, 11775–11783 (2015).

5. Alfakes, B., Garlisi, C., Villegas, J., Al-hagri, A., Tamalampudi, S., Rajput, N. S., Lu, J., Lewin, E., Sá, J., Almansouri, I., Palmisano, G. & Chiesa, M. Enhanced photoelectrochemical performance of atomic layer deposited Hf- doped ZnO. *Surf. Coat. Technol.* **385**, 125352 (2020).

6. Leskala, M. & Ritala, M. Atomic layer deposition (ALD) : from precursors to thin film structures. *Thin Solid Films* **409**, 138–146 (2002).

7. Eswar, N. K. R., Singh, S. A. & Heo, J. Atomic layer deposited photocatalysts : and reactor design approaches for photo-mediated. *J. Mater. Chem. A* **7**, 17703–17734 (2019).

8. Niemelä, J. P., Marin, G. & Karppinen, M. Titanium dioxide thin films by atomic layer

deposition: A review. *Semiconductor Science and Technology* vol. 32 (2017).

9. Ramachandran, R. K., Dendooven, J. & Detavernier, C. Plasma enhanced atomic layer deposition of Fe2O3 thin films. *J. Mater. Chem. A* **2**, 10662–10667 (2014).

10. Martinson, A. B. F., Devries, M. J., Libera, J. A., Christensen, S. T., Hupp, J. T., Pellin, M. J. & Elam, J. W. Atomic layer deposition of Fe2O3 using ferrocene and ozone. *J. Phys. Chem. C* **115**, 4333–4339 (2011).

11. Pore, V., Rahtu, A., Leskelä, M., Ritala, M., Sajavaara, T. & Keinonen, J. Atomic layer deposition of photocatalytic TiO2 thin films from titanium tetramethoxide and water. *Chem. Vap. Depos.* **10**, 143–148 (2004).

12. Bachmann, J., Jing, J., Knez, M., Barth, S., Shen, H., Mathur, S., Gösele, U. & Nielsch, K. Ordered iron oxide nanotube arrays of controlled geometry and tunable magnetism by atomic layer deposition. *J. Am. Chem. Soc.* **129**, 9554–9555 (2007).

13. Sridharan, K., Jang, E., Park, Y. M. & Park, T. J. Superior Photostability and Photocatalytic Activity of ZnO Nanoparticles Coated with Ultrathin TiO2 Layers through Atomic-Layer Deposition. *Chem. - A Eur. J.* **21**, 19136–19141 (2015).

14. Kao, E., Park, H. S., Zang, X. & Lin, L. Atomic Layer Deposition of TiO 2 Nanocoatings on ZnO Nanowires for Improved Photocatalytic Stability. **2019**, (2019).

15. Lie, M., Fjellvåg, H. & Kjekshus, A. Growth of Fe2O3 thin films by atomic layer deposition. *Thin Solid Films* **488**, 74–81 (2005).

16. B. J. Y. Tan, †, C. H. Sow, *, T. S. Koh, †, K. C. Chin, ‡, A. T. S. Wee, †, A. & Ong†, C. K. Fabrication of Size-Tunable Gold Nanoparticles Array with Nanosphere Lithography, Reactive Ion Etching, and Thermal Annealing. *J. Phys. Chem. B* **109**, 11100 (2005).

17. Hanske, C., Sanz-ortiz, M. N. & Liz-marzán, L. M. Silica-Coated Plasmonic Metal

Nanoparticles in Action. **1707003**, 1–28 (2018).

18. Carretero-Palacios, S., Jiménez-Solano, A. & Míguez, H. Plasmonic Nanoparticles as Light-Harvesting Enhancers in Perovskite Solar Cells: A User's Guide. *ACS Energy Lett.* **1**, 323–331 (2016).

19. Zhang, W., Saliba, M., Stranks, S. D., Sun, Y., Shi, X., Wiesner, U. & Snaith, H. J. Enhancement of perovskite-based solar cells employing core-shell metal nanoparticles. *Nano Lett.* **13**, 4505–4510 (2013).

20. Zhang, X., Zhu, Y., Yang, X., Wang, S., Shen, J., Lin, B. & Li, C. Enhanced visible light photocatalytic activity of interlayer-isolated triplex Ag@SiO2@TiO2 core-shell nanoparticles. *Nanoscale* **5**, 3359–3366 (2013).

21. Abdi, F. F., Dabirian, A., Dam, B. & Van De Krol, R. Plasmonic enhancement of the optical absorption and catalytic efficiency of BiVO 4 photoanodes decorated with Ag@SiO 2 core–shell nanoparticles. *Phys. Chem. Chem. Phys. Phys. Chem. Chem. Phys* **16**, 15272–15277 (1527).

22. Thimsen, E., Le Formal, F., Grätzel, M. & Warren, S. C. Influence of Plasmonic Au Nanoparticles on the Photoactivity of Fe 2 O 3 Electrodes for Water Splitting. *Nano Lett.* **11**, 35–43 (2011).

23. Li, J., Cushing, S. K., Meng, F., Senty, T. R., Bristow, A. D. & Wu, N. Plasmon-induced resonance energy transfer for solar energy conversion. *Nat. Photonics* **9**, 601–607 (2015).

24. Pala, R. A., White, J., Barnard, E., Liu, J. & Brongersma, M. L. Design of plasmonic thin-film solar cells with broadband absorption enhancements. *Adv. Mater.* **21**, 3504–3509 (2009).

25. Jahn, M. *et al.* Plasmonic nanostructures for surface enhanced spectroscopic methods. *Analyst* **141**, 756–793 (2016).

26. Lu, Y., Yin, Y., Li, Z.-Y. & Xia, Y. Synthesis and Self-Assembly of Au@SiO 2 Core−Shell Colloids. *Nano Lett.* **2**, 785–788 (2002).

27. Li, J., Cushing, S. K., Zheng, P., Meng, F., Chu, D. & Wu, N. Plasmon-induced photonic and energy-transfer enhancement of solar water splitting by a hematite nanorod array. *Nat. Commun.* **4**, 2651 (2013).

28. Sabaeian, M., Heydari, M. & Ajamgard, N. Plasmonic excitation-assisted optical and electric enhancement in ultra-thin solar cells: The influence of nano-strip cross section. *AIP Adv.* **5**, (2015).

29. Kasap, S., Koughia, C. & Ruda, H. E. Electrical Conduction in Metals and Semiconductors. in *Springer Handbook of Electronic and Photonic Materials* (eds. Kasap, S. & Capper, P.) 1 (Springer International Publishing, 2017).

30. De Faria, D. L. A., Venâncio Silva, S. & De Oliveira, M. T. Raman microspectroscopy of some iron oxides and oxyhydroxides. *J. Raman Spectrosc.* **28**, 873–878 (1997).

31. Tipler, Paul A.; Llewellyn, R. a. Modern Physics - Vol.2. in *Modern Physics Fifth Edition* (ed. Tipler, Paul A.; Llewellyn, R. a.) 196 (W. H. Freeman and Company, 2008).

32. Lohaus, C., Klein, A. & Jaegermann, W. Limitation of Fermi level shifts by polaron defect states in hematite photoelectrodes. *Nat. Commun.* **9**, 1–7 (2018).

33. Zhou, Y., Shim, J. W., Fuentes-Hernandez, C., Sharma, A., Knauer, K. A., Giordano, A. J., Marder, S. R. & Kippelen, B. Direct correlation between work function of indium-tin-oxide electrodes and solar cell performance influenced by ultraviolet irradiation and air exposure. *Phys. Chem. Chem. Phys.* **14**, 12014–12021 (2012).

34. Dweydari, A. W. & Mee, C. H. B. Work function measurements on (100) and (110) surfaces of silver. *Phys. status solidi* **27**, 223–230 (1975).

35. Michaelson, H. B. The work function of the elements and its periodicity. *J. Appl. Phys.* **48**, 4729–4733 (1977).

36. Kittel, C. Introduction to Solid State Physics, 8th edition. *Wiley & Sons, New York, NY* (2004).

37. Garnett, E. C., Smith, W. A., Digdaya, I. A., Adhyaksa, G. W. P. & Trzes, B. J. Interfacial engineering of metal-insulator- semiconductor junctions for efficient and stable photoelectrochemical water oxidation. *Nat. Commun.* **8**, 1–8 (2017).

9. Molecular Conductance Measurements on Plasmonic Substrates

9.1. Overview

This section outlines the attempts to observe the effects of performing molecular conductance measurements through molecules attached to plasmonic nanoparticles on a substrate. Figure 9-1 shows schematics of the molecules that were tested, these were A.) 1,9-nonanedithiol, B.) 1-decanethiol, and C.) a molecular wire referred to as 9V9. Of these molecules only the conductance value for the 1-decanethiol has been measured and directly explicitly reported in literature.[1] The conductance values of 1,10-decanethiol has been reported in the literature[2] and it is expected that 1,9-nonanedithiol will be more conductive due to the shorter carbon chain.[3] The value for conductance of 1,9-nonanedithiol for comparison in this work was at 1.39 nS, extrapolated from a graph published by Haiss[3]. The conductance value for 1-decanethiol given by Frisbie[1] using a similar technique on a gold slide was 0.077nS. Viologen containing molecular wires with ethyl chains of 10 carbons (10V10) have been measured and the conductance reported. It can be expected that the measured value for 9V9 will be higher than the 0.10 to 0.19nS range measured for 10V10.[4]

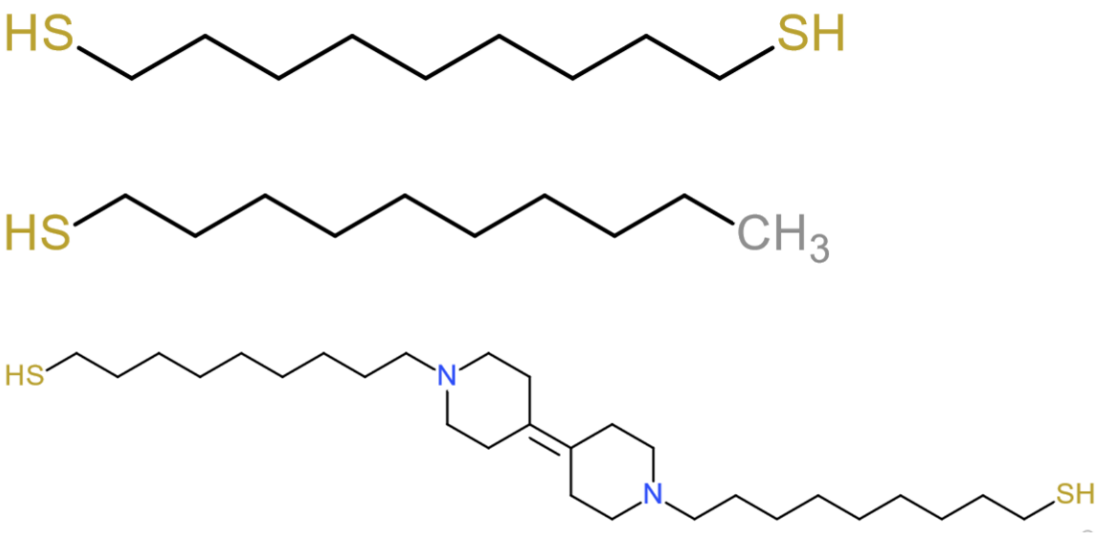

Figure 9-1 Schematics of the molecules that were tested for conductance on plasmonic substrates.A.) 1,9-nonanedithiol, B.) 1-decanethiol, and C.) a molecular wire referred to as 9V9.

Two types of plasmonic substrates were utilised during this work schematics of the experimental configurations are shown in Figure 9-2. Initially, synthesised spherical gold nanoparticles (AuNPs) were immobilized onto a gold substrate through immersion, acting as a plasmonic substrate as shown in Figure 9-2. The spherical AuNPS were attached to the monolayers grown on the gold slides through immersion in NP solution for 20 minutes. The triangular array substrates were fabricated through nanosphere shadow lithography as described previously. As shown in figure 9-2 the self-assembled monolayers of the molecules were formed directly onto the nanostructure surface by immersing the nanostructured slides in solution of the target molecule.

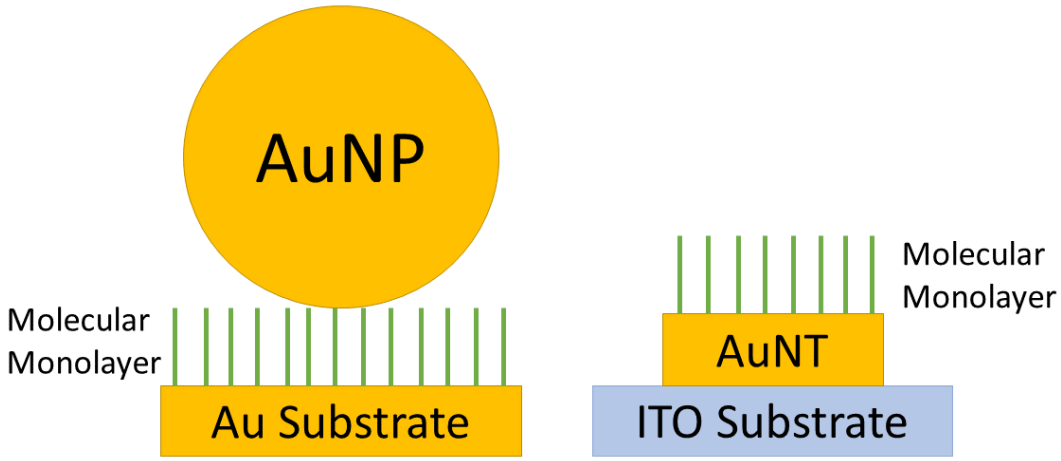

Figure 9-2 Diagrams showing the two different plasmonic configurations. A.) Molecular monolayer is grown onto the gold substrate, the AuNPs are then immobilized on top of the monolayer through immersion. AFM tip is brought into contact with the AuNP. B.) monolayer grown directly onto the gold nanotriangles. AFM tip is brought into contact with the monolayer.

Conductance measurements were taken using contact mode conductive atomic force microscopy (C-AFM) as outlined by Frisbie[1] and scanning tunnelling microscopy (STM). Molecular monolayers were grown on top of Gold on glass substrates and gold plasmonic nanostructures. The conductive probes were used to contact the molecular layers and run current-voltage measurements, which could then be used to determine the measured

conductance. Conductance values were calculated by taking the gradient of the curve around the origin of the current-voltage plots.

9.2. Introduction

Conductance determination of molecular wires has been well studied through various techniques such as mechanical break-junction, contact-mode AFM, and STM based methods such as STM break-junction and the time-dependent I(t) method. Plasmonic nanoparticles have also been used to enhance the measured conductance of molecular wires by integrating plasmonic nanostructures into the measurement architecture.[3,4]

The AFM method for contacting the monolayer or nanoparticle in this chapter was taken from Wold and Frisbie.[1] In the paper they probe the conductance of self-assembled monolayers (SAMs) of alkanethiols on Au substrates using conducting probe atomic force microscopy (C-AFM) with a gold coated SiN_3 tip. When using AFM techniques to contact molecular monolayers it is important to calibrate the force applied to the monolayer in order to avoid breaking through the monolayer and contacting either the molecules in the chain, or the substrate below.[1–3,5,6] By taking current voltage characteristics of the monolayer at a range of applied forces it is possible to calibrate the experiment to ensure that the cantilever tip is in contact with the SAM and not penetrating the monolayer, or directly contacting the substrate below. This is important in order to get accurate readings as penetrating the monolayer would result in lower resistances as the molecular wire length decreases.[1] The observed conductance should lower as the force increases due to the tip penetrating the monolayer. Current-voltage characteristics of metal-metal contact are observed at high enough forces for the monolayer to be completely penetrated and contact to be made with the substrate below.[1] This calibrated force can then be used in the subsequent data acquisitions.

Once the setpoint has been calibrated data can then be collected. Electrical contact is made to the samples such that they are connected to a common earth with the C-AFM module. Tip-sample bias voltages can be controlled through the external electronics of the C-AFM apparatus[5,7,8] The C-AFM tip provides a nanoscale electrical probe which means that increased voltage results in very high energy densities and a propensity to damage or sputter the molecular monolayers. Due to the high resistance in the molecular wires and necessity for low voltages, highly sensitive current meters must be used. [1,5,9,10] With control of the applied voltage across the tip and sample and sensitive measurement of the current flow, current-voltage (I/V) measurements can be taken.

Scanning tunnelling microscopy can also be used to measure molecular conductance through methods such as the STM break-junction[3,11–13] and STM I(t) method[3,7,8]. The scanning tunnelling microscopy techniques used in this work operate in much the same way as the C-AFM technique, referred to as the STM I(V) method[4]. The STM set-point is calibrated in the same way as C-AFM and the sample is electrically connected through a picoammeter in the external electronics in an identical manner.[14] Current voltage statistics are measured by bringing the STM tip to a tip-molecule separation distance defined by the calibrated set-point to make contact with the molecular monolayer. It is then possible to take readings of the current whilst a bias voltage is swept.[4,7,8,14]

For both the AFM and STM methods typically 100s of current-voltage scans are taken with the probe in the same position. These scans can then be filtered so that erroneous scans where the junction was broken can be removed. The data can then be averaged to show an average trace for the molecular junction[1,3,4,7,8,11,13,14] The I/V curves can be interpreted in multiple ways depending on the electronic properties of the junction. The first derivative of an I/V measurement gives the resistance of the junction at that point, the reciprocal of the resistance then gives the conductance. In order to quote an accurate value for the

conductance of a molecular junction the gradient of the I(V) curve is measured at the linear section at low voltages or simple where the plot crosses the origin.

9.3. Substrate Preparation and Characterization

9.3.1. Immobilization of AuNPs onto molecular monolayer

Synthesised spherical AuNPs were attached on top of the molecular monolayers that were to be tested. This was done by initially growing the molecular monolayers on gold substrates and then immersing the substrates in an aqueous AuNP solution. In order to optimise the AuNP coverage on the gold substrate various immersion times were applied to different substrates and imaged using AFM.

Au substrates were cleaned by sonication in isopropanol and ethanol. Cleaned Au substrates were immersed in a 2mM 9V9 in methanol solution for 18hrs in order to cover the slides with a monolayer of the 9V9 molecule. The slides were then rinsed with ethanol to rinse off the excess 9V9 solution. The functionalised slides were then immersed in the as-synthesised solution of AuNPs. The estimated concentration of NPs in this solution was 7.6×10^{11} NPs/ml taken from the paper by Bastús[15]. The slides were immersed for 2 mins, 20 mins, and 2hrs individually and imaged using AFM. Good coverage of the particles is necessary in order to find isolated nanoparticles easily. If the particles are sparse then it will be inefficient to search for suitable nanoparticles that can be tested for conductance. Good spacing is necessary to ensure only one particle is contacted and that there is no coupling of the plasmonic resonance between particles. Too high a coverage would result in large aggregations and isolated particles will be difficult to find and measure.

Figure 9-5 shows the AFM images of the substrates after the various immersion times. Figures 9-5a, 9-5b and 9-5d were taken using contact mode AFM. The particles appear triangular in shape and are aligned in the same direction. This is actually due to tip-imaging in this scanning configuration and is not a true image. In Fig. 6-5c non-contact (AAC) mode

was used and the nanoparticles appear more spherical. Fig. 6-5a shows an AFM image of the gold substrate that was immersed in the AuNP solution for 2 mins. The gold nanoparticles sparsely populated the surface and large aggregations were seen at Au substrate crystal boundaries. Crystal boundaries on the substrate surface are visible here due to the different surface energies interacting with the AFM tip. Figs. 6-5b and 6-5c show AFM images taken of the substrate that was immersed for 20 minutes. In Fig. 6-5b aggregation is seen around the crystal boundaries on the substrate but isolated particles were easily identified across the substrate area. Figure 9-5c shows a good area of isolated nanoparticles that were easily located. Figure 9-5d shows a contact mode AFM image of the substrate that was immersed for 2 hours. The surface large areas of nanoparticles that have aggregated together, and although single particles are visible, they are not sufficiently separated from neighbouring particles. Therefore a 20-minute immersion was chosen for optimal coverage of nanoparticles. Herein, gold substrates were immersed in the AuNP solution for 20 minutes.

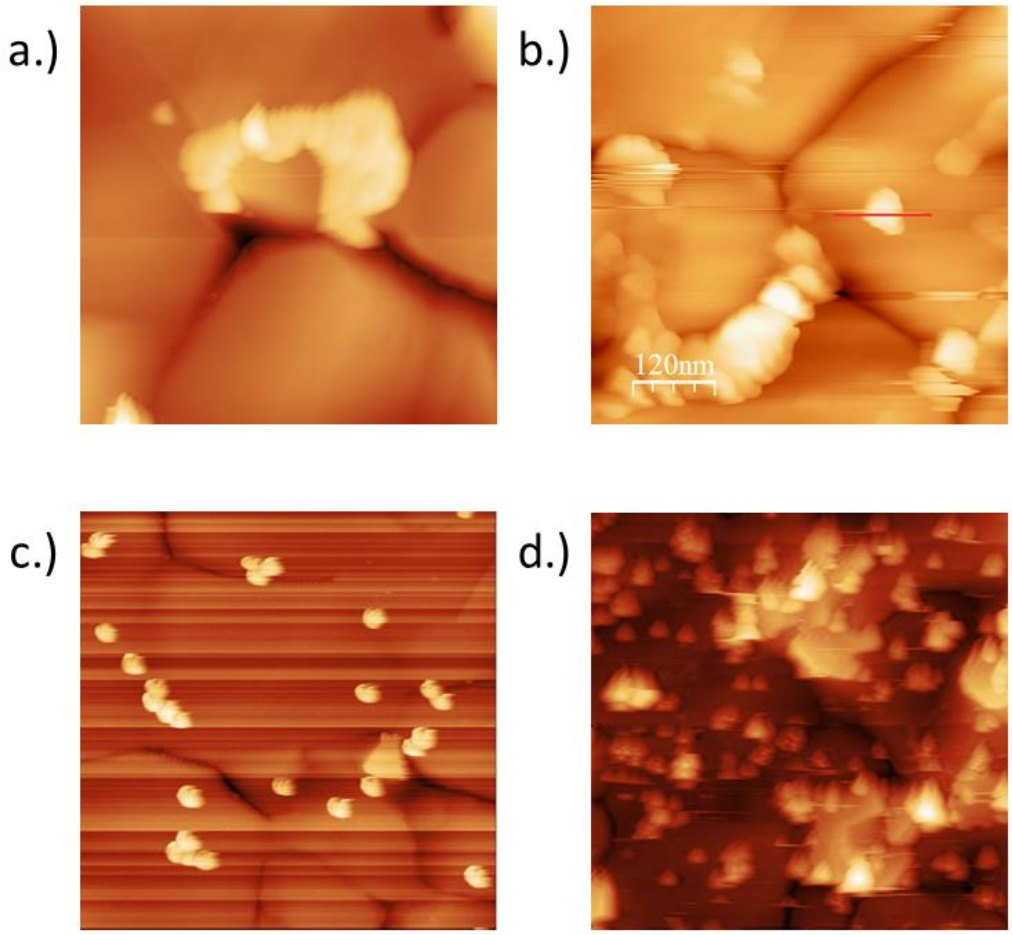

Figure 9-3- AFM images of Au substrate immersed in the AuNP solution for various times. A.) Contact mode 2 min immersion showing low coverage. B.) Contact mode 20 min immersion showing good coverage. C.) Non-contact AFM image of 20-minute immersion showing good coverage. D.) Contact mode AFM image of 2 hr immersion showing substrate completely covered.

9.3.2. Triangular nanoarrays

Nanostructured plasmonic substrates were fabricated through the nanosphere shadow lithography process outlined in the experimental methods section using both the 800nm and 300nm diameter latex beads. The 800nm bead mask produced nanotriangle arrays with an average side length of 200nm. As seen from the UV-Vis spectroscopy results in figure 9-6, these nanostructures did not show a strong absorbance or well-defined LSPR in the visible range which was to be expected due to their large size. The 300nm bead mask revealed nanotriangle arrays with average triangle side length of 90nm. These nanostructured substrates showed a large absorption peak at 800nm. Initially the larger nanotriangle arrays

were utilised in order to test the methodology of the conductance methods, before the 90nm side length arrays were tested.

In order to functionalize the gold nanotriangles, the 9V9 molecule was firstly deprotected as described by Haiss et al.[4] 9V9 monolayers were grown the Au nanotriangle decorated ITO slides through an 18hr immersion in a 2mM 9V9 MeOH solution.

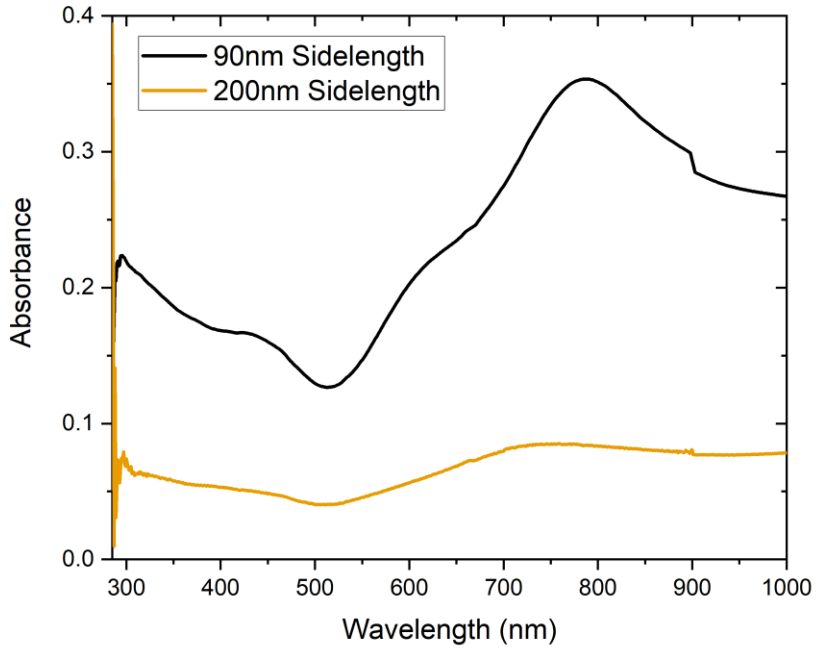

Figure 9-4 - UV-Vis spectroscopy results for the 90nm side length Au triangular arrays (black line) and the 200nm side length Au triangular arrays (yellow line). Shows higher absorbance from the smaller nanoparticles. 90nm Au nanotriangles show LSPR absorbance peak at ~780nm.

9.4. The Effects of Plasmonic Spherical AuNPs on Molecular Conductance

In order to perform I-V measurements on the SAMs, contact mode C-AFM was used. A conductive Au or Pt tip was used in order to come into contact with the surface by controlling the AFM set-point. The probes used were NT-MDT Contact STM probes CSG10 series with Pt

or Au coatings. For each contact point at least 200 scans were taken. Previously Figure 9-2 shows diagrams of the two substrate configurations that were used. For the AuNP configuration a self-assembled monolayer of the molecule that was to be tested was grown directly onto the gold substrate, the 31nm AuNPs were attached to the monolayer by submerging the gold slides into the AuNP solution as discussed previously. The substrates were then imaged in the AFM to locate isolated spherical nanoparticles and to verify that the immobilization of the nanoparticles was successful. The imaging AFM tip was changed to a conductive tip and a suitable isolated nanoparticle was located. Additionally, STM was used to measure the effects of the plasmonic AuNPS on the conductance of the molecular monolayer, this a similar method using an STM probe instead of AFM. A similar process was used for the nanotriangle array structures. The molecular monolayers were grown directly onto the gold nanodecorated substrates and then rinsed and placed into the AFM. An area of good, consistent coverage of nanotriangle was located using the AFM imaging. When an ideal location was found the tip was changed for the conductive AFM tip. This was made possible as the ideal areas in the nanotriangle arrays were of large scale due to the lithography process and certain substrate areas were identifiable through the optical camera in the AFM set-up. The conductive AFM was then brought directly into contact with the nanotriangle that was to be tested.

9.4.1. C-AFM measurements of 9V9 monolayers.

The 9V9 molecule was attached to the gold slide surface by immersing the cleaned gold slides in a 2mM solution of 9V9 in MeOH. The gold spherical nanoparticles were immobilized onto the surface by submerging the functionalised gold slides in the AuNP solution for 20 minutes. AuNPs on the surface were successfully imaged using both contact and non-contact mode AFM with non-conductive SiN AFM tips. However, when the gold coated conductive tip was used to image the surface the nanoparticles disappeared. It was not possible to image the surface in non-contact mode with the gold coated conductive AFM tip as the conductive tips

are too stiff to drive at resonance without breaking the cantilever. The contact-mode imaging with the conductive tip led to the tip lifting the nanoparticles and sweeping them aside. This made it impossible to properly contact a AuNP attached to the surface as they could not be properly located without sweeping them away. This was due to an experimental issue that could not be resolved. With a conductive tip attached it was not possible to image the surface in non-contact or tapping mode due to the rigidity of the cantilever and therefore contact mode AFM imaging had to be used. Although possible the NanoNavigator software would not allow for a low enough set-point force to be used when imaging and therefore the tip was heavily contacting the surface and disrupting the nanoparticles as the raster scanning was performed.

9.4.2. STM conductance measurements of 9V9 monolayers.

Due to the inability of the C-AFM method to contact AuNPs on the 9V9 monolayer STM was employed. The substrates used were identical to those used in the C-AFM measurements. Au and Pt STM tips were used and compared for the results. The conductance was measured by running I-V measurements once the surface had been contacted. The I-V curves were taken in contact with an AuNP and contacting the monolayer directly on the substrate. The substrate was successfully imaged to locate isolated NPs on the surface.

9.4.2.1. STM Set-point Optimization

In order to make a good electrical contact with the AuNPs a suitable STM setpoint must be chosen. This setpoint defines the force at which the STM tip connects to the NP surface. In order to identify a good setpoint to use, I/V curves at various setpoints were taken on a AuNP immobilized onto the gold substrate. Conductance values are measured by taking the gradient of the line about the origin.

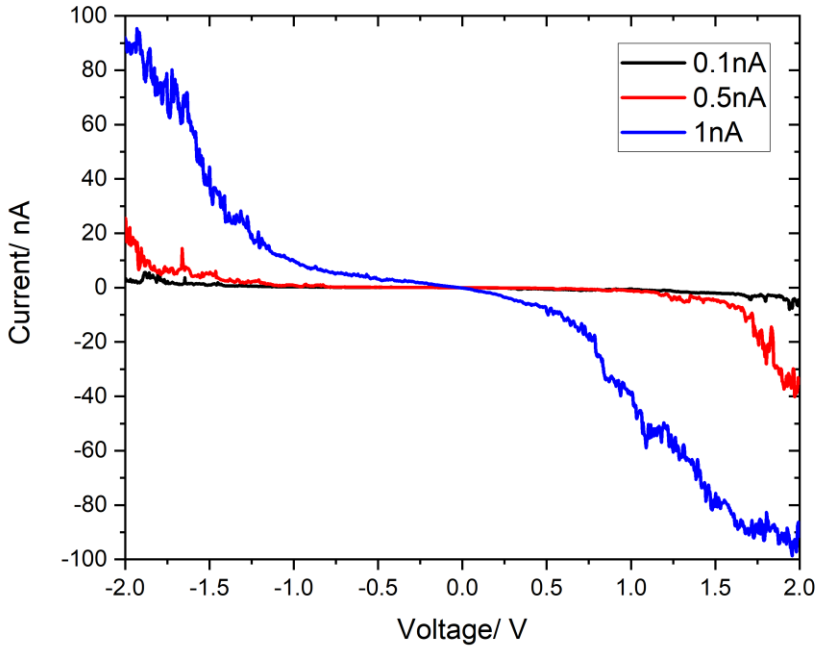

Figure 9-5 – I/V characteristics for 9V9 on Au substrate taken with the STM tip placed above an AuNP immobilized on the monolayer at various setpoints.

Figure 9-5 shows the I/V data taken from the STM tip placed above a AuNP on the 9V9 monolayer. At a setpoint of 0.1nA there is only a very slight current at extreme biases, this suggests that the tip is not contacting the NP surface. At 0.5nA there is clearly higher current measured at the ends of the bias range. This shows that the tip is closer to the surface and now contacting the AuNP surface. At a setpoint of 1nA the current increase massively suggesting that the AuNP is now being pushed into the monolayer creating higher conductance pathways in the monolayer. When the tip contacts the metal substrate directly a short circuit is expected showing a near infinite conductance and saturation of the current. At 0V bias there should also be a 0A current measurement, in the figure there is clearly an offset which is caused by the instrument pre-amplifier.

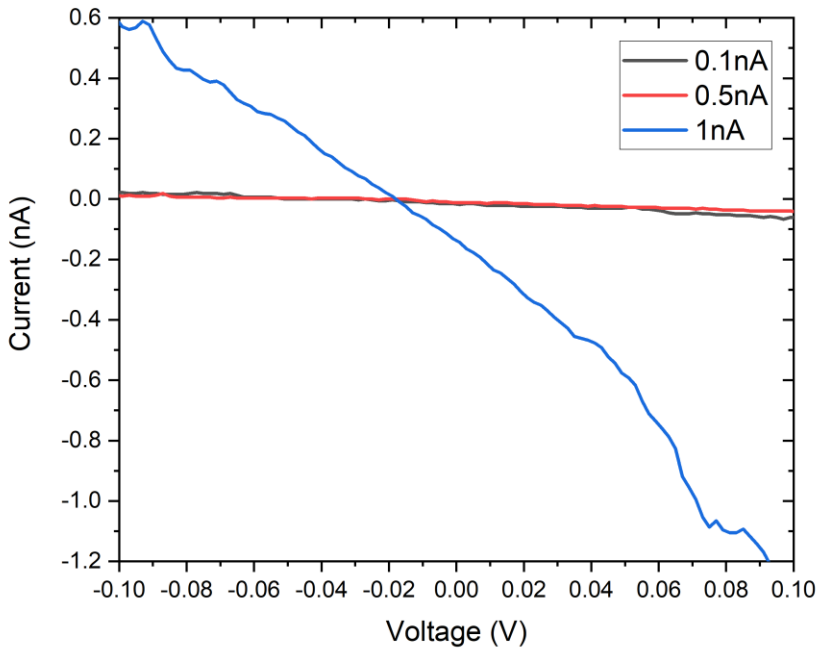

Figure 9-6- I/V characteristics from Figure 1-17 showing where the fits were chosen from. The data was fitted between -0.05V and 0.05V.

In order to find the conductance measured in the system the graph is isolated between -0.1V and 0.1V. The gradient of the line around the origin gives the measured conductance. Figure 9-6 shows the same data as in figure 9-5 but confined to -0.1V and 0.1V on the x-axis. A linear fit was done in OriginPro across the -0.1V to 0.1V range in order to find the conductance and the error. At 0.1nA and 0.5nA the measured conductance values were (0.37±0.01) nS and (0.32±0.01) nS, respectively. This shows very little change in measured conductance despite the change in contact to the AuNP. At 1nA setpoint the conductance was measured to be (8.08±0.05) nS which is far higher than the expected value for 9V9. This confirms that the monolayer is now being compressed forming higher conductance pathways.

Further experiments used a set-point of 0.1nA, this was shown to be sufficient to achieve reliable conductance measurements without contacting the nanoparticle on the substrate. Direct contact of the nanoparticle should be avoided as it is possible for the AuNP to

functionalise to the metal tip and be removed from the substrate, contaminating the STM tip in the process.

9.4.2.2. Au STM Tip vs Pt STM Tip

When using an Au STM tip in conjunction with an Au substrate it is possible to excite plasmon modes in the tip-substrate gap. This phenomenon has been used in tip enhanced Raman spectroscopy (TERS) in order to boost the sensitivity of Raman on single or multiple molecules.[16,17] This gap mode could interfere with the results when attempting to observe plasmon enhanced molecular conductance using an Au STM tip on a gold substrate through hybridization of the plasmon modes. The differences between results taken using a plasmonic and non-plasmonic metal tip were compared in order to detect whether an Au tip would create unwanted plasmonic interference.

The lasers were set to illuminate the substrate from the side as the gold slides were not transparent. A red 644nm laser and a blue 473nm laser were used to illuminate the substrates as I/V curves were taken. The I/V curves were taken between a voltage range of −0.8V to 0.8V. The current voltage measurements were taken with no illumination and under the illumination of either laser. These measurements were done on both contact with a AuNP and by contacting the monolayer on the substrate directly nearby the AuNP.

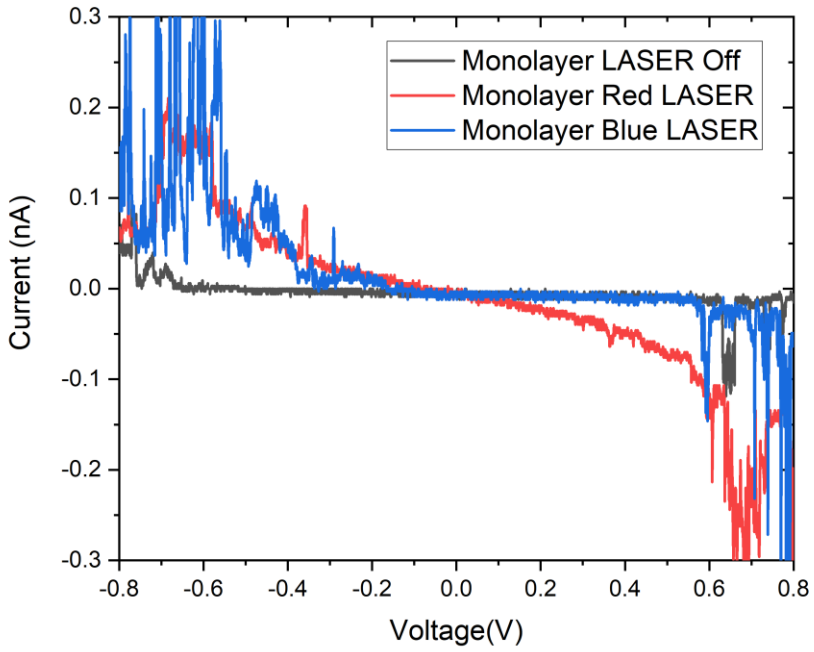

Figure 9-7 – I/V characteristics for 9V9 on Au substrate taken using Au Tip contacted to the monolayer with no illumination and illuminated by either the red 644nm laser (red line) or blue 473nm laser (blue line).

Figure 9-7 shows the I/V measurements taken using an Au STM tip in contact with the monolayer directly on the Au substrate. Without illumination very little current was measured over the bias range. The system is essentially non-conductive with a calculated conductance between ±0.5V of (7.9±0.1) pS which is below the sensitivity of the equipment. The IV curve for the blue laser illumination shows a rectification pattern. The conductance measured between -0.5V and 0V by taking the gradient of the line was (0.177±0.03) nS whereas between 0V and 0.5V the conductance was (9.9±0.5) pS. This shows the rectification for reverse bias whereby at negative bias the system shows conductance similar to the red illumination trace and at positive bias voltages no conductance is measured as per the unilluminated case. The gradient of the line between ±0.5V, averaging over the rectification effect for the blue illumination was (0.067±0.001) nS. When the substrate was illuminated with the 644nm red laser the system became conductive. By taking the gradient of the line

between ±0.5V a conductance of (0.1164±0.0005) nS was measured. This represents an enhancement factor of 14.7. Disregarding the rectification effects seen for the blue laser, the highest consistent conductance was seen when illuminating the surface using the red laser. This could be due to some plasmonic effects. For example, if there is a plasmonic nanogap mode between the tip and gold substrate. As seen in the FDTD simulations (figure 6-7b) with an AuNP on an Au substrate, a strong field enhancement is seen in a gap of 1nm. The set-up with an Au STM tip contacting a short molecule on an Au substrate is analogous to the AuNP on Au substrate with a 1nm gap configuration and therefore a strong E-field intensity enhancement would be expected in this gap. The excitation of this plasmonic mode could act to boost the conductance of the molecules in the junction by exciting charge carriers through resonant energy transfer. It is also possible that the laser is heating the substrate and increasing charge transfer between the tip and the substrate through the molecule.

In both illuminated cases conductance value was increased compared to the unilluminated system. Under blue illumination this conductance showed rectifying behaviour. The conductance values may have been increased by a higher temperature aiding the flow of charge carriers through the molecules or some tip enhanced plasmon mechanism, such as in TERS, whereby a large e-field enhancement is seen in the STM tip/substrate gap as in the simulation previously with AuNPs.[16–18] To observe whether the laser light is heating the substrate and the effects seen are temperature dependent a Pt tip was used. With a Pt tip there would be no tip/substrate gap mode so if enhancement is seen with a Pt tip then plasmonic effects would be ruled out.

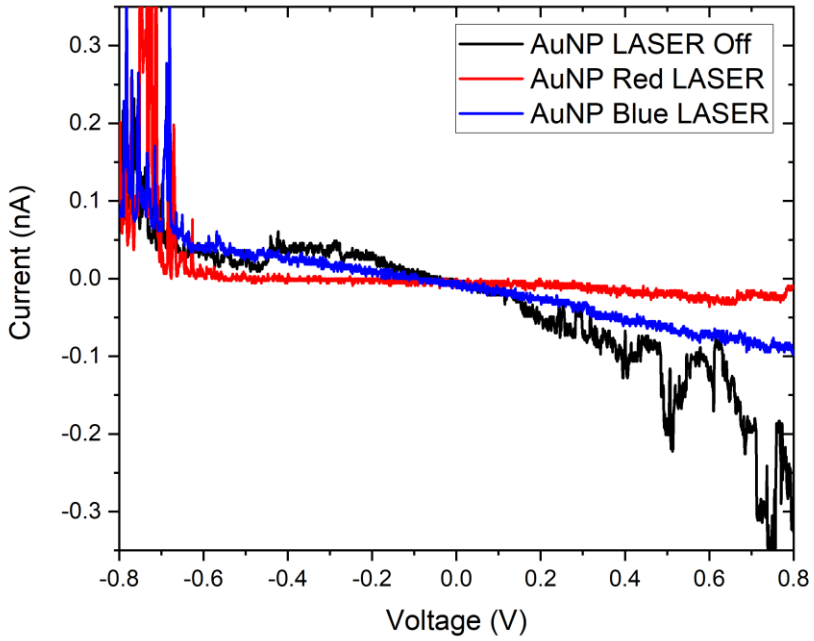

Figure 9-8 - I/V characteristics for 9V9 on Au substrate taken using Au Tip contacted to an AuNP immobilized on to the monolayer with no illumination and illuminated by either red 644nm laser (red line) or blue 473nm laser (blue line).

Figure 9-8 shows the I/V traces taken with the Au STM tip placed above an AuNP immobilized on the surface. Here a different trend is observed with both the unilluminated and the blue laser traces now showing conductance and the red laser trace showing very little to no conductance. Under no illumination the conductance measured between ±0.5V was (0.152±0.001) nS. It is expected that a higher conductance would be measured by contacting an AuNP on the surface than the monolayer directly because there is likely to be more molecules in the conduction pathway. This is because the AuNP contacts more molecules on the substrate than the STM tip alone due to the larger surface area. From the graph it is clear that the red laser illuminated trace is showing little conductance. Measured using the gradient the conductance between ±0.5 V was (0.0184±0.0002) nS. For the blue laser trace the conductance was (0.0957±0.0002) nS. In both the illuminated cases the conductance of the system was reduced. This is the opposite effect than was seen in the tip-to-substrate

configuration. It is expected that the presence of the Au-tip and its associated plasmon modes will interfere with the AuNP and substrate plasmon modes. The AuNP plasmonic modes may be damped by the presence of the Au STM tip and this would result in no plasmonic enhancement in the conductance. That would likely result in similar conductance measured for all illumination states but here that is not the case. Both illuminated experiments revealed lower conductance than the nonilluminated experiment. It is possible that an increase in temperature locally is confined to the AuNP-substrate gap and molecules are ejected from the gap reducing the conductance.[18,19] In each of these cases however mor data must be taken to fully realise the effects seen. This data was taken as an optimization step for further experimentation and therefore may be insufficient to reach strong conclusions.

To investigate whether any of the effects seen above were due to the presence of a gold STM tip, and therefore due to some added plasmon modes, the same experiments were ran using a Pt STM tip. The Pt metal tip should not induce any gap or tip plasmon modes and therefore, by comparing the two datasets, it may be possible to account for any additional plasmonic effects due to Au tip. Figures 9-9 and 9-10 show the I/V characteristics taken using the Pt STM tip placed above the monolayer and the AuNP respectively. Gradients of the lines were used to find the measured conductance of the system.

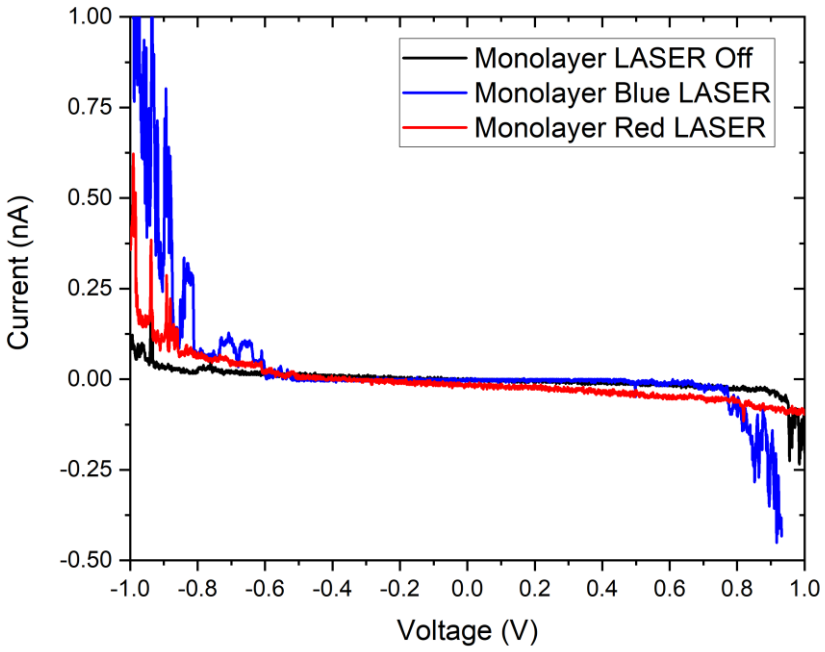

Figure 9-9 - I/V characteristics for 9V9 on Au substrate taken using Pt Tip contacted to the monolayer with no illumination and illuminated by either the red 644nm laser (red line) or blue 473nm laser (blue line).

Figure 9-9 shows the I/V curves taken using the Pt Tip taken above the monolayer directly. These I/V measurements were taken between ±1.0 V bias voltages. Without the laser the trace looks fairly nonconductive across most of the voltage range with some current flow at the extreme biases. With the blue laser on, the I/V still shows little conduction across most of the voltage range but with a lower breakdown voltage where the current seems to take off at around ±0.6 V. There is a clear gradient across the I/V line for the red laser experiment. This suggests some conductance in the system.

Gradients for each line were taken between ±0.5V using linear fitting tool in OriginPro. The measured conductance for the unilluminated data was (0.0209±0.0002) nS. This shows a higher conductance compared to the same measurement taken using the Au tip. This could be due to the Pt tip contacting more molecules on the surface due to a different tip geometry than the Au tip used previously. The measured conductance for the blue laser experiment

was (0.0019±0.0002) nS which suggests that the blue laser illumination acts to quench the conductance compared to the nonilluminated experiment. There was no clear rectification effect in this experiment which was seen using the Au tip. The measured conductance for the red laser experiment was (0.0443±0.0002) nS This is higher than the other experiments in this dataset but lower than the (0.1164±0.0005) nS conductance measured using the Au tip. Here a higher conductance was measured using the red laser as was seen when the Au tip was used. However, the enhancement factor here is lower than what was seen using the

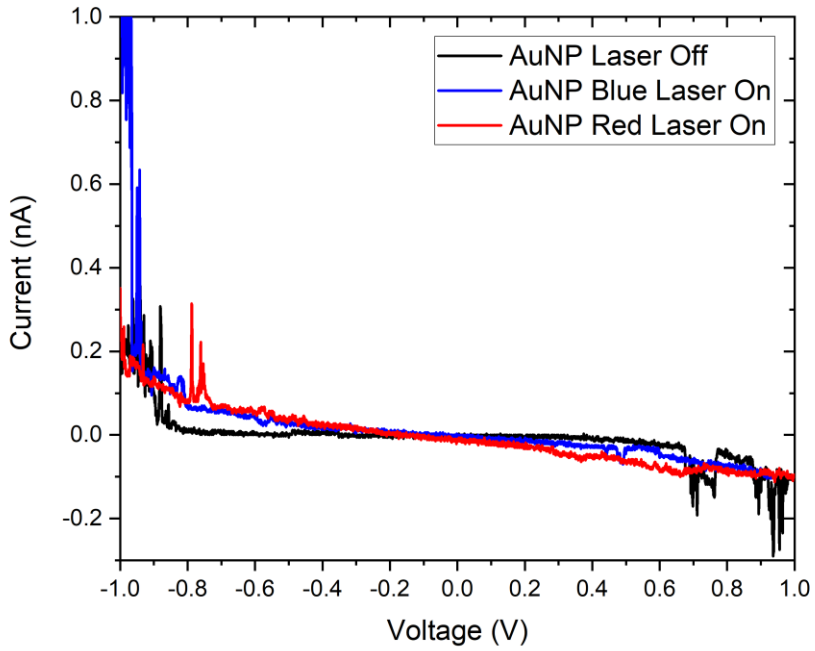

Figure 9-10 - I/V characteristics for 9V9 on Au substrate taken using Pt Tip contacted to an AuNP immobilized on to the monolayer with no illumination and illuminated by either red 644nm laser (red line) or blue 473nm laser (blue line).

Au tip. With the Pt tip and the red laser, the enhancement factor for the conductance is 2.1. This shows that the red laser could be acting to heat the substrate and therefore boosting charge carriers however, the much higher enhancement factor for the Au tip suggests that there is some plasmonic activity that acts between the au tip and the Au substrate which increase the conductance in the junction.

Figure 9-10 shows the I/V traces taken using the Pt tip above a AuNP on the monolayer. The nonilluminated trace appears to show low conductance in the system with some breakdown current at the bias extremities. The blue and red laser illuminated traces appear to show conductance in the system with a higher conductance in the red trace. The measured conductance was taken from the gradient of the lines between ±0.5V. For the nonilluminated case the measured conductance was (0.0133±0.0002) nS which is lower than the same experiment using the Au tip. The lower conductance here is most likely due to poor contact with the molecule using the Pt tip as the hanging thiol group does not attach to platinum as well as it does to gold. The measured conductance for the blue laser illuminated experiment was (0.0602±0.0004) nS. This shows a higher conductance value than the nonilluminated experiment suggesting that the blue laser acts to boost the conductance of the system. The measured conductance for the red laser illuminated experiment was (0.0939±0.0003) nS showing that the illumination from the red laser boosts the conductance compared to the other experiments. Both the illuminated cases in this experiment showed enhanced conductance. The blue laser illumination resulted in a conductance enhancement factor of 4.5 with the red laser giving an enhancement factor of 7.1. This suggests that there is some plasmonic enhancement occurring due to the AuNP. With the gold STM tip the conductance values were quenched under illumination and as discussed, this is likely due to the Au tip plasmon modes interacting with the AuNP modes. Here, with the Pt tip, there is no plasmonic mechanism due to the tip presence. Therefore, the AuNP/substrate plasmonic modes are not affected and plasmonic enhancement can occur. From the UV-vis of the AuNPs in solution we expect a plasmon resonance in the 525nm region. Both the red and blue lasers excite the surface at either side of this resonance. Using a green laser to drive the AuNP plasmons at resonance could reveal whether these effects are truly plasmonic in nature. In order to make more conclusive assertions, extra datasets should be taken of these experiments.

9.5. Molecular Conductance on Au Nanotriangle Arrays

Due to the effect of the conducting AFM tip sweeping the nanoparticles aside when imaging, a configuration using a plasmonic nanostructured substrate was required. Therefore, the Au nanotriangle arrays fabricated using nanosphere shadow lithography were utilised. Initially the 200nm average side length nanotriangle arrays were used in order to test the methodology of contacting molecules on nanostructures. These nanostructures were fabricated using the 800nm diameter polystyrene beads as the bead mask in the NSL method. Once the 90nm side length nanotriangle fabrication was developed, these nanostructures were then used to assess whether plasmonic effects were observable.

Molecular self-assembled monolayers were grown directly onto the nanostructured substrates by immersing the substrates in solution. The specified anchor groups meant that the molecules preferentially adhered to the gold nanostructures rather than the ITO substrate. The substrates were imaged using the conductive gold-coated AFM tips to locate isolated nanotriangles. The current-voltage measurements were taken by probing the tip at the centre of the nanoparticle using the 1nA setpoint. Samples were tested with no illumination (dark) and in four illumination conditions. Samples were illuminated using either a 473nm blue, 532nm green, 644nm red, and a 783nm wavelength red laser. For each experiment at least 200 I/V scans were taken, this data was plotted as histograms and the averages were taken. The average IV plots are shown here.

The raw data files are sorted in order to evaluate which traces were successful. Unsuccessful IV measurements usually show a flat current profile as no contact has been made between the AFM tip and the substrate. Current-voltage measurements were also taken on an uncoated nanostructured sample as a control experiment. These traces, as shown in figure 9-11, show good Ohmic contact with complete saturation in the current preamplifier. These

z-shaped traces show that the experiment is successful and that the equipment functions properly.

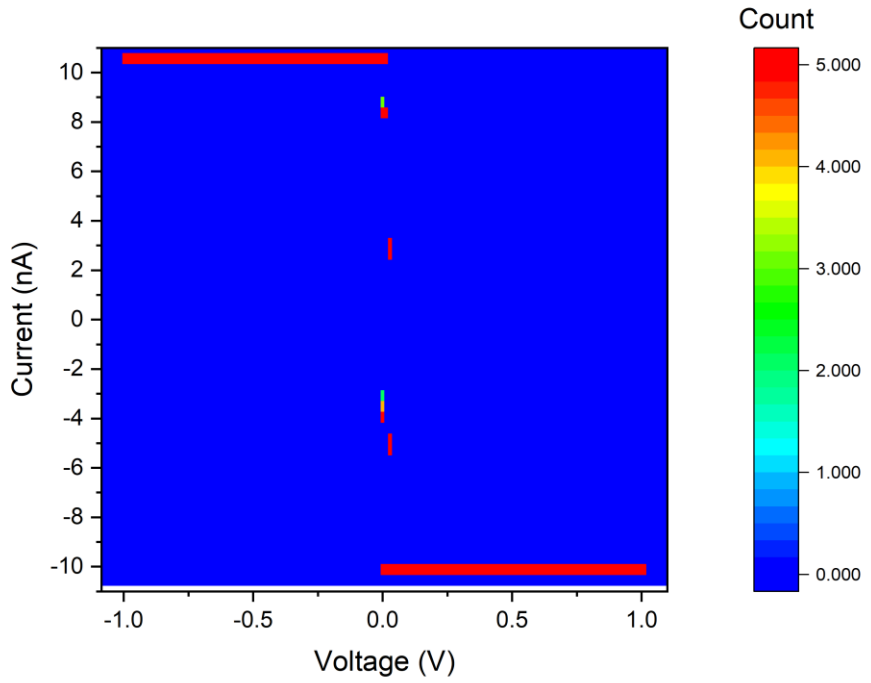

Figure 9-11 - 3D histograms showing Ohmic contact between Au AFM tip and uncoated Au nanostructures.

9.5.1. 1-Decanethiol conductance measurements on 200nm nanotriangle arrays

The molecular wires tested on the 200nm side length nanotriangles were 1-decanethiol, 9V9, and 1,9-nonanedithiol. The molecular conductance measurements were then taken using conductive mode AFM to locate isolated nanotriangles and perform I/V measurements. The nanotriangles were probed at the centre of the nanostructure. Each experiment was done by taking at least 200 I/V scans on each particle, if the AFM tip drifted the measurement was stopped, faulty datasets removed and the AFM tip was recentred over the nanoparticle before the experiment was restarted. Lasers were used to illuminate the samples and the experiments were repeated for each illumination condition subsequently.

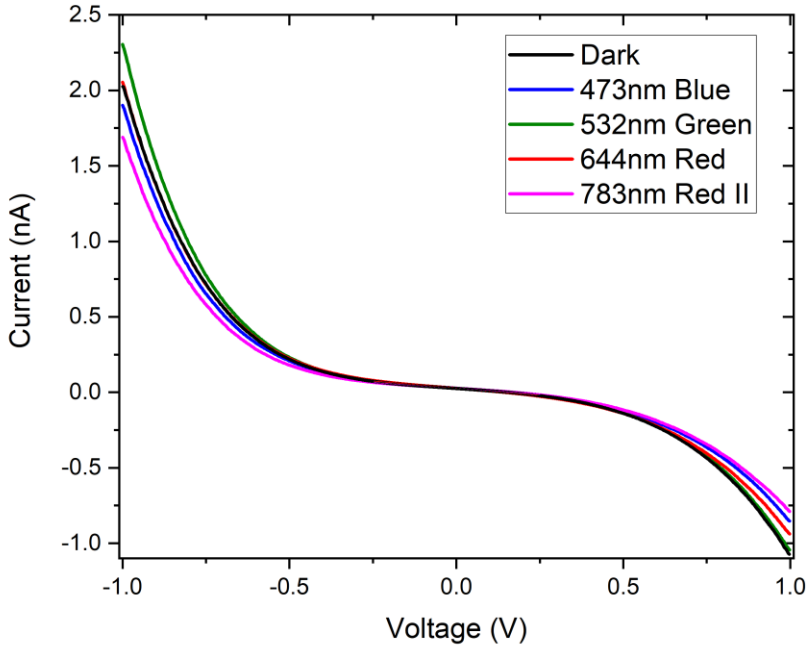

Figure 9-12 – Average C-AFM I/V characteristics of 1-decanethiol on 200nm side-length Au nanotriangles under the various illumination conditions. Data taken from NSL sample 1.

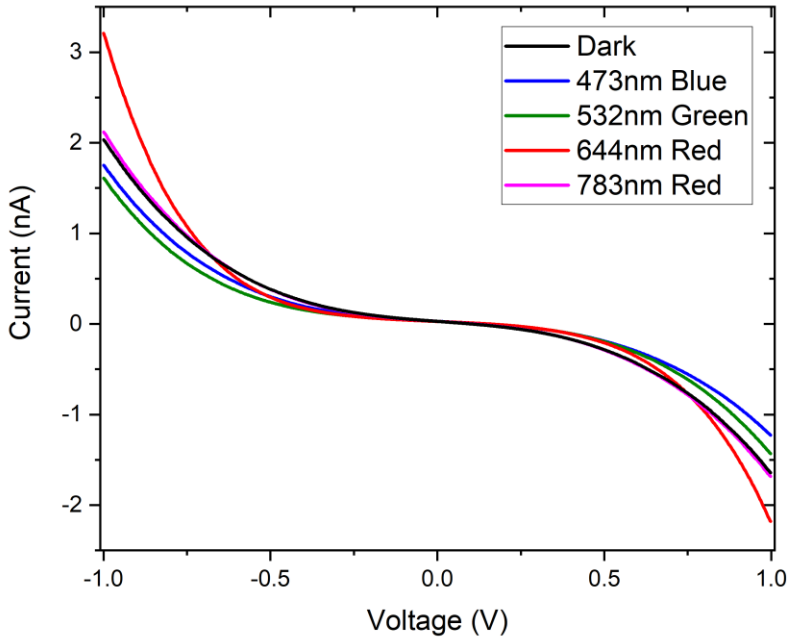

Figure 9-13 – Average C-AFM I/V characteristics of 1-decanethiol on Au 200nm side-length nanotriangles under the various illumination conditions. Data taken from NSL sample 2.

The 1-decanethiol monolayers were grown onto the nanostructured substrates by immersing the substrates in a 0.1mM solution of 1-decanethiol in ethanol for 20 hours. Figure 9-12 and 6-13 show the averaged I/V traces for each illumination condition on separate nanotriangle decorated samples. The experiments were also taken on a standard gold slide, this data is shown in figure 9-14. The maximum currents measured on the nanoparticles is much higher than on the gold slide suggesting better contact to the monolayer and better conductance.

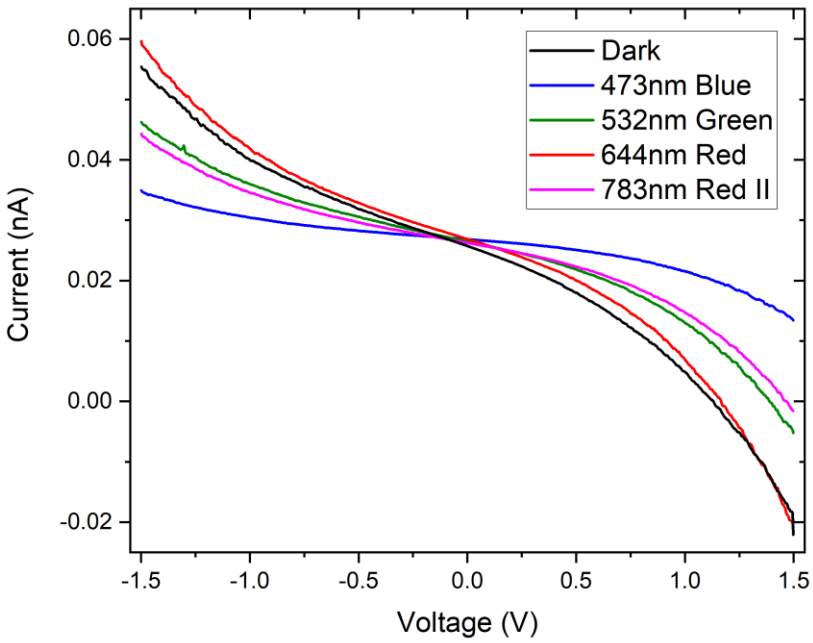

Figure 9-14 – Average C-AFM I/V characteristics of 1-decanethiol on gold substrate under the various illumination conditions. Data taken from the gold slide.

The measured average conductance is calculated by taking the gradient of each line between ±0.1V, the data is shown in table 1. The error of the values is given as the error on the linear fit. The conductance values taken on the nanostructured samples are higher than the gold slide sample. The nanotriangle samples, referred to as sample 1 and sample 2, were nominally the same and fabricated in the exact same way. On sample 1 the conductance

values are fairly similar across the illumination conditions suggesting very little effect on the conductance. The highest conductance was measured for the 644nm laser illuminated experiment, with the 473nm blue laser giving the second highest value. For sample 2 the highest conductance value is taken from the dark scan showing a reduction in the illuminated experiments. This is inconsistent with the first sample values suggesting no overall pattern from illuminating the samples using lasers. The conductance values measured on the gold slide are far lower than the nanostructured substrates by nearly an order of magnitude. This suggests that less molecules are contacted on the gold slide.

	Sample 1 (nS)	Sample 2 (nS)	Gold Slide (nS)
Dark	(0.1525±0.0002)	(0.2811±0.0005)	(0.0126±0.0002)
Blue	(0.1674±0.0002)	(0.1933±0.0005)	(0.00272±0.000007)
Green	(0.1522±0.0002)	(0.1779±0.0002)	(0.00769±0.00001)
Red	(0.1717±0.0002)	(0.1643±0.0002)	(0.0112±0.00001)
Red II	(0.1403±0.0002)	(0.2605±0.0005	(0.00642±0.000008)

Table 1 – Conductance values measured for 1-decanethiol on different samples under each illumination condition measured between ±0.1V. Sample 1 and sample 2 were nominally the same. The gold slide was a standard gold substrate as used in previous experiments.

The dark conditions conductance values for 1-decanethiol on the nanostructured substrate given here are higher than the value given by Frisbie[1] of 0.077 nS. With the sample 1 result being higher by a factor of just under 2 and the sample 2 value being larger by a factor of 3.6. This suggests that in both of these cases multiple molecular wires are contacted by the AFM tip. This could be verified by measuring the tip radius in order to find the conducting area and dividing the values measured accordingly.[1,20] The value calculated from the measurements on the gold slide is lower than the calculated value by Frisbie by a factor of 0.16. It is difficult to qualitatively explain this inaccuracy but it is possible that poor monolayer formation is to blame.

9.5.2. 9V9 Conductance Measurements on 200nm side-length AuNT Arrays

Self-assembled monolayers of the 9V9 molecule were deposited onto the nanostructured substrate by immersing the substrate in a 0.1mM 9V9 in ethanol solution for 20 hours. The sample was then placed in the AFM and the same experiments were performed. For each illumination condition at least 200 I/V scans were taken as before.

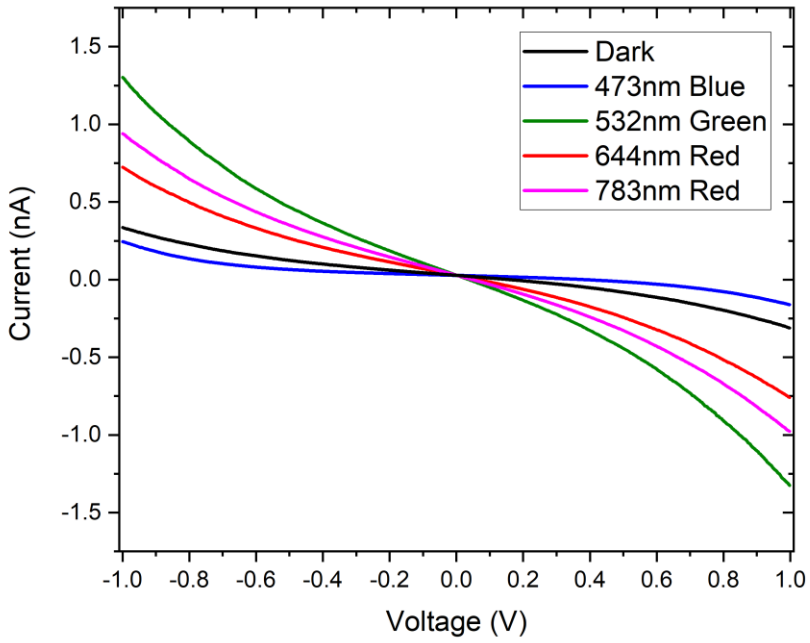

Figure 9-15 Average C-AFM I/V characteristics of 9V9 on 200nm side-length Au nanotriangle under the various illumination conditions.

Figure 9-15 shows the average IV curves for the different illumination conditions of the 9V9 coated sample. The conductance values were calculated by taking the gradient of each line between ±0.1V. This figure clearly shows varying conductance values for each of the illumination conditions, it is unlikely that this is due to some plasmonic effect from the gold nanostructures as, from the UV-Vis, very little plasmonic behaviour is expected from the 200nm nanotriangle substrates. Table 2 shows the conductance values that were calculated

by taking the gradient of the lines. The dark scan gives a conductance value for the 9V9 monolayer of (0.1671±0.0001) nS. The highest average conductance was measured for the 532nm laser illuminated experiment at (0.7792±0.0004) nS. The lowest average conductance was measured for the experiment with the blue laser light illumination. The value for the conductance of the 9V9 monolayer was (0.05637±0.00004) nS suggesting some quenching due to the incident blue illumination. These results show various effects of the illumination from a quenching of the conductance under the 473nm laser of 64%, to an enhancement by a factor of 4 under 532nm laser light. Due to the absorption characteristics of the nanostructured substrates, it is unlikely that these effects are due to the plasmonic properties of the substrate alone. However, it is possible that these show plasmonic enhancement from some gap mode between the Au tip and the Au nanoparticle but that was not shown in the 1-decanethiol experiments.

Illumination Condition	9V9 Conductance (nS)
Dark	0.1671±0.0001
Blue	0.05637±0.00004
Green	0.7792±0.0004
Red	0.4287±0.0004
Red II	0.5894±0.0003

Table 2 - Conductance Values for 9V9 measured on 200nm side-length Au nanotriangle array under various illumination conditions. Taken from data in figure 1-27 measured between between ±0.1V

For 10V10 Haiss et al.[4] measured a conductance value of 0.13nS, and for 9V9, with a shorter carbon chain length it is expected that the conductance will be higher. In this work a conductance value of 0.1671nS is measured which is, as expected, higher than the 10V10 value. However, the 9V9 molecule should be measured using other methods such as STM I(s) and STM I(v) to verify this experiment. Differences in conductance values were observed when the illumination conditions changed alluding to the possibility of plasmonic interaction

and enhancement. Additional experiments to verify the dark conductance value and therefore the experiment would make this result more conclusive.

9.5.3. 1,9-Nonanedithiol Conductance Measurements on 200nm side-length AuNT Arrays.

Self-assembled monolayers of 1,9-nonanedithiol were prepared on the nanostructured substrates by immersing the substrate in a 0.1mM 1,9-nonanedithiol in ethanol solution. The substrates were then tested using C-AFM as before under the different illumination conditions. Conductance values were calculated by taking the line gradient between ±0.1V.

For the -dithiol molecules the hanging functional -thiol group led to the molecules coating the gold AFM tips. This meant that the tips were quickly contaminated with the molecule from the monolayer. This led to poor results from the conductance measurements. The tips could be sputtered clean by running an I/V scan with high bias but the measurements were still affected. The deep red laser was not used for this experiment as it was unavailable at the time.

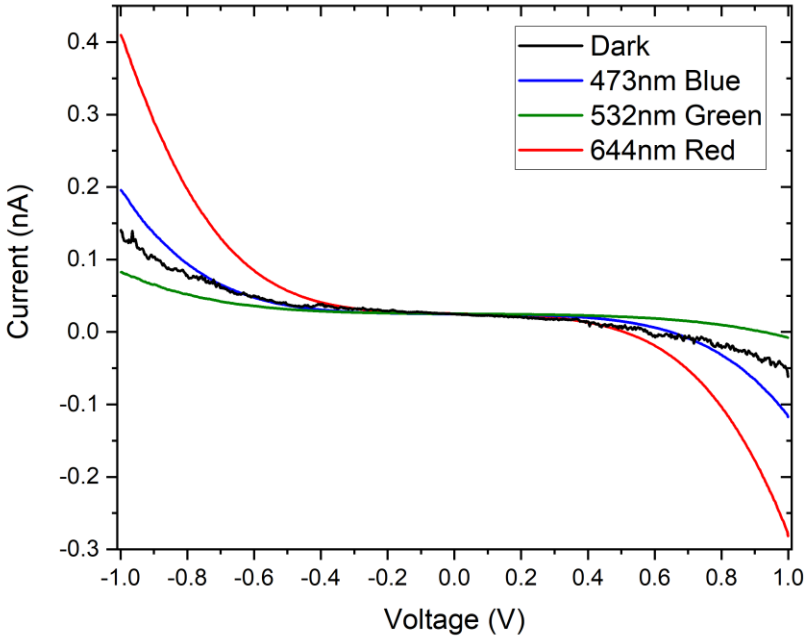

Figure 9-16 -Average C-AFM I/V characteristics for 1-,9 nonanedithiol monolayers on 200nm side-length Au nanotriangle arrays under the various illumination conditions

Figure 9-16 shows the average I/V curves for the 1,9-nonanedithiol monolayer on the nanostructured substrate. The traces show very similar lines in the low bias range but with varying breakdown, or take-off, currents. The calculated conductance values are shown in Table 3. The dark experiment gave the highest measured conductance at (0.0245±0.0004) nS with the illuminated experiments all giving much lower values than this. Of the illuminated experiments, the red laser gave the highest conductance value at (0.00879±0.00004) nS. This gives and decrease in conductance compared to the dark experiment of 64%. The lowest conductance value was taken from the green laser experiment, with a calculated conductance value of (0.00359±0.00003) nS and the blue laser illuminated experiment performed similarly at (0.00374±0.00002) nS. These values give a reduction in conductance of roughly 85% for both experiments.

Illumination Condition	1,9-nonanedithiol Conductance (nS)
Dark	0.0245±0.0004
Blue Laser	0.00374±0.00002
Green Laser	0.00359±0.00003
Red Laser	0.00879±0.00004

Table 3 - Conductance Values for 1,9-Nonanedithiol on 200nm side-length Au nanotriangle arrays under the various illumination conditions. Measured using data in figure 1-28 between ±0.1V.

For the 1,9-nonanedithiol, the use of any external lasers resulted in a reduction of the measured conductance values similar to what was seen for the decanethiol experiments. The quenching of the conductance seen in the 1,9-nonanedithiol is much more severe than previous molecules. When extrapolating from the figure in the paper by Haiss[3] the values given for 1,9-nonandithiol were 0.39 nS, 1.57 nS, and 6.7 nS for the low, medium, and high conductance values respectively. In this work the dark conductance value is lower than even the low conductance mode value given by over an order of magnitude. This is because the -dithiol experiments were difficult to perform due to contamination of the tip from the hanging functional groups on the molecules. In the work by Haiss[3] the molecules are trapped between the AuNP and the substrate by functionalization, this means that the AFM tip is protected by contamination, in this work the hanging thiol groups were able to functionalize to the probing tip and disrupt the experiment. This showed that molecules with functional groups at either end of the molecular wire were unsuitable for this experiment, unless the AFM or STM tips are properly protected.[20]

9.6. Conclusions

Molecular conductance values for 9V9 were measured in an Au tip-molecule-Au junction with potential plasmonic enhancement observed. Conductance values for 9V9 have not been previously reported in the literature. The 1-nonanedithiol and 9V9 molecules were attached directly to Au nanotriangles with an average side-length of 200nm nanostructures on a conductive glass substrate, fabricated using NSL. The conductance values of these molecules were measured by contact with a conductive AFM tip directly to the monolayer. There was enhancement of the conductance value for 9V9 was enhanced under illumination. This suggests potential plasmonic enhancement from a gap plasmon mode between the Au AFM tip and surface of the Au nanostructures. The conductance of molecules attached directly to triangular nanostructures fabricated through NSL has not been previously reported.

The conductance of the 9V9 molecule was measured using Au and Pt STM tips, and under illumination from a variety of lasers, in order to assess any differences through choice of tip material. When measured directly in contact with the monolayer with no external illumination the conductance values for the 9V9 were calculated to be 0.008 nS and 0.02 nS for the Au and Pt tips respectively. The samples were then illuminated using a red and blue laser and the I/V characteristics were again taken. For the Au tip contacting the monolayer under red light illumination the conductance value measured was 0.12 nS. This gives an enhancement factor compared to the dark conditions of 14.6. Under blue illumination the conductance value was 0.07 nS giving an enhancement factor of 8. This suggests that either the incident light is heating the monolayer, and having some effect, or, there is some nanogap plasmon mode with a strong e-field contribution boosting the conductance of the molecule trapped in the gap. With the Pt tip directly contacting the monolayer and illuminated by the red laser the conductance value was 0.044ns giving an enhancement factor of 2.1. Under blue illumination the value was lower than the dark condition value at

0.002nS, showing quenching of the conductance value. As no gap plasmon mode is expected with the Pt tip it is likely that the red laser has some thermal effect on the molecules in the monolayer leading to slightly better conductance. However, the enhancement under red light illumination with the Au tip is much higher than the Pt tip meaning that the enhancement must not be all due to heating and an expected gap mode may be active. This is also strengthened by the fact that enhancement was seen for blue light illumination with the Au tip whereas a reduction in conductance was seen for Pt. Further work should be done in order to confirm the plasmon mode between the gold tip and the Au substrate.

Gold nanotriangles fabricated through the nanosphere shadow lithography were then used as plasmonic substrates in order to observe the effects on molecular conductance measurements. Initially, arrays of larger nanotriangles with average side-lengths of 200nm were used in order to assess the experimental conditions needed. Conductance mode AFM techniques were employed to image and then probe the conductance of molecular monolayers on the substrate. The first molecule tested was the 1-decanethiol, two nanostructured samples and one standard gold slide sample were tested. In dark conditions the conductance values for the nanostructured samples were 0.15nS and 0.28nS, the gold slide sample returned a conductance value of 0.012nS. The conductance value for 1-decanethiol given by Frisbie[1] using a similar technique on a gold slide was 0.077nS. Therefore, the results here are likely due to multiple molecules trapped in the junction. The dark experiment value from the first sample is close to double the value given by Frisbie suggesting that 2 molecules on average are measured in the junction. The 0.28nS value given in the second sample is 3.6 times higher than the value given by Frisbie suggesting on average around 4 molecules are trapped in the junction.

The next molecule tested was the 9V9, under dark conditions the conductance value measured of 0.17 nS is within a 10% deviation of the 0.15n S measured using the spherical

AuNP and STM method. This value is also consistent with what is expected for 9V9, which was a value slightly higher than the 0.12 nS measured for 10V10 by Haiss[4]. Under the different illumination conditions considerable differences in the conductance values of the 9V9 measured were observed. The maximum enhancement was seen under illumination from the green 532nm laser with an enhancement factor of 4.7. Under blue laser illumination with a wavelength of 478nm the conductance value was 0.056nS showing a quenching of the conductance by a factor of 0.34. From optical spectroscopy results from the nanodecorated substrate there is not a plasmonic resonance peak expected to exist in the optical range from the 200nm nanotriangles. However, a gap mode between the Au tip and the nanostructure surface is likely. The enhancement seen here could be attributed to this gap mode and is either due to the localised electric field enhancing the conductance of single molecules or resulting in more molecules trapped in the junction.

9.7. Bibliography

1. Wold, D. J. & Frisbie, C. D. Formation of a Metal - Molecule - Metal Junction by Contacting an Alkanethiol Self-Assembled Monolayer with Formation of Metal - Molecule - Metal Tunnel Junctions : Microcontacts to Alkanethiol Monolayers with a Conducting AFM Tip Department of Chemical E. *J. Am. Chem. Soc* **122**, 2970–2971 (2000).

2. Morita, T. & Lindsay, S. Determination of single molecule conductances of alkanedithiols by conducting-atomic force microscopy with large gold nanoparticles. *J. Am. Chem. Soc.* **129**, 7262–7263 (2007).

3. Haiss, W., Martín, S., Leary, E., Van Zalinge, H., Higgins, S. J., Bouffier, L. & Nichols, R. J. Impact of junction formation method and surface roughness on single molecule conductance. *J. Phys. Chem. C* **113**, 5823–5833 (2009).

4. Haiss, W., Nichols, R. J., Higgins, S. J., Bethell, D., Höbenreich, H. & Schiffrin, D. J. Wiring nanoparticles with redox molecules. *Faraday Discuss.* **125**, 179–194 (2004).

5. Oxford Instruments. AFM Tools for Nanoscale Electrical Characterization. *Asylum Res.* **12**, 42 (2009).

6. NT-MDT Spectrum Instruments. The Principles of Operation of an Atomic Force Microscope (AFM) dc Contact Techniques. 1–10 (2015).

7. Haick, H. & Cahen, D. Making contact: Connecting molecules electrically to the macroscopic world. *Prog. Surf. Sci.* **83**, 217–261 (2008).

8. Cui, X. D., Primak, A., Zarate, X., Tomfohr, J., Sankey, O. F., Moore, A. L., Moore, T. A., Gust, D., Harris, G. & Lindsay, S. M. Reproducible measurement of single-molecule

conductivity. *Science (80-.).* **294**, 571–574 (2001).

9. Dai, H., Wong, E. W. & Lieber, C. M. Probing electrical transport in nanomaterials: Conductivity of individual carbon nanotubes. *Science (80-.).* **272**, 523–526 (1996).

10. Alperson, B., Cohen, S., Rubinstein, I. & Hodes, G. Room-temperature conductance spectroscopy of CdSe quantum dots using a modified scanning force microscope. *Phys. Rev. B* **52**, 17–20 (1995).

11. Fung, E. D., Adak, O., Lovat, G., Scarabelli, D. & Venkataraman, L. Too Hot for Photon-Assisted Transport: Hot-Electrons Dominate Conductance Enhancement in Illuminated Single-Molecule Junctions. *Nano Lett.* **17**, 1255–1261 (2017).

12. Rubio-Bollinger, G., Castellanos-Gomez, A., Bilan, S., Zotti, L. A., Arroyo, C. R., Agraït, N. & Cuevas, J. C. Carbon-fiber tips for scanning probe microscopes and molecular electronics experiments. *Nanoscale Res. Lett.* **7**, 2–5 (2012).

13. Tao, N. J. Electron transport in molecular junctions. in *Nanoscience and Technology: A Collection of Reviews from Nature Journals* vol. 1 185–193 (2009).

14. Haiss, W., Wang, C., Grace, I., Batsanov, A. S., Schiffrin, D. J., Higgins, S. J., Bryce, M. R., Lambert, C. J. & Nichols, R. J. Precision control of single-molecule electrical junctions. *Nat. Mater.* **5**, 995–1002 (2006).

15. Bastús, N. G., Comenge, J. & Puntes, V. Kinetically controlled seeded growth synthesis of citrate-stabilized gold nanoparticles of up to 200 nm: Size focusing versus ostwald ripening. *Langmuir* **27**, 11098–11105 (2011).

16. Chen, X., Goubert, G., Jiang, S. & Van Duyne, R. P. Electrochemical STM Tip-Enhanced Raman Spectroscopy Study of Electron Transfer Reactions of Covalently Tethered Chromophores on Au(111). *J. Phys. Chem. C* **122**, 11586–11590 (2018).

17. Schultz, Z. D., Marr, J. M. & Wang, H. Tip enhanced Raman scattering: Plasmonic enhancements for nanoscale chemical analysis. *Nanophotonics* vol. 3 91–104 (2014).

18. Zhang, W., Schmid, T., Yeo, B. S. & Zenobi, R. Near-field heating, annealing, and signal loss in tip-enhanced Raman spectroscopy. *J. Phys. Chem. C* **112**, 2104–2108 (2008).

19. Baffou, G. & Quidant, R. Nanoplasmonics for chemistry. *Chem. Soc. Rev.* **43**, 3898–3907 (2014).

20. Engelkes, V. B., Beebe, J. M. & Frisbie, C. D. Analysis of the Causes of Variance in Resistance Measurements on Metal-Molecule-Metal Junctions Formed by Conducting-Probe Atomic Force Microscopy. *J. Phys. Chem. B* **109**, 16801–16810 (2005).

10.Conclusions and Further Work

The work in this thesis aimed to observe the effects of plasmonic substrates on the photocatalytic ability of hematite photoanodes and the conductance of molecular wires. A platform of plasmonic substrates was developed using nanosphere shadow lithography and it was shown to be possible to control size and shape through the size selection of beads in the mask, angled deposition, and radial etching times. The plasmon resonance peak position of these substrates could also be controlled through size and metal choice with Au, Ag, Al and Cu nanostructures developed.

These substrates were shown to enhance the photocatalytic ability of electrodeposited α-Fe_2O_3 films using photoelectrochemical experiments. A tin-doped hematite electrodeposition method was developed in order to reliably fabricate functioning hematite films on top of the plasmonic substrates. The undecorated Sn-doped hematite films showed an average photocurrent density of (11±2) $\mu A.cm^{-2}$. Hematite electrodes developed on top of the Au 88nm triangular nanostructures gave enhanced photocurrent densities with an average of (20±5) $\mu A.cm^{-2}$ giving an average enhancement factor of 1.9. The champion electrode had a photocurrent density of 42.4 $\mu A.cm^{-2}$ resulting in a maximum plasmonic enhancement factor of 3.6. It is proposed that the mechanism by which these nanostructures enhance the photocurrent is through plasmon-induced resonant energy transfer. The low overlap between the LSPR peak position and hematite absorption rules out light-scattering and Förster resonant energy transfer. Hot hole injection could also contribute to the enhancement factor but was not proved. Simulations shown in chapter 6 show large electric field enhancement confined to the triangle vertices and these highly resonant fields can promote charge carrier production in semiconductors.

Ag/TiO_2 composite nanostructured substrates were developed by including rf-sputtering of a TiO_2 target. The 88nm Ag nanostructures were capped with TiO_2 by sputtering the TiO_2 through the nanosphere mask after the Ag metal had been deposited. These nanostructured substrates were then coated in hematite through electrodeposition realising the largest plasmonic enhancement of hematite seen in this work. The average photocurrent density was (40±10) $\mu A.cm^{-2}$ giving an average enhancement factor of 3.6. The champion electrode gave a photocurrent density of 82.3 $\mu A.cm^{-2}$ giving the highest enhancement factor of 7.5. The TiO_2 layer acted as a hole blocking layer to reduce recombination at the Ag/hematite interface. There is good spectral overlap with the Ag LSPR and hematite absorption suggesting that light-scattering is a possible mechanism for this enhancement. Resonant energy transfer is also possible due to the enhanced fields discussed previously. Further work is required to fully understand the mechanism by which these nanostructures increase the photocatalytic ability of the electrodeposited hematite films, such as transient absorption spectroscopy to observe charge transfer.

Atomic layer deposition was also used to fabricate nanostructure decorated hematite films. The ALD deposited electrodes gave reduced photocurrent densities when the metal nanostructure layers were included. However, relative spectral enhancement was seen in the incident photon to electron efficiency (IPCE) measurements. This suggests that there are competing mechanisms surrounding the plasmonic effects on the nanostructures that result in an overall photocurrent reduction. Alumina intermittent layers were added to the ALD deposited films between the metal nanostructures and the hematite. Overall, the photocurrents were reduced by the addition of this layer however the relative reduction between the undecorated and decorated samples was narrowed. Real spectral enhancement was also seen in the IPCE for the Au/Al_2O_3/hematite between 360-440 nm. Relative spectral enhancement was seen in the IPCE for Ag/Al_2O_3/hematite and

Al/Al_2O_3/hematite electrodes. This suggested that the alumina layer assisted with selectively blocking some charge carriers but the necessary electron extraction was hindered.

Better understanding of these mechanisms could be found by altering the deposition techniques to selectively cap the nanostructures as was achieved in chapter 7. Selective capping of the metal nanostructures could help to isolate them from the hematite film without detrimentally affecting charge extraction from the semiconductor layer. This could be done chemically in a similar way to how SHINs are made or using physical deposition techniques as was done in chapter 7. Increasing the film thickness of the hematite could allow for a more accurate study on light-scattering as the increased pathlength of the scattered light would have a more observable effect. Observing the effects of additional intermittent layers such as TiO_2 or a material that could act as an electron blocking layer with higher conduction and valence band energies to verify that hole-blocking was the working mechanism.

Conductance measurements using SPM techniques were performed on the plasmonic substrates to attempt to observe plasmonic effects on single molecule junctions. This is the first reported time of molecular conductance measurements performed directly on nanostructures fabricated using NSL. This establishes a methodology platform for the measurement of conductance, and observation of potential plasmonic enhancement, for molecules directly attached to nanostructured substrates, such as those fabricated using NSL. Self-assembled monolayers were formed on top of 200nm average side length Au nanotriangle arrays that were fabricated through NSL. Conductance values were taken by contacting the monolayer on top of the nanostructures. No overall enhancement in conductance was observed however some reductions were seen under illumination. More data and rigorous statistical analysis are needed to draw conclusions for these effects. The AFM tip geometry needs to be considered in order to calculate the contact area in these

configurations. Measurements should also be taken with protected AFM tips in order to reduce statistical variance.

Au nanospheres were synthesised and immobilized on self-assembled monolayers of 9V9 and were contacted using STM. STM measurements were also taken of the 9V9 molecule on the gold slide using a gold STM tip. The conductance values were measured under blue (473nm) and red (644nm) laser illumination and an effect on the conductance was seen. Under red illumination the conductance was seen to increase in the STM tip/molecule/substrate configuration. It was not possible to make conclusions until more identical measurements were taken and statistically analysed. At least ~200 scans are generally required to make effects statistically relevant and to draw conclusions.